

1 A search for sparticles in zero lepton final states

2 Russell W. Smith

3 Submitted in partial fulfillment of the

4 requirements for the degree of

5 Doctor of Philosophy

6 in the Graduate School of Arts and Sciences

7 COLUMBIA UNIVERSITY

8 2016

9

© 2016

10

Russell W. Smith

11

All rights reserved

12

ABSTRACT

13

A search for sparticles in zero lepton final states

14

Russell W. Smith

15 TODO : Here's where your abstract will eventually go. The above text is all in the
16 center, but the abstract itself should be written as a regular paragraph on the page,
17 and it should not have indentation. Just replace this text.

Contents

19	Contents	i
20	1 Introduction	1
21	2 The Standard Model	5
22	2.1 Overview	5
23	2.2 Field Content	5
24	2.3 Deficiencies of the Standard Model	15
25	3 Supersymmetry	21
26	3.1 Supersymmetric theories : from space to superspace	21
27	3.2 Minimally Supersymmetric Standard Model	24
28	3.3 Phenomenology	30
29	3.4 How SUSY solves the problems with the SM	33
30	3.5 Conclusions	35
31	4 The Large Hadron Collider	37
32	4.1 Basics of Accelerator Physics	37
33	4.2 Accelerator Complex	39
34	4.3 Large Hadron Collider	41
35	4.4 Dataset Delivered by the LHC	43
36	5 The ATLAS detector	49

37	5.1	Magnets	50
38	5.2	Inner Detector	52
39	5.3	Calorimetry	56
40	5.4	Muon Spectrometer	61
41	5.5	Trigger System	66
42	6	Object Reconstruction	73
43	6.1	Primitive Object Reconstruction	73
44	6.2	Physics Object Reconstruction and Quality Identification	79
45	7	Recursive Jigsaw Reconstruction	105
46	7.1	Razor variables	105
47	7.2	Recursive Jigsaw Reconstruction	110
48	7.3	Variables used in the search for zero lepton SUSY	116
49	8	A search for supersymmetric particles in zero lepton final states with the Recursive Jigsaw Technique	123
50	8.1	Simulation samples	123
51	8.2	Event selection	127
52	8.3	Background estimation	134
54	9	Results	159
55	9.1	Statistical Analysis	159
56	9.2	Signal Region distributions	159
57	9.3	Pull Plots	160
58	9.4	Exclusion plots	160
59	Conclusion		165
60	9.5	New Section	165

61	Bibliography	167
62	Quantum Field Theory and Symmetries	179
63	Quantum Field Theory	179
64	Symmetries	180
65	Local symmetries	182
66	Additional N-1 plots	187
67	Compressed region N-1 plots	187

Acknowledgements

Dedication

Introduction

72 Particle physics is a remarkably successful field of scientific inquiry. The ability to
 73 precisely predict the properties of a exceedingly wide range of physical phenomena,
 74 such as the description of the cosmic microwave background [1, 2], the understanding
 75 of the anomalous magnetic dipole moment of the electron [3, 4], and the measurement
 76 of the number of weakly-interacting neutrino flavors [5] is truly amazing.

77 The theory that has allowed this range of predictions is the *Standard Model*
 78 of particle physics (SM). The Standard Model combines the electroweak theory of
 79 Glashow, Weinberg, and Salam [6–8] with the theory of the strong interactions, as
 80 first envisioned by Gell-Mann and Zweig [9, 10]. This quantum field theory (QFT)
 81 contains a tiny number of particles, whose interactions describe phenomena up to at
 82 least the TeV scale. These particles are manifestations of the fields of the Standard
 83 Model, after application of the Higgs Mechanism. The particle content of the SM
 84 consists only of the six quarks, the six leptons, the four gauge bosons, and the scalar
 85 Higgs boson.

86 Despite its impressive range of described phenomena, the Standard Model has
 87 some theoretical and experimental deficiencies. The SM contains 26 free parameters
 88 ¹. It would be more theoretically pleasing to understand these free parameters in
 89 terms of a more fundamental theory. The major theoretical concern of the Standard
 90 Model, as it pertains to this thesis, is the *hierarchy problem*[11–15]. The light mass

¹This is the Standard Model corrected to include neutrino masses. These parameters are the fermion masses (6 leptons, 6 quarks), CKM and PMNS mixing angles (8 angles, 2 CP-violating phases), W/Z/Higgs masses (3), the Higgs field expectation value, and the couplings of the strong, weak, and electromagnetic forces (3 α_{force}).

of the Higgs boson (125 GeV) should be quadratically dependent on the scale of UV physics, due to the quantum corrections from high-energy physics processes. The most perplexing experimental issue is the existence of *dark matter*, as demonstrated by galactic rotation curves [16–22]. This data has shown that there exists additional matter which has not yet been seen interacting with the particles of the Standard Model. There is no particle in the SM which can act as a candidate for dark matter.

Both of these major issues, as well as numerous others, can be solved by the introduction of *supersymmetry* (SUSY) [15, 23–35]. In supersymmetric theories, each SM particles has a so-called *superpartner*, or sparticle partner, differing from given SM particle by 1/2 in spin. These theories solve the hierarchy problem, since the quantum corrections induced from the superpartners exactly cancel those induced by the SM particles. In addition, these theories are usually constructed assuming *R*–parity, which can be thought of as the “charge” of supersymmetry, with SM particles having $R = 1$ and sparticles having $R = -1$. In collider experiments, since the incoming SM particles have total $R = 1$, the resulting sparticles are produced in pairs. This produces a rich phenomenology, which is characterized by significant hadronic activity and large missing transverse energy (E_T^{miss}), which provide significant discrimination against SM backgrounds [36].

Despite the power of searches for supersymmetry where E_T^{miss} is a primary discriminating variable, there has been significant interest in the use of other variables to discriminate against SM backgrounds. These include searches employing variables such as αT , $M_{T,2}$, and the razor variables (M_R, R^2) [37–47]. In this thesis, we will present the first search for supersymmetry using the novel Recursive Jigsaw Reconstruction (RJR) technique. RJR can be considered the conceptual successor of the razor variables. We impose a particular final state “decay tree” on an events, which roughly corresponds to a simplified Feynmann diagram in decays containing weakly-interacting particles. We account for the missing degrees of freedom associated

118 to the weakly-interacting particles by a series of simplifying assumptions, which allow
119 us to calculate our variables of interest at each step in the decay tree. This allows an
120 unprecedented understanding of the internal structure of the decay and the ability to
121 construct additional variables to reject Standard Model backgrounds.

122 This thesis details a search for the superpartners of the gluon and quarks, the
123 gluino and squarks, in final states with zero leptons, with 13.3 fb^{-1} of data using the
124 ATLAS detector. We organize the thesis as follows. The theoretical foundations of
125 the Standard Model and supersymmetry are described in Chapters 2 and 3. The
126 Large Hadron Collider and the ATLAS detector are presented in Chapters 4 and 5.
127 Chapter 5 provides a detailed description of Recursive Jigsaw Reconstruction and a
128 description of the variables used for the particular search presented in this thesis.
129 Chapter 6 presents the details of the analysis, including details of the dataset, object
130 reconstruction, and selections used. In Chapter 7, the final results are presented;
131 since there is no evidence of a supersymmetric signal in the analysis, we present the
132 final exclusion curves in simplified supersymmetric models.

135 2.1 Overview

136 A Standard Model is another name for a theory of the internal symmetry group
 137 $SU(3)_C \otimes SU(2)_L \otimes U(1)_Y$, with its associated set of parameters. *The Standard*
 138 Model refers specifically to a Standard Model with the proper parameters to describe
 139 the universe. The SM is the culmination of years of work in both theoretical
 140 and experimental particle physics. In this thesis, we take the view that theorists cite

141 construct a model with the field content and symmetries as inputs, and write down the
 142 most general Lagrangian consistent with those symmetries. Assuming this model is
 143 compatible with nature (in particular, the predictions of the model are consistent with
 144 previous experiments), experimentalists are responsible measuring the parameters of
 145 this model. This will be applicable for this chapter and the following one.

146 Additional theoretical background is in 9.5. The philosophy and notations are
 147 inspired by [48, 49].

148 2.2 Field Content

The Standard Model field content is

$$\begin{aligned} \text{Fermions} &: Q_L(3, 2)_{+1/3}, U_R(3, 1)_{+4/3}, D_R(3, 1)_{-2/3}, L_L(1, 2)_{-1}, E_R(1, 1)_{-2} \\ \text{Scalar (Higgs)} &: \phi(1, 2)_{+1} \\ \text{Vector Fields} &: G^\mu(8, 1)_0, W^\mu(1, 3)_0, B^\mu(1, 1)_0 \end{aligned} \tag{2.1}$$

149 where the $(A, B)_Y$ notation represents the irreducible representation under $SU(3)$
150 and $SU(2)$, with Y being the electroweak hypercharge. Each of these fermion fields
151 has an additional index, representing the three generation of fermions.

152 We observed that Q_L, U_R , and D_R are triplets under $SU(3)_C$; these are the *quark*
153 fields. The *color* group, $SU(3)_C$ is mediated by the *gluon* field $G^\mu(8, 1)_0$, which has
154 8 degrees of freedom. The fermion fields $L_L(1, 2)_{-1}$ and $E_R(1, 1)_{-2}$ are singlets under
155 $SU(3)_C$; we call them the *lepton* fields.

156 Next, we note the “left-handed” (“right-handed”) fermion fields, denoted by L (R)
157 subscript, The left-handed fields form doublets under $SU(2)_L$. These are mediated
158 by the three degrees of freedom of the “W” fields $W^\mu(1, 3)_0$. These fields only act
159 on the left-handed particles of the Standard Model. This is the reflection of the
160 “chirality” of the Standard Model; the left-handed and right-handed particles are
161 treated differently by the electroweak forces. The right-handed fields, U_R, D_R , and
162 E_R , are singlets under $SU(2)_L$.

163 The $U(1)_Y$ symmetry is associated to the $B^\mu(1, 1)_0$ boson with one degree of
164 freedom. The charge Y is known as the electroweak hypercharge.

165 To better understand the phenomenology of the Standard Model, let us investigate
166 each of the *sectors* of the Standard Model separately.

167 Electroweak sector

The electroweak sector refers to the $SU(2)_L \otimes U(1)_Y$ portion of the Standard
Model gauge group. Following our philosophy of writing all gauge-invariant and
renormalizable terms, the electroweak Lagrangian can be written as

$$\mathcal{L} = W_a^{\mu\nu} W_{\mu\nu}^a + B^{\mu\nu} B_{\mu\nu} + (D^\mu \phi)^\dagger D_\mu \phi - \mu^2 \phi^\dagger \phi - \lambda (\phi^\dagger \phi)^2. \quad (2.2)$$

where $W_a^{\mu\nu}$ are the three ($a = 1, 2, 3$) gauge bosons associated to the $SU(2)_L$ gauge
group, $B^{\mu\nu}$ is the one gauge boson of the $U(1)_Y$ gauge group, and ϕ is the complex

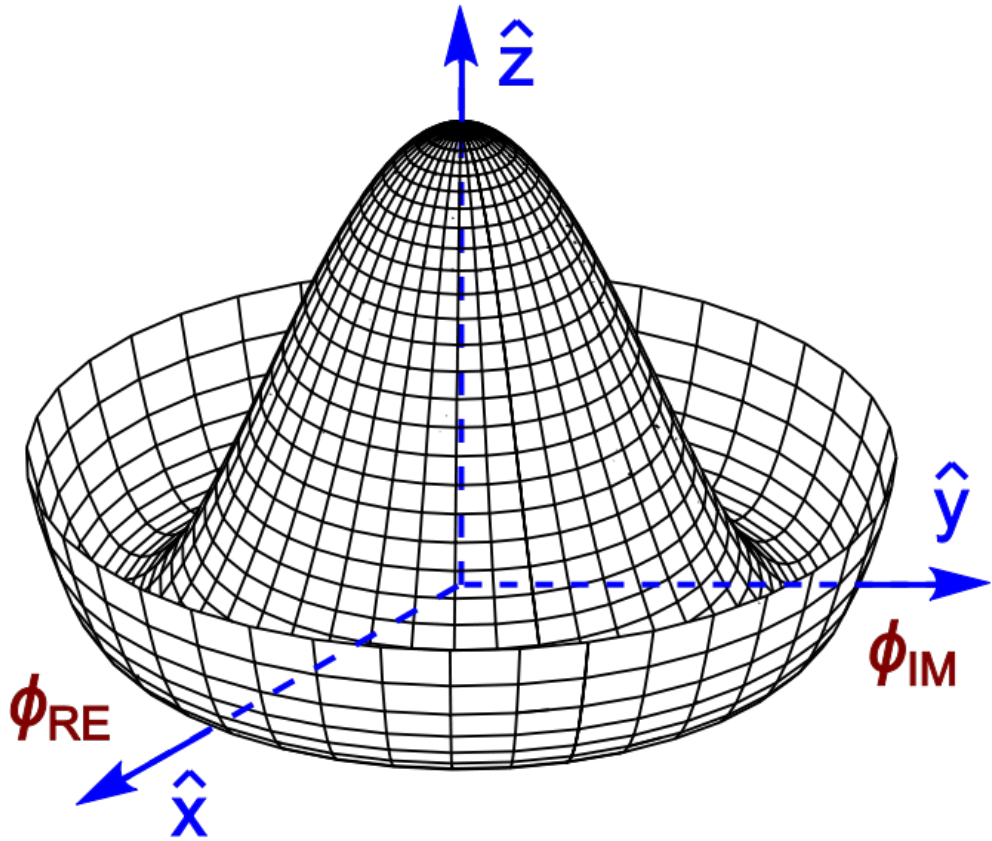


Figure 2.1: Sombrero potential

Higgs multiplet. The covariant derivative D^μ is given by

$$D^\mu = \partial^\mu + \frac{ig}{2}W_a^\mu\sigma_a + \frac{ig'}{2}B^\mu \quad (2.3)$$

where $i\sigma_a$ are the Pauli matrices times the imaginary constant, which are the generators for $SU(2)_L$, and g and g' are the $SU(2)_L$ and $U(1)_Y$ coupling constants, respectively. The field strength tensors $W_a^{\mu\nu}$ and $B^{\mu\nu}$ are given by the commutator of the covariant derivative associated to each field

$$B^{\mu\nu} = \partial^\mu B^\nu - \partial^\nu B^\mu \quad (2.4)$$

$$W_a^{\mu\nu} = \partial^\mu W_a^\nu - \partial^\nu W_a^\mu - g\epsilon_{abc}W_a^\mu W_b^\nu, \quad i = 1, 2, 3$$

169 The terms in the Lagrangian 2.2 proportional to μ^2 and λ make up the “Higgs
 170 potential” [50]. As normal (see Appendix 9.5), we restrict $\lambda > 0$ to guarantee our
 171 potential is bounded from below, and we also require $\mu^2 < 0$, which gives us the
 172 standard “sombrero” potential shown in 2.1.

This potential has infinitely many minima at $\langle \phi \rangle = \sqrt{2m/\lambda}$; the ground state is *spontaneously* broken by the choice of ground state, which induces a vacuum expectation value (VEV). Without loss of generality, we can choose the Higgs field ϕ to point in the real direction, and write the Higgs field ϕ in the following form :

$$\phi = \frac{1}{\sqrt{2}} \exp\left(\frac{i}{v} \sigma_a \theta_a\right) \begin{pmatrix} 0 \\ v + h(x) \end{pmatrix}. \quad (2.5)$$

We choose a gauge to rotate away the dependence on θ_a , such that we can write simply

$$\phi = \frac{1}{\sqrt{2}} \begin{pmatrix} 0 \\ v + h(x) \end{pmatrix}. \quad (2.6)$$

Now, we can see how the masses of the vector bosons are generated from the application of the Higgs mechanism. We plug Eq.2.6 back into the electroweak Lagrangian, and only showing the relevant mass terms in the vacuum state where $h(x) = 0$ see that (dropping the Lorentz indices) :

$$\begin{aligned} \mathcal{L}_M &= \frac{1}{8} \left| \begin{pmatrix} gW_3 + g'B & g(W_1 - iW_2) \\ g(W_1 + iW_2) & -gW_3 + g'B \end{pmatrix} \begin{pmatrix} 0 \\ v \end{pmatrix} \right|^2 \\ &= \frac{g^2 v^2}{8} \left[W_1^2 + W_2^2 + \left(\frac{g'}{g} B - W_3 \right)^2 \right] \end{aligned} \quad (2.7)$$

Defining the Weinberg angle $\tan(\theta_W) = g'/g$ and the following *physical* fields :

$$W^\pm = \frac{1}{\sqrt{2}} (W_1 \mp iW_2) \quad (2.8)$$

$$Z^0 = \cos \theta_W W_3 - \sin \theta_W B$$

$$A^0 = \sin \theta_W W_3 + \cos \theta_W B$$

we can write the piece of the Lagrangian associated to the vector boson masses as

$$\mathcal{L}_{MV} = \frac{1}{4}g^2 v^2 W^+ W^- + \frac{1}{8}(g^2 + g'^2)v^2 Z^0 Z^0. \quad (2.9)$$

and we have the following values of the masses for the vector bosons :

$$\begin{aligned} m_W^2 &= \frac{1}{4}v^2 g^2 \\ m_Z^2 &= \frac{1}{4}v^2(g^2 + g'^2) \\ m_A^2 &= 0 \end{aligned} \quad (2.10)$$

We thus see how the Higgs mechanism gives rise to the masses of the W^\pm and Z boson in the Standard Model; the mass of the photon is zero, as expected. The $SU(2)_L \otimes U(1)_Y$ symmetry of the initially massless $W_{1,2,3}$ and B fields is broken to the $U(1)_{EM}$. Of the four degrees of freedom in the complex Higgs doublet, three are “eaten” when we give mass to the W^\pm and Z_0 , while the other degree of freedom is the Higgs particle, as found in 2012 by the ATLAS and CMS collaborations [51, 52].

179 Quantum Chromodynamics

Quantum chromodynamics (or the theory of the *strong* force) characterizes the behavior of *colored* particles, collectively known as *partons*. The partons of the Standard Model are the (fermionic) quarks, and the (bosonic) gluons. The strong force is governed by $SU(3)_C$, an unbroken symmetry in the Standard Model, which implies the gluon remains massless. Defining the covariant derivative for QCD as

$$D^\mu = \partial^\mu + ig_s G_a^\mu L_a, a = 1, \dots, 8 \quad (2.11)$$

where L_a are the generators of $SU(3)_C$, and g_s is the coupling constant of the strong force. The QCD Lagrangian then is given by

$$\mathcal{L}_{QCD} = i\bar{\psi}_f D_\mu \gamma^\mu \psi_f - \frac{1}{4}G_{a,\mu\nu} G_a^{\mu\nu} \quad (2.12)$$

where the summation over f is for quarks *families*, and $G_a^{\mu\nu}$ is the gluon field strength tensor, given by

$$G_a^{\mu\nu} = \partial^\mu G_a^\nu - \partial^\nu G_a^\mu - g_s f^{abc} G_b^\mu G_c^\nu, a, b, c = 1, \dots, 8 \quad (2.13)$$

180 where f^{abc} are the structure constants of $SU(3)_C$, which are analogous to ϵ_{abc} for
 181 $SU(2)_L$. The kinetic term for the quarks is contained in the standard ∂_μ term, while
 182 the field strength term contains the interactions between the quarks and gluons, as
 183 well as the gluon self-interactions.

184 Written down in this simple form, the QCD Lagrangian does not seem much
 185 different from the QED Lagrangian, with the proper adjustments for the different
 186 group structures. The gluon is massless, like the photon, so one could naïvely expect
 187 an infinite range force, and it pays to understand why this is not the case. The
 188 reason for this fundamental difference is the gluon self-interactions arising in the
 189 field strength tensor term of the Lagrangian. This leads to the phenomena of *color*
 190 *confinement*, which describes how one only observes color-neutral particles alone in
 191 nature. In contrast to the electromagnetic force, particles which interact via the
 192 strong force experience a *greater* force as the distance between the particles increases.
 193 At long distances, the potential is given by $V(r) = -kr$. At some point, it is more
 194 energetically favorable to create additional partons out of the vacuum than continue
 195 pulling apart the existing partons, and the colored particles undergo *fragmentation*.
 196 This leads to *hadronization*. Bare quarks and gluons are actually observed as sprays
 197 of hadrons (primarily kaons and pions); these sprays are known as *jets*, which are
 198 what are observed by experiments.

199 It is important to recognize the importance of understanding these QCD inter-
 200 actions in high-energy hadron colliders such as the LHC. Since protons are hadrons,
 201 proton-proton collisions such as those produced by the LHC are primarily governed by
 202 the processes of QCD. In particular, by far the most frequent process observed in LHC
 203 experiments is dijet production from gluon-gluon interactions (see Fig.2.2). These

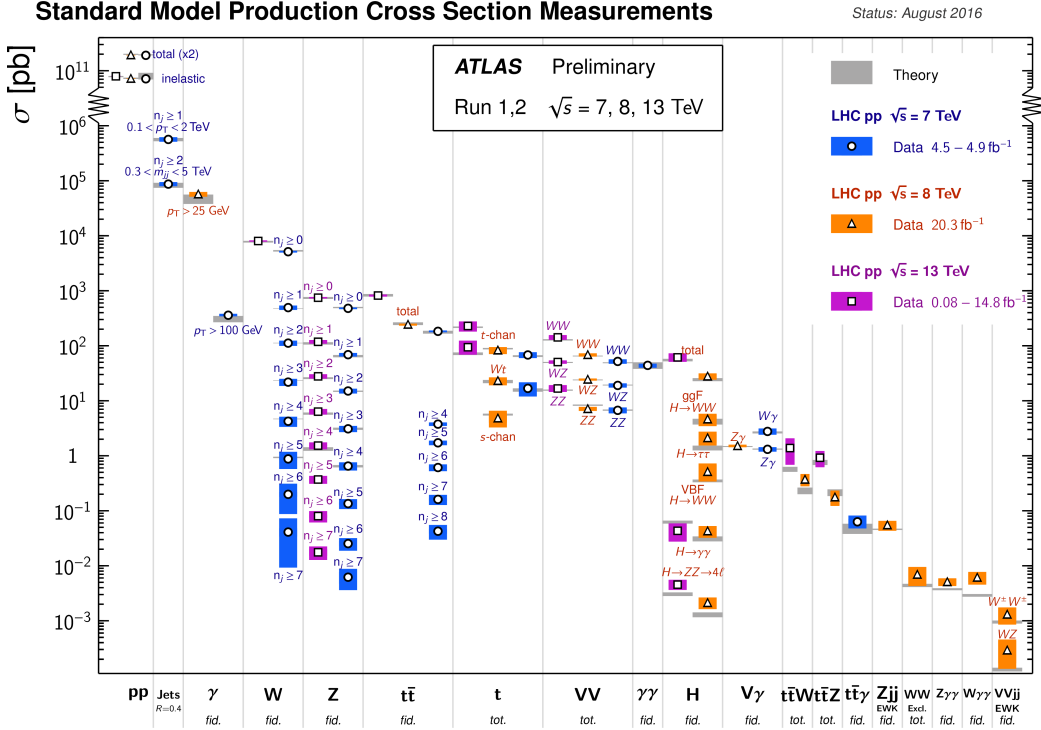


Figure 2.2: Cross-sections of various Standard Model processes

204 gluons that interact are part of the *sea* particles inside the proton; the simple $p = uud$
 205 model does not apply. The main *valence* uud quarks are constantly interacting via
 206 gluons, which can themselves radiate gluons or split into quarks, and so on. A more
 207 useful understanding is given by the colloquially-known *bag* model [53, 54], where the
 208 proton is seen as a “bag” of (in principle) infinitely many partons, each with energy
 209 $E < \sqrt{s} = 6.5$ TeV. One then collides this (proton) bag with another, and views the
 210 products of this very complicated collision, where calculations include many loops in
 211 nonperturbative QCD calculations.

212 Fortunately, we are generally saved by the QCD factorization theorems [55]. This
 213 allows one to understand the hard (i.e. short distance or high energy) $2 \rightarrow 2$ parton
 214 process using the tools of perturbative QCD, while making series of approximations
 215 known as a *parton shower* model to understand the additional corrections from
 216 nonperturbative QCD. We will discuss the reconstruction of jets by experiments in
 217 Ch.5.

218 **Fermions**

219 We will now look more closely at the fermions in the Standard Model [56].

220 As noted earlier in Sec.2.2, the fermions of the Standard Model can be first
 221 distinguished between those that interact via the strong force (quarks) and those
 222 which do not (leptons).

There are six leptons in the Standard Model, which can be placed into three
generations.

$$\begin{pmatrix} e \\ \nu_e \end{pmatrix}, \begin{pmatrix} \mu \\ \nu_\mu \end{pmatrix}, \begin{pmatrix} \tau \\ \nu_\tau \end{pmatrix} \quad (2.14)$$

223 There is the electron (e), muon (μ), and tau (τ), each of which has an associated
 224 neutrino (ν_e, ν_μ, ν_τ). Each of the so-called charged (“electron-like”) leptons has
 225 electromagnetic charge -1 , while the neutrinos all have $q_{EM} = 0$.

226 Often in an experimental context, lepton is used to denote the stable electron
 227 and metastable muon, due to their striking experimental signatures. Taus are often
 228 treated separately, due to their much shorter lifetime of $\tau_\tau \sim 10^{-13}s$; these decay
 229 through hadrons or the other leptons, so often physics analyses at the LHC treat
 230 them as jets or leptons, as will be done in this thesis.

231 As the neutrinos are electrically neutral, nearly massless, and only interact via the
 232 weak force, it is quite difficult to observe them directly. Since LHC experiments rely
 233 overwhelmingly on electromagnetic interactions to observe particles, the presence of
 234 neutrinos is not observed directly. Neutrinos are instead observed by the conservation
 235 of four-momentum in the plane transverse to the proton-proton collisions, known as
 236 *missing transverse energy*.

There are six quarks in the Standard Model : up, down, charm, strange, top, and
 bottom. Quarks are similar organized into three generations :

$$\begin{pmatrix} u \\ d \end{pmatrix}, \begin{pmatrix} c \\ s \end{pmatrix}, \begin{pmatrix} t \\ b \end{pmatrix} \quad (2.15)$$

237 where we speak of “up-like” quarks and “down-like” quarks.

238 Each up-like quark has charge $q_{up} = 2/3$, while the down-like quarks have $q_{down} =$
239 $-1/3$. At the high energies of the LHC, one often makes the distinction between
240 the light quarks (u, d, c, s), the bottom quark, and top quark. In general, due to
241 the hadronization process described above, the light quarks, with masses $m_q < \sim$
242 1.5GeV are indistinguishable by LHC experiments. Their hadronic decay products
243 generally have long lifetimes and they are reconstructed as jets.¹. The bottom quark
244 hadronizes primarily through the B -mesons, which generally travels a short distance
245 before decaying to other hadrons. This allows one to distinguish decays via b -quarks
246 from other jets; this procedure is known as *b-tagging* and will be discussed more in
247 Ch.5. Due to its large mass, the top quark decays before it can hadronize; there
248 are no bound states associated to the top quark. The top is of particular interest at
249 the LHC; it has a striking signature through its most common decay mode $t \rightarrow Wb$.
250 Decays via tops, especially $t\bar{t}$ are frequently an important signal decay mode, or an
251 important background process.

252 **Interactions in the Standard Model**

253 We briefly overview the entirety of the fundamental interactions of the Standard
254 Model; these can also be found in 2.3.

255 The electromagnetic force, mediated by the photon, interacts with via a three-
256 point coupling all charged particles in the Standard Model. The photon thus interacts
257 with all the quarks, the charged leptons, and the charged W^\pm bosons.

258 The weak force is mediated by three particles : the W^\pm and the Z^0 . The Z^0 can
259 interacts with all fermions via a three-point coupling. A real Z_0 can thus decay to
260 a fermion-antifermion pair of all SM fermions except the top quark, due to its large

¹In some contexts, charm quarks are also treated as a separate category, although it is quite difficult to distinguish charm quarks from the other light quarks.

Standard Model Interactions (Forces Mediated by Gauge Bosons)



Figure 2.3: The interactions of the Standard Model

mass. The W^\pm has two important three-point interactions with fermions. First, the W^\pm can interact with an up-like quark and a down-like quark; an important example in LHC experiments is $t \rightarrow Wb$. The coupling constants for these interactions are encoded in the unitary matrix known as the Cabibbo–Kobayashi–Maskawa (CKM) matrix [57, 58], and are generally known as flavor-changing interactions. Secondly, the W^\pm interacts with a charged lepton and its corresponding neutrino. In this case, the unitary matrix that corresponds to CKM matrix for quarks is the identity matrix, which forbids (fundamental) vertices such as $\mu \rightarrow We$. For leptons, instead this is a two-step process : $\mu \rightarrow \nu_m u W \rightarrow \nu_m u \bar{\nu}_e e$. Finally, there are the self-interactions

270 of the weak gauge bosons. There is a three-point and four-point interaction; all
271 combinations are allowed which conserve electric charge.

272 The strong force is mediated by the gluon, which as discussed above also carries
273 the strong color charge. There is the fundamental three-point interaction, where a
274 quark radiates a gluon. Additionally, there are the three-point and four-point gluon-
275 only interactions.

276 2.3 Deficiencies of the Standard Model

277 At this point, it is quite easy to simply rest on our laurels. This relatively simple
278 theory is capable of explaining a very wide range of phenomena, which ultimately
279 break down only to combinations of nine diagrams shown in Fig.2.3. Unfortunately,
280 there are some unexplained problems with the Standard Model. We cannot go
281 through all of the potential issues in this thesis, but we will motivate the primary
282 issues which naturally lead one to *supersymmetry*, as we will see in Ch.3.

The Standard Model has many free parameters; see Table 2.1 In general, we prefer models with less free parameters. A great example of this fact, and the primary experimental evidence for EWSB, is the relationship between the couplings of the weak force and the masses of the gauge bosons of the weak force :

$$\rho \equiv \frac{m_W^2}{m_Z^2 \cos^2 \theta_W} \stackrel{?}{=} 1 \quad (2.16)$$

283 where ? indicates that this is a testable prediction of the Standard Model (in
284 particular, that the gauge bosons gain mass through EWSB). This relationship has
285 been measured within experimental and theoretical predictions. We would like to
286 produce additional such relationships, which would exist if the Standard Model is a
287 low-energy approximation of some other theory.

288 An additional issue is the lack of *gauge coupling unification*. The couplings of
289 any quantum field theory “run” as a function of the distance scales (or inversely,

m_e	Electron mass	511 keV
m_μ	Muon mass	105.7 MeV
m_τ	Tau mass	1.78 GeV
m_u	Up quark mass	1.9 MeV ($m_{\bar{MS}} = 2\text{GeV}$)
m_d	Down quark mass	4.4 MeV ($m_{\bar{MS}} = 2\text{GeV}$)
m_s	Strange quark mass	87 MeV ($m_{\bar{MS}} = 2\text{GeV}$)
m_c	Charm quark mass	1.32 GeV ($m_{\bar{MS}} = m_c$)
m_b	Bottom quark mass	4.24 GeV ($m_{\bar{MS}} = m_b$)
m_t	Top quark mass	172.7 GeV (on-shell renormalization)
θ_{12} CKM	12-mixing angle	13.1°
θ_{23} CKM	23-mixing angle	2.4°
θ_{13} CKM	13-mixing angle	0.2°
δ CKM	CP-violating Phase	0.995
g'	U(1) gauge coupling	0.357 ($m_{\bar{MS}} = m_Z$)
g	SU(2) gauge coupling	0.652 ($m_{\bar{MS}} = m_Z$)
g_s	SU(3) gauge coupling	1.221 ($m_{\bar{MS}} = m_Z$)
θ_{QCD}	QCD vacuum angle	~0
VEV	Higgs vacuum expectation value	246 GeV
m_H	Higgs mass	125 GeV

Table 2.1: Parameters of the Standard Model. For values dependent on the renormalization scheme, we use a combination of the on-shell normalization scheme [59–62] and modified minimal subtraction scheme with $m_{\bar{MS}}$ as indicated in the table[63]

290 energy scales) of the theory. The idea is closely related to the unification of the
 291 electromagnetic and weak forces at the so-called *electroweak scale* of $O(100 \text{ GeV})$.
 292 One would hope this behavior was repeated between the electroweak forces and the
 293 strong force at some suitable energy scale. The Standard Model does automatically
 294 not exhibit this behavior, as we can see in Fig.2.4.

The most significant problem with the Standard Model is the *hierarchy problem*. In its most straightforward incarnation, the Higgs scalar field is subject to quantum corrections through loop diagrams, as shown in Fig.2.5. For demonstration, we use the contributions from the top quark, since the top quark has the largest Higgs Yukawa coupling due to its large mass. In general, we should expect these corrections to quadratically depend on the scale of the ultraviolet physics, Λ . Briefly assume there is no new physics before the Planck scale of gravity, $\Lambda_{\text{Planck}} = 10^{19} \text{ GeV}$. In this

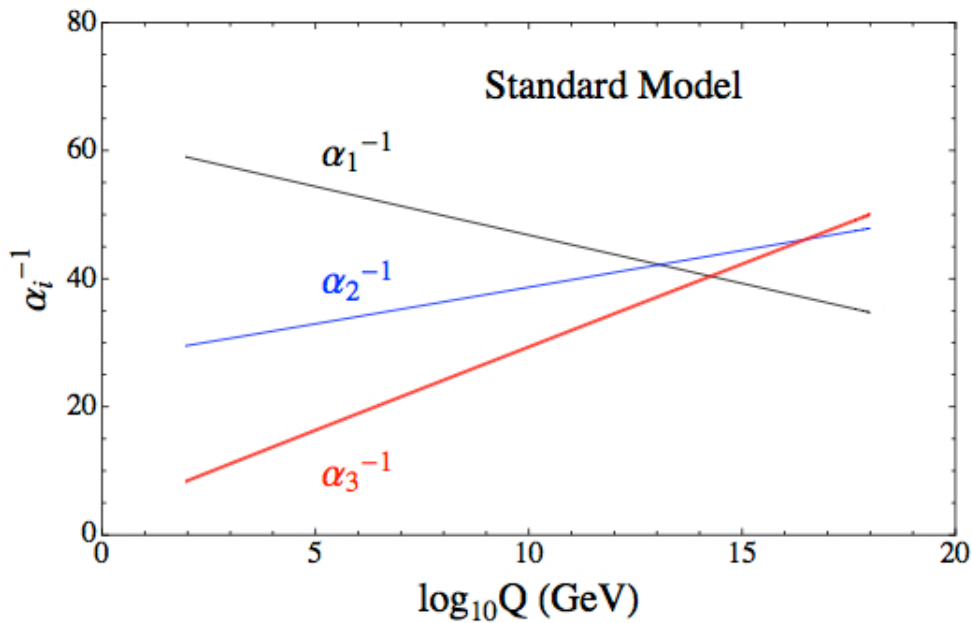


Figure 2.4: The running of Standard Model gauge couplings. The Standard Model couplings do not unify at high energies, which indicates it cannot completely describe nature through the Planck scale.

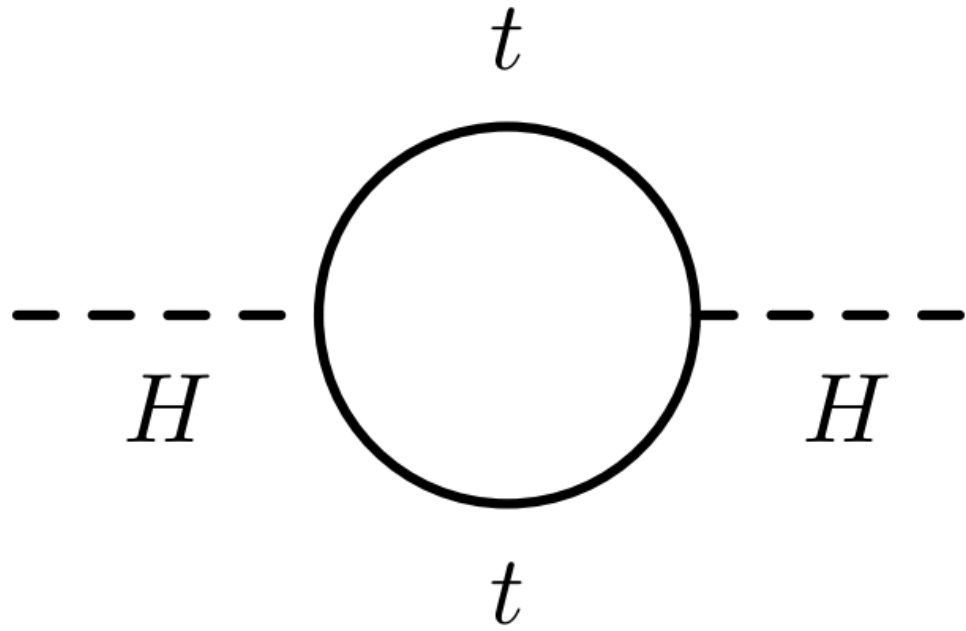


Figure 2.5: The dominant quantum loop correction to the Higgs mass in the Standard Model.

case, we expect the corrections to the Higgs mass like

$$\delta m_H^2 \approx \left(\frac{m_t}{8\pi^2 \langle \phi \rangle_{VEV}} \right)^2 \Lambda_{Planck}^2. \quad (2.17)$$

To achieve the miraculous cancellation required to get the observed Higgs mass of 125 GeV, one needs to then set the bare Higgs mass m_0 , our input to the Standard Model Lagrangian, itself to a *precise* value $\sim 10^{19}$ GeV. This extraordinary level of parameter finetuning is quite undesirable, and within the framework of the Standard Model, there is little that can be done to alleviate this issue.

An additional concern, of a different nature, is the lack of a *dark matter* candidate in the Standard Model. Dark matter was discovered by observing galactic rotation curves, which showed that much of the matter that interacted gravitationally was invisible to our (electromagnetic) telescopes [16–22]. The postulation of the existence of dark matter, which interacts at least through gravity, allows one to understand these galactic rotation curves. Unfortunately, no particle in the Standard Model could possibly be the dark matter particle. The only candidate truly worth another look is the neutrino, but it has been shown that the neutrino content of the universe is simply too small to explain the galactic rotation curves [22, 64]. The experimental evidence from the galactic rotations curves thus show there *must* be additional physics beyond the Standard Model, which is yet to be understood.

In the next chapter, we will see how these problems can be alleviated by the theory of supersymmetry.

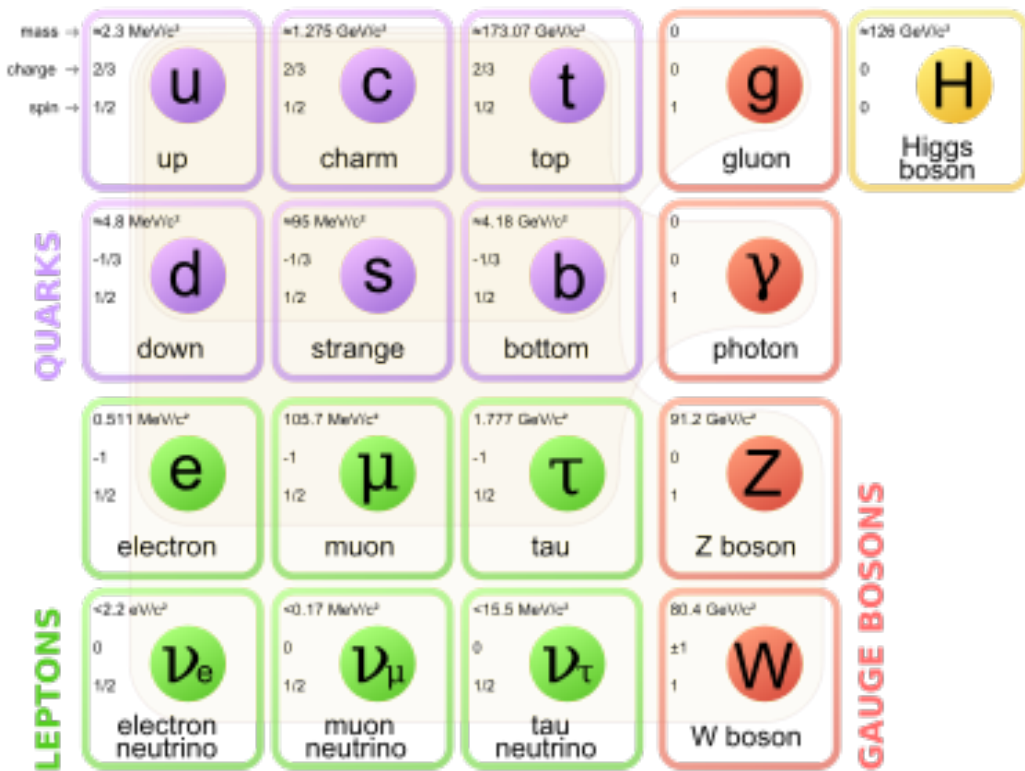


Figure 2.6: Particles of the Standard Model

313

Chapter 3

314

Supersymmetry

315 This chapter will introduce supersymmetry (SUSY) [15, 23–35]. We will begin by
 316 introducing the concept of a *superspace*, and discuss some general ingredients of
 317 supersymmetric theories. This will include a discussion of how the problems with the
 318 Standard Model described in Ch.2 are naturally fixed by these theories.

319 The next step is to discuss the particle content of the *Minimally Supersymmetric*
 320 *Standard Model* (MSSM). As its name implies, this theory contains the minimal
 321 additional particle content to make Standard Model supersymmetric. We then discuss
 322 the important phenomenological consequences of this theory, especially as it would
 323 be observed in experiments at the LHC.

324 **3.1 Supersymmetric theories : from space to
 325 superspace**

326 **Coleman-Mandula “no-go” theorem**

327 We begin the theoretical motivation for supersymmetry by citing the “no-go” theorem
 328 of Coleman and Mandula [65]. This theorem forbids *spin-charge unification*; it
 329 states that all quantum field theories which contain nontrivial interactions must be
 330 a direct product of the Poincarégroup of Lorentz symmetries, the internal product
 331 from of gauge symmetries, and the discrete symmetries of parity, charge conjugation,
 332 and time reversal. The assumptions which go into building the Coleman-Mandula

theorem are quite restrictive, but there is one unique way out, which has become known as *supersymmetry* [26, 66]. In particular, we must introduce a *spinorial* group generator Q . Alternatively, and equivalently, this can be viewed as the addition of anti-commuting coordinates; space plus these new anti-commuting coordinates is then called *superspace* [67]. We will not investiage this view in detail, but it is also a quite intuitive and beautiful way to construct supersymmetry[15].

339 **Supersymmetry transformations**

340 A *supersymmetric* transformation Q transforms a bosonic state into a fermionic state,
 341 and vice versa :

$$Q |\text{Fermion}\rangle = |\text{Boson}\rangle \quad (3.1)$$

$$Q |\text{Boson}\rangle = |\text{Fermion}\rangle \quad (3.2)$$

To ensure this relation holds, Q must be an anticommuting spinor. Additionally, since spinors are inherently complex, Q^\dagger must also be a generator of the supersymmetry transformation. Since Q and Q^\dagger are spinor objects (with $s = 1/2$), we can see that supersymmetry must be a spacetime symmetry. The Haag-Lopuszanski-Sohnius extension [66] of the Coleman-Mandula theorem [65] is quite restrictive about the forms of such a symmetry. Here, we simply write the (anti-) commutation relations [15] :

$$Q_\alpha, Q_{\dot{\alpha}}^\dagger = -2\sigma_{\alpha\dot{\alpha}\mu} P_\mu \quad (3.3)$$

$$Q_\alpha, Q_{\dot{\beta}} = Q_{\dot{\alpha}}^\dagger, Q_{\dot{\beta}}^\dagger = 0 \quad (3.4)$$

$$[P^\mu, Q_\alpha] = [P^\mu, Q_{\dot{\alpha}}^\dagger] = 0 \quad (3.5)$$

342 **Supermultiplets**

343 In a supersymmetric theory, we organize single-particle states into irreducible
344 representations of the supersymmetric algebra which are known as *supermultiplets*.
345 Each supermultiplet contains a fermion state $|F\rangle$ and a boson state $|B\rangle$; these two
346 states are the known as *superpartners*. These are related by some combination of
347 Q and Q^\dagger , up to a spacetime transformation. Q and Q^\dagger commute with the mass-
348 squared operator $-P^2$ and the operators corresponding to the gauge transformations
349 [15]; in particular, the gauge interactions of the Standard Model. In an unbroken
350 supersymmetric theory, this means the states $|F\rangle$ and $|B\rangle$ have exactly the same mass,
351 electromagnetic charge, electroweak isospin, and color charges. One can also prove
352 [15] that each supermultiplet contains the exact same number of bosonic (n_B) and
353 fermion (n_F) degrees of freedom. We now explore the possible types of supermultiples
354 one can find in a renormalizable supersymmetric theory.

355 Since each supermultiplet must contain a fermion state, the simplest type of
356 supermultiplet contains a single Weyl fermion state ($n_F = 2$) which is paired with
357 $n_B = 2$ scalar bosonic degrees of freedom. This is most conveniently constructed as
358 single complex scalar field. We call this construction a *scalar supermultiplet* or *chiral*
359 *supermultiplet*. The second name is indicative; only chiral supermultiplets can contain
360 fermions whose right-handed and left-handed components transform differently under
361 the gauge interactions (as of course happens in the Standard Model).

362 The second type of supermultiplet we construct is known as a *gauge* supermul-
363 tiplet. We take a spin-1 gauge boson (which must be massless due to the gauge
364 symmetry, so $n_B = 2$) and pair this with a single massless Weyl spinor¹. The gauge
365 bosons transform as the adjoint representation of the their respective gauge groups;
366 their fermionic partners, which are known as gauginos, must also. In particular,
367 the left-handed and right-handed components of the gaugino fermions have the same

¹Choosing an $s = 3/2$ massless fermion leads to nonrenormalizable interactions.

368 gauge transformation properties.

369 Excluding gravity, this is the entire list of supermultiplets which can participate
370 in renormalizable interactions in what is known as $N = 1$ supersymmetry. This
371 means there is only one copy of the supersymmetry generators Q and Q^\dagger . This is
372 essentially the only “easy” phenomenological choice, since it is the only choice in four
373 dimensions which allows for the chiral fermions and parity violations built into the
374 Standard Model, and we will not look further into $N > 1$ supersymmetry in this thesis.

375 The primary goal, after understanding the possible structures of the multiplets
376 above, is to fit the Standard Model particles into a multiplet, and therefore make
377 predictions about their supersymmetric partners. We explore this in the next section.

378 **3.2 Minimally Supersymmetric Standard Model**

379 To construct what is known as the MSSM [15, 68–71], we need a few ingredients and
380 assumptions. First, we match the Standard Model particles with their corresponding
381 superpartners of the MSSM. We will also introduce the naming of the superpartners
382 (also known as *sparticles*). We discuss a very common additional restraint imposed on
383 the MSSM, known as *R*–parity. We also discuss the concept of soft supersymmetry
384 breaking and how it manifests itself in the MSSM.

385 **Chiral supermultiplets**

386 The first thing we deduce is directly from Sec.???. The bosonic superpartners
387 associated to the quarks and leptons *must* be spin 0, since the quarks and leptons must
388 be arranged in a chiral supermultiplet. This is essentially the note above, since the
389 chiral supermultiplet is the only one which can distinguish between the left-handed
390 and right-handed components of the Standard Model particles. The superpartners of
391 the quarks and leptons are known as *squarks* and *sleptons*, or *sfermions* in aggregate.

392 (for ‘‘scalar quarks’’, ‘‘scalar leptons’’, and ‘‘scalar fermion’’²). The ‘‘s-’’ prefix
 393 can also be added to the individual quarks i.e. *selectron*, *sneutrino*, and *stop*. The
 394 notation is to add a \sim over the corresponding Standard Model particle i.e. \tilde{e} , the
 395 selectron is the superpartner of the electron. The two-component Weyl spinors of the
 396 Standard Model must each have their own (complex scalar) partner i.e. e_L, e_R have
 397 two distinct partners : \tilde{e}_L, \tilde{e}_R . As noted above, the gauge interactions of any of the
 398 sfermions are identical to those of their Standard Model partners.

Due to the scalar nature of the Higgs, it must obviously lie in a chiral supermultiplet. To avoid gauge anomalies and ensure the correct Yukawa couplings to the quarks and leptons[15], we must add additional Higgs bosons to any supersymmetric theory. In the MSSM, we have two chiral supermultiplets. The SM (SUSY) parts of the multiplets are denoted $H_u(\tilde{H}_u)$ and $H_d(\tilde{H}_d)$. Writing out H_u and H_d explicitly:

$$H_u = \begin{pmatrix} H_u^+ \\ H_u^0 \end{pmatrix} \quad (3.6)$$

$$H_d = \begin{pmatrix} H_d^0 \\ H_d^- \end{pmatrix} \quad (3.7)$$

(3.8)

399 we see that H_u looks very similar to the SM Higgs with $Y = 1$, and H_d is symmetric
 400 to this with $+ \rightarrow -$, with $Y = -1$. The SM Higgs boson, h_0 , is a linear superposition
 401 of the neutral components of these two doublets. The SUSY parts of the Higgs
 402 multiplets, \tilde{H}_u and \tilde{H}_d , are each left-handed Weyl spinors. For generic spin-1/2
 403 sparticles, we add the ‘‘-ino’’ suffix. We then call the partners of the two Higgs
 404 collectively the *Higgsinos*.

²The last one should probably have bigger scare quotes.

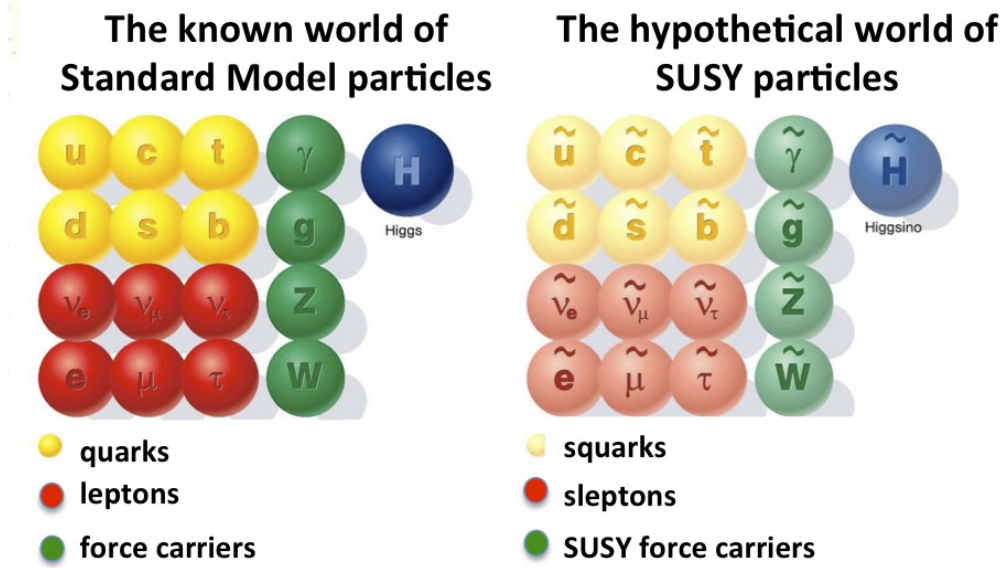


Figure 3.1: Particles of the MSSM

405 Gauge supermultiplets

406 The superpartners of the gauge bosons must all be in gauge supermultiplets since
 407 they contain a spin-1 particle. Collectively, we refer to the superpartners of the
 408 gauge bosons as the gauginos.

409 The first gauge supermultiplet contains the gluon, and its superpartner, which is
 410 known as the *gluino*, denoted \tilde{g} . The gluon is of course the SM mediator of $SU(3)_C$;
 411 the gluino is also a colored particle, subject to $SU(3)_C$. From the SM before EWSB,
 412 we have the four gauge bosons of the electroweak symmetry group $SU(2)_L \otimes U(1)_Y$:
 413 $W^{1,2,3}$ and B^0 . The superpartners of these particles are thus the *winos* $W^{\tilde{1},\tilde{2},\tilde{3}}$ and
 414 *bino* \tilde{B}^0 , where each is placed in another gauge supermultiplet with its corresponding
 415 SM particle. After EWSB, without breaking supersymmetry, we would also have the
 416 zino \tilde{Z}^0 and photino $\tilde{\gamma}$.

417 The entire particle content of the MSSM can be seen in Fig.3.1.

418 At this point, it's important to take a step back. Where are these particles?
 419 As stated above, supersymmetric theories require that the masses and all quantum



Figure 3.2: This Feynmann diagram shows how proton decay is induced in the MSSM, if one does not impose R -parity.

420 numbers of the SM particle and its corresponding sparticle are the same. Of course,
 421 we have not observed a selectron, squark, or wino. The answer, as it often is, is that
 422 supersymmetry is *broken* by the vacuum state of nature [15].

423 **R -parity**

This section is a quick aside to the general story. R – parity refers to an additional discrete symmetry which is often imposed on supersymmetric models. For a given particle state, we define

$$R = (-1)^{3(B-L)+2s} \quad (3.9)$$

424 where B, L is the baryon (lepton) number and s is the spin. The imposition of
 425 this symmetry forbids certain terms from the MSSM Lagrangian that would violate
 426 baryon and/or lepton number. This is required in order to prevent proton decay, as
 427 shown in Fig.3.2³. .

428 In supersymmetric models, this is a \mathbb{Z}_2 symmetry, where SM particles have $R = 1$
 429 and sparticles have $R = -1$. We will take R – parity as part of the definition of
 430 the MSSM. We will discuss later the *drastic* consequences of this symmetry on SUSY
 431 phenomenology

³Proton decay can actually be prevented by allowing only one of the four potential R-parity violating terms to survive.

432 **Soft supersymmetry breaking**

The fundamental idea of *soft* supersymmetry breaking[15, 34, 35, 72, 73] is that we would like to break supersymmetry without reintroducing the quadratic divergences we discussed at the end of Chapter 2. We write the Lagrangian in a form :

$$\mathcal{L}_{\text{MSSM}} = \mathcal{L}_{\text{SUSY}} + \mathcal{L}_{\text{soft}} \quad (3.10)$$

433 In this sense, the symmetry breaking is “soft”, since we have separated out the
 434 completely symmetric terms from those soft terms which will not allow the quadratic
 435 divergences to the Higgs mass.

436 The explicitly allowed terms in the soft-breaking Lagrangian are [35].

- 437 • Mass terms for the scalar components of the chiral supermultipletss
 438 • Mass terms for the Weyl spinor components of the gauge supermultipletss
 439 • Trilinear couplings of scalar components of chiral supermultiplets

In particular, using the field content described above for the MSSM, the softly-broken portion of the MSSM Lagrangian can be written

$$\mathcal{L}_{\text{soft}} = -\frac{1}{2} \left(M_3 \tilde{g} \tilde{g} + M_2 \tilde{W} \tilde{W} + M_1 \tilde{B} \tilde{B} + c.c. \right) \quad (3.11)$$

$$- \left(\tilde{u} a_u \tilde{Q} H_u - \tilde{d} a_d \tilde{Q} H_d - \tilde{e} a_e \tilde{L} H_d + c.c. \right) \quad (3.12)$$

$$- \tilde{Q}^\dagger m_Q^2 \tilde{Q} - \tilde{L}^\dagger m_L^2 \tilde{L} - \tilde{u} m_u^2 \tilde{u}^\dagger - \tilde{d} m_d^2 \tilde{d}^\dagger - \tilde{e} m_e^2 \tilde{e}^\dagger \quad (3.13)$$

$$- m_{H_u}^2 H_u^* H_u - m_{H_d}^2 H_d^* H_d - (b H_u H_d + cc). \quad (3.14)$$

440 where we have introduced the following notations :

441 1. M_3, M_2, M_1 are the gluino, wino, and bino masses.

442 2. a_u, a_d, a_e are complex 3×3 matrices in family space.

443 3. $m_Q^2, m_u^2, m_d^2, m_L^2, m_e^2$ are hermitian 3×3 matrices in family space.

444 4. $m_{H_u}^2, m_{H_d}^2, b$ are the SUSY-breaking contributions to the Higgs potential.

445 We have written matrix terms without any sort of additional notational decoration
 446 to indicate their matrix nature, and we now show why. The first term 1 are
 447 straightforward; these are just the straightforward mass terms for these fields. There
 448 are strong constraints on the off-diagonal terms for the matrices of 2 [74, 75]; for
 449 simplicity, we will assume that each $a_i, i = u, d, e$ is proportional to the Yukawa
 450 coupling matrix : $a_i = A_{i0}y_i$. The matrices in ?? can be similarly constrained by
 451 experiments [68, 75–82] Finally, we assume that the elements 4 contributing to the
 452 Higgs potential as well as all of the 1 terms must be real, which limits the possible
 453 CP-violating interactions to those of the Standard Model. We thus only consider
 454 flavor-blind, CP-conserving interactions within the MSSM.

The important mixing for mass and gauge interaction eigenstates in the MSSM occurs within electroweak sector, in a process akin to EWSB in the Standard Model. The neutral portions of the Higgsinos doublets and the neutral gauginos $(\tilde{H}_u^0, \tilde{H}_d^0, \tilde{B}^0, \tilde{W}^0)$ of the gauge interaction basis mix to form what are known as the *neutralinos* of mass basis :

$$M_{\tilde{\chi}} = \begin{pmatrix} M_1 & 0 & -c_\beta s_W m_Z & s_\beta s_W m_Z \\ 0 & M_2 & c_\beta c_W m_Z & -s_\beta c_W m_Z \\ -c_\beta s_W m_Z & c_\beta c_W m_Z & 0 & -\mu \\ s_\beta s_W m_Z & -s_\beta c_W m_Z & -\mu & 0 \end{pmatrix} \quad (3.15)$$

455 where $s(c)$ are the sine and cosine of angles related to EWSB, which introduced
 456 masses to the gauginos and higgsinos. Diagonalization of this matrix gives the four
 457 neutralino mass states, listed without loss of generality in order of increasing mass :
 458 $\tilde{\chi}_{1,2,3,4}^0$.

459 The neutralinos, especially the lightest neutralino $\tilde{\chi}_1^0$, are important ingredients
 460 in SUSY phenomenology.

461 The same process can be done for the electrically charged gauginos with
462 the charged portions of the Higgsino doublets along with the charged winos
463 $(\tilde{H}_u^+, \tilde{H}_d^+, \tilde{W}^+, \tilde{W}^-)$. This leads to the *charginos*, again in order of increasing mass
464 : $\tilde{\chi}_{1,2}^\pm$.

465

3.3 Phenomenology

466 We are finally at the point where we can discuss the phenomenology of the MSSM,
467 in particular as it manifests itself at the energy scales of the LHC.

468 As noted above in Sec.3.2, the assumption of *R*-parity has important conse-
469 quences for MSSM phenomenology. The SM particles have $R = 1$, while the sparticles
470 all have $R = -1$. Simply, this is the “charge” of supersymmetry. Since the particles of
471 LHC collisions (pp) have total incoming $R = 1$, we must expect that all sparticles will
472 be produced in *pairs*. An additional consequence of this symmetry is the fact that the
473 lightest supersymmetric particle (LSP) is *stable*. Off each branch of the Feynmann
474 diagram shown in Fig., we have $R = -1$, and this can only decay to another sparticle
475 and a SM particle. Once we reach the lightest sparticle in the decay, it is absolutely
476 stable. This leads to the common signature E_T^{miss} for a generic SUSY signal.

477 For this thesis, we will be presenting an inclusive search for squarks and gluinos
478 with zero leptons in the final state. This is a very interesting decay channel⁴, due
479 to the high cross-sections of $\tilde{g}\tilde{g}$ and $\tilde{q}\tilde{q}$ decays, as can be seen in Fig.?? [83]. This
480 is a direct consequence of the fact that these are the colored particles of the MSSM.
481 Since the sparticles interact with the gauge groups of the SM in the same way as their
482 SM partners, the colored sparticles, the squarks and gluinos, are produced and decay
483 as governed by the color group $SU(3)_C$ with the strong coupling g_S . The digluino
484 production is particularly copious, due to color factor corresponding to the color octet

⁴Prior to Run1, probably the most *most* interesting SUSY decay channel.

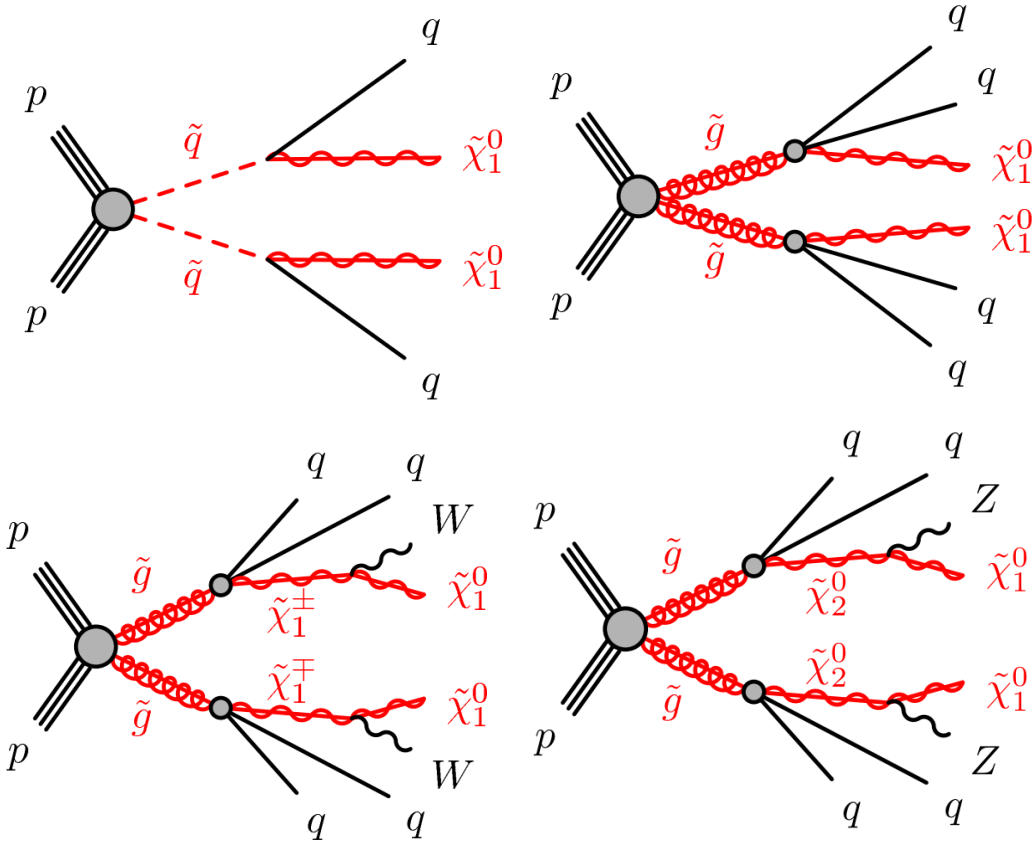


Figure 3.3: SUSY signals considered in this thesis

485 of $SU(3)C$.

486 In the case of disquark production, the most common decay mode of the squark in
 487 the MSSM is a decay directly to the LSP plus a single SM quark [15]. This means the
 488 basic search strategy of disquark production is two jets from the final state quarks,
 489 plus missing transverse energy for the LSPs. There are also cascade decays, the most
 490 common of which, and the only one considered in this thesis, is $\tilde{q} \rightarrow q\chi_1^\pm \rightarrow qW^\pm\chi_1^0$.

491 For digluino production, the most common decay is $\tilde{g} \rightarrow g\tilde{q}$, due to the large
 492 g_S coupling. The squark then decays as listed above. In this case, we generically
 493 search for four jets and missing transverse energy from the LSPs. We can also have
 494 the squark decay in association with a W^\pm or Z^0 ; in this thesis, we are interested in
 495 those cases where this vector boson goes hadronically.

496 In the context of experimental searches for SUSY, we often consider *simplified*

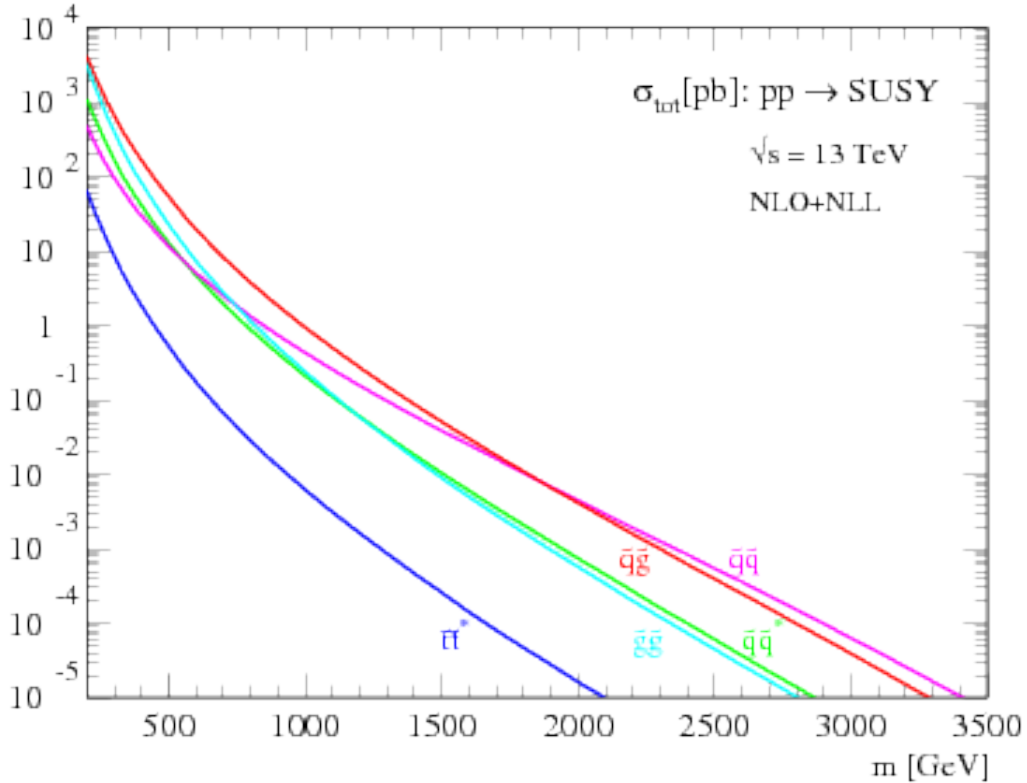


Figure 3.4: SUSY production cross-sections as a function of sparticle mass at $\sqrt{s} = 13$ TeV.

497 *models*. These models make certain assumptions which allow easy comparisons of
 498 results by theorists and rival experimentalists. In the context of this thesis, the
 499 simplified models will make assumptions about the branching ratios described in the
 500 preceding paragraphs. In particular, we will often choose a model where the decay of
 501 interest occurs with 100% branching ratio. This is entirely for ease of interpretation
 502 by other physicists⁵, but it is important to recognize that these are more a useful
 503 comparison tool, especially with limits, than a strict statement about the potential
 504 masses of sought-after beyond the Standard Model particle.

⁵In the author's opinion, this often leads to more confusion than comprehension. We will revisit the shortcomings of simplified models in the Conclusion to this thesis.

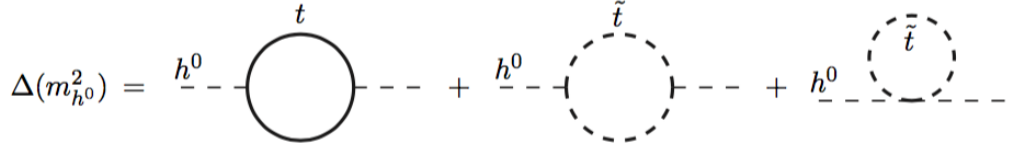


Figure 3.5: Loop diagrams correct the Higgs mass in the MSSM

505 3.4 How SUSY solves the problems with the SM

506 We now return to the issues with the Standard Model as described in Ch.2 to see
 507 how these issues are solved by supersymmetry.

508 Quadratic divergences to the Higgs mass

The quadratic divergences induced by the loop corrections to the Higgs mass, for example from the top Yukawa coupling, goes as

$$\delta m_H^2 \approx \left(\frac{m_t}{8\pi^2 \langle \phi \rangle_{VEV}} \right)^2 \Lambda_{Planck}^2. \quad (3.16)$$

509 The miraculous thing about SUSY is each of these terms *automatically* comes
 510 with a term which exactly cancels this contribution[15]. The fermions and bosons
 511 have opposite signs in this loop diagram to all orders in perturbation theory, which
 512 completely solves the hierarchy problem. This is the most well-motivated reason for
 513 supersymmetry.

514 Gauge coupling unification

515 An additional motivation for supersymmetry is seen by the gauge coupling unification
 516 high scales. In the Standard Model, as we saw the gauge couplings fail to unify at
 517 high energies. In the MSSM and many other forms of supersymmetry, the gauge
 518 couplings unify at high energy, as can be seen in Fig.???. This provides additional
 519 aesthetic motivation for supersymmetric theories.



Figure 3.6: The running of Standard Model gauge couplings; compare to Fig.2.4. The MSSM gauge couplings nearly intersect at high energies.

520 Dark matter

As we discussed previously, the lack of any dark matter candidate in the Standard Model naturally leads to beyond the Standard Model theories. In the Standard Model, there is a natural dark matter candidate in the lightest supersymmetric particle[15]. The LSP would in dark matter experiments be called a *weakly-interacting massive particle* (WIMP), which is a type of cold dark matter [22, 84]. These WIMPS would only interact through the weak force and gravity, which is exactly as a model like the MSSM predicts for the neutralino. In Fig.3.7, we can see the current WIMP exclusions for a given mass. The range of allowed masses which have not been excluded for LSPs and WIMPs have significant overlap. This provides additional motivation outside of the context of theoretical details.



Figure 3.7: WIMP exclusions from direct dark matter detection experiments.

531 3.5 Conclusions

532 Supersymmetry is the most well-motivated theory for physics beyond the Standard
 533 Model. It provides a solution to the hierarchy problem, leads to gauge coupling
 534 unification, and provides a dark matter candidate consistent with galactic rotation
 535 curves. As noted in this chapter, due to the LSPs in the final state, most SUSY
 536 searches require a significant amount of missing transverse energy in combination
 537 with jets of high transverse momentum. However, there is some opportunity to do
 538 better than this, especially in final states where one has two weakly-interacting LSPs
 539 on opposite sides of some potentially complicated decay tree. We will see how this is
 540 done in Ch.??.

541

Chapter 4

542

The Large Hadron Collider

543 The Large Hadron Collider (LHC) produces high-energy protons which are collided
 544 at the center of multiple large experiments at CERN on the outskirts of Geneva,
 545 Switzerland [85]. The LHC produces the highest energy collisions in the world,
 546 with design center-of-mass energy of $\sqrt{s} = 14$ TeV, which allows the experiments
 547 to investigate physics far beyond the reach of previous colliders. This chapter will
 548 summarize the basics of accelerator physics, especially with regards to discovering
 549 physics beyond the Standard Model. We will describe the CERN accelerator complex
 550 and the LHC.

551 **4.1 Basics of Accelerator Physics**

552 This section follows closely the presentation of [86].

Simple particle accelerators simply rely on the acceleration of charged particles in a static electric field. Given a field of strength E , charge q , and mass m , this is simply

$$a = \frac{qE}{m}. \quad (4.1)$$

553 For a given particle with a given mass and charge, this is limited by the static electric
 554 field which can be produced, which in turn is limited by electrical breakdown at high
 555 voltages.

556 There are two complementary solutions to this issue. First, we use the *radio*
 557 *frequency acceleration* technique. We call the devices used for this *RF cavities*. The

558 cavities produce a time-varied electric field, which oscillate such that the charged
 559 particles passing through it are accelerated towards the design energy of the RF
 560 cavity. This oscillation also induces the particles into *bunches*, since particles which
 561 are slightly off in energy from that induced by the RF cavity are accelerated towards
 562 the design energy.

Second, one bends the particles in a magnetic field, which allows them to pass through the same RF cavity over and over. This second process is often limited by *synchrotron radiation*, which describes the radiation produced when a charged particle is accelerated. The power radiated is

$$P \sim \frac{1}{r^2} \left(E/m \right)^4 \quad (4.2)$$

563 where r is the radius of curvature and E, m is the energy (mass) of the charged
 564 particle. Given an energy which can be produced by a given set of RF cavities (which
 565 is *not* limited by the mass of the particle), one then has two options to increase the
 566 actual collision energy : increase the radius of curvature or use a heavier particle.
 567 Practically speaking, the easiest options for particles in a collider are protons and
 568 electrons, since they are (obviously) copious in nature and do not decay¹. Given the
 569 dependence on mass, we can see why protons are used to reach the highest energies.
 570 The tradeoff for this is that protons are not point particles, and we thus we don't
 571 know the exact incoming four-vectors of the protons, as discussed in Ch.2.

The particle *beam* refers to the bunches all together. An important property of a beam of a particular energy E , moving in uniform magnetic field B , containing particles of momentum p is the *beam rigidity* :

$$R \equiv rB = p/c. \quad (4.3)$$

572 The linear relation between r and p , or alternatively B and p have important
 573 consequences for LHC physics. For hadron colliders, this is the limiting factor on

¹Muon colliders are a really cool option at high energies, since the relativistic γ factor gives them a relatively long lifetime in the lab frame.

574 going to higher energy scales; one needs a proportionally larger magnetic field to
575 keep the beam accelerating in a circle.

576 Besides the rigidity of the beam, the most important quantities to characterize
577 a beam are known as the (normalized) *emittance* ϵ_N and the *betatron function* β .
578 These quantities determine the transverse size σ of a relativistic beam $v \gtrsim c$ beam :
579 $\sigma^2 = \beta^* \epsilon_N / \gamma_{\text{rel}}$, where β^* is the value of the betatron function at the collision point
580 and γ_{rel} is the Lorentz factor.

These quantities determine the *instantaneous luminosity* L of a collider, which combined with the cross-section σ of a particular physics process, give the rate of this physics process :

$$R = L\sigma. \quad (4.4)$$

The instantaneous luminosity L is given by :

$$L = \frac{f_{\text{rev}} N_b^2 F}{4\pi\sigma^2} = \frac{f_{\text{rev}} n N_b^2 \gamma_{\text{rel}} F}{4\pi\beta^* \epsilon_N}. \quad (4.5)$$

581 Here we have introduced the frequency of revolutions f_{rev} , the number of bunches n ,
582 the number of protons per bunch N_b^2 , and a geometric factor F related to the crossing
583 angle of the beams.

The *integrated luminosity* $\int L$ gives the total number of a particular physics process P , with cross-section σ_P .

$$N_P = \sigma_P \int L. \quad (4.6)$$

584 Due to this simple relation, one can also quantify the “amount of data delivered” by
585 a collider simply by $\int L$.

586 4.2 Accelerator Complex

587 The Large Hadron Collider is the last accelerator in a chain of accelerators which
588 together form the CERN accelerator complex, which can be seen in 4.1. The protons



Figure 4.1: The CERN accelerator complex.

begin their journey to annihilation in a hydrogen source, where they are subsequently ionized. The first acceleration occurs in the Linac 2, a linear accelerator composed of RF cavities. The protons leave the Linac 2 at an energy of 50 MeV and enter the Proton Synchrotron Booster (PSB). The PSB contains four superimposed rings, which accelerate the protons to 1.4 GeV. The protons are then injected into the Proton Synchrotron (PS). This synchrotron increases the energy up to 25 GeV. After leaving the PS, the protons enter the Super Proton Synchrotron (SPS). This is the last step before entering the LHC ring, and the protons are accelerated to 450 GeV. From the SPS, the protons are injected into the beam pipes of the LHC. The process to fill the LHC rings with proton bunches from start to finish typically takes about four minutes.

600 4.3 Large Hadron Collider

The Large Hadron Collider is the final step in the CERN accelerator complex, and produces the collisions analyzed in this thesis. From the point of view of experimentalists on the general-purpose ATLAS and CMS experiments, the main goal of the LHC is to deliver collisions at the highest possible energy, with the highest possible instantaneous luminosity. The LHC was installed in the existing 27 km tunnel used by the Large Electron Positron (LEP) collider [87]. This allowed the existing accelerator complex at CERN, described in the previous section, to be used as the injection system to prepare the protons up to 450 GeV. Many aspects of the LHC design were decided by this very fact, and specified the options allowed to increase the energy or luminosity. In particular, the radius of the tunnel was already specified; from Eq.4.3, this implies the momentum (or energy) of the beam is entirely determined by the magnetic field. Given the 27 km circumference of the LEP tunnel, one can calculate the required magnetic field to reach the 7 TeV per proton design energy of the LHC :

$$r = C/2\pi = 4.3 \text{ km} \quad (4.7)$$

$$\rightarrow B = \frac{p}{rc} = 5 \text{ T} \quad (4.8)$$

601 In fact, the LHC consists of 8 528 m straight portions consisting of RF cavities, used
602 to accelerate the particles, and 8 circular portions which bend the protons around the
603 LHC ring. These circular portions actually have a slightly smaller radius of curvature
604 $r = 2804 \text{ m}$, and we require $B = 8.33 \text{ T}$. To produce this large field, we need to use
605 superconducting magnets, as discussed in the next section.

606 Magnets

607 There are many magnets used by the LHC machine, but the most important are the
608 1232 dipole magnets; a schematic is shown in Fig.4.2 and a photograph is shown in



CERN AC/DI/MM — 2001/06

Figure 4.2: Schematic of an LHC dipole magnet.

609 Fig.4.3.

610 The magnets are made of Niobium and Titanium. The maximum field strength is
 611 10 T when cooled to 1.9 Kelvin. The magnets are cooled by superfluid helium, which
 612 is supplied by a large cryogenic system. Due to heating between the eight helium
 613 refrigerators and the beampipe, the helium is cooled in the refrigerators to 1.8 K.

614 A failure in the cooling system can cause what is known as a *quench*. If the
 615 temperature goes above the critical superconducting temperature, the metal loses its
 616 superconducting properties, which leads to a large resistance in the metal. This leads
 617 to rapid temperature increases, and can cause extensive damages if not controlled.

618 The dipole magnets are 16.5 meters long with a diameter of 0.57 meters. There
 619 are two individual beam pipes inside each magnet, which allows the dipoles to house
 620 the beams travelling in both directions around the LHC ring. They curve slightly,
 621 at an angle of 5.1 mrad, which carefully matches the curvature of the ring. The

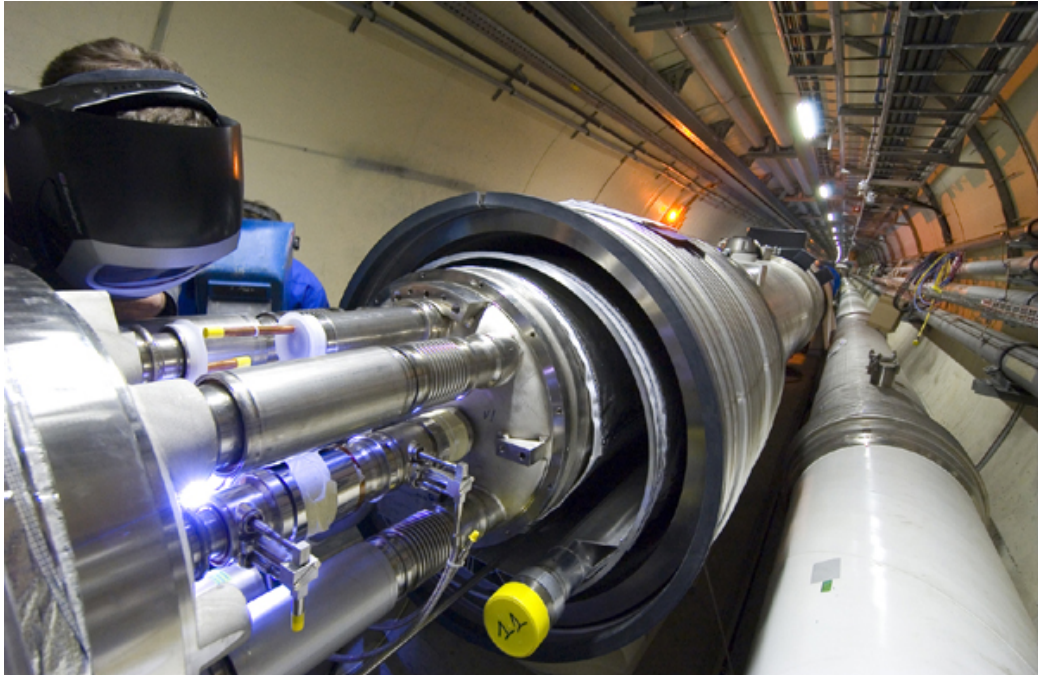


Figure 4.3: Photograph of a technician connecting an LHC dipole magnet.

622 beampipes inside of the magnets are held in high vacuum, to avoid stray particles
623 interacting with the beam.

624 **4.4 Dataset Delivered by the LHC**

625 In this thesis, we analyze the data delivered by the LHC to ATLAS in the 2015 and
626 2016 datasets. The beam parameters relevant to this dataset are available in Table
627 [4.1](#).

628 The peak instantaneous luminosity delivered in 2015 (2016) was $L =$
629 $5.2(11) \text{ cm}^{-2}\text{s}^{-1} \times 10^{33}$. One can note that the instantaneous luminosity delivered in
630 the 2016 dataset exceeds the design luminosity of the LHC. The total integrated
631 luminosity delivered was 13.3 fb^{-1} . In Figure [4.4](#), we display the integrated luminosity
632 as a function of day for 2015 and 2016.

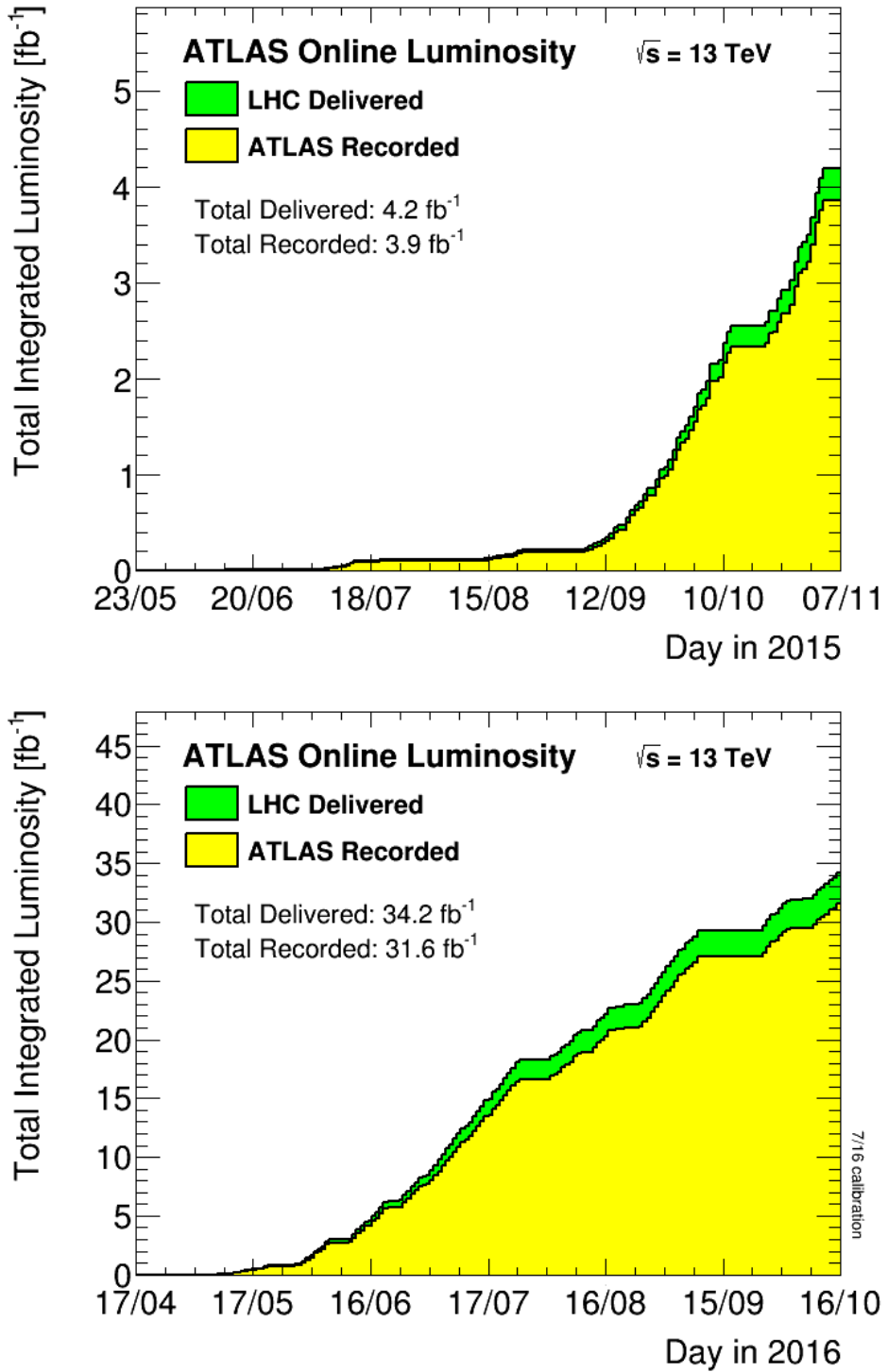


Figure 4.4: Integrated Luminosity delivered by the LHC and collected by ATLAS in the 2015 and 2016 datasets.

Parameter	Injection	Extraction
Energy (GeV)	450	7000
Rigidity (T-m)	3.8	23353
Bunch spacing (ns)	25	25
Design Luminosity ($\text{cm}^{-2}\text{s}^{-1} \times 10^3$)	-	1.0
Bunches per proton beam	2808	2808
Protons per bunch	1.15 e11	1.15 e11
Beam lifetime (hr)	-	10
Normalized Emittance ϵ_N (mm μrad)	3.3	3.75
Betatron function at collision point β^* (cm)	-	55

Table 4.1: Beam parameters of the Large Hadron Collider.

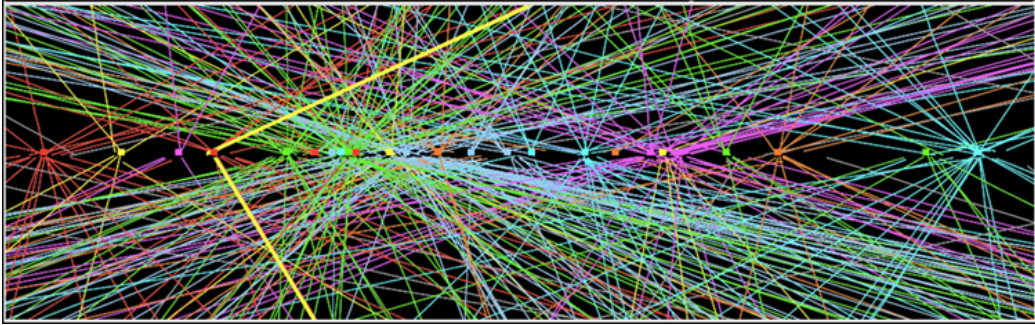


Figure 4.5: Simulated event with many pileup vertices.

633 Pileup

634 *Pileup* is the term for the additional proton-proton interactions which occur during
 635 each bunch crossing of the LHC. At the beginning of the LHC physics program, there
 636 had not been a collider which averaged more than a single interaction per bunch
 637 crossing. In the LHC, each bunch crossing (or *event*) generally contains multiple
 638 proton-proton interactions. An simulated event with many *vertices* can be seen in
 639 Fig.4.5. The so-called *primary vertex* (or *hard scatter vertex*) refers to the vertex
 640 which has the highest Σp_T^2 ; this summation occurs over the *tracks* in the detector,
 641 which we will describe later[**ATL-INDET-PUB-2009-001**]. We then distinguish
 642 between *in-time* pileup and *out-of-time* pileup. In-time pileup refers to the additional
 643 proton-proton interactions which occur in the event. Out-of-time pileup refers to
 644 effects related to proton-proton interactions previous bunch crossings.

645 We quantify in-time pileup by the number of “primary”² vertices in a particular
646 event. To quantify the out-of-time pileup, we use the average number of interactions
647 per bunch crossing $\langle \mu \rangle$ over some human-scale time. In Figure 4.6, we show the
648 distribution of μ for the dataset used in this thesis.

²The primary vertex is as defined above, but we unfortunately use the same name here.



Figure 4.6: Mean number of interactions per bunch crossing in the 2015 and 2016 datasets.

The ATLAS detector

651 The dataset analyzed in this thesis was taken by the ATLAS detector [88], which is
 652 located at the “Point 1” cavern of the LHC beampipe, just across the street from
 653 the main CERN campus. The much-maligned acronym stands for *A Toroidal LHC*
 654 *ApparatuS*. ATLAS is a massive cylindrical detector, with a radius of 12.5 m and a
 655 length of 44 m, with nearly hermitic coverage around the collision point. It consists
 656 of multiple subdetectors; each plays a role in ATLAS’s ultimate purpose of measuring
 657 the energy, momentum, and type of the particles produced in collisions delivered by
 658 the LHC. These subdetectors are immersed in a hybrid solenoid-toroid magnet system
 659 whichs forces charged particles to curve, which allows for precise measurements of
 660 their momenta. These magnetic fields are maximized in the central solenoid magnet,
 661 which contains a magnetic field of 2 T. A schematic of the detector can be seen in
 662 [5.1](#).

663 The *inner detector* (ID) lies closest to the collision point, and contains three
 664 separate subdetectors. It provides pseudorapidity¹coverage of $|\eta| < 2.5$ for charged
 665 particles to interact with the tracking material. The tracks reconstructed from the
 666 inner detector hits are used to reconstruct the primary vertices, as noted in Ch.??,

¹ATLAS uses a right-handed Cartesian coordinate system; the origin is defined by the nominal beam interaction point. The positive- z direction is defined by the incoming beam travelling counterclockwise around the LHC. The positive- x direction points towards the center of the LHC ring from the origin, and the positive- y direction points upwards towards the sky. For particles of transverse (in the $x - y$ plane) momentum $p_T = \sqrt{p_x^2 + p_y^2}$ and energy E , it is generally most convenient fully describe this particle’s kinematics as measured by the detector in the (p_T, ϕ, η, E) basis. The angle $\phi = \arctan(p_y/p_x)$ is the standard azimuthal angle, and $\eta = \ln \tan(\theta/2)$ is known as the pseudorapidity, and defined based on the standard polar angle $\theta = \arccos(p_z/p_T)$. For locations of i.e. detector elements, both (r, ϕ, η) and (z, ϕ, η) can be useful.



Figure 5.1: The ATLAS detector

and to determine the momemta of charged particles. The ATLAS *calorimeter* consists of two subdetectors, known as the *electromagnetic* and *hadronic* calorimeters. These detectors stop particles in their detector material, and measure the energy deposition inside, which measures the energy of the particles deposited. The calorimeters provide coverage out to pseudorapidity of $|\eta| < 4.9$. The muon spectrometer is aptly named; it is specifically used for muons, which are the only particles which generally reach the outer portions of the detector. In this region, we have the large tracking systems of the muon spectrometer, which provide precise measurements of muon momenta. The muon spectrometer has pseudorapidity coverage of $|\eta| < 2.7$.

5.1 Magnets

ATLAS contains multiple magnetic systems; primarily, we are concerned with the solenoid, used by the inner detector, and the toroids located outside of the ATLAS calorimeter. A schematic is shown in Fig.5.2. These magnetic fields are used to bend

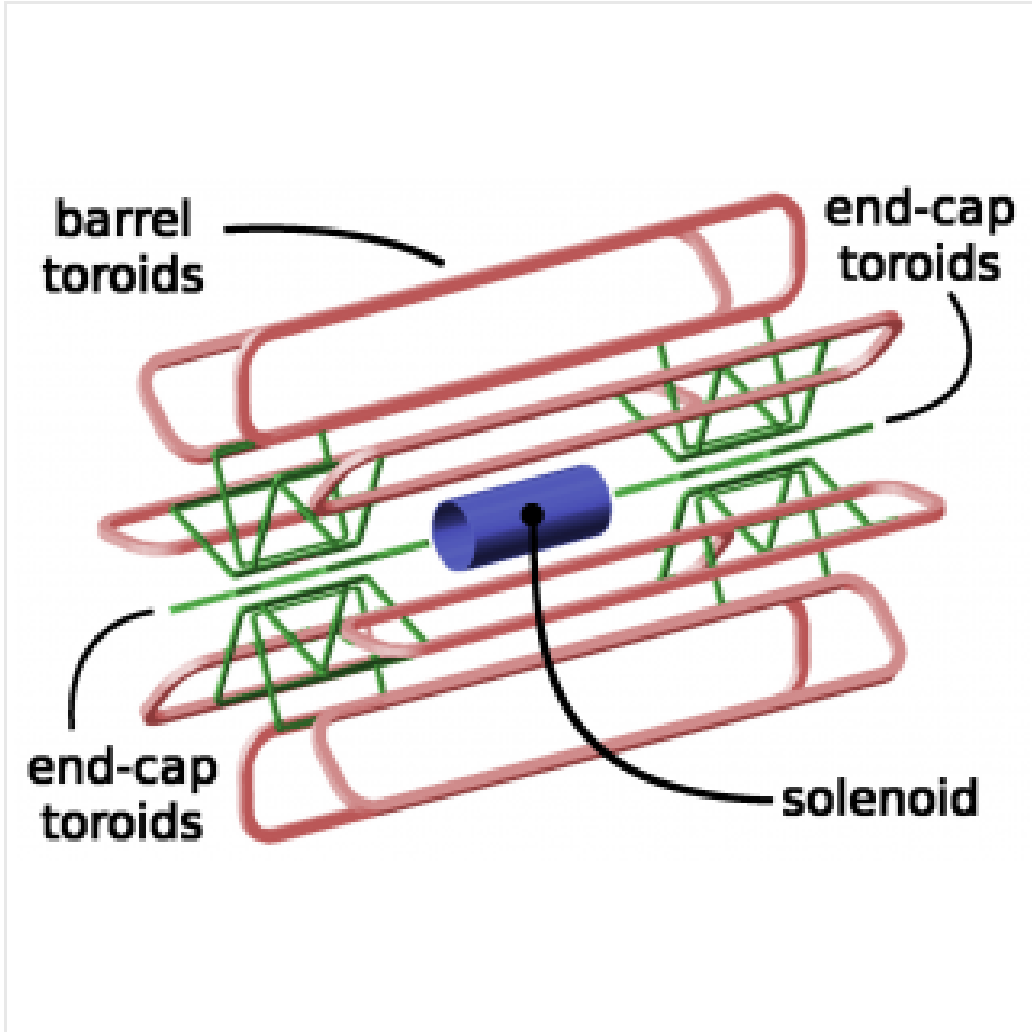


Figure 5.2: The ATLAS magnet system

680 charged particles under the Lorentz force, which subsequently allows one to measure
681 their momentum.

682 The ATLAS central solenoid is a 2.3 m diameter, 5.3 m long solenoid at the center
683 of the ATLAS detector. It produces a uniform magnetic field of 2 T; this strong field
684 is necessary to accurately measure the charged particles in this field. An important
685 design constraint for the central solenoid was the decision to place it in between the
686 inner detector and the calorimeters. To avoid excessive impacts on measurements in
687 the calorimetry, the central solenoid must be as transparent as possible².

²This is also one of the biggest functional differences between ATLAS and CMS; in CMS, the



Figure 5.3: The ATLAS inner detector

688 The toroid system consists of eight air-core superconducting barrel loops; these
 689 give ATLAS its distinctive shape. There are also two endcap air-core magnets. These
 690 produce a magnetic field in a region of approximately 26 m in length and 10 m of
 691 radius. The magnetic field in this region is non-uniform, due to the prohibitive costs
 692 of a solenoid magnet of that size.

693 **5.2 Inner Detector**

694 The ATLAS inner detector consists of three separate tracking detectors, which are
 695 known as, in order of increasing distance from the interaction point, the Pixel
 696 Detector, Semiconductor Tracker (SCT), and the Transition Radiation Tracker
 697 (TRT). When charged particles pass through these tracking layers, they produce
 698 *hits*, which using the known 2 T magnetic field, allows the reconstruction of *tracks*.
 699 Tracks are used as inputs for reconstruction of many higher-level physics objects,

solenoid is outside of the calorimeters.

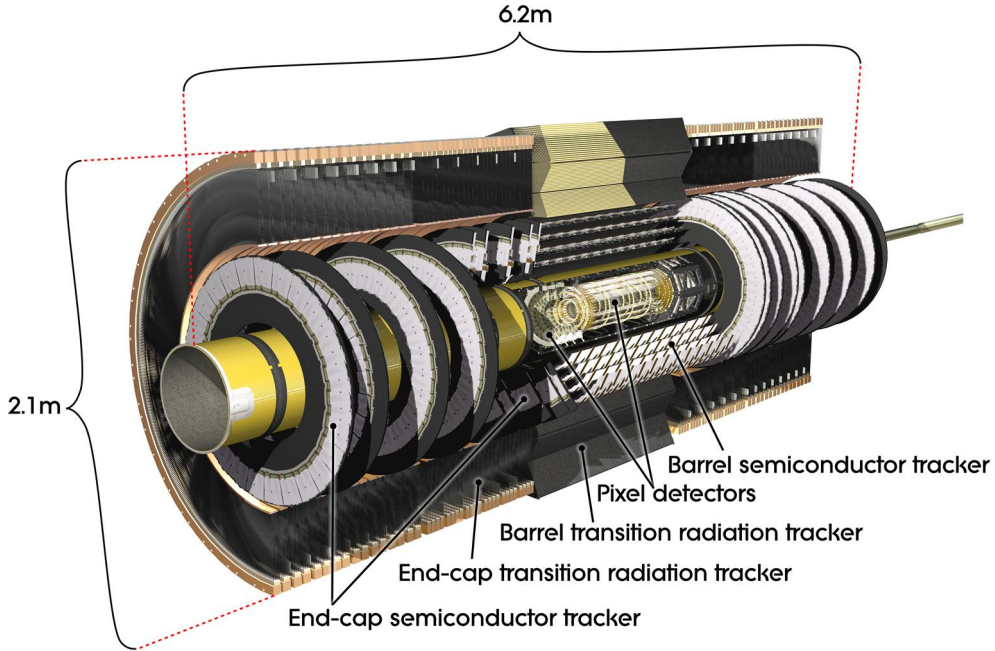


Figure 5.4: The ATLAS pixel detector

such as electrons, muons, photons, and E_T^{miss} . Accurate track reconstruction is thus crucial for precise measurements of charged particles.

Pixel Detector

The ATLAS pixel detector consists four layers of silicon “pixels”. This refers to the segmentation of the active medium into the pixels; compare to the succeeding silicon detectors, which will use silicon “strips”. This provides precise 3D hit locations. The layers are known as the “Insertable”³B-Layer (IBL), the B-Layer (or Layer-0), Layer-1, and Layer-2, in order of increasing distance from the interaction point. These layers are very close to the interaction point, and therefore experience a large amount of radiation.

Layer-1, Layer-2, and Layer-3 were installed with the initial construction of ATLAS. They contain front-end integrated electronics (FEI3s) bump-bonded to 1744

³Very often, the IBL is mistakenly called the Inner B-Layer, which would have been a much more sensible name.

712 silicon modules; each module is $250\ \mu\text{m}$ in thickness and contains 47232 pixels. These
713 pixels have planar sizes of $50 \times 400\ \mu\text{m}^2$ or $50 \times 600\ \mu\text{m}^2$, to provide highly accurate
714 location information. The FEI3s are mounted on long rectangular structures known
715 as staves, which encircle the beam pipe. A small tilt to each stave allows full coverage
716 in ϕ even with readout systems which are installed. These layers are at radia of 50.5
717 mm, 88.5 mm, and 122.5 mm from the interaction point.

718 The IBL was added to ATLAS after Run1 in 2012 at a radius of 33 mm from the
719 interaction point. The entire pixel detector was removed from the center of ATLAS
720 to allow an additional pixel layer to be installed. The IBL was required to preserve
721 the integrity of the pixel detector as radiation damage leads to inoperative pixels in
722 the other layers. The IBL consists of 448 FEI4 chips, arranged onto 14 staves. Each
723 FEI4 has 26880 pixels, of planar size $50 \times 250\ \mu\text{m}$. This smaller granularity was
724 required due to the smaller distance to the interaction point.

725 In total, a charged particle passing through the inner detector would expect to
726 leave four hits in the pixel detector.

727 Semiconductor Tracker

728 The SCT is directly beyond Layer-2 of the pixel detector. This is a silicon strip
729 detector, which do not provide the full 3D information of the pixel detector. The
730 dual-sensors of the SCT contain 2×768 individual strips; each strip has area $6.4\ \text{cm}^2$.
731 The SCT dual-sensor is then double-layered, at a relative angle of 40 mrad;
732 together these layers provide the necessary 3D information for track reconstruction.
733 There are four of these double-layers, at radia of 284 mm, 355 mm, 427 mm, and 498
734 mm. These double-layers provide hits comparable to those of the pixel detector, and
735 we have four additional hits to reconstruct tracks for each charged particle.

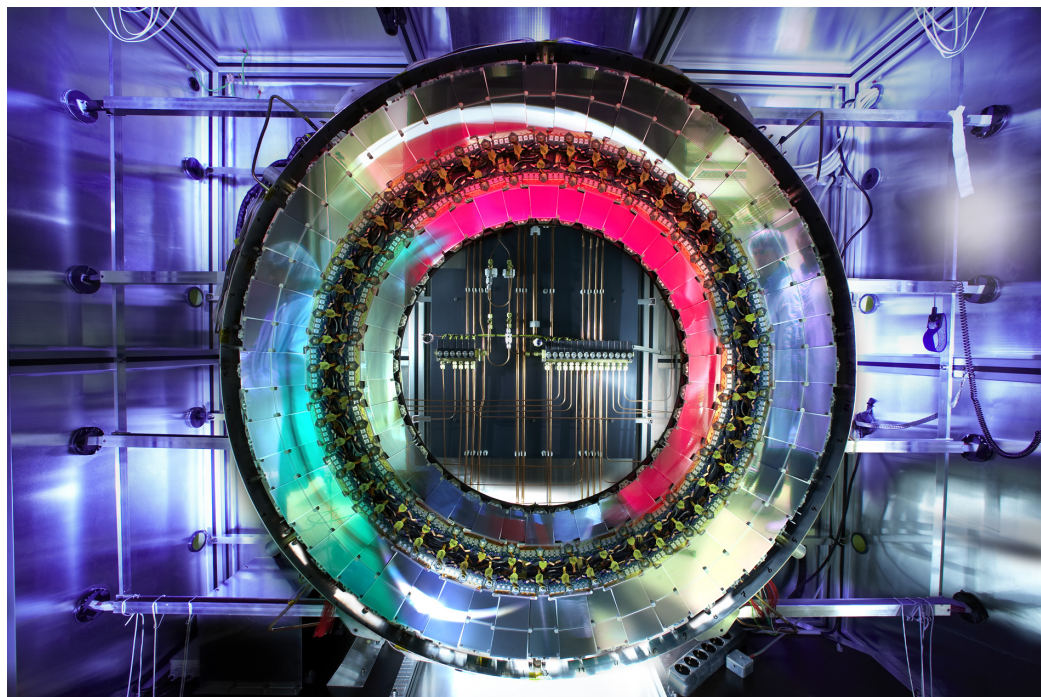


Figure 5.5: A ring of the Semiconductor Tracker

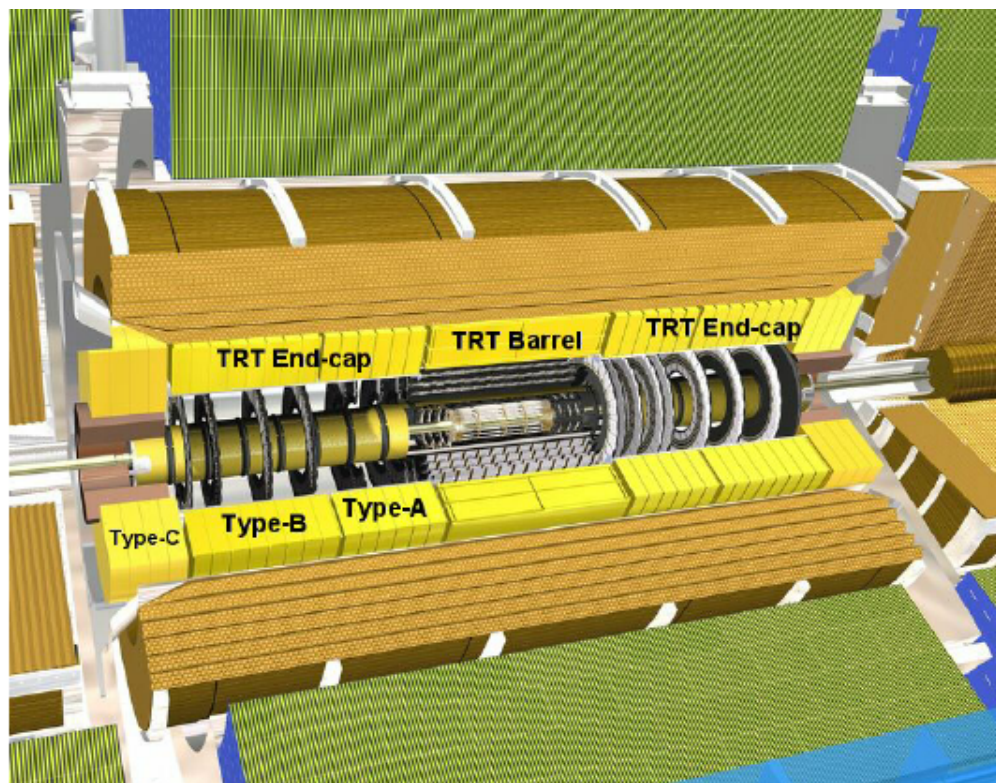


Figure 5.6: A schematic of the Transition Radiation Tracker

736 **Transition Radiation Tracker**

737 The Transition Radiation Tracker is the next detector radially outward from the SCT.
738 It contains straw drift tubes; these contain a tungsten gold-plated wire of $32 \mu\text{m}$
739 diameter held under high voltage (-1530 V) with the edge of the Kapton-aluminum
740 tube. They are filled with a gas mixture of primarily xenon that is ionized when
741 a charged particle passes through the tube. The ions are collected by the “drift”
742 due to the voltage inside the tubes, which is read out by the electronics. This gives
743 so-called “continuous tracking” throughout the tube, due to the large number of ions
744 produced.

745 The TRT is so-named due to the *transition radiation* (TR) it induces. Due to
746 the dielectric difference between the gas and tubes, TR is induced. This is important
747 for distinguishing electrons from their predominant background of minimum ionizing
748 particles. Generally, electrons have a much larger Lorentz factor than minimum
749 ionizing particles, which leads to additional TR. This can be used as an additional
750 handle for electron reconstruction.

751 **5.3 Calorimetry**

752 The calorimetry of the ATLAS detector also includes multiple subdetectors; these sub-
753 detectors allow precise measurements of the electrons, photons, and hadrons produced
754 by the ATLAS detector. Generically, calorimeters work by stopping particles in their
755 material, and measuring the energy deposition. This energy is deposited as a cascade
756 particles induce from interactions with the detector material known *showers*. ATLAS
757 uses *sampling* calorimeters; these alternate a dense absorbing material, which induces
758 showers, with an active layer which measures energy depositions by the induced
759 showers. Since some energy is deposited into the absorption layers as well, the energy
760 depositions must be properly calibrated for the detector.

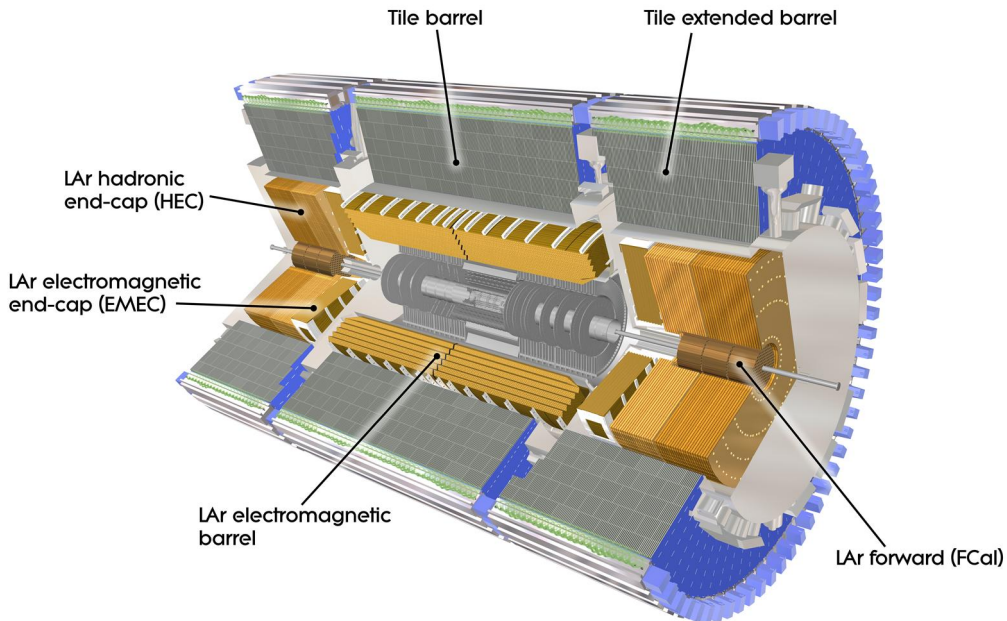


Figure 5.7: The ATLAS calorimeter

761 Electromagnetic objects (electrons and photons) and hadrons have much different
 762 interaction properties, and thus we need different calorimeters to accurately measure
 763 these different classes of objects; we can speak of the *electromagnetic* and *hadronic*
 764 calorimeters. ATLAS contains four separate calorimeters : the liquid argon (LAr)
 765 electromagnetic barrel calorimeter, the Tile barrel hadronic calorimeter, the LAr
 766 endcap electromagnetic calorimeter, the LAr endcap hadronic calorimeter, and the
 767 LAr Forward Calorimeter (FCal). Combined, these provide full coverage in ϕ up to
 768 $|\eta| < 4.9$, and can be seen in Fig.5.7.

769 **Electromagnetic Calorimeters**

770 The electromagnetic calorimeters of the ATLAS detector consist of the barrel and
 771 endcap LAr calorimeters. These are arranged into an ingenious “accordion” shape,
 772 shown in 5.8, which allows full coverage in ϕ and exceptional coverage in η while
 773 still allowing support structures for detector operation. The accordion is made of



Figure 5.8: A schematic of a subsection of the barrel LAr electromagnetic calorimeter

774 layers with liquid argon (active detection material) and lead (absorber) to induce
 775 electromagnetic showers. The LAr EM calorimeters are each more than 20 radiation
 776 lengths deep, which provides the high stopping power necessary to properly measure
 777 the electromagnetic showers.

778 The barrel component of the LAr EM calorimeter extends from the center of the
 779 detector out to $|\eta| < 1.475$. The calorimeter has a presampler, which measures the
 780 energy of any EM shower induced before the calorimeter. This has segmentation of
 781 $\Delta\eta = 0.025, \Delta\phi = .01$. There are three “standard” layers in the barrel, which have
 782 decreasing segmentation into calorimeter *cells* as one travels radially outward from
 783 the interaction point. The first layer has segmentation of $\Delta\eta = 0.003, \Delta\phi = .1$, and
 784 is quite thin relative to the other layers at only 4 radiation lengths deep. It provides
 785 precise η and ϕ measurements for incoming EM objects. The second layer is the
 786 deepest at 16 radiation lengths, with a segmentation of $\Delta\eta = 0.025, \Delta\phi = 0.025$. It



Figure 5.9: A schematic of Tile hadronic calorimeter

is primarily responsible for stopping the incoming EM particles, which dictates its large relative thickness, and measures most of the energy of the incoming particles. The third layer is only 2 radiation lengths deep, with a rough segmentation of $\Delta\eta = 0.05$, $\Delta\phi = .025$. The deposition in this layer is primarily used to distinguish hadrons interacting electromagnetically and entering the hadronic calorimeter from the strictly EM objects which are stopped in the second layer.

The barrel EM calorimeter has a similar overall structure, but extends from $1.4 < |\eta| < 3.2$. The segmentation in η is better in the endcap than the barrel; the ϕ segmentation is the same. In total, the EM calorimeters contain about 190000 individual calorimeter cells.

Hadronic Calorimeters

The hadronic calorimetry of ATLAS sits directly outside the EM calorimetry. It contains three subdetectors : the barrel Tile calorimeter, the endcap LAr calorimeter,

800 and the Forward LAr Calorimeter. Similar to the EM calorimeters, these are
801 sampling calorimeters that alternate steel (dense material) with an active layer
802 (plastic scintillator).

803 The barrel Tile calorimeter extends out to $|\eta| < 1.7$. There are again three layers,
804 which combined give about 10 interactions length of distance, which provides excellent
805 stopping power for hadrons. This is critical to avoid excess *punchthrough* to the muon
806 spectrometer beyond the hadronic calorimeters. The first layer has a depth of 1.5
807 interaction lengths. The second layer is again the thickest at a depth of 4.1 interaction
808 lengths; most of the energy of incoming particle is deposited here. Both the first and
809 second layer have segmentation of about $\Delta\eta = 0.1, \Delta\phi = 0.1$. Generally, one does not
810 need as fine of granularity in the hadronic calorimeter, since the energy depositions
811 in the hadronic calorimeters will be summed into the composite objects we know as
812 jets. The third layer has a thickness of 1.8 interaction lengths, with a segmentation of
813 $\Delta\eta = 0.2, \Delta\phi = 0.1$. The use of multiple layers allows one to understand the induced
814 hadronic shower as it propagates through the detector material.

815 The endcap LAr hadronic calorimeter covers the region $1.5 < |\eta| < 3.2$. It is
816 again a sampling calorimeter; the active material is LAr with a copper absorbed. It
817 does not use the accordion shape of the other calorimeters; it has a “standard” flat
818 shape perpendicular to the interaction point. The segmentation varies with η . For
819 $1.5 < |\eta| < 2.5$, the cells are $\Delta\eta = 0.1, \Delta\phi = 0.1$; in the region $2.5 < |\eta| < 3.2$, the
820 cells are $\Delta\eta = 0.2, \Delta\phi = 0.2$ in size.

821 The final calorimeter in ATLAS is the forward LAr calorimeter. Of those
822 subdetectors which are used for standard reconstruction techniques, the FCal sits
823 at the most extreme values of $3.1 < |\eta| < 4.9$. The FCal itself is made of three
824 subdetectors; FCal1 is actually an electromagnetic module, while FCal2 and FCal3
825 are hadronic. The absorber in FCal1 is copper, with a liquid argon active medium.
826 FCal2 and FCal3 also use a liquid argon active medium, with a tungsten absorber.

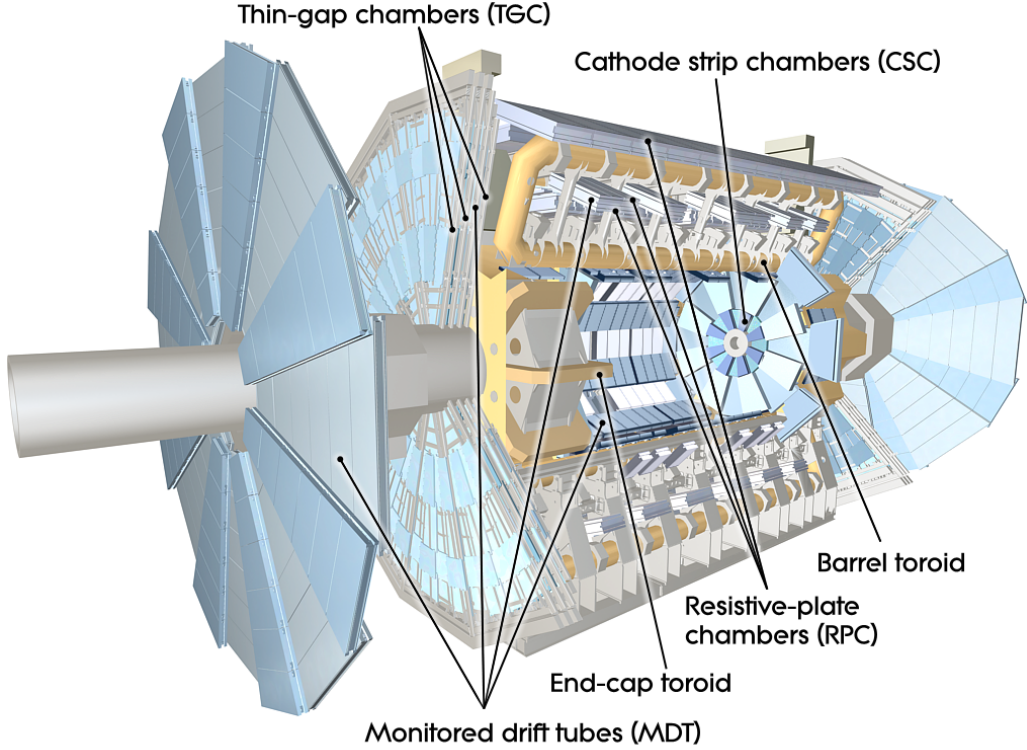


Figure 5.10: The ATLAS muon spectrometer

827 5.4 Muon Spectrometer

828 The muon spectrometer is the final major subdetector of the ATLAS detector.
829 The muon spectrometer sits outside the hadronic calorimetry, with pseudorapidity
830 coverage out to $|\eta| < 2.7$. The MS is a huge detector, with some detector elements
831 existing as far as 11 m in radius from the interaction point. This system is used
832 almost exclusively to measure the momenta of muons; these are the only measured
833 SM particles which consistently exit the hadronic calorimeters. These systems provide
834 a rough measurement, which is used in triggering (described in Ch.5.5), and a precise
835 measurement to be used in offline event reconstruction as described in Ch.???. The
836 MS produces tracks in a similar way to the ID; the hits in each subdetector are
837 recorded and then tracks are produced from these hits. Muon spectrometer tracks are
838 largely independent of the ID tracks due to the independent solenoidal and toroidal
839 magnet systems used in the ID and MS respectively. The MS consists of four separate

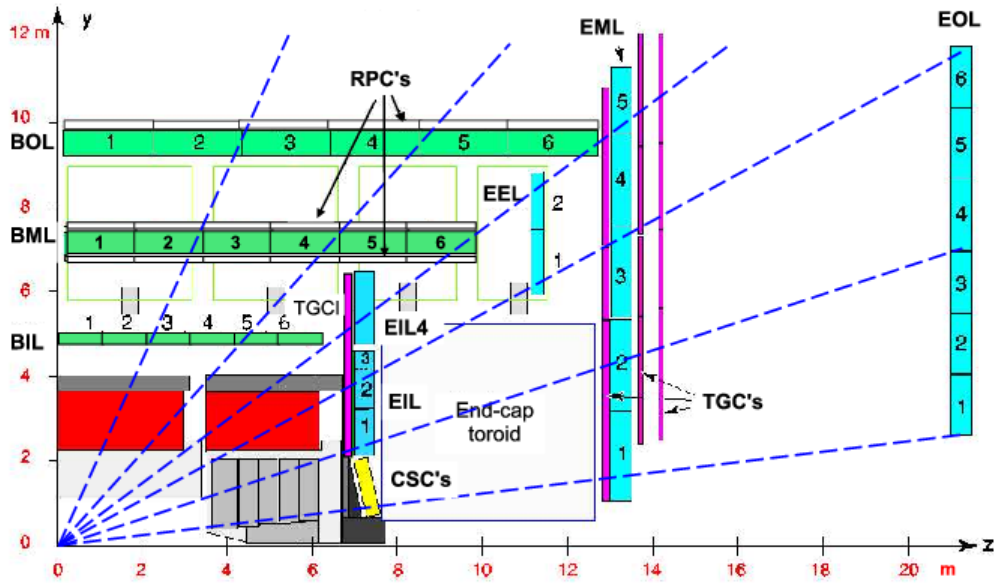


Figure 5.11: A schematic in z/η showing the location of the subdetectors of the muon spectrometer

840 subdetectors: the barrel region is covered by the Resistive Plate Chambers (RPCs)
 841 and Monitored Drift Tubes (MDTs) while the endcaps are covered by MDTs, Thin
 842 Gap Chambers (TGCs), and Cathode Strip Chambers (CSCs).

843 Monitored Drift Tubes

844 The MDT system is the largest individual subdetector of the MS. MDTs provide
 845 precision measurements of muon momenta as well as fast measurements used for
 846 triggers. There are 1088 MDT chambers providing coverage out to pseudorapidity
 847 $|\eta| < 2.7$; each consists of an aluminum tube containing an argon- CO_2 gas mixture.
 848 In the center of each tube there $50\mu\text{m}$ diameter tungsten-rhenium wire at a voltage of
 849 3080 V. A muon entering the tube will induce ionization in the gas, which will “drift”
 850 towards the wire due to the voltage. One measures this ionization as a current in the
 851 wire; this current comes with a time measurement related to how long it takes the
 852 ionization to drift to the wire.

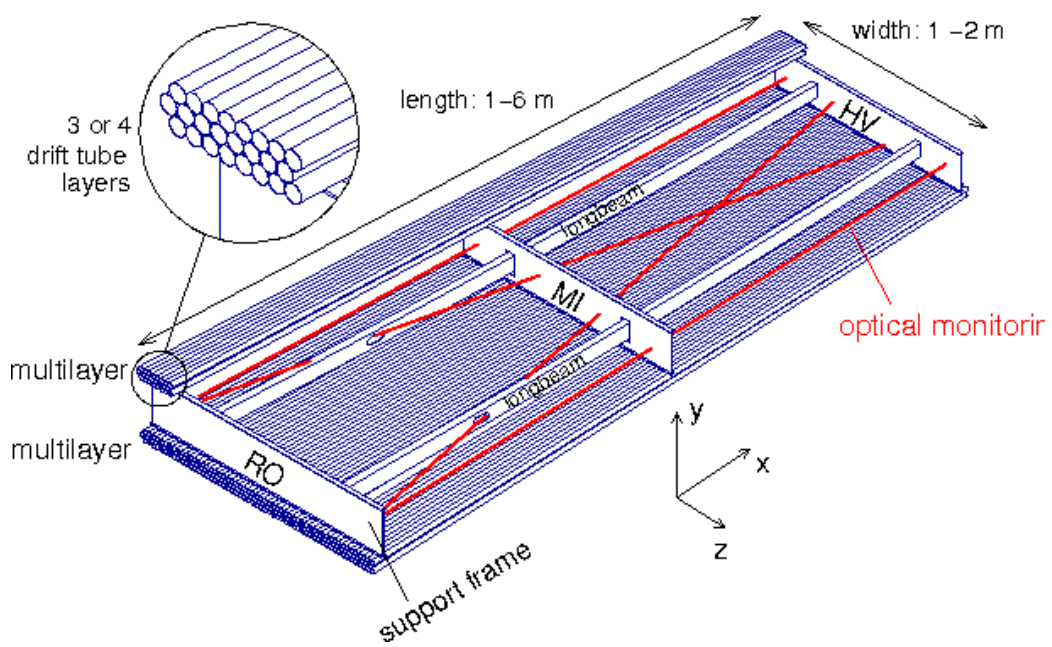


Figure 5.12: Schematic of a Muon Drift Tube chamber

853 These tubes are layered in a pattern shown in Fig.5.12. Combining the measure-
854 ments from the tubes in each layer gives good position resolution. The system consists
855 of three subsystems of these layers, at 5 m, 7m, and 9 m from the interaction point.
856 The innermost layer is directly outside the hadronic calorimeter. The combination of
857 these three measurements gives precise momenta measurements for muons.

858 Resistive Plate Chambers

859 The RPC system is alternated with the MDT system in the barrel; the first two layers
860 of RPC detectors surround the second MDT layer while the third is outside the final
861 MDT layer. The RPC system covers pseudorapidity $|\eta| < 1.05$. Each RPC consists
862 of two parallel plates at a distance of 2 mm surrounding a $\text{C}_2\text{H}_2\text{F}_4$ mixture. The
863 electric field between these plates is 4.9k kV/mm. Just as in the MDTs, an incoming
864 muon ionizes the gas, and the deposited ionization is collected by the detector (in this
865 case on the plates). It is quite fast, but with a relatively poor spatial resolution of
866 1 cm. Still, it can provide reasonable ϕ resolution due to its large distance from the
867 interaction point. This is most useful in triggering, where the timing requirements are
868 quite severe. The RPCs are also complement the MDTs by providing a measurement
869 of the non-bending coordinate.

870 Cathode Strip Chambers

871 The CSCs are used in place of MDTs in the first layer of the endcaps. This region, at
872 $2.0 < |\eta| < 2.7$, has higher particle multiplicity at the close distance to the interaction
873 point from low-energy photons and neutrons. The MDTs were not equip to deal with
874 the higher particle rate of this region, so the CSCs were designed to deal with this
875 deficiency.

876 Each CSC consists multiwire proportional chambers, oriented radially outward
877 from the interaction point. These chambers overlap partially in ϕ . The wires contain



Figure 5.13: Photo of the installation of Cathode Strip Chambers and Monitored Drift Tubes

878 a gas mixture of argon and CO₂, which is ionized when muons enter. The detectors
879 operate with a voltage of 1900 V, with much lower drift times than the MDTs. They
880 provide less hits than MDTs, but their lower drift times lower uptime and reduce the
881 amount of detector overload.

882 The CSCs are arranged into four planes on the wheels of the muon spectrometer,
883 as seen in Fig.???. There are 32 CSCs in total, with 16 on each side of the detector
884 in η .

885 **Thin Gap Chambers**

886 The TGCs serve the purpose of the RPCs in the endcap at pseudorapidity of $1.05 <$
887 $|\eta| < 2.4$; they provide fast measurements used in triggering. The TGCs are also
888 multiwire proportional chambers a la the CSCs. The fast readouts necessary for
889 trigger are provided by a high electric field and a small wire-to-wire distance of 1.8
890 mm. These detectors provide both η and ϕ information, allowing the trigger to use
891 as much information as possible when selecting events.



Figure 5.14: Photo of a muon Big Wheel, consisting of Thin Gap Chambers

892 5.5 Trigger System

893 The data rate delivered by the LHC is staggering [89]. In the 2016 dataset, the
894 collision rate was 40 MHz, meaning a *bunch spacing* of 25 ns. In each of the event,
895 as we saw in Ch.??, there are many proton-proton collisions. Most of the collisions
896 are uninteresting, such as elastic scattering of protons, or even inelastic scattering
897 leading to low-energy dijet events. These types of events have been studied in detail
898 in previous experiments.

899 Even if one is genuinely interested in these events, it's *impossible* to save all of
900 the information available in each event. If all events were written "to tape" (as the
901 jargon goes), ATLAS would store terabytes of data per second. We are limited to only
902 about 1000 Hz readout by computing processing time and storage space. We thus
903 implement a *trigger* which provides fast inspection of events to drastically reduce
904 the data rate from the 40 MHz provided by the LHC to the 1000 Hz we can write to
905 tape for further analysis.

906 The ATLAS trigger system consists of a two-level trigger, known as the Level-
907 1 trigger (L1 trigger) and the High-Level Trigger (HLT)⁴. Trigger selections are
908 organized into *trigger chains*, where events passing a particular L1 trigger are passed
909 to a corresponding HLT trigger. For example, one would require a particular high- p_T
910 muon at L1, with additional quality requirements at HLT. One can also use HLT
911 triggers as prerequisites for each other, as is done in some triggers requiring both jets
912 and E_T^{miss} .

913 **Level-1 Trigger**

914 The L1 trigger is hardware-based, and provides the very fast rejection needed to
915 quickly select events of interest. The L1 trigger uses only what is known as *prompt*
916 data to quickly identify interesting events. Only the calorimeters and the triggering
917 detectors (RPCs and TGCs) of the MS are fast enough to be considered at L1,
918 since the tracking reconstruction algorithms used by the ID and the more precise
919 MS detectors are very slow. This allows quick identification of events with the
920 most interesting physical objects : large missing transverse momentum and high-
921 p_T electrons, muons, and jets.

922 L1 trigger processing is done locally. This means that events are selected without
923 considering the entire available event. Energy deposits over some threshold are
924 reconstructed as *regions of interest*. These RoIs are then compared using pattern
925 recognition hardware to “expected” patterns for the given RoIs. Events with RoIs
926 matching these expected patterns are then handed to the HLT through the Central
927 Trigger Processor. This step alone lowers the data rate down by about three orders
928 of magnitude.

⁴In Run1, ATLAS ran with a three-level trigger system. The L1 was essentially as today; the HLT consisted of two separate systems known as the L2 trigger and the Event Filter (EF). This was changed to the simpler system used today during the shutdown between Run1 and Run2.

929 **High-Level Trigger**

930 The HLT performs the next step, taking the incoming data rate from the L1 trigger
931 of ~ 75 kHz down to the ~ 1 kHz that can be written to tape. The HLT really
932 performs much like a simplified offline reconstruction, using many common quality
933 and analysis cuts to eliminate uninteresting events. This is done by using computing
934 farms located close to the detector, which process events in parallel. Individually, each
935 event which enters the computing farms takes about 4 seconds to reconstruct; the
936 HLT reconstruction time also has a long tail, which necessitates careful monitoring
937 of the HLT to ensure smooth operation.

938 HLT triggers are targetted to a particular physics process, such as a E_T^{miss} trigger,
939 single muon trigger, or multijet trigger. The collection of all triggers is known as
940 the trigger *menu*. Since many low-energy particles are produced in collisions, it is
941 necessary to set a *trigger threshold* on the object of interest; this is really just a fancy
942 naming for a trigger p_T cut. Due to the changing luminosity conditions of the LHC,
943 these thresholds change constantly, mostly by increasing thresholds with increasing
944 instantaneous luminosity. This allows an approximately constant number of events to be
945 written for further analysis. Triggers which have rates higher than those designated
946 by the menu are *prescaled*. This means writing only some fraction of the triggered
947 events. Of course, for physics analyses, one wishes to investigate all data events
948 passing some set of analysis cuts, so often one uses the “lowest threshold unprescaled
949 trigger”. *Turn-on curves* allow one to select the needed offline analysis cut to ensure
950 the trigger is fully efficient. An example turn-on curve for the E_T^{miss} triggers used in
951 the signal region of this analysis is shown in ??.

952 The full set of the lowest threshold unprescaled triggers considered here can be
953 found in Table 5.1. These are the lowest unprescaled triggers associated to the SUSY
954 signal models and Standard Model backgrounds considered in this thesis. More
955 information can be found in [89].

Physics Object	Trigger	p_T (GeV)	Threshold	Level-1 Seed	Additional Requirements	Approximate Rate (Hz)
2015 Data						
E_T^{miss}	HLT_xe70	70	L1_XE50	-	60	
Muon	HLT_mu24_iloose_L1MU15	50	L1_MU15	isolated, loose	130	
Muon	HLT_mu50	50	L1_MU15	-	30	
Electron	HLT_e24_1hmedium_llbase_L1EM20VH		L1_EM20VH	medium OR isolated, loose	140	
Electron	HLT_e60_1hmedium	60	L1_EM20VH	medium	10	
Electron	HLT_e120_1hloose	120	L1_EM20VH	loose	<10	
Photon	HLT_g120_loose	120	L1_EM20VH	loose	20	
2016 Data						
E_T^{miss}	HLT_xe100_mht_L1XE5000		L1_XE50	-	180	
Muon	HLT_mu24_ivarmedium4		L1_MU20	medium	120	
Muon	HLT_mu50	50	L1_MU20	-	40	
Electron	HLT_e24_1htight_noD1ivarloose		L1_EM22VHI	tight with no d_0 or loose	110	
Electron	HLT_e60_1hmedium_nd60		L1_EM22VHI	medium with no d_0	10	
Electron	HLT_e140_1hloose_noD0		L1_EM22VHI	loose with no d_0	<10	
Photon	HLT_g140_loose	140	L1_EM22VHI	loose	20	

Table 5.1: High-Level Triggers used in this thesis. Descriptions of loose, medium, tight, and isolated can be found in [89]. The d_0 cut refers to a quality cut on the vertex position; this was removed from many triggers in 2016 to increase sensitivity to displaced vertex signals. For most triggers, the increased thresholds in 2016 compared to 2016 were designed to keep the rate approximately equal. The exception is the E_T^{miss} triggers; see 5.5.

956 **Razor Triggers**

957 For the analysis presented in this thesis, the *razor triggers* were developed. These are
958 topological triggers, combining both jet and E_T^{miss} information to select interesting
959 events. In particular, they use the razor variable M_{Δ}^R which will be described in
960 Chapter ??.

961 Based on 2015 run conditions, these triggers would have allowed the use of a lower
962 offline E_T^{miss} cut with a similar rate to the nominal E_T^{miss} triggers. This can be seen
963 in the turn-on curves shown in Figure 5.15. The razor triggers are fully efficient at
964 nearly 100 GeV lower than the corresponding E_T^{miss} triggers in M_{Δ}^R .

965 There was a quite big change in the 2016 menu, which increased the rate given to
966 E_T^{miss} triggers drastically. This can be seen in the difference in rate shown between
967 E_T^{miss} triggers in 2015 and 2016 in Table 5.1. This allowed the E_T^{miss} triggers to
968 maintain a lower threshold throughout the dataset used in this thesis.

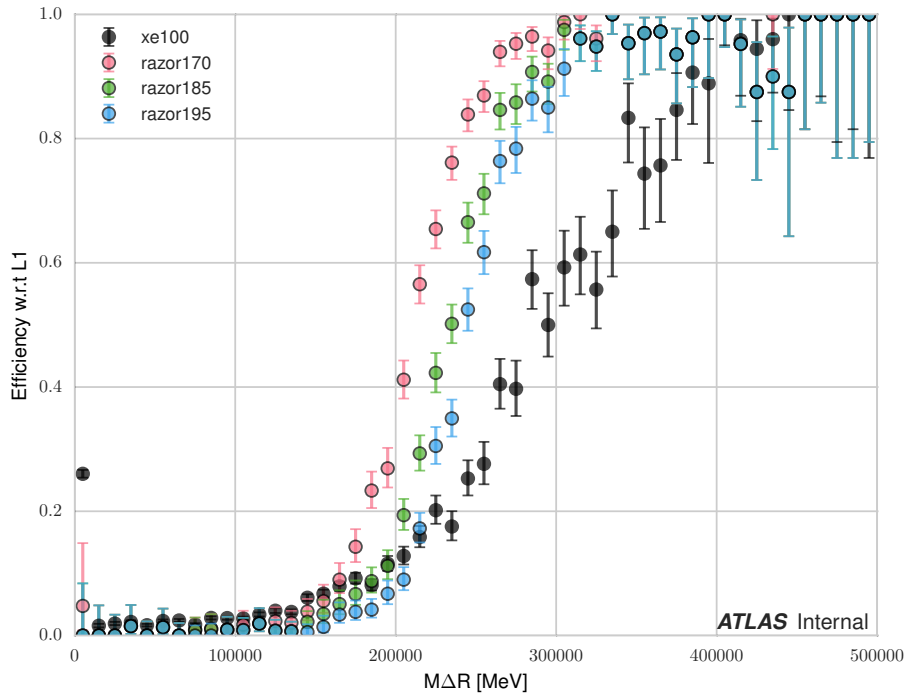
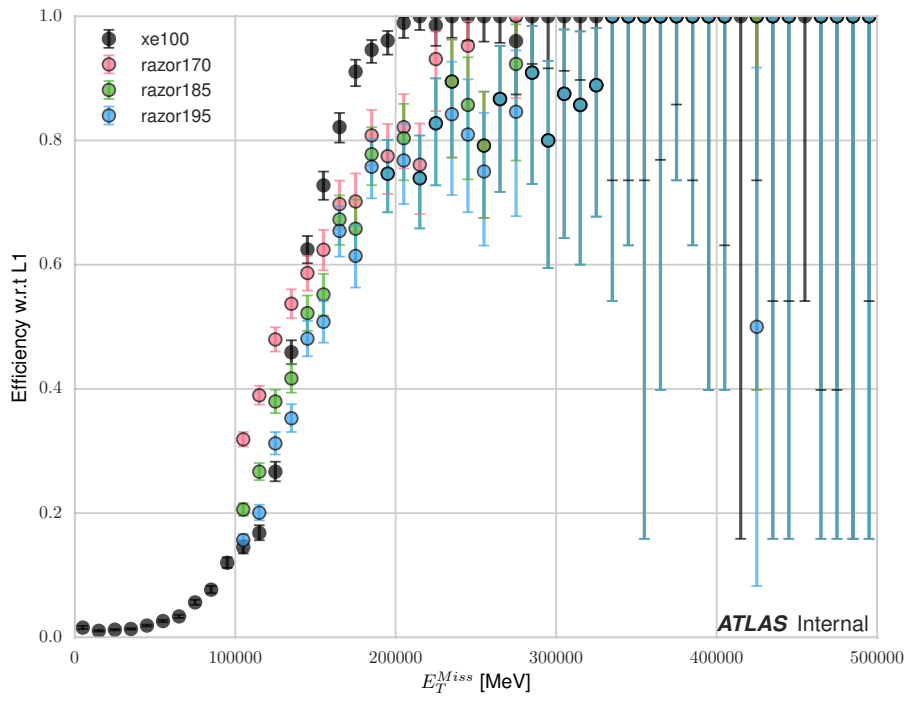


Figure 5.15: Turn-on curves for the razor triggers and nominal E_T^{miss} trigger. The razor triggers show a much sharper turn-on in M_{Δ}^R relative to the E_T^{miss} trigger. The converse is true for the E_T^{miss} triggers.

Object Reconstruction

971 This chapter describes the reconstruction algorithms used within ATLAS. We will
972 make the distinction between the “primitive” objects which are reconstructed from
973 the detector signals from the “composite” physics objects we use in measurements
974 and searches for new physics.

975 **6.1 Primitive Object Reconstruction**

976 The primitive objects reconstructed by ATLAS are *tracks* and (calorimeter) *clusters*.
977 These are reconstructed directly from tracking hits and calorimeter energy deposits
978 into cells. Tracks can be further divided into inner detector and muon spectrom-
979 eter tracks. Calorimeter clusters can be divided into sliding-window clusters and
980 topological clusters (topoclusters).

981 **Inner Detector Tracks**

982 Inner detector tracks are reconstructed from hits in the inner detector [90, 91] These
983 hits indicate that a charged particle has passed through the detector material. Due
984 to the 2 T solenoid in the inner detector, the hits associated with any individual
985 particle will be curved. The amount of curvature determines the momentum of the
986 particle. In any given event, there are upwards of 10^4 hits, making it impossible to do
987 any sort of combinatorics to reconstruct tracks. There are two algorithms used by
988 ATLAS track reconstruction, known as *inside-out* and *outside-in*.

989 ATLAS first employs the inside-out algorithm. One assumes the track begins
990 at the interaction point. Moving out from the interaction point, one creates track
991 seeds. Track seeds are proto-tracks constructed from three hits. These hits can be
992 distributed as three pixel hits, two pixel hits and one SCT hit, or three SCT hits.
993 One extrapolates the track and uses a combinatorial Kalman filter[90], which adds
994 the rest of the pixel and SCT hits to the seeds. This is done seed by seed, so it
995 avoids the combinatorial complexity involved with checking all hits with all seeds.
996 At this point, the algorithm applies an additional filter to avoid ambiguities from
997 nearby tracks. The TRT hits are added to the seeds using the same method. After
998 this procedure, all hits are associated to a track.

999 The next step is to figure out the correct kinematics of the track. This is
1000 done by applying a fitting algorithm which outputs the best-fit track parameters
1001 by minimizing the track distance from hits, weighted by each hit's resolution. These
1002 parameters are $(d_0, z_0, \eta, \phi, q/p)$ where d_0 (z_0) is the transverse (longitudinal) impact
1003 parameter and q/p is the charge over the track momenta. This set of parameters
1004 uniquely defines the measurement of the trajectory of the charged particle associated
1005 to the track. An illustration of a track with these parameters is shown in Fig.6.1.

1006 The other track reconstruction algorithm is the outside-in algorithm. As the
1007 name implies, we start from the outside of the inner detector, in the TRT, and
1008 extend the tracks in toward the interaction point. One begins by seeding from
1009 TRT hits, and extending the track back towards the center of the detector. The
1010 same fitting procedure is used as in the inside-out algorithm to find the optimal
1011 track parameters. This algorithm is particularly important for finding tracks which
1012 originate from interactions with the detector material, especially the SCT. For tracks
1013 from primary vertices, this often finds the same tracks as the inside-out algorithm,
1014 providing an important check on the consistency of the tracking procedure.

1015 In the high luminosity environment of the LHC, even the tracks reconstructed

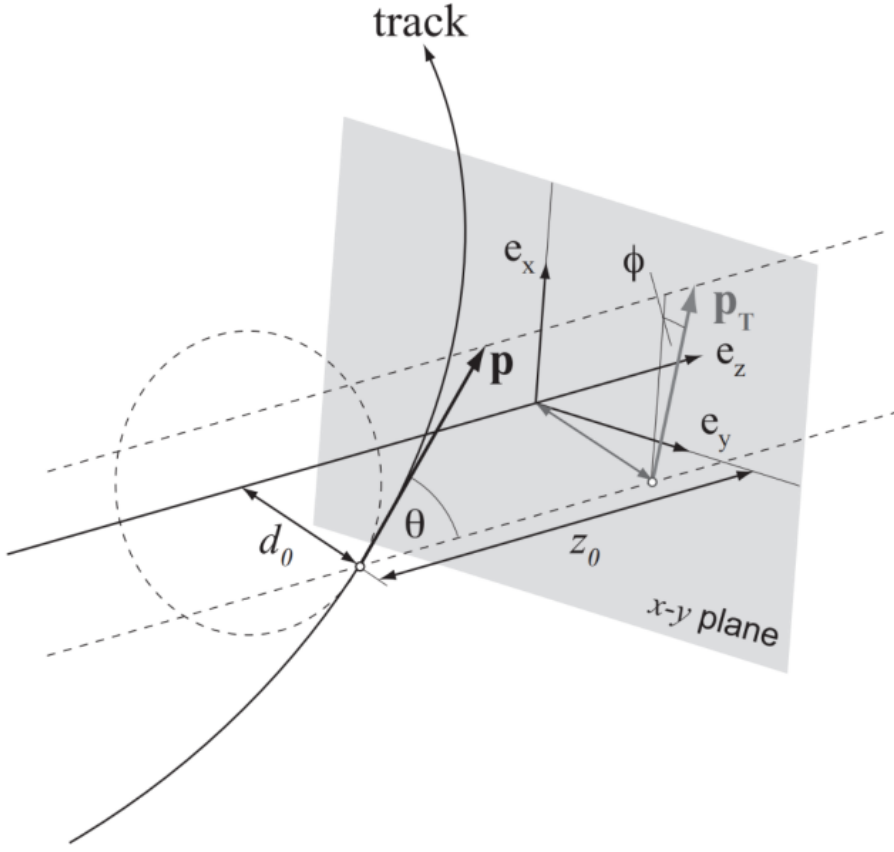


Figure 6.1: The parameters associated to a track.

from precision detectors such as those of ATLAS inner detector can sometimes lead to fake tracks from simple combinatoric chance. Several quality checks are imposed after track fitting which reduce this background. Seven silicon (pixel + SCT) hits are required for all tracks. No more than two *holes* are allowed in the pixel detector. Holes are expected measurements from the track that are missing in the pixel detector. Finally, tracks with poor fit quality, as measured by χ^2/ndf , are also rejected. Due to the high quality of the silicon measurements in the pixel detector and SCT, these requirements give good track reconstruction efficiency, as seen in Fig.6.2 for simulated events[92].



(a) Track reconstruction as a function of p_T . (b) Track reconstruction as a function of η .

Figure 6.2: Track reconstruction efficiency as a function of track p_T and η . The efficiency is defined as the number of reconstructed tracks divided by the number of generate charged particles.

1025 Sliding-window clusters

1026 The sliding-window algorithm is a way to combine calorimeter cells into composite
 1027 objects (clusters) to be used as inputs for other algorithms[93]. Sliding-window
 1028 clusters are the primary inputs to electron and photon reconstruction, as described
 1029 below. The electromagnetic calorimeter has high granularity, with a cell size of
 1030 $(\eta, \phi) = (.025, .025)$ in the coarsest second layer throughout most of the calorimeter.
 1031 The “window” consists of 3 by 5 cells in the (η, ϕ) space. All layers are added on
 1032 this same 2D space. One translates this window over the space and seeds a cluster
 1033 whenever the energy sum of the cells is maximized. If the seed energy is greater
 1034 than 2.5 GeV, this seed is called a sliding-window cluster. This choice was motivated
 1035 to optimize the reconstruction efficiency of proto-electrons and proto-photons while
 1036 rejecting fakes from electronic noise and additional particles from pileup vertices.

1037 Topological clusters

1038 Topoclusters are the output of the algorithm used within ATLAS to combine
1039 hadronic and electromagnetic calorimeter cells in a way which extracts signal from
1040 a background of significant electronic noise[94]. They are the primary input to the
1041 algorithms which reconstruct jets.

1042 Topological clusters are reconstructed from calorimeter cells in the following way.
1043 First, one maps all cells onto a single $\eta - \phi$ plane so one can speak of *neighboring*
1044 cells. Two cells are considered neighboring if they are in the same layer and directly
1045 adjacent, or if they are in adjacent layers and overlap in $\eta - \phi$ space. The *significance*
1046 ξ_{cell} of a cell during a given event is

$$\xi_{\text{cell}} = \frac{E_{\text{cell}}}{\sigma_{\text{noise},\text{cell}}} \quad (6.1)$$

1047 where $\sigma_{\text{noise},\text{cell}}$ is measured for each cell in ATLAS and E_{cell} measures the current
1048 energy level of the cell. One thinks of this as the measurement of the energy *over*
1049 *threshold* for the cell.

1050 Topocluster *seeds* are defined as calorimeter cells which have a significance $\xi_{\text{cell}} >$
1051 4. These are the inputs to the algorithm. One iteratively tests all cells adjacent
1052 to these seeds for $\xi_{\text{cell}} > 2$. Each cells passing this selection is then added to the
1053 topocluster, and the procedure is repeated. When the algorithm reaches the point
1054 where there are no additional adjacent cells with $\xi_{\text{cell}} > 2$, every positive-energy cell
1055 adjacent to the current proto-cluster is added. The collection of summed cells is a
1056 topocluster. An example of this procedure for a simulation dijet event is shown in
1057 Fig.6.3.

1058 There are two calibrations used for clusters[95]. These are known as the
1059 electromagnetic (EM) scale and the local cluster weighting (LCW) scale. The EM
1060 scale is the energy read directly out of the calorimeters as described. This scale
1061 is appropriate for electromagnetic processes. The LCW scale applies additional



Figure 6.3: Example of topoclustering on a simulated dijet event.

1062 scaling to the clusters based on the shower development. The cluster energy can be
1063 corrected for calorimeter non-compensation and the differences in the hadronic and
1064 electromagnetic calorimeters' responses. This scale provides additional corrections
1065 that improve the accuracy of hadronic energy measurements. This thesis only uses
1066 the EM scale corrections. LCW scaling requires additional measurements that only
1067 became available with additional data. Due to the jet calibration procedure that
1068 we will describe below, it is also a relatively complicated procedure to rederive the
1069 "correct" jet energy.

1070 Muon Spectrometer Tracks

1071 Muon spectrometer tracks are fit using the same algorithms as the ID tracks, but
1072 different subdetectors. The tracks are seeded by hits in the MDTs or CSCs. After
1073 seeding in the MDTs and CSCs, the hits from all subsystems are refit as the final
1074 MS track. These tracks are used as inputs to the muon reconstruction, as we will see
1075 below.

1076 6.2 Physics Object Reconstruction and Quality

1077 Identification

1078 There are essentially six objects used in ATLAS searches for new physics: electrons,
1079 photons, muons, τ -jets, jets, and E_T^{miss} . The reconstruction of these objects is
1080 described here. In this thesis, τ lepton jets are not treated differently from other
1081 hadronic jets, and we will not consider their reconstruction algorithms. A very
1082 convenient summary plot is shown in Fig.6.4.

1083 One often wishes to understand "how certain" we are that a particular object
1084 is truly the underlying physics object. In ATLAS, we often generically consider, in



Figure 6.4: The interactions of particles with the ATLAS detector. Solid lines indicate the particle is interacting with the detector, while dashed lines are shown where the particle does not interact.

1085 order, *very loose*, *loose*, *medium*, and *tight* objects¹. These are ordered in terms of
 1086 decreasing object efficiency, or equivalently, decreasing numbers of fake objects. We
 1087 will also describe briefly the classification of objects into these categories.

1088 In this thesis, since we present a search for new physics in a zero lepton final state,
 1089 we will provide additional details about jet and E_T^{miss} reconstruction.

¹ These are not all used for all objects, but it's conceptually useful to think of these different categories.

1090 **Electrons and Photons**

1091 **Reconstruction**

1092 The reconstruction of electrons and photons (often for brevity called “electromagnetic
1093 objects”) is very similar [93, 96, 97]. This is because the reconstruction begins with
1094 the energy deposit in the calorimeter in the form of an electromagnetic shower. For
1095 any incoming e/γ , this induces many more electrons and photons in the shower. The
1096 measurement in the calorimeter is similar for these two objects.

1097 One begins the reconstruction of electromagnetic objects from the sliding-window
1098 clusters reconstructed from the EM calorimeter. These $E > 2.5$ GeV clusters the
1099 the primary seed for electrons and photons. One then looks for all ID tracks within
1100 $\Delta R < 0.3$, where $\Delta R = \sqrt{\Delta\eta^2 + \Delta\phi^2}$. We “match” the track and cluster if they are
1101 within $\Delta\phi < 0.2$ in the direction of track curvature, or $\Delta\phi < 0.05$ in the direction
1102 opposite the track curvature. Those track-cluster seeds with tracks pointing to the
1103 primary vertex are reconstructed as electrons.

1104 For photons, we have two options to consider, known as *converted* and *unconverted*
1105 photons. Due to the high energy of the LHC collisions, typical photons have energy
1106 $>\sim 1$ GeV. At this scale, photons interact almost exclusively via pair-production in
1107 the presence of the detector material, as shown in Fig.6.5 [56]. If the track-cluster seed
1108 has a track which does not point at the primary vertex, we reconstruct this object as a
1109 converted photon. This happens since the photon travels a distance before decay into
1110 two electrons, and see the tracks coming from this secondary vertex. Those clusters
1111 which do not have any associated tracks are then reconstruced as an unconverted
1112 photon.

1113 The final step in electromagnetic object reconstruction is the final energy value
1114 assigned to these objects. This process is different between electrons and photons due
1115 to their differing signatures in the EM calorimeter. In the barrel, electrons energies

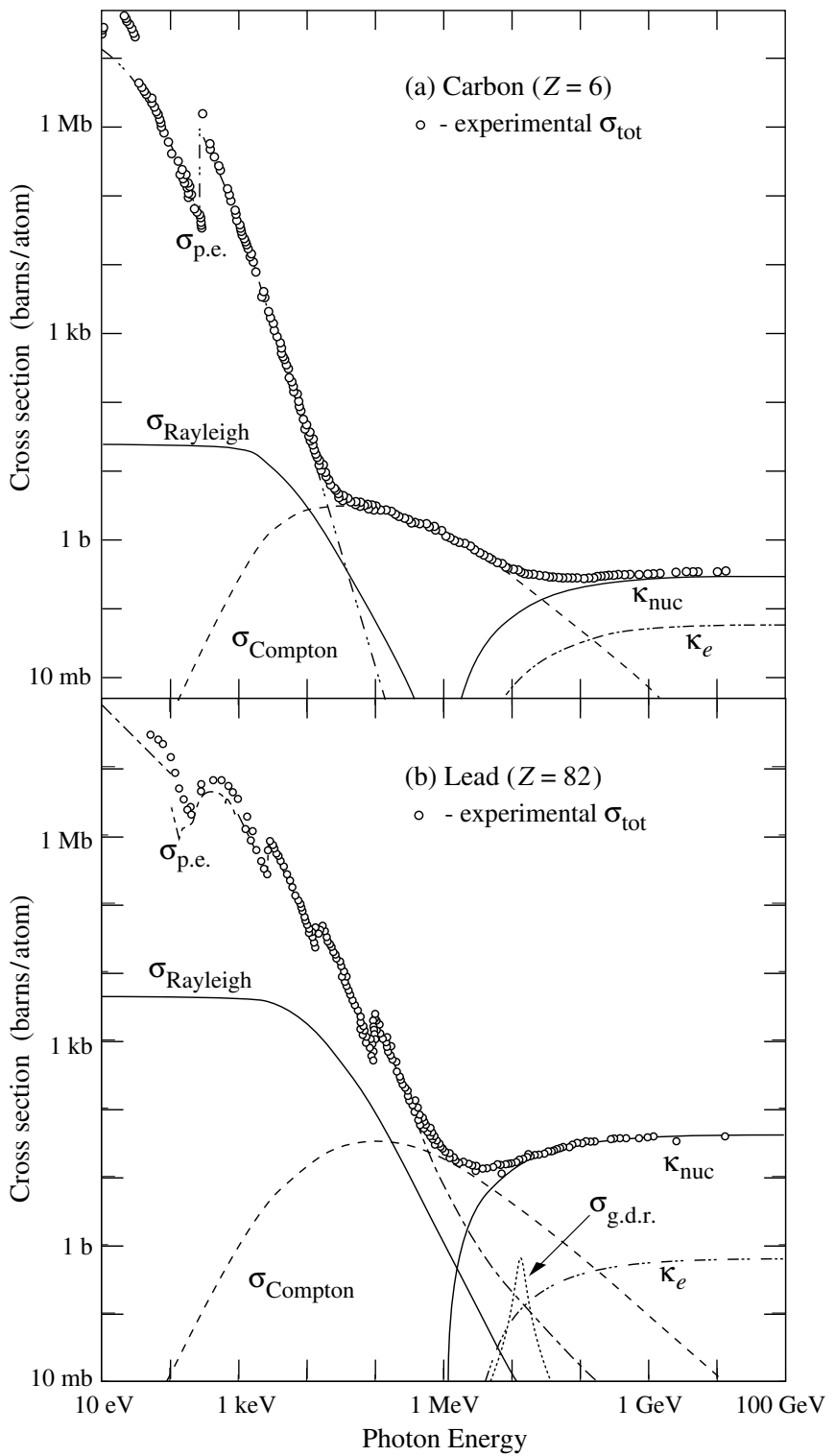


Figure 6.5: Photon total cross sections as a function of energy in carbon and lead, showing the contributions of different processes[56].

1116 are assigned as the sum of the 3 clusters in η and 7 clusters in ϕ to account for the
1117 electron curving in the ϕ direction. Barrel photons are assigned the energy sum of
1118 (3, 5) clusters in (η, ϕ) space. In the endcap, the effect of the magnetic field on the
1119 electrons is smaller, and there is a coarser granularity. Both objects sum the (5, 5)
1120 clusters for their final energy value.

1121 Quality Identification

1122 Electrons have a number of important backgrounds which can give fakes. Fake
1123 electrons come primarily from secondary vertices in hadron decays or misidentified
1124 hadronic jets. To reduce these backgrounds, quality requirements are imposed on
1125 electron candidates. Loose electrons have requirements imposed on the shower
1126 shapes in the electromagnetic calorimeter and on the quality of the associated ID
1127 track. There is also a requirement that there is a small energy deposition in the
1128 hadronic calorimeter behind the electron, to avoid jets being misidentified as electrons
1129 (low hadronic leakage). Medium and tight electrons have increasingly stronger
1130 requirements on these variables, and additional requirements on the isolation (as
1131 measured by ΔR) and matching of the ID track momentum and the calorimeter
1132 energy deposit.

1133 Photons are relatively straightforward to measure, since there are few background
1134 processes[98]. The primary one is pion decays to two photons, which can cause a jet
1135 to be misidentified as photon. Loose photons have requirements on the shower shape
1136 and hadronic leakage. Tight photons have tighter shower shape cuts, especially on
1137 the high granularity first layer of the EM calorimeter. The efficiency for unconverted
1138 tight photons as a function of p_T is shown in

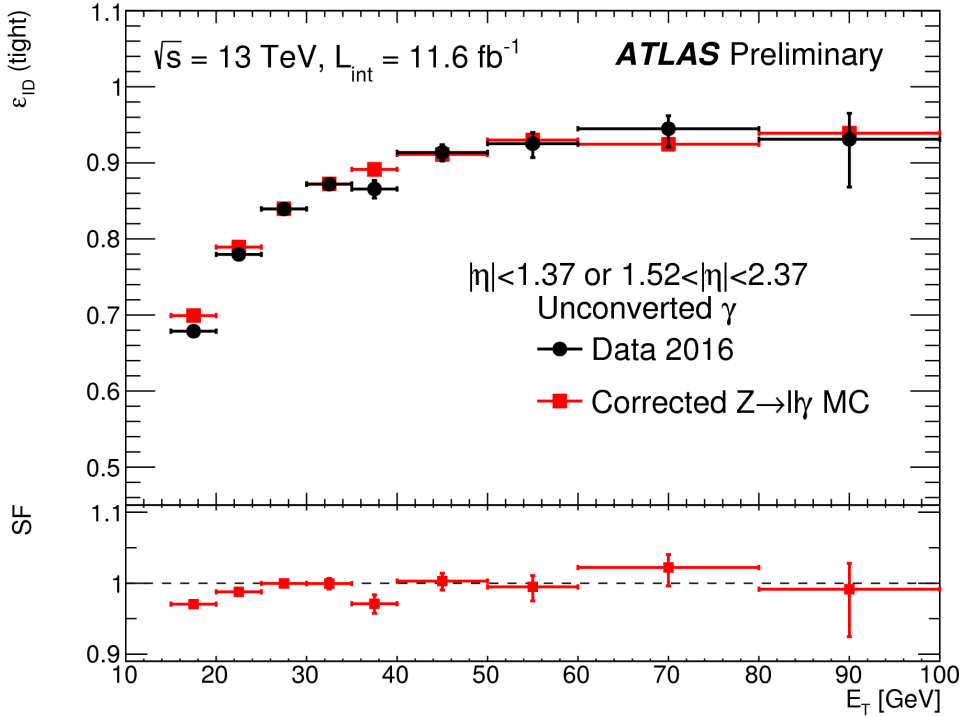


Figure 6.6: Unconverted photon efficiency as measured in [98].

1139 Muons

1140 Reconstruction

1141 Muons are reconstructed using measurements from all levels of the ATLAS detec-
 1142 tor[99]. They leave a ID track, a small, characteristic deposition in the EM calorime-
 1143 ter, and then a track in the muon spectrometer. The primary reconstruction technique
 1144 produces a so-called *combined* muon. “Combined” means using a combination of the
 1145 ID and MS tracks to produce the final reconstructed muon kinematics. This is done
 1146 by refitting the hits associated to both tracks, and using this refit track for the muon
 1147 kinematics. This process produces the best measured muons, although several other
 1148 worse algorithms are used when the full detector information is missing. An example
 1149 is in the region $2.5 < |\eta| < 2.7$ outside the ID acceptance, where MS tracks are used
 1150 without the corresponding ID tracks.

1151 **Quality Identification**

Several additional criteria are used to assure muon measurements are free of significant background contributions, especially from pion and kaon decays to muons. Muons produced via these decay processes are often characterized by a “kink”. Candidate muons with a poor fit quality, characterized by $\chi^2/\text{n.d.f.}$, are thus rejected. Additionally, the absolute difference in momentum measurements between the ID and MS provide another handle, since the other decay products from hadron decays carry away some amount of the initial hadron momentum. This is measured by

$$\rho' = \frac{|p_T^{\text{ID}} - p_T^{\text{MS}}|}{p_T^{\text{Combined}}}. \quad (6.2)$$

Additionally, there is a requirement on the q/p significance, defined as

$$S_{q/p} = \frac{|(q/p)^{\text{ID}} - (q/p)^{\text{MS}}|}{\sqrt{\sigma_{\text{ID}}^2 + \sigma_{\text{MS}}^2}}. \quad (6.3)$$

1152 The $\sigma_{\text{ID,MS}}$ in the denominator of Eq.6.3 are the uncertainties on the corresponding
1153 quantity from the numerator. Finally, cuts are placed on the number of hits in the
1154 various detector elements.

1155 Subsequently tighter cuts on these variables allow one to define the different muon
1156 identification criteria. Loose muons have the highest reconstruction efficiency, but
1157 the highest number of fake muons, since there are no requirements on the number
1158 of subdetector hits and the loosest requirements on the suite of quality variables.
1159 Medium muons consist of Loose muons with tighter cuts on the quality variables.
1160 They also require more than three MDT hits in at least two MDT layers. These are
1161 the default used by ATLAS analyses. Tight muons have stronger cuts than those of
1162 the medium selection, and reducing the reconstruction efficiency. The reconstruction
1163 efficiency as a function of p_T can be seen for Medium muons in Fig.6.7.

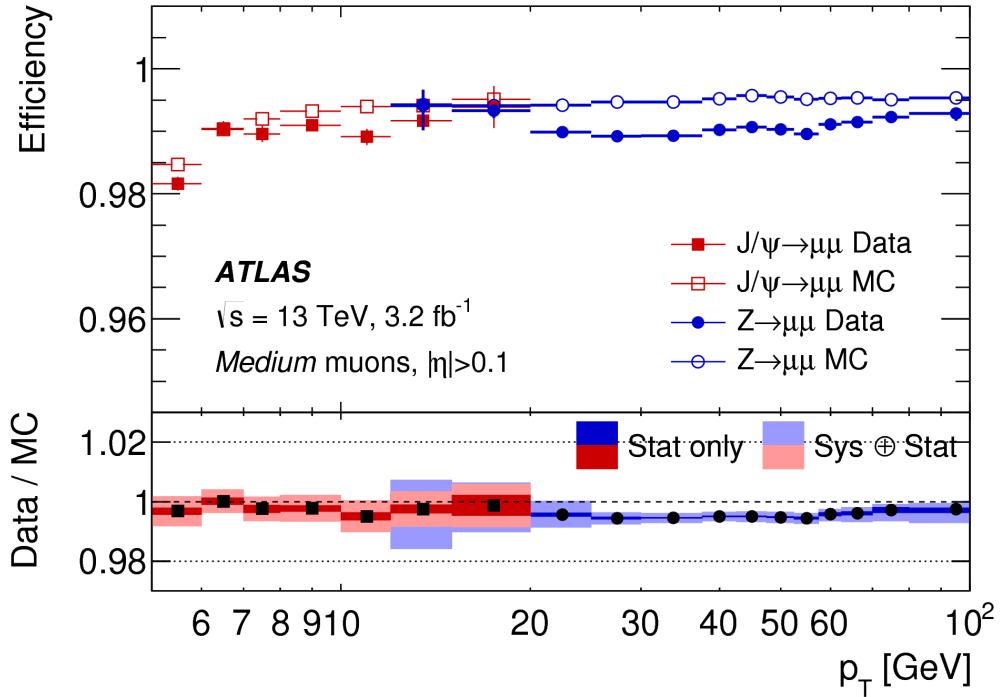


Figure 6.7: Medium muon efficiency as measured in [99].

1164 Jets

1165 Jets are composite objects corresponding to many physical particles [56, 100, 101]
 1166 This is a striking difference from the earlier particles. Fortunately, we normally (and
 1167 in this thesis) care about the original particle produced in primary collision. In the
 1168 SM, this corresponds to quarks and gluons. Due to the hadronization process, free
 1169 quarks and gluons spontaneously hadronize and produce a hadronic shower, which
 1170 we call a jet. These showers can be measured by the EM and hadronic calorimeters,
 1171 and the charged portions can be measured in the ID. The first question is how to
 1172 combine these measurements into a composite object representing the underlying
 1173 physical parton. This is done via jet algorithms.

1174 **Jet Algorithms**

1175 It might seem straightforward to combine the underlying physical particles into a
1176 jet. There are three important characteristics required for any jet reconstruction
1177 algorithm to be used by ATLAS.

- 1178 • Collinear safety - if any particle with four-vector p is replaced by two particles
1179 of p_1, p_2 with $p = p_1 + p_2$, the subsequent jet should not change

1180 • Radiative (infrared) safety - if any particle with four-vector p radiates a particle
1181 of energy $\alpha \rightarrow 0$, the subsequent jet should not change

1182 • Fast - the jet algorithm should be “fast enough” to be useable by ATLAS
1183 computing resources

1184 The first two requirements can be seen in terms of requirements on soft gluon emission.
1185 Since partons emit arbitrarily soft gluons freely, one should expect the algorithms
1186 to not be affected by this emission. The final requirement is of course a practical
1187 limitation.

The algorithms in use by ATLAS (and CMS) which satisfies these requirements are collectively known as the k_T algorithms [102–104]. These algorithms iteratively combine the “closest” objects, defined using the following distance measures :

$$d_{ij} = \min(k_{T,i}^{2p}, k_{T,j}^{2p}) \frac{\Delta_{ij}^2}{R^2} \quad (6.4)$$
$$d_{iB} = k_{Ti}^{2p}$$

1188 In Eq.6.4, k_T, i is the transverse momentum of i -th jet *constituent*, Δ_{ij} is the angular
1189 distance between the constituents. Both R and p are adjustable parameters: R is
1190 known as the (jet) *cone size* and p regulates the power of the energy versus the
1191 geometrical scales. The algorithm sequence, for a given set of objects i with four-
1192 vector k :

- 1193 1. Find the minimum distance in the set of all d_{ij} and d_{iB} .

1194 2. If the distance is one of the d_{ij} , combine the input pair of object i, j and return
1195 to (1). If the distance is one of the d_{iB} , remove the object from the list, call it
1196 a jet, and return to (1).

1197 This process ends when all objects i have been added to a jet.

1198 Any choice of (p, R) has the requirements of collinear and radiative safety. In
1199 essence, the choice is then to optimize based on speed and the potential for new
1200 physics discoveries. In ATLAS, we make the choice of $p = -1$ which is also known
1201 as the *anti- k_T* algorithm. The choice of $R = 0.4$ is used for the distance parameter of
1202 the jets.

1203 The primary “nice” quality of this algorithm can be seen with the following
1204 example. Consider three inputs to an anti- k_T algorithm, all with $\eta = 0$:

- 1205 • Object 1 : $(p_T, \phi) = (30 \text{ GeV}, 0)$
- 1206 • Object 2 : $(p_T, \phi) = (20 \text{ GeV}, -0.2)$
- 1207 • Object 3 : $(p_T, \phi) = (10 \text{ GeV}, 0.2)$
- 1208 • Object 4 : $(p_T, \phi) = (1 \text{ GeV}, 0.5)$

1209 . In the case shown, it seems natural to first combine the “bigger” objects 1 and 2.
1210 These then pick up the extra small object 3, and object 4 is not included in the jet.
1211 This is exactly what is done by the anti- k_T algorithm. The (normal) k_T algorithm with
1212 $p = 1$ instead combines the smallest objects, 3 and 4, first. Object 1 and 2 combine
1213 to form their own jet, instead of these jets picking up object 3. This behavior is not
1214 ideal due to the effects of pileup, as we will see in the next section.

1215 Jet Reconstruction

1216 In ATLAS, jets are reconstructed using multiple different objects as inputs, including
1217 tracks, “truth” objects, calorimeter clusters, and *particle flow objects* (PFOs). For

1218 physics analyses, ATLAS primarily uses jets reconstructed from calorimeter clusters,
1219 but we will describe the others here, as they are often used for derivations of
1220 systematic uncertainties or future prospects.

1221 Calorimeter jets are reconstructed using topoclusters using the anti- k_T algorithm
1222 with $R = 0.4$. The jet reconstruction algorithm is run on the collection of all
1223 topoclusters reconstructed as in Sec.6.1. Both EM and LCW scale clusters are used
1224 in the ATLAS reconstruction software and produce two sets of jets for analysis. As
1225 stated above, this thesis presents an analysis using jets reconstructed using EM scale
1226 clusters, which we refer to these as *EM jets*.

1227 Tracks can be used as inputs to jet reconstruction algorithms. Jets reconstructed
1228 from tracks are known as *track jets*. Since the ID tracks do not measure neutral
1229 objects, these jets measure an incorrect energy. However, these are still useful for
1230 checks and derivations of systematic uncertainties.

1231 *Truth* jets are reconstructed from *truth* particles. In this case, truth is jargon for
1232 simulation. In simulation, the actual simulated particles are available and used as
1233 inputs to the jet reconstruction algorithms. Similarly to track jets, these are not useful
1234 in and of themselves. Instead, truth jets are used for comparisons and derivations of
1235 systematic uncertainties.

1236 The last object used as inputs to jet reconstruction algorithms are *particle flow*
1237 *objects* (PFOs). These are used extensively as the primary input to jet particle
1238 reconstruction algorithms by the CMS collaboration[105]. Particle flow objects are
1239 reconstructed by associating tracks and clusters through a combination of angular
1240 distance measures and detector response measurements to create a composite object
1241 which contains information from both the ID and the calorimeters. For calorimeter
1242 clusters which do not have any associated ID track, the cluster is simply the PFO.
1243 The natural association between tracks and clusters provides easy pileup subtraction
1244 since tracks are easily associated to the primary vertex. This technique is generally

1245 used in CMS, and ATLAS has been slow to adopt the same. As pileup has increased,
1246 the utility of using PFOs as inputs to jet reconstruction has increased as well.

1247 **Jet Calibration**

1248 Jets as described in the last section are still *uncalibrated*. Even correcting the cluster
1249 energies using the LCW does not fully correct the jet energy, due to particles losing
1250 energy in the calorimeters. The solution to this is the *jet energy scale* (JES). The
1251 JES is a series of calibrations which on average restore the correct truth jet energy
1252 for a given reconstructed jet. These steps are shown in Fig.6.8 and described here.

1253 The first step is the origin correction. This adjusts the jet to point at the
1254 primary vertex. Next, is the jet-area based pileup correction. This step subtracts
1255 the “average” pileup as measured by the energy density ρ outside of the jets and
1256 assumes this is a good approximation for the pileup inside the jet. One then removes
1257 energy $\Delta E = \rho \times A_{\text{jet}}$ in this step. The residual pileup correction makes a final offset
1258 correction by parametrizing the change in jet energy as a function of the number of
1259 primary vertices N_{PV} and the average number of interactions μ .

1260 The next step is the most important single correction, known as the AbsoluteEta-
1261 JES step. Due to the use of non-compensation and sampling calorimeters in ATLAS,
1262 the measured energy of a jet is a fraction of the true energy of the outgoing parton.
1263 Additionally, due to the use of different technologies and calorimeters throughout the
1264 detector, there are directional biases induced by these effects. The correction bins a
1265 multiplicative factor in p_{T} and η which scales the reconstructed jets to corresponding
1266 truth jet p_{T} . This step does not entirely correct the jets, since it is entirely a
1267 simulation-based approach.

1268 The final steps are known as the global sequential calibration (GSC) and the
1269 residual in-situ calibration. The GSC uses information about the jet showering shape
1270 to apply additional corrections based on the expected shape of gluon or quark jets.

1271 The final step is the residual in-situ calibration, which is only applied to data. This
1272 step uses well-measured objects recoiling off a jet to provide a final correction to the
1273 jets in data. In the low p_T region ($20 \text{ GeV} \sim < p_{T,\text{jet}} \sim < 200 \text{ GeV}$), $Z \rightarrow ll$ events are
1274 used as a reference object. In the middle p_T region ($100 \text{ GeV} \sim < p_{T,\text{jet}} \sim < 600 \text{ GeV}$),
1275 the reference object is a photon, while in the high p_T region ($p_{T,\text{jet}} \sim > 200 \text{ GeV}$),
1276 the high p_T jet is compared to multiple smaller p_T jets. The reference object is this
1277 group of multijets. After this final correction, the data and MC scales are identical
1278 up to the corresponding uncertainties. The combined JES uncertainty as a function
1279 of p_T is shown in Fig.6.9.

1280 Jet Vertex Tagger

1281 The *jet vertex tagger* (JVT) technique is used to separate pileup jets from those
1282 associated to the hard primary vertex[106]. The technique for doing so first involves
1283 *ghost association*[107]. Ghost association runs the anti- k_T jet clustering algorithm on
1284 a combined collection of the topoclusters and tracks. The tracks *only* momenta are
1285 set to zero², with only the directional information is included. As discussed above,
1286 the anti- k_T algorithm is “big to small”; tracks are associated to the “biggest” jet near
1287 them in (η, ϕ) . This method uniquely associates each track to a jet, without changing
1288 the final jet kinematics.

1289 The JVT technique uses a combination of these track variables to determine the
1290 likelihood that the jet originated at the primary vertex. For jets which have associated
1291 tracks from ghost association, this value ranges from 0 (likely pileup jet) to 1 (likely
1292 hard scatter jet). Jets without associated tracks are assigned $\text{JVT} = -.1$. The
1293 working point of $\text{JVT} > .59$ is used for jets in this thesis.

²Well, not exactly zero, since zero momentum tracks wouldn’t have a well-defined (η, ϕ) coordinate, but set to a value obeying $p_{T,\text{track}} << 400 \text{ MeV} = p_{\text{track,min}}$. This is the minimum momentum for a track to reach the ATLAS inner detector.

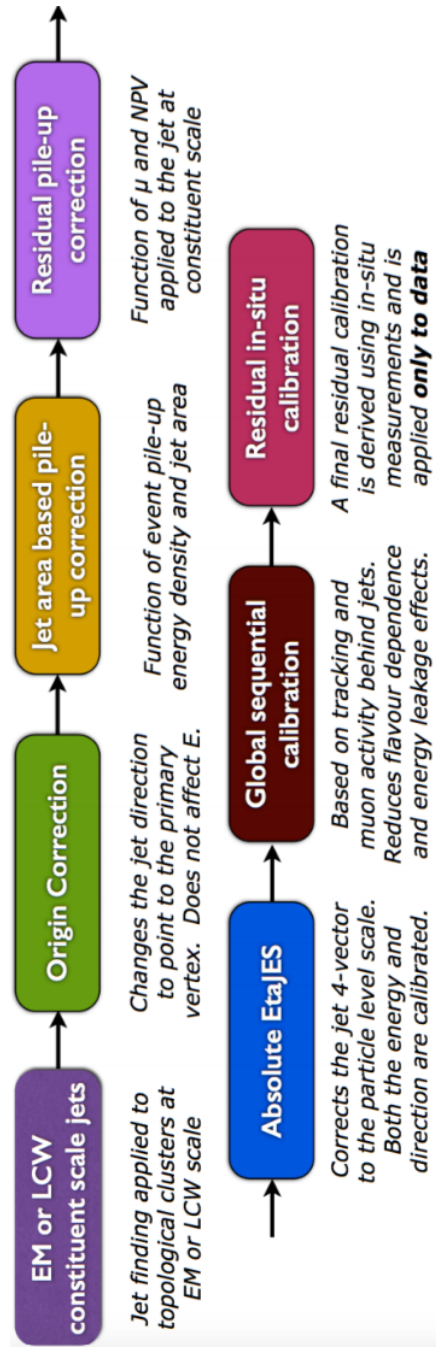


Figure 6.8: The steps used by ATLAS to calibrate jets

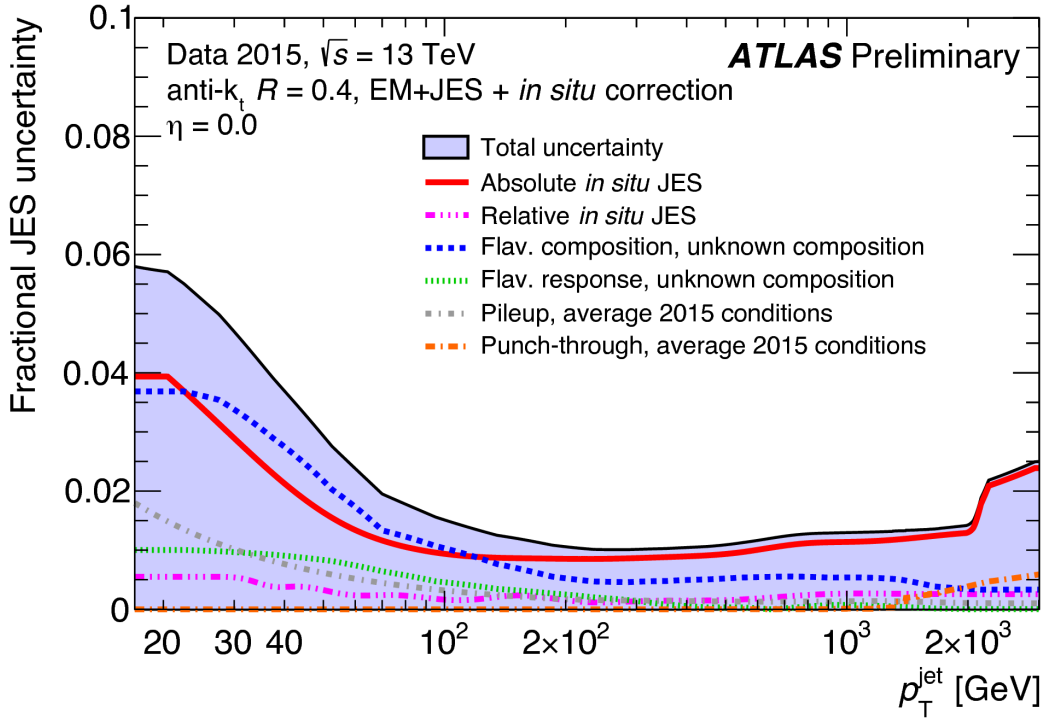


Figure 6.9: Combined jet energy scale uncertainty as a function of p_T at $\eta = 0$.

1294 B-jets

1295 Jets originating from bottom quarks (b-jets) are interesting physical phenomena that
 1296 can be *tagged* by the ATLAS detector[Aad:2015ydr, 108]. B-hadrons, which have
 1297 a comparatively long lifetime compared to hadrons consisting of lighter quarks, can
 1298 travel a macroscopic distance inside the ATLAS detector. The high-precision tracking
 1299 detectors identify the secondary vertices from these decays and the jet matched to
 1300 that vertex is called a *b-jet*. The “MV2c10” algorithm, based on boosted decision
 1301 trees, identifies these jets using a combination of variables sensitive to the difference
 1302 between light-quark and b-quark jets. The efficiency of this tagger is 77%, with a
 1303 rejection factor of 134 for light-quarks and 6 for charm jets.

1304 Missing Transverse Momentum

1305 Missing transverse momentum E_T^{miss} [109] is a key observable in searches for new
1306 physics, especially in SUSY searches[110, 111]. However, E_T^{miss} is not a uniquely
1307 defined object when considered from the detector perspective (as compared to the
1308 Feynammn diagram), and it is useful to understand the choices that affect the
1309 performance of this observable in searches for new physics.

1310 E_T^{miss} Definitions

Hard objects refers to all physical objects as defined in the previous sections. The
 E_T^{miss} reconstruction procedure uses these hard objects and the *soft term* to provide
a value and direction of the missing transverse momentum. The $E_{x(y)}^{\text{miss}}$ components
are calculated as:

$$E_{x(y)}^{\text{miss}} = E_{x(y)}^{\text{miss, } e} + E_{x(y)}^{\text{miss, } \gamma} + E_{x(y)}^{\text{miss, jets}} + E_{x(y)}^{\text{miss, } \mu} + E_{x(y)}^{\text{miss, soft}}, \quad (6.5)$$

1311 where each value $E_{x(y)}^{\text{miss, } i}$ is the negative vectorial sum of the calibrated objects defined
1312 in the previous sections.

1313 For purposes of E_T^{miss} reconstruction, we must assign an ordering of *overlap*
1314 *removal*. This is to avoid double counting of the underlying primitive objects (clusters
1315 and tracks) which are inputs to the reconstruction of the physics objects. We resolve
1316 this in the following order : electrons, photons , jets and muons. This is motivated
1317 by the performance of the reconstruction of these objects in the calorimeters.

1318 The soft term $E_{x(y)}^{\text{miss, soft}}$ contains all of the primitive objects which are not
1319 associated to any of the reconstructed physics objects. Of course, we need to choose
1320 which primitive object to use. The primary choices which have been used within
1321 ATLAS are the *calorimeter-based soft term* (CST) and the *track-based soft term*
1322 (TST). Based on the soft term choice, we then call E_T^{miss} built with a CST (TST)

1323 soft term simply CST (TST) E_T^{miss} . An additional option, which will be important
1324 as pileup continues to increase, particle flow E_T^{miss} (PFlow E_T^{miss}).

1325 The CST E_T^{miss} was used for much of the early ATLAS data-taking. CST E_T^{miss} is
1326 built from the calibrated hard objects, combined with the calorimeter clusters which
1327 are *not* assigned to any of those hard objects. In the absence of pileup, it provides the
1328 best answer for the “true” E_T^{miss} in a given event, due to the impressive hermiticity of
1329 the calorimeters. Unfortunately, the calorimeters do not know “where” from where
1330 their energy deposition came, and thus CST is susceptible to drastically reduced
1331 performance as pileup is increased.

1332 TST E_T^{miss} is the standard for ATLAS searches as currently performed by ATLAS.
1333 TST E_T^{miss} is built by using the calibrated hard objects and the soft term is built from
1334 the tracks which are not assigned to any of those hard objects. In particular, due
1335 to the impressive track-vertex association efficiency, one chooses tracks which only
1336 come from the primary vertex. This drastically reduces the pileup contributions to
1337 the E_T^{miss} measurement. However, since the ID tracking system is unable to measure
1338 neutral objects, the TST E_T^{miss} is “wrong”. This bias is important to understand for
1339 many measurements. However, in most searches for new physics, the soft E_T^{miss} is
1340 generally a small fraction of the total E_T^{miss} , and thus this bias is not particularly
1341 hurtful.

1342 PFlow E_T^{miss} uses the PFOs described above to build the E_T^{miss} . The PFOs which
1343 are assigned to hard objects are calibrated, and the PFOs which are not assigned
1344 to any hard object are added to the soft term. In this context, it is convenient to
1345 distinguish between “charged” and “neutral” PFOs. Charged PFOs can be seen as a
1346 topocluster which has an associated track, while neutral PFOs do not. This charged
1347 PFO is essentially a topocluster that we are “sure” comes from the primary vertex.
1348 The neutral PFOs are in the same status as the original topoclusters. Thus a “full”
1349 PFlow E_T^{miss} should have performance somewhere between TST E_T^{miss} and CST E_T^{miss} ³.

1350 A *charged* PFlow E_T^{miss} should for sanity be the same as TST.

1351 **Measuring E_T^{miss} Performance : event selection**

1352 The question is now straightforward: how do we compare these different algorithms?
1353 We compare these algorithms in $Z \rightarrow \ell\ell + \text{jets}$ and $W \rightarrow \ell\nu + \text{jets}$ events. Due to
1354 the presence of leptons, these events are well-measured “standard candles”. Here
1355 we present the results in early 2015 data with $Z \rightarrow \mu\mu$ and $W \rightarrow e\nu$ events, as
1356 shown in [112, 113]. This result was important to assure the integrity of the E_T^{miss}
1357 measurements at the higher energy and pileup environment of Run-2.

1358 The $Z \rightarrow \ell\ell$ selection is used to measure the intrinsic E_T^{miss} resolution of the
1359 detector. The only possible source of neutrinos in these decays is from heavy-flavor
1360 decays inside of jets, and thus $Z \rightarrow \ell\ell$ events they have very low E_T^{miss} . This provides
1361 an ideal event topology to understand the modelling of E_T^{miss} mismeasurement.
1362 Candidate $Z \rightarrow \mu\mu$ events are first required to pass a muon or electron trigger, as
1363 described in Table 5.1. Offline, the selection of $Z \rightarrow \mu\mu$ events requires exactly two
1364 medium muons. The muons are required to have opposite charge and $p_T > 25 \text{ GeV}$,
1365 and mass of the dimuon system is required to be consistent with the Z mass
1366 $|m_{ll} - m_Z| < 25 \text{ GeV}$.

$W \rightarrow \ell\nu$ events are an important topology to evaluate the E_T^{miss} modelling in
an event with real E_T^{miss} . This E_T^{miss} is from the neutrino, which is not detected.
The E_T^{miss} in these events has a characteristic distribution with a peak at $\frac{1}{2}m_W$. The
selection of $W \rightarrow e\nu$ events begins with the selection of exactly one electron of medium
quality. A selection on TST $E_T^{\text{miss}} > 25 \text{ GeV}$ drastically reduces the background from
multijet events where the jet fakes an electron. The transverse mass is used to select

³Naively, due to approximate isospin symmetry, about 2/3 of the hadrons will be charged and 1/3 will be neutral.

the $W \rightarrow e\nu$ events :

$$m_T = \sqrt{2p_T^\ell E_T^{\text{miss}}(1 - \cos \Delta\phi)}, \quad (6.6)$$

1367 where $\Delta\phi$ is the difference in the ϕ between the E_T^{miss} and the electron. m_T is required
1368 to be greater than 50 GeV.

1369 There are two main ingredients to investigate : the E_T^{miss} resolution and the E_T^{miss}
1370 scale.

1371 Measuring E_T^{miss} Performance in early 2015 data : metrics

1372 To compare these algorithms we use the E_T^{miss} resolution, E_T^{miss} scale, and the
1373 linearity. Representative distributions of TST E_x^{miss} , E_y^{miss} , and E_T^{miss} from early
1374 2015 datataking are shown in Fig.6.10.

The E_T^{miss} resolution is an important variable due to the fact that the bulk of the distributions associated to $E_{x(y)}^{\text{miss}}$ are Gaussian distributed [Aad2012]. However, to properly measure the tails of this distribution, especially when considering non-calorimeter based soft terms, it is important to use the root-mean square as the proper measure of the resolution. This is strictly larger than a resolution as measured using a fit to a Gaussian, due to the long tails from i.e. track mismeasurements. The resolution is measured with respect to two separate variables : $\sum E_T$ and N_{PV} . $\sum E_T$ is an important measure of the “total event activity”. It is defined as

$$\sum E_T = \sum p_T^e + \sum p_T^\gamma + \sum p_T^\tau + \sum p_T^{\text{jets}} + \sum p_T^\mu + \sum p_T^{\text{soft}}. \quad (6.7)$$

1375 The measurement as a function of N_{PV} is useful to understand the degradation of
1376 E_T^{miss} performance with increasing pileup. Figure 6.11 shows the E_T^{miss} resolution in
1377 the early 2015 data. The degradation of the E_T^{miss} performance is shown as a function
1378 of pileup N_{PV} and total event activity $\sum E_T$.

Another important performance metric is the E_T^{miss} scale, or how “right” we are in our E_T^{miss} calculation. This can be off in various directions, as CST E_T^{miss} contains

additional particles from pileup, while soft neutral particles⁴ are ignored by TST E_T^{miss} .

To measure this in data, we again use $Z \rightarrow \mu\mu$ events, where the $Z \rightarrow \mu\mu$ system is treated as a well-measured reference object. The component of E_T^{miss} which is in the same direction as the reconstructed $Z \rightarrow \mu\mu$ system is sensitive to potential biases in the detector response. The unit vector \mathbf{A}_Z of the Z system is defined as

$$\mathbf{A}_Z = \frac{\vec{p}_T^{\ell^+} + \vec{p}_T^{\ell^-}}{|\vec{p}_T^{\ell^+} + \vec{p}_T^{\ell^-}|}, \quad (6.8)$$

where $\vec{p}_T^{\ell^+}$ and $\vec{p}_T^{\ell^-}$ are the transverse momenta of the leptons from the Z boson decay. The relevant scale metric is then the mean value of the \vec{E}_T^{miss} projected onto \mathbf{A}_Z : $\langle \vec{E}_T^{\text{miss}} \cdot \mathbf{A}_Z \rangle$. In Figure 6.12, the scale is shown for the early 2015 dataset. The negative bias, which is maximized at about 5 GeV, is a reflection of two separate effects. The soft neutral particles are missed by the tracking system, and thus ignored in TST E_T^{miss} . Missed particles due to the limited ID acceptance can also affect the scale.

For events with real E_T^{miss} , one can also look at the *linearity* in simulation. This is defined as

$$\text{linearity} = \left\langle \frac{E_T^{\text{miss}} - E_T^{\text{miss,Truth}}}{E_T^{\text{miss,Truth}}} \right\rangle. \quad (6.9)$$

$E_T^{\text{miss,Truth}}$ refers to “truth” particles as defined before, or the magnitude of the vector sum of all noninteracting particles. The linearity is expected to be zero if the E_T^{miss} is reconstructed at the correct scale.

1389 Particle Flow Performance

As described above, the resolution, scale, and linearity are the most important metrics to understand the performance of the different E_T^{miss} algorithms. In this section, we present comparisons of the different algorithms, including particle flow, in simulation

⁴“Soft” here means those particles which are not hard enough to be reconstructed as their own particle, using the reconstruction algorithms above.

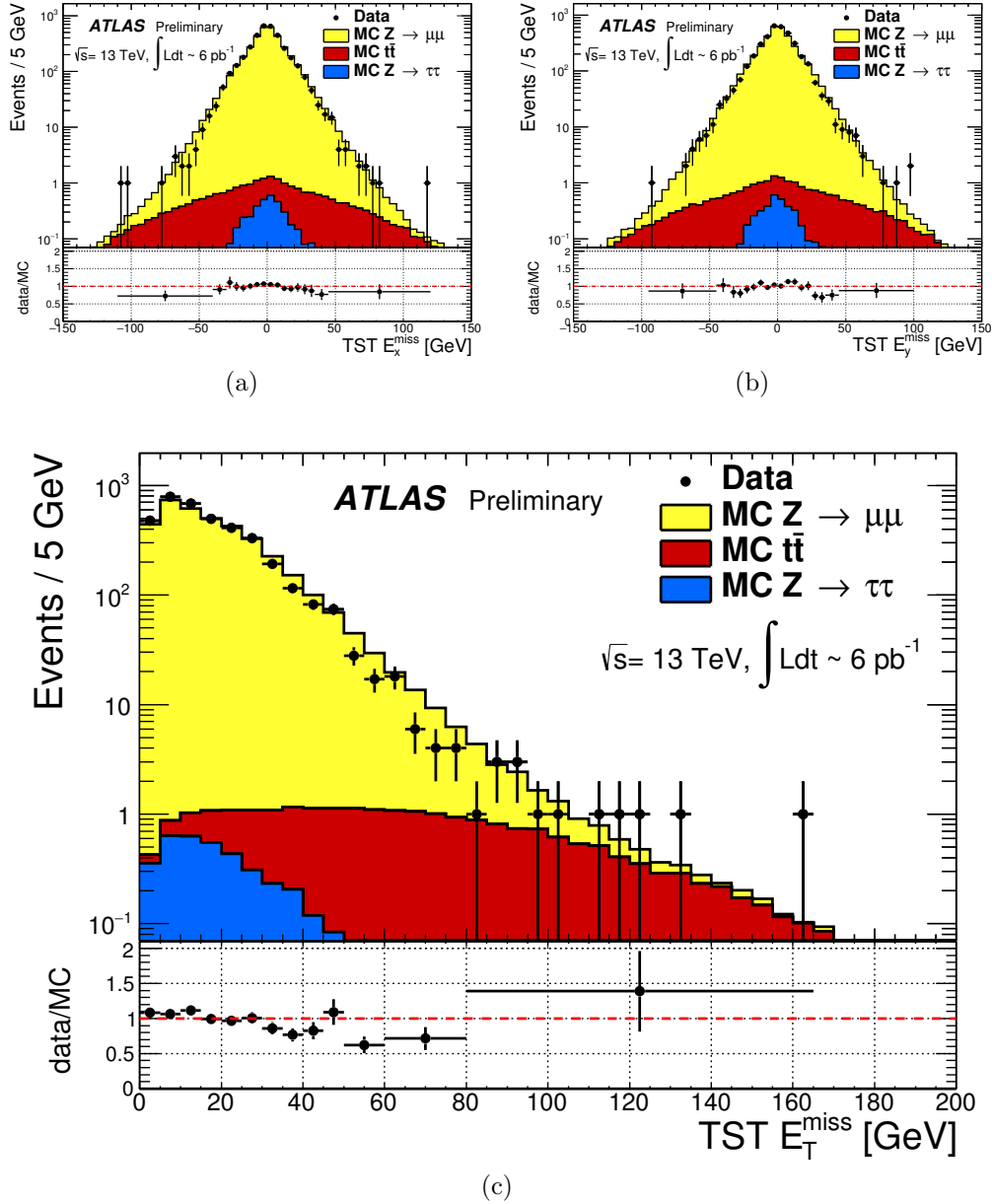


Figure 6.10: TST E_{x}^{miss} , E_{y}^{miss} , and $E_{\text{T}}^{\text{miss}}$ distributions of early $\sqrt{s} = 13$ TeV data compared with simulation after the $Z \rightarrow \mu\mu$ selection described in Sec. 6.2. The data sample consists of 6 pb^{-1} .

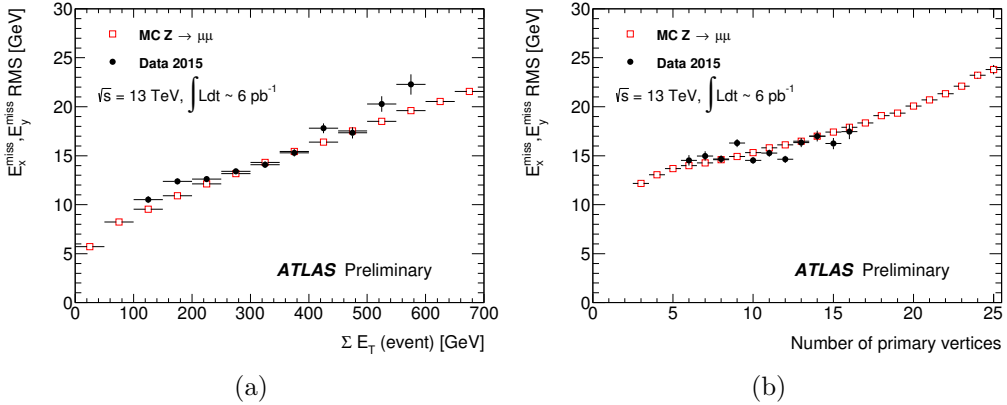


Figure 6.11: Resolution of TST E_T^{miss} of early $\sqrt{s} = 13$ TeV data compared with simulation after the $Z \rightarrow \mu\mu$ selection described in Sec.6.2. The data sample consists of 6 pb^{-1} .

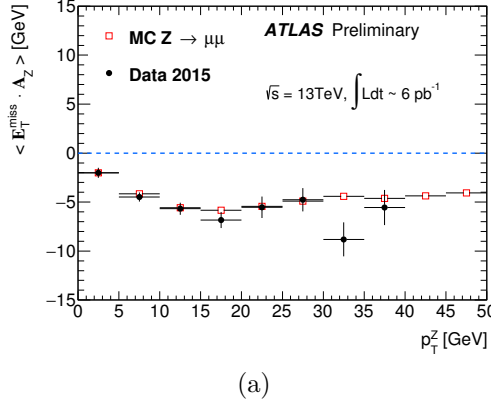


Figure 6.12: Scale of TST E_T^{miss} of early $\sqrt{s} = 13$ TeV data compared with simulation after the $Z \rightarrow \mu\mu$ selection described in Sec.6.2. The data sample consists of 6 pb^{-1} .

1393 and using a data sample from 2015 of 80 pb^{-1} . In these plots, ‘‘MET_PFlow-TST’’
 1394 refers to charged PFlow E_T^{miss} , while the other algorithms are as described above.

1395 Figures ?? show the resolution and scale in simulated $Z \rightarrow \mu\mu$ events. The
 1396 resolution curves follow the ‘‘intuitive’’ behavior discussed before. Due to the high
 1397 pileup in 2015 run conditions, the CST E_T^{miss} resolution is poor, and becomes even
 1398 poorer with increasing pileup and event activity. The ‘‘regular’’ PFlow E_T^{miss} shows
 1399 reduces pileup and event activity dependence as compared to the CST. As stated
 1400 earlier, the E_T^{miss} from the PFlow algorithm can be seen as a hybrid of TST E_T^{miss}

1401 and CST E_T^{miss} . The charged PFOs ($\sim 2/3$) are pileup suppressed, while the neutral
1402 PFOs (or topoclusters) are not. Both charged PFlow and TST E_T^{miss} show only a
1403 small residual dependence on N_{PV} and $\sum E_T$, since they have fully pileup suppressed
1404 inputs through the track associations.

1405 The scale plots are shown for $Z + \text{jets}$ events and Z events with no jets. For the
1406 nonsuppressed CST, the scale continues to worsen with increasing p_T^Z . It is almost
1407 always the worst performing algorithm. The standard PFlow algorithm performs the
1408 second worst in the region of high p_T^Z , but is the best at low p_T^Z . The most exciting note
1409 in this plot is the improved scale of the charged PFlow E_T^{miss} compared to the TST
1410 E_T^{miss} . Considering the resolution is essentially identical, the PFlow algorithm is better
1411 picking up the contributions from additional neutral particles. In events with no jets,
1412 the soft term is essentially the only indication of the E_T^{miss} mismeasurement, since
1413 the muons will be well-measured. In this case, the pileup effects cancel, on average,
1414 due to the $U(1)_\phi$ symmetry of the ATLAS detector, and CST performs rather well
1415 compared to the more complicated track-based algorithms. The full PFlow algorithm
1416 performs best, since it provides a small amount of pileup suppression on the neutral
1417 components from CST.

1418 The resolution and linearity are shown in simulated $W \rightarrow e\nu$ events in Figure ???.
1419 The resolution in $W \rightarrow e\nu$ events shows a similar qualitative behavior to that shown
1420 in $Z \rightarrow \mu\mu$ events. The CST E_T^{miss} has the worst performance, with charged PFlow
1421 E_T^{miss} performing best. The surprise here is that the scale associated to TST E_T^{miss} in
1422 these events is best throughout the space parameterized by $E_T^{\text{miss,Truth}}$, except for one
1423 bin at $40 \text{ GeV} < E_T^{\text{miss,Truth}} < 50 \text{ GeV}$. The scale in these events is best measured
1424 using a track-based soft term.

1425 The resolution also investigated in real data passing the $Z \rightarrow \mu\mu$ selection
1426 described above. A comparison of the E_T^{miss} between real data and simulation for
1427 each algorithm is presented in Figure 6.16. The resolution as a function of $\sum E_T$ and

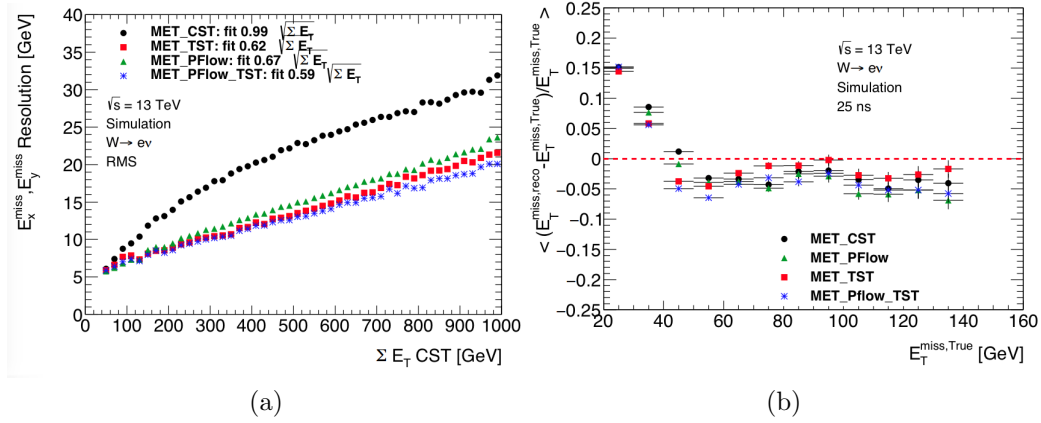


Figure 6.13: Comparison of E_T^{miss} resolution and linearity using different E_T^{miss} algorithms with simulated $W \rightarrow e\nu$ events.

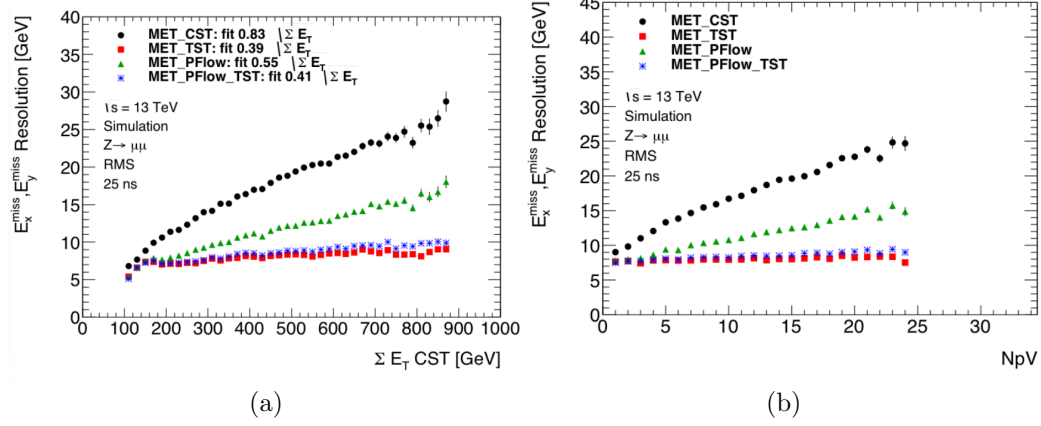


Figure 6.14: Comparison of E_T^{miss} resolution using different E_T^{miss} algorithms with simulated $Z \rightarrow \mu\mu$ events.

1428 N_{PV} is shown in Figure 6.17 for this dataset. Overall, this plot shows the same general
 1429 features as the simulation dataset in terms of algorithm performance. However, the
 1430 performance of all algorithms seems to be significantly worse in data. This is likely due
 1431 to simplifications made in the simulation: soft interactions that cannot be simulated
 1432 can have a significant effect on an event level variable such as the E_T^{miss} resolution.

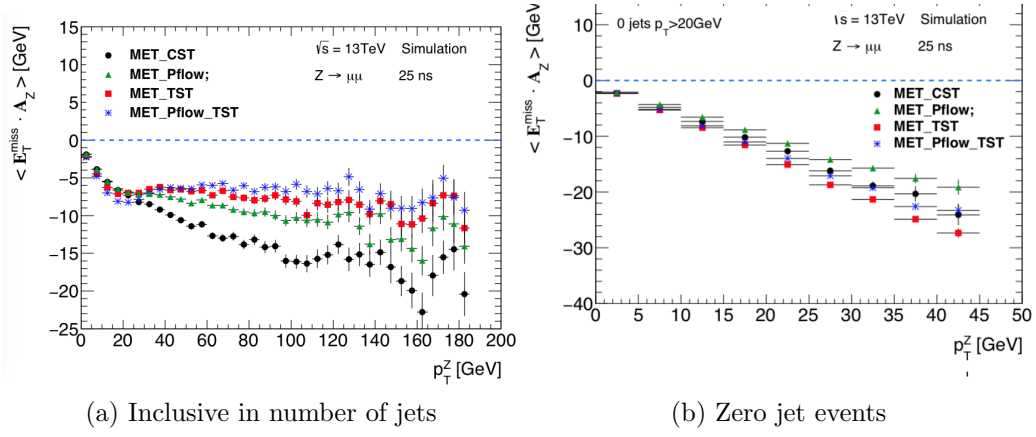


Figure 6.15: Comparison of E_T^{miss} scale using different E_T^{miss} algorithms with simulated $Z \rightarrow \mu\mu$ events.

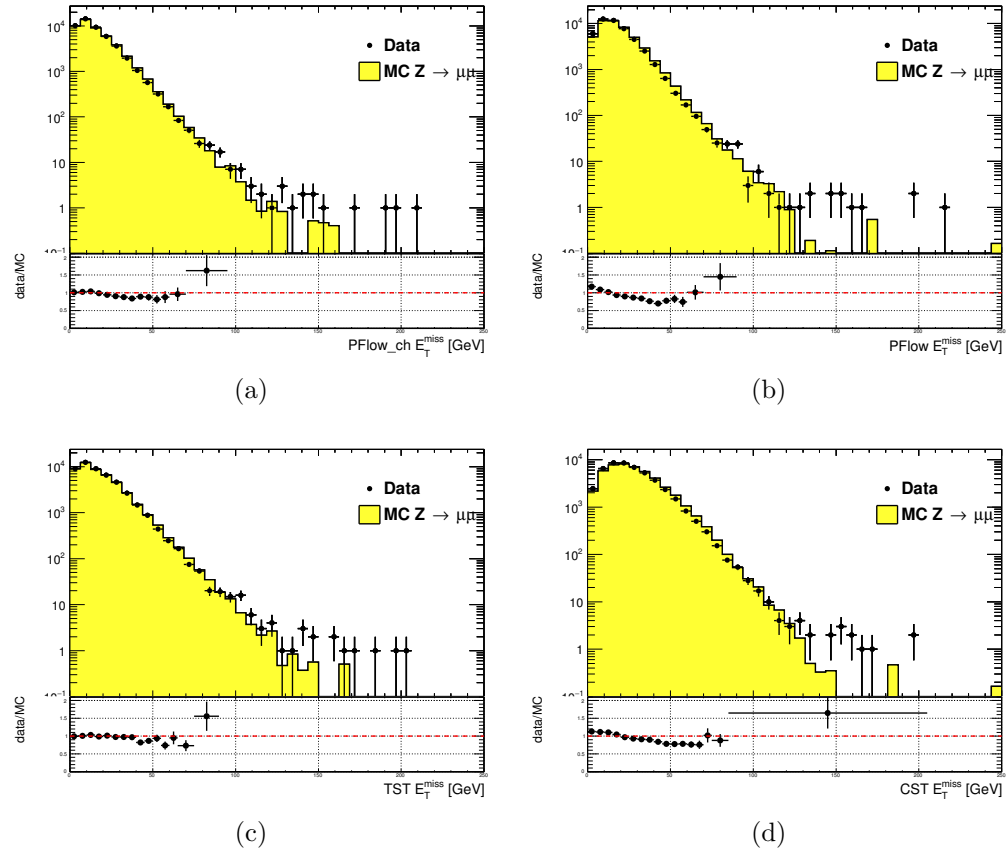


Figure 6.16: Comparison of E_T^{miss} distributions using different E_T^{miss} algorithms with a data sample of 80 pb^{-1} after the $Z \rightarrow \mu\mu$ selection described in Sec.6.2

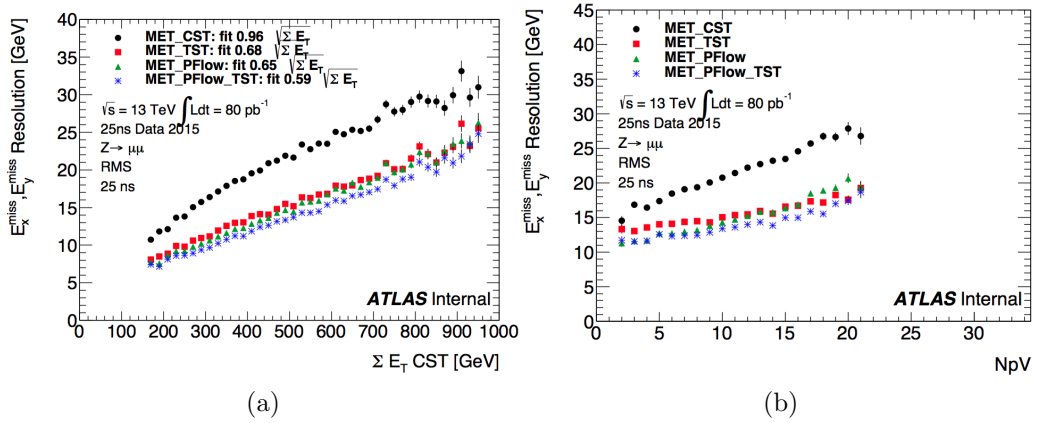


Figure 6.17: Comparison of E_T^{miss} resolution using different E_T^{miss} algorithms with a data sample of 80 pb^{-1} after the $Z \rightarrow \mu\mu$ selection described in Sec.6.2

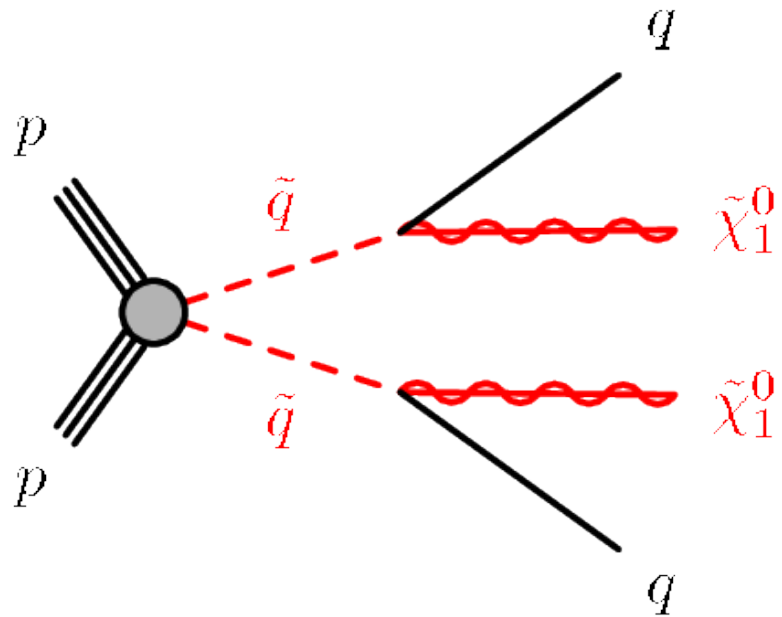
Recursive Jigsaw Reconstruction

1435 *Recursive Jigsaw Reconstruction* (RJR) [114, 115] is a novel algorithm used for the
 1436 analysis presented in this thesis. RJR is the conceptual successor to the razor
 1437 technique [116, 117], which has been used successfully in many new physics searches
 1438 [37, 38, 40, 41, 47, 118]. In this chapter, we will first present the razor technique,
 1439 and describe the razor variables. We will then present the RJR algorithm. After the
 1440 description of the algorithm, we will describe the precise RJR variables used by this
 1441 thesis and attempt to provide some physical intuition of what they describe.

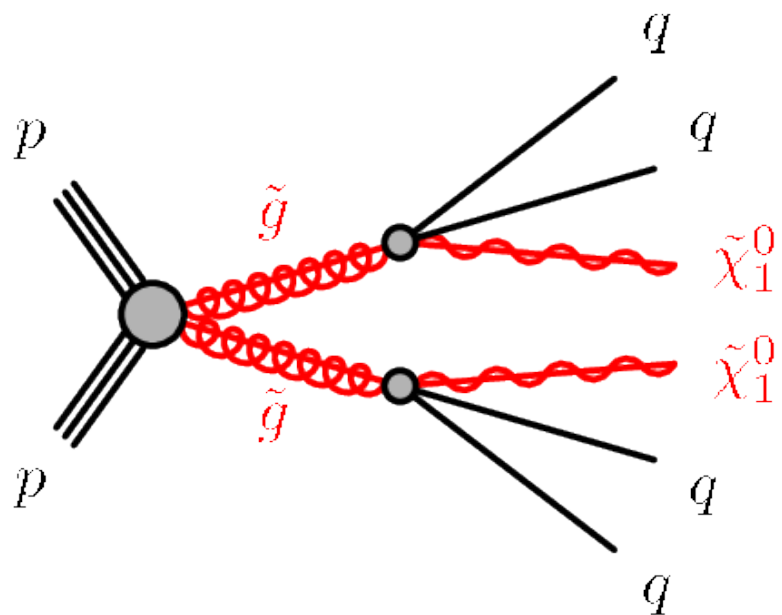
1442 **7.1 Razor variables**1443 **Motivation**

1444 In this thesis, we consider SUSY models where gluinos and squarks are pair-produced.
 1445 Pair-production is a consequence of the R -parity imposed in many SUSY models.
 1446 R -parity violation is highly constrained by limits on proton decay[15], and is often
 1447 assumed in SUSY model building. The Feynman diagrams considered are shown in
 1448 Fig.7.1.

1449 As discussed previously, the consequences of this \mathbb{Z}_2 symmetry are drastic. To un-
 1450 derstand the utility of the razor variables, the stability of the lightest supersymmetric
 1451 particle is very important. In many SUSY models, including the ones considered in
 1452 this thesis, this is the lightest neutralino $\tilde{\chi}_1^0$. This means that on either side of a
 1453 SUSY decay process, where we begin with disparticle production, we have a final



(a) Disquark production



(b) Digluino production

Figure 7.1: Feynman diagrams for the SUSY signals considered in this thesis

1454 state particle which is not detected. Generically, this leads to E_T^{miss} . Selections based
1455 on E_T^{miss} are very good at reducing dominant backgrounds, for example from QCD
1456 backgrounds.

1457 However, there are limitations to searches based on E_T^{miss} . Due to jet mismeasurements,
1458 instrumental failures, finite detector acceptance, nongaussian tails in the
1459 detector response, and production of neutrinos inside of jets, there are many sources of
1460 “fake” E_T^{miss} which does not correspond to a Standard Model neutrino or new physics
1461 object such as an LSP. An additional limitation is the complete lack of longitudinal
1462 information. As events from i.e. QCD backgrounds tend to have higher boosts along
1463 the z -direction, this is ignoring an important handle in searches for new physics.
1464 Finally, E_T^{miss} is only one object, which is a measurement for *two* separate LSPs. If one
1465 could factorize this information somehow, this would provide additional information
1466 to potentially discriminate against backgrounds. The *razor variables* (M_{Δ}^R, R^2) are
1467 more robust than standard variables against these effects[[116](#), [117](#)].

1468 Derivation of the razor variables

1469 To derive the razor variables (M_{Δ}^R, R^2), we start with a generic situation of the pair
1470 production of heavy sparticles with mass m_{Heavy} .¹ Each sparticle decays to a number
1471 of observable objects (in this thesis, jets), and an unobservable $\tilde{\chi}_1^0$ of mass $m_{\tilde{\chi}_1^0}$. We
1472 will combine all of the jets into a *megajet*; this process will be described below. We
1473 begin by analyzing the decay in the “rough-approximation”, or in modern parlance,
1474 *razor frame* (*R-frame*). This is the frame where each sparticle is at rest. The complete
1475 set of frames considered in the case of the razor variables is shown in [7.2](#).

In the *R-frame*, the decay is straightforward to analyze. By construction, there
are in fact two *R-frame* s, and they have identical kinematics. Each megajet has

¹The razor variables have undergone confusing notational changes over the years. We will be self-consistent, but the notation used here may be different from references.

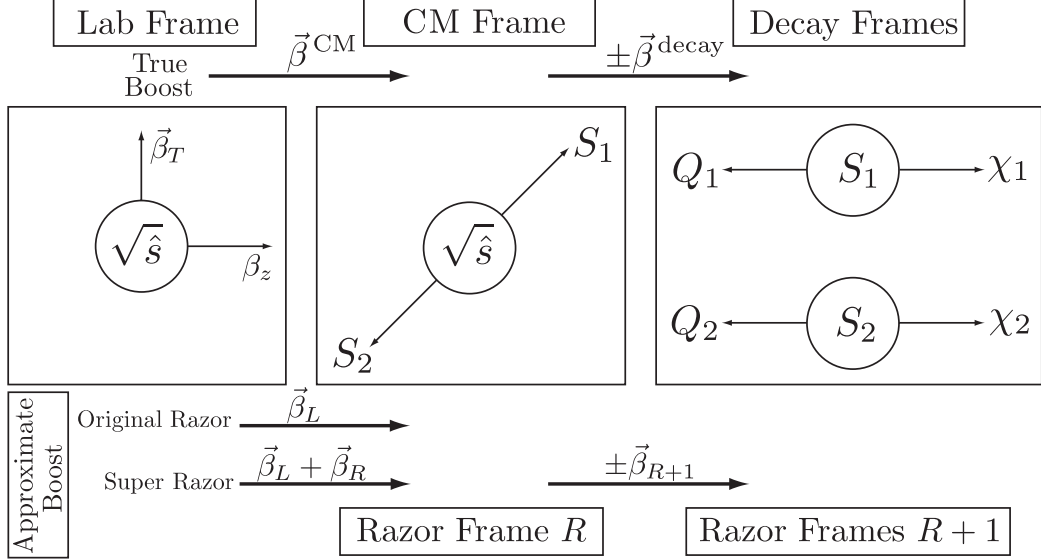


Figure 7.2: Frames considered when applying the razor technique, from [117].

energy E_1^R, E_2^R in the frame of its parent sparticle, and we define a characteristic mass M_R :

$$E_1^R = E_2^R = \frac{m_{\text{Heavy}}^2 - m_{\tilde{\chi}_1^0}^2}{2m_{\text{Heavy}}} \quad (7.1)$$

$$M_R = 2 \times E_1^R = 2 \times E_2^R = \frac{m_{\text{Heavy}}^2 - m_{\tilde{\chi}_1^0}^2}{m_{\text{Heavy}}} \quad (7.2)$$

For cases where $m_{\text{Heavy}} \gg m_{\tilde{\chi}_1^0}$, M_R is an estimator of m_{Heavy} . This scenario happens in the SM, such as in $t\bar{t}$ and WW events, where the $\tilde{\chi}_1^0$ is instead a neutrino.

The question now is how to use this simple derivation in the lab frame, where we actually have measurements. There are two related issues: how to combine the jets into the megajets, and how to “transform” (or *boost*) to the R -frame.

To construct the megajets, the procedure is the following. For a given set of jets $j_i, i = 0, \dots, n_{\text{jet}}$, we construct *all* combinations of their four-momenta such that there is at least one jet inside each megajet. Among this set of possible megajets $\{J_{1,2}\}$, we make the following unique choice for the megajets. We minimize the following quantity:

$$m_{J_1}^2 + m_{J_2}^2. \quad (7.3)$$

1481 In modern parlance, this is known as a *jigsaw*. It is important to note, this is a
 1482 *choice*. It may have nice physical qualities or satisfy some convenient intuition about
 1483 the events, but as we will see later, other choices are possible.

We now describe how we translate our megajet kinematics, measured in the lab frame, to the R -frame. This is a two-step procedure. We perform two *boosts*: a longitudinal boost β_L and a transverse boost β_T . Schematically,

$$J_1^R \xrightarrow{\beta_T} J_1^{CM} \xrightarrow{\beta_L} J_1^{\text{lab}} \quad (7.4)$$

$$J_2^R \xrightarrow{-\beta_T} J_2^{CM} \xrightarrow{\beta_L} J_2^{\text{lab}} \quad (7.5)$$

$$(7.6)$$

1484 The $J_{1,2}^{\text{lab}}$ correspond directly to those in the megajet construction. We drop the
 1485 “lab” designation for the rest of the discussion. The question is how to compute the
 1486 magnitudes of these boosts, given the missing degrees of freedom.

For the transverse boost β_T , recall the two megajets have equal energies in their R -frame by construction. This constraint can be reexpressed as a constraint on the magnitude of this boost, in terms of the boost velocity β_L (and Lorentz factor γ_L):

$$\beta_T = \frac{\gamma_L(E_1 - E_2) - \gamma_L\beta_L(p_{1,z} - p_{2,z})}{\hat{\beta}_T \cdot (\vec{p}_{1,T} + \vec{p}_{2,T})} \quad (7.7)$$

where we have denoted the lab frame four-vectors as $p_i = (E_i, \vec{p}_{i,T}, p_z)$. We now make the *choice* for the direction of the transverse boost $\hat{\beta}_T$:

$$\hat{\beta}_T = \frac{\vec{p}_{1,T} + \vec{p}_{2,T}}{|\vec{p}_{1,T} + \vec{p}_{2,T}|}. \quad (7.8)$$

1487 This choice forces the denominator of 7.7 to unity, and corresponds to aligning the
 1488 transverse boost direction with the sum of the two megajets transverse directions.

For the longitudinal boost, we choose $\vec{\beta}_L$ along the z -direction, with magnitude:

$$\beta_L = \frac{p_{1,z} + p_{2,z}}{E_1 + E_2}. \quad (7.9)$$

1489 Viewed in terms of the original parton-parton interactions, this is the choice which
 1490 “on average” gives $p_{z,\text{CM}} = 0$, as we would expect. This well-motivated choice due to
 1491 the total z symmetry.

We now have well-motivated guesses for both boosts, which allow us write our original characteristic mass M_R in terms of the lab frame variables, by application of these two Lorentz boosts to the energies of 7.1:

$$M_R^2 \xrightarrow{\beta_T} M_{R,\text{CM}}^2 \xrightarrow{\beta_L} M_{R,\text{lab}}^2 = (E_1 + E_2)^2 - (p_{1,z} + p_{2,z})^2. \quad (7.10)$$

Finally, we define an additional mass variable, which include the missing transverse energy $E_{\text{T}}^{\text{miss}}$. Importantly, note that we did not use the $E_{\text{T}}^{\text{miss}}$ in the definition of M_R , which depends only on the energies of the megajets. Backgrounds with no invisible particles (such as multijet events) must have J_1 and J_2 back to back. Thus, we define the transverse mass:

$$(M_R^T)^2 = \frac{1}{2} \left[E_{\text{T}}^{\text{miss}}(p_{1,T} + p_{2,T}) - \vec{E}_{\text{T}}^{\text{miss}} \cdot (\vec{p}_{1,T} + \vec{p}_{2,T}) \right]. \quad (7.11)$$

Generally, we have $M_R^T < M_R$, so we define a dimensionless ratio (“the razor”):

$$R^2 = \left(\frac{M_R^T}{M_R} \right)^2. \quad (7.12)$$

1492 For signal events, we expect R to peak around $R \sim 1/4$, while backgrounds without
 1493 real $E_{\text{T}}^{\text{miss}}$ are expected to have $R \sim 0$.

1494 7.2 Recursive Jigsaw Reconstruction

1495 Recursive Jigsaw Reconstruction is an algorithm allowing the imposition of a decay
 1496 tree interpretation on an particular event[114, 115]. The idea is to construct the
 1497 underlying kinematic variables (the masses and decay angles) on an event-by-event
 1498 level. This is done “recursively” through a decay tree which corresponds (sometimes
 1499 approximately) to the Feynmann diagram for the signal process of interest. After

1500 each step of the recursive procedure, the objects are “placed” into one bucket (or
1501 branch) of the decay tree, and the process is repeated on each frame we have imposed.
1502 The imposition of these decay trees is done by *jigsaw* rule: a procedure to resolve
1503 combinatoric or kinematic ambiguities while traversing the decay tree. This procedure
1504 is performed by the `RestFrames` software packages [119]

1505 In events where all objects are fully reconstructed, this is straightforward, and
1506 of course has been used for many years in particle physics experiments. Events
1507 which contain E_T^{miss} are more difficult, due to the loss of information: the potential
1508 for multiple mismeasured or simply unmeasureable objects, such as neutrinos or the
1509 LSP in SUSY searches. There can also be combinatoric ambiguities in deciding how
1510 to group objects of the same type; specifically here, we will be concerned with the
1511 jigsaw rule to associate jets to a particular branch of a decay tree. The jigsaw rules
1512 we impose will remove these ambiguities. First, we will describe the decay trees used
1513 in this thesis, and then describe the jigsaw rules we will use. Finally, we will describe
1514 the variables used in the all-hadronic SUSY search presented in this thesis.

1515 Decay Trees

1516 The decay trees imposed in this thesis are shown in 7.3. Leaving temporarily the
1517 question of “how” we apply the jigsaw rules, let us compare these trees to the signal
1518 processes of interest. In particular, we want to compare the Feynman diagrams of 7.1
1519 with the decay trees of 7.3. The decay tree in ?? corresponds exactly to that expected
1520 from disquark production, and matches very closely with the principles of the razor
1521 approach. We first apply a jigsaw rule, indicated by a line, to the kinematics of the
1522 objects in the *lab* frame. This outputs the kinematics of our event in the *parent-parent*
1523 (*PP*) frame, or in the razor terminology, the CM frame. That is, the kinematics of
1524 this frame are an estimator for the kinematics in the center of mass frame of the
1525 disquark system. We apply another jigsaw, which splits the objects in the *PP* frame

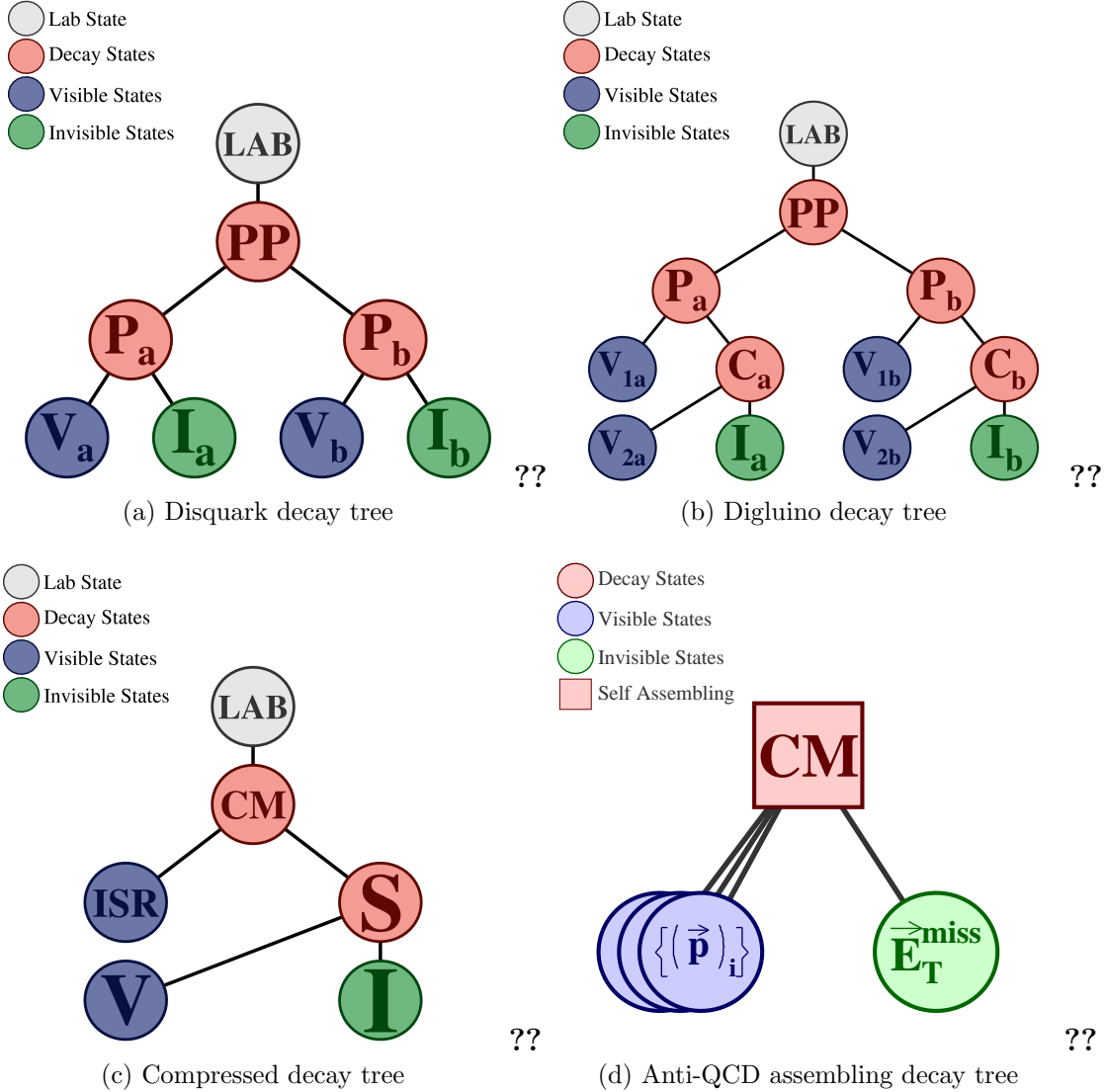


Figure 7.3: RJR decay trees imposed in this thesis

1526 into two new frames, known as the P_a and P_b systems. These are equivalent to the
 1527 razor frames of the razor technique, and represent proxy frames where each squark
 1528 is at rest. In $P_a(P_b)$, the decay is symmetric between the visible $V_a(V_b)$ objects and
 1529 the invisible system $I_a(I_b)$. To generate the estimator of the kinematics of the V_a , V_b ,
 1530 I_a , and I_b systems in the P_a and P_b systems, we apply another jigsaw rule to split the
 1531 total E_T^{miss} between P_a and P_b , which allows calculations of these kinematics in these
 1532 frames. For the case of disquark production, this is the expected decay tree, and we

1533 stop the recursive calculation at that level.

1534 In the case of digluino production, we expect two additional jets, and we can
1535 perform an additional boost in each of P_a and P_b , to what we call the C_a and C_b frames.
1536 The decay tree is shown in ?? . In this case we apply a jigsaw at the level of $P_a(P_b)$
1537 which separates a single visible object V_{1a} (V_{2a}) from the child frame $C_a(C_b)$. This
1538 child frame represents the hypothesized squark after the decay $\tilde{g} \rightarrow g\tilde{q}$, which then
1539 decays as in the squark case. This gives additional information which will be exploited
1540 for the gluino specific search regions.

The third decay tree used in this thesis is the *compressed* decay tree. Compressed refers to signal models which have a small splitting between the mass of the proposed sparticle and the $\tilde{\chi}_1^0$. In this case, the sparticle decay products (i.e. the jets and E_T^{miss}) do not generally have large scale[114]. Instead, the strategy is generally to look for a large-scale initial state radiation (ISR) jet which is recoiling off the disparticle system. In the case where the LSPs receive no momentum from the sparticle decays, the following approximation holds:

$$E_T^{\text{miss}} \sim -p_T^{\text{ISR}} \times \frac{m_{\tilde{\chi}_1^0}}{m_{\text{sparticle}}} \quad (7.13)$$

1541 where p_T^{ISR} is the transverse momentum associated to the entire ISR system.

1542 RJR offers a natural and straightforward way to exploit this feature in events
1543 containing ISR. One imposes the simple decay tree in ?? with associated jigsaw rules.
1544 With suitable jigsaw rules, this decay tree “picks out” the large p_T ISR jet, recoiling
1545 off the E_T^{miss} and additional radiation from the sparticle decays. This provides a
1546 convenient set of variables to understand compressed scenarios.

1547 There is one other decay tree, shown in ?? . This is special, as it is only used for
1548 the purpose of QCD rejection, and does not directly map to a sparticle decay chain.
1549 Due to the large production cross-sections of QCD events, even very rare large jet
1550 mismeasurements can lead to significant E_T^{miss} which can enter the signal region. To
1551 reduce these backgrounds, one usually rejects events which contain jets which are

1552 “too close” by some distance metric to the E_T^{miss} in the event. Generally, in the past,
1553 the distance metric has been defined as simply the angular distance ΔR .

1554 The *self-assembling tree* can be seen as defining a distance metric which depends
1555 on the magnitudes of the E_T^{miss} and jets rather than simply their distance in angular
1556 space. Depending on the exact kinematics, the one or two closest jets are found, and
1557 label the E_T^{miss} *siblings*.

1558 In this section, we have seen how one imposes particular decay trees on an event
1559 to produce a basis of kinematic variables in the approximated frames relevant to
1560 the hypothesized sparticle decay chain. This explains why we call this procedure
1561 “recursive”: we can continue the procedure through as many steps of a decay tree as
1562 we want, and each application of a jigsaw rule is dependent on the variables produced
1563 in the last step. The question, of course, is *what are these jigsaw rules?*.

1564 Jigsaw Rules

1565 Jigsaw rules are the fundamental step that allow the recursive definitions of the
1566 variables of interest. We want rules which allow us to fully define kinematic variables
1567 at each step in a decay tree. The only possible solution to fully define the event
1568 kinematics in terms of the frames of the hypothesized decays is the imposition of
1569 external constraints to eliminate additional degrees of freedom. In principle, these
1570 need not have any particular physical motivation. Instead, the jigsaw rules are a
1571 way to resolve the mathematical ambiguities to fully reconstruct the full decay chain
1572 kinematics. However, most practical jigsaw rules also have some reasonable physical
1573 motivation, which we will also elucidate.

1574 In the original razor point of view, some jigsaw rules can be seen as the definitions
1575 of the boosts which relate the different frames of interest, while other rules allow one
1576 to combine multiple objects and place them into a particular hemisphere (previously
1577 megajet). These are the two forms of jigsaw rules: combinatoric and kinematic. As

1578 we have stressed before, the jigsaw rules are a *choice*; as long as a particular jigsaw
1579 rule allows the definition of variables at each step in a decay tree, it is “as valid” as
1580 any other rule.

Practically speaking, in this thesis we use only a small subset of possible jigsaw rules. The combinatoric jigsaw rule we use has already been introduced as megajet construction above. The minimization of

$$m_{J_1}^2 + m_{J_2}^2. \quad (7.14)$$

1581 is a jigsaw rule to deal with the combinatoric ambiguity implicit in which jets go in
1582 which hemisphere. This is the jigsaw rule used in the decay trees when going from
1583 one frame to two frames such as $PP \rightarrow P_a, P_b$.

1584 We will use three other jigsaw rules, which are both kinematic jigsaw rules. One
1585 has already been used in the razor technique. The minimization of β_L will be used
1586 as the jigsaw rule in the first step of each decay tree: the lab frame to the PP/CM
1587 frame. This is in effect the imposition of longitudinal boost invariance, as we expect
1588 on average $p_{z,PP,\text{CM}} = 0$. One defines a unique longitudinal boost by imposition of
1589 this external constraint.

1590 The final two jigsaw rules used in this thesis was not used in the razor technique.
1591 We describe them here.

The first kinematic ambiguity is the total mass of the invisible system M_I . We guess this to be:

$$M_I^2 = M_V^2 - 4M_{V_a}M_{V_b}. \quad (7.15)$$

1592 As we stated above, there is no need to “justify” the jigsaw rules, as they are in some
1593 ways a mathematical trick to fully resolve the event kinematics. However in this case,
1594 there is a nice property of this guess. The symmetry of the production mechanism,
1595 where we have two decay products V_i and I_i produced from the decay of the same
1596 heavy sparticle, is explicit with this jigsaw choice.

1597 The final jigsaw rule we employ in this thesis is used to resolve the “amount” of
1598 E_T^{miss} that “belongs” to each hemisphere, and therefore how to impose the transverse
1599 boost onto each of i.e. P_a and P_b from PP . Equivalently, it can be seen as the
1600 resolution of the kinematics of the I_a and I_b objects in the disquark and digluino
1601 decay trees. Recall that at this point, we have already approximated the boost
1602 of the PP frame. The choice we use is to minimize the masses P_a and P_b , while
1603 simultaneously constraining $P_a = P_b$. As is the case in the last step, there is a
1604 straightforward physical interpretation of this choice. In the signal models we are
1605 considering, P_a and P_b are the estimated frames of the squark or gluino pair-produced
1606 as a heavy resonance. We then of course expect $M_{P_a} = M_{P_b}$.

1607 The imposition of the decay trees, with ambiguities resolved through the jigsaw
1608 rules, give a full set of boosts relating the frames of each decay tree. In each frame,
1609 we have estimates for the frame mass and decay angles, which can be used in searches
1610 for new physics. In the next section, we describe the variables that are used in this
1611 thesis in more details.

1612 **7.3 Variables used in the search for zero lepton**

1613 **SUSY**

1614 We describe here the variables used in the search described in ???. These were
1615 reconstructed using the RJR algorithm as just described, using the RestFrames
1616 packages[119]. In these frames, the momenta of all objects placed into that branch
1617 of the decay tree are available (after application of the approximated boost), and in
1618 principle we can calculate any variable of interest such as invariant masses or the
1619 angles between these objects. The truly useful set of variables are highly dependent
1620 on the signal process, and we leave their discussion to the subsequent chapters. It is
1621 useful to understand the philosophy employed in the construction of these variables.

1622 In general, we can split variables useful for searches for new physics into two
1623 categories: *scaleful* and *scaleless* variables. In this search, we will use a set of scaleful
1624 variables called the H variables. The scaleless variables will consists of ratios and
1625 angles. In general, we want to limit the number of scaleful cuts we apply, for two
1626 reasons. Different scaleful variables are often highly correlated, and this of course
1627 limits the utility of additional cuts. Addtionally, selections based on many scaleful
1628 variables often “over-optimize” for particular signal model of interest, especially as
1629 related to the mass difference chosen between the sparticle and the LSP. To avoid
1630 this, each decay tree will only use two scale variables, one of which quantifies the
1631 overall mass scale of the event, and another which acts as a measure of the event
1632 balance.

1633 **Squark and gluino variables**

1634 Taking our general philosophy to a particular case, we here describe the variables
1635 used by the squark and gluino searches. We have a suite of scale variables which we
1636 will call the H variables, and a suite of angles and ratios.

1637 As we have described above, the RJR algorithm gives us access to the masses of
1638 each frame of interest. It maybe seem natural, then, that these variables would be the
1639 most useful for discrimination of the signal from background processes. However, due
1640 to the all hadronic state considered in this thesis, the that can be constructed such
1641 as M_{PP} can be affected by extra QCD radiation, which can promote the background
1642 processes to large scales. The H variables show a resilience to this effect. They
1643 take their name from the commonly used variable H_T , which is the scalar sum of
1644 the visible momentum. However, due to the RJR technique, we can evaluate these
1645 variables in the non-lab frame, including longitudinal information. They are also
1646 constructed with *aggregate* momenta using a similar mass minimization procedure
1647 as we have already described.

We label these variables as $H_{n,m}^F$. The frame from where they are evaluated is denoted F ; practically, this means $F \in \{\text{lab}, PP, P_a, P_b\}$. When the discussion applies to both P_a and P_b , we will write P_i . The subscripts n and m denote the number of visible and invisible vectors considered, respectively. When there are more vectors available than n or m , we add up vectors using the hemisphere (megajet) jigsaw rule until there are n (m) objects.² In the opposite case, where n or m is greater than the number of available objects, one simply considers the available objects. The $H_{n,m}^F$ variables are then defined as

$$H_{n,m}^F = \sum_i^n |\vec{p}_{\text{vis},i}^F| + \sum_j^m |\vec{p}_{\text{inv},i}^F|. \quad (7.16)$$

It may not be clear that these variables encode independent information. Fundamentally, this is just an expression of the triangle inequality $\sum |\vec{p}| \geq |\sum \vec{p}|$. The different combinations can then include independent information. The final note on the H variables is that we can also consider purely transverse versions of these variables, which we will denote $H_{T,n,m}^F$. Including this view, it is easy to see how the H variables are extensions of the normal H_T variables, as

$$H_T = H_{T,\infty,0}^{\text{lab}}. \quad (7.17)$$

1648 Although the H variables are interesting in their own right, the true power of the
 1649 RJR technique comes from the construction of scaleless variables with the technique.
 1650 This is because the scaleless ratios and angles are in fact measured in the “right”
 1651 frame, where right here means an approximation of the correct frame. This provides
 1652 a less correlated set of variables than those measured in the lab frame, due to the
 1653 corrections to the disparticle or sparticle system boosts from the RJR technique.
 1654 For the search for noncompressed disquark production, we use will use the
 1655 following set of RJR variables.

²Recall that these vectors are constructed by the imposition of the decay tree with the relevant jigsaw rules.

- 1656 • $H_{1,1}^{PP}$ - scale variable useful for discrimination against QCD backgrounds and
 1657 used in a similar way to E_T^{miss}

- 1658 • $H_{T,2,1}^{PP}$ - scale variable providing information on the overall mass scale of the
 1659 event for disquark signal production. We will often call this the *full* scale
 1660 variable.

- 1661 • $H_{T,1,1}^{PP}/H_{2,1}^{PP}$ - ratio used to prevent imbalanced events where the scale variable
 1662 is dominated by one high p_T jet or high E_T^{miss}

- 1663 • $p_{PP,z}^{\text{LAB}}/(p_{PP,z}^{\text{LAB}} + H_{T,2,1}^{PP})$ - ratio used to prevent significant boosts in the
 1664 z -direction. $p_{PP,z}^{\text{LAB}}$ is a measure of the total boost of the PP system from the lab
 1665 frame

- 1666 • $p_{T,j2}^{PP}/H_{T,2,1}^{PP}$ - ratio to force the second leading jet in the PP frame to carry a
 1667 significant portion of the total scalar sum in that frame. This requirement is
 1668 another balance requirement, on the total p_T of that second jet in the PP frame.

1669 First, we note that there is an implicit requirement that each hemisphere has at least
 1670 one jet (to even reconstruct the P_a and P_b frames), these variables are implicitly using
 1671 two or more jets, as we expect in disquark production. The other important thing
 1672 to note is that all of the ratios use the full scale variable as the denominator. This
 1673 is sensible, as we expect all of these effects to be scaled with the full scale variable
 1674 $H_{T,2,1}^{PP}$. We will see a similar behavior for the gluino regions, with a new full scale
 1675 variable.

1676 For the search for noncompressed digluino production, we use will use the following
 1677 set of RJR variables. Due to the increased complexity of the event topology with four
 1678 jets, there are additional handles we can exploit:

- 1679 • $H_{1,1}^{PP}$ - same as disquark production

- 1680 • $H_{T,4,1}^{PP}$ - scale variable providing information on the overall mass scale of the
 1681 event for digluino signal production. As before, we often call this the *full* scale
 1682 variable. Since this variable allows the jets to be separated in the *PP*frame, it
 1683 is more appropriate for digluino production.
- 1684 • $H_{T,1,1}^{PP}/H_{4,1}^{PP}$ - ratio used to prevent imbalanced events where the scale variable
 1685 is dominated by one high p_T jet or high E_T^{miss}
- 1686 • $H_{T,4,1}^{PP}/H_{4,1}^{PP}$ - ratio used to measure the fraction of the total scalar sum of the
 1687 momentum in the transverse plane. Digluino production is expected to be fairly
 1688 central
- 1689 • $p_{PP,z}^{\text{LAB}}/(p_{PP,z}^{\text{LAB}} + H_{T,4,1}^{PP})$ - ratio to used to prevent significant boosts in the
 1690 z -direction
- 1691 • $\min(p_{T,j2_i}^{PP}/H_{T,2,1_i}^{PP})$ - ratio to require the second leading jet in *both* squark-like
 1692 hemispheres C_a and C_b to contain a significant portion of *that frame's* momenta.
 1693 This is similar to the $p_{T,j2}^{PP}/H_{T,2,1}^{PP}$ disquark discriminator, but applied to both
 1694 hemispheres C_a and C_b .
- 1695 • $\max(H_{1,0}^{P_i}/H_{2,0}^{P_i})$ - ratio requiring one jet in each of the P_i to not take too much
 1696 of the total momentum of that frame. This ratio is generally a very loose cut.

1697 Compressed variables

1698 As we saw above, the decay tree imposed for compressed spectra is simpler. We do
 1699 not attempt to fully reconstruct the details of the system recoiling of the ISR system,
 1700 but use a straightforward set of variables in this case. One additional simplification
 1701 is that all variables are force to be transverse in this case; we simply do not include
 1702 the η/z information of the objects as inputs to the RJR reconstruction. We still use
 1703 the philosophy of limiting our scaleful variables to just two. The compressed scenario
 1704 uses the following set of RJR variables:

1705 • $p_{T,S}^{\text{ISR}}$ - scale variable that is the magnitude of the total transverse momenta of all
 1706 jets associated to the ISR system, as evaluated in the CM frame

1707 • $R_{\text{ISR}} \equiv p_I^{\hat{\text{CM}}} \cdot p_{T,S}^{\hat{\text{CM}}} / p_{T,S}^{\text{CM}}$ - this ratio is our measurement for the ratio of the LSP
 1708 mass to the compressed sparticle mass. These are the values in the CM frame
 1709 In compressed cases, this should be large, as this estimates the amount of the
 1710 total CM $\rightarrow S$ boost is carried by the invisible system.

1711 • $M_{T,S}$ - the transverse mass of the S system

1712 • N_{jet}^V - the number of jets associated to the visible system V

1713 • $\Delta\phi_{\text{ISR},I}$ - the opening angle between the ISR system and the invisible system
 1714 measured in the lab frame. As the invisible system is expected to carry much
 1715 of the total S system momentum, this should be large, as we expect the ISR
 1716 system to recoil directly opposite the I system in that case.

1717 Anti-QCD variables

1718 For the self-assembling tree, we construct two variables, which we combine to form a
 1719 single variable which rejects QCD events. In this case, we use the mass minimization
 1720 jigsaw, with a fully transverse version of the event (i.e. we set all jet z/η components
 1721 to 0). This jigsaw defines the distance metric, and provides us with one or two jets
 1722 known as the $E_{\text{T}}^{\text{miss}}$ siblings. We define \vec{p}_{sib} as the sum of these jets, and define the
 1723 following quantities.

We calculate a ratio observable which examines the relative magnitude of the sibling vector \vec{p}_{sib} and $E_{\text{T}}^{\text{miss}}$, and an angle relating \vec{p}_{sib} and $E_{\text{T}}^{\text{miss}}$:

$$R(\vec{p}_{\text{sib}}, E_{\text{T}}^{\text{miss}}) \equiv \frac{\vec{p}_{\text{sib}} \cdot \hat{E}_{\text{T}}^{\text{miss}}}{\vec{p}_{\text{sib}} \cdot \hat{E}_{\text{T}}^{\text{miss}} + |\vec{E}_{\text{T}}^{\text{miss}}|} \quad (7.18)$$

$$\cos \theta(\vec{p}_{\text{sib}}, E_{\text{T}}^{\text{miss}}) \equiv \frac{(\vec{p}_{\text{sib}} + \vec{E}_{\text{T}}^{\text{miss}}) \cdot \vec{p}_{\text{sib}}^{\text{miss}}}{|\vec{p}_{\text{sib}}| + E_{\text{T}}^{\text{miss}}} \quad (7.19)$$

These observables are highly correlated, but taking the following fractional difference provides strong discrimination between SUSY signal and QCD background events:

$$\Delta_{\text{QCD}} \equiv \frac{1 + \cos \theta(\vec{p}_{\text{sib}}, E_{\text{T}}^{\text{miss}}) - 2R(\vec{p}_{\text{sib}}, E_{\text{T}}^{\text{miss}})}{1 + \cos \theta(\vec{p}_{\text{sib}}, E_{\text{T}}^{\text{miss}}) + 2R(\vec{p}_{\text{sib}}, E_{\text{T}}^{\text{miss}})}. \quad (7.20)$$

1724 We will use this variable in the next chapter.

Title of Chapter 1

1727 This section presents the details of the first search employing RJR variables as
 1728 discriminating variables, as described in ???. We will describe the simulation samples
 1729 used, and then define the selections where we search for new SUSY phenomena, which
 1730 we call the *signal regions* (SRs) Afterwards, we describe the background estimation
 1731 techniques used in the analysis. Finally, we discuss the treatment of systematic
 1732 uncertainties, and how we combine them using a likelihood method[120].

1733 **8.1 Simulation samples**

1734 We discussed the collision data sample provided by the LHC for the analysis in this
 1735 thesis. The primary point is the delivery of 13.3 fb^{-1} of collision data, at $\sqrt{s} = 13 \text{ TeV}$.
 1736 To select events in data, we use the trigger system as previously discussed, and use
 1737 the lowest unprescaled trigger which is available for a particular Standard Model
 1738 background. We now discuss the simulation samples used for this search.

1739 Simulated data is fundamentally important to the ATLAS physics program.
 1740 Calibrations, measurements, and searches use Monte Carlo (MC) simulations¹ to
 1741 compare with collision data. In this thesis, MC samples are used to optimize the
 1742 signal region selections, assist in background estimation, and assess the sensitivity to
 1743 specific SUSY signal models. The details of Monte Carlo production, accuracy, and
 1744 utility are far beyond the scope of this thesis, but we provide a short description here.

¹In jargon, often just called “Monte Carlo” or MC.

1745 The first step is MC *generation*. A program is run which does a matrix-element
1746 calculation, sometimes with additional corrections, which produces a set of output
1747 particles from the parton interactions. These output particles are then decayed via
1748 another (or the same) simulation program. This produces a set of *truth* particles,
1749 which are the output of event generation. The details of which generator to use are
1750 the subject of much discussion, and generally (many) comparisons are made between
1751 them, for different processes of interest. Additionally, differences between generators
1752 are often a starting point for the calculation of systematic uncertainties.

1753 The next step is the *simulation*. The detector response to the truth particles
1754 is simulated, and simulated hits are produced. After simulation, the standard
1755 reconstruction algorithms described previously are run with the simulated hits. This
1756 procedure ensures “as close as possible” treatment of simulation and collision data.

1757 We give a brief description of which samples use which generators; additional
1758 details are available in ??.

MAKE 1759 Signal (diguino and disquark) samples are generated with up to two extra
BETTER 1760 partons in the matrix element using MG5_aMC@NLO 2.2.2 event generator [Alwall:2014hca] interfaced to PYTHIA 8.186 [Sjostrand:2014zea]. The nominal cross-section is taken from an envelope of cross-section predictions using different PDF sets and factorization and renormalization scales, as described in Ref. [Kramer:2012bx], considering only light-flavour quarks (u, d, s, c). For the light-flavour squarks (gluinos) in case of gluino- (squark-) pair production, cross-sections are evaluated assuming masses of 450 TeV. The free parameters are $m_{\tilde{\chi}_1^0}$ and $m_{\tilde{g}} (m_{\tilde{s}})$ for gluino-pair (squark-pair) production models.

explain 1767 Boson (W, Z, γ) plus jet events are simulated using different SHERPA generators,
we have a 1768 with COMIX and OPENLOOPS matrix-element generators[comix, openloops, 121].
“grid” of 1769 Photons are required to have transverse momentum of > 35 GeV. Importantly, the
these signal 1770 $W(Z)+\text{jet}$ events are calculated at NLO while the the $\gamma+\text{jet}$ events are calculated
models 1771 samples

1772 at LO. The $W/Z +$ jets events are normalized to their NNLO cross-sections
1773 [Catani:2009sm]. The $\gamma+$ jets LO cross-section is taken directly from SHERPA; we
1774 will apply a correction factor to be described later.

1775 The various $t\bar{t}$ and single-top processes[122] are generated using two versions of
1776 POWHEG-Box [**powheg-box**, 122]. These are calculated at NLO and normalized
1777 to various orders ranging from NLO to NNLO+NNLL in the different processes,
1778 which can be seen in 8.1[Czakon:2013goa, Czakon:2011xx, Aliev:2010zk,
1779 Kant:2014oha, Kidonakis:2010ux, Kidonakis:2011wy].

1780 Diboson processes (WW , WZ , ZZ) [123] are simulated using the SHERPA 2.1.1
1781 generator. For processes with four charged leptons (4ℓ), three charged leptons and
1782 a neutrino ($3\ell+1\nu$) or two charged leptons and two neutrinos ($2\ell+2\nu$), the matrix
1783 elements contain all diagrams with four electroweak vertices, and are calculated for
1784 up to one (4ℓ , $2\ell+2\nu$) or no partons ($3\ell+1\nu$) at NLO and up to three partons at LO
1785 using the COMIX and OPENLOOPS matrix-element generators, and merged with the
1786 SHERPA parton shower using the ME+PS@NLO prescription. For processes in which
1787 one of the bosons decays hadronically and the other leptonically, matrix elements
1788 are calculated for up to one (ZZ) or no (WW , WZ) additional partons at NLO
1789 and for up to three additional partons at LO using the COMIX and OPENLOOPS
1790 matrix-element generators, and merged with the SHERPA parton shower using the
1791 ME+PS@NLO prescription. In all cases, the CT10 PDF set is used in conjunction
1792 with a dedicated parton-shower tuning developed by the authors of SHERPA. The
1793 generator cross-sections are used in this case.

1794 The multi-jet background is generated with PYTHIA 8.186 using the A14
1795 underlying-event tune and the NNPDF2.3LO parton distribution functions.

1796 A summary of the SM background processes together with the MC generators,
1797 cross-section calculation orders in α_s , PDFs, parton shower and tunes used is given
1798 in Table 8.1.

Physics process	Generator	Cross-section normalization	PDF set	Parton shower	Tune
$W(\rightarrow \ell\nu) + \text{jets}$	SHERPA 2.2.0	NNLO	NNPDF3.0NNLO	SHERPA	SHERPA default
$Z/\gamma^*(\rightarrow \ell\bar{\ell}) + \text{jets}$	SHERPA 2.2.0	NNLO	NNPDF3.0NNLO	SHERPA	SHERPA default
$\gamma + \text{jets}$	SHERPA 2.1.1	LO	CT10	SHERPA	SHERPA default
$t\bar{t}$	Powheg-Box v2	NNLO+NNLL	CT10	PYTHIA 6.428	PERUGIA2012
Single top (Wt -channel)	Powheg-Box v2	NNLO+NNLL	CT10	PYTHIA 6.428	PERUGIA2012
Single top (s -channel)	Powheg-Box v2	NLO	CT10	PYTHIA 6.428	PERUGIA2012
Single top (t -channel)	Powheg-Box v1	NLO	CT10f4	PYTHIA 6.428	PERUGIA2012
$t\bar{t} + W/Z/WW$	MG5_aMC@NLO 2.2.3	NLO	NNPDF2.3LO	PYTHIA 8.186	A14
WW, WZ, ZZ	SHERPA 2.1.1	NLO	CT10	SHERPA	SHERPA default
Multi-jet	PYTHIA 8.186	LO	NNPDF2.3LO	PYTHIA 8.186	A14

Table 8.1: The Standard Model background Monte Carlo simulation samples used in this thesis. The generators, the order in α_s of cross-section calculations used for yield normalization, PDF sets, parton showers and tunes used for the underlying event are shown.

1799 For all SM background samples the response of the detector to particles is
 1800 modelled with a full ATLAS detector simulation [**:2010wqa**] based on GEANT4
 1801 [**Agostinelli:2002hh**]. Signal samples are prepared using a fast simulation based on
 1802 a parameterization of the performance of the ATLAS electromagnetic and hadronic
 1803 calorimeters [**ATLAS:2010bfa**] and on GEANT4 elsewhere.

1804 All simulated events are overlaid with multiple pp collisions simulated with
 1805 the soft QCD processes of PYTHIA 8.186 using the A2 tune [**A14tune**] and the
 1806 MSTW2008LO parton distribution functions [**Martin:2009iq**]. The simulations are
 1807 reweighted to match the distribution of the mean number of interactions observed in
 1808 data.

1809 **8.2 Event selection**

1810 This section describes the selection of events. We begin by describing the *preselection*,
1811 which is used to remove problematic events and reduce the dataset to a manageable
1812 size. We then describe the signal region strategy, and present the signal regions used
1813 in the analysis.

1814 **Preselection**

1815 The preselection is used to reduce the dataset to that of interest in this thesis. The
1816 table containing the preselection cuts is shown in 8.2. This selection is also used for
1817 the samples used for background estimation, except for the lepton veto.

1818 The cuts [1] and [4] are a set of cleaning cuts to remove problematic events.
1819 The *Good Runs List* is a centrally-maintained list of data runs which have been
1820 determined to be “good for physics”. This determination is made by analysis of the
1821 various subdetectors, and monitoring of their status. Event cleaning is used to veto
1822 events which could be affected by noncollision background, noise bursts, or cosmic
1823 rays.

1824 We require the lowest unprescaled E_T^{miss} trigger for the data run of interest, as
1825 described previously, in cut [2]. The lepton veto is applied in cut [5]. These two cuts
1826 are only used for the signal region selection.

1827 The rest of the preselection is used for the signal region and background estimation
1828 samples. These cuts are mostly used for the reduction of the dataset to a manageable
1829 Signal models with sensitivity to lower values of these scale variables have been ruled
1830 out by previous searches[124]. The final cut is on m_{eff} , which is the scalar sum of all
1831 jets and E_T^{miss} . This is the final discriminating variable used in the complementary
1832 search to this thesis, which is also presented in ??.

Cut	Description	
1	Good Runs List	Veto events with intolerable detector errors
2	Trigger	HLT_xe70 (2015), HLT_xe80_tclcw_L1XE50, or HLT_xe100_mht_L1XE50 (2016)
3	Event cleaning	Veto for noncollision background, noise bursts, and cosmic rays
4	Lepton veto	No leptons with $p_T > 10$ GeV after overlap removal
5	E_T^{miss} [GeV] >	250
6	$p_T(j_1)$ [GeV] >	200
7	$p_T(j_2)$ [GeV] >	50
8	m_{eff} [GeV] >	800

Table 8.2: Preselection for the various event topologies used in the analysis.

Signal regions

We define a set of signal regions using the RJR variables previously described. These signal regions are split into three general categories: squark pair production SRs, gluino pair production SRs, and compressed production SRs. Within these general SRs, we have a set of signal regions targetting different mass splittings of the sparticle and LSP.

A schematic of this strategy is shown in ???. This type of plane is how most ($R-$ parity conserving) SUSY searches are organized in both ATLAS and CMS. The horizontal axis is the mass of the sparticle considered. In the case of this thesis, this will be the squark or gluino mass. On the horizontal axis, we place the LSP mass. These are the two free parameters of the simplified models considered here. Our search occurs in this two-parameter space. Each signal region targets some portion of this plane. As shown in the figure, a new iteration of a search will use a set of signal regions which have sensitivity just beyond those of the previous exclusions. The choice of how many signal regions to use to fully cover this plane is in many ways a matter of judgment, as it is essentially a matter of under/over-fitting to the signal models of interest. One signal region will obscure the different phenomena in

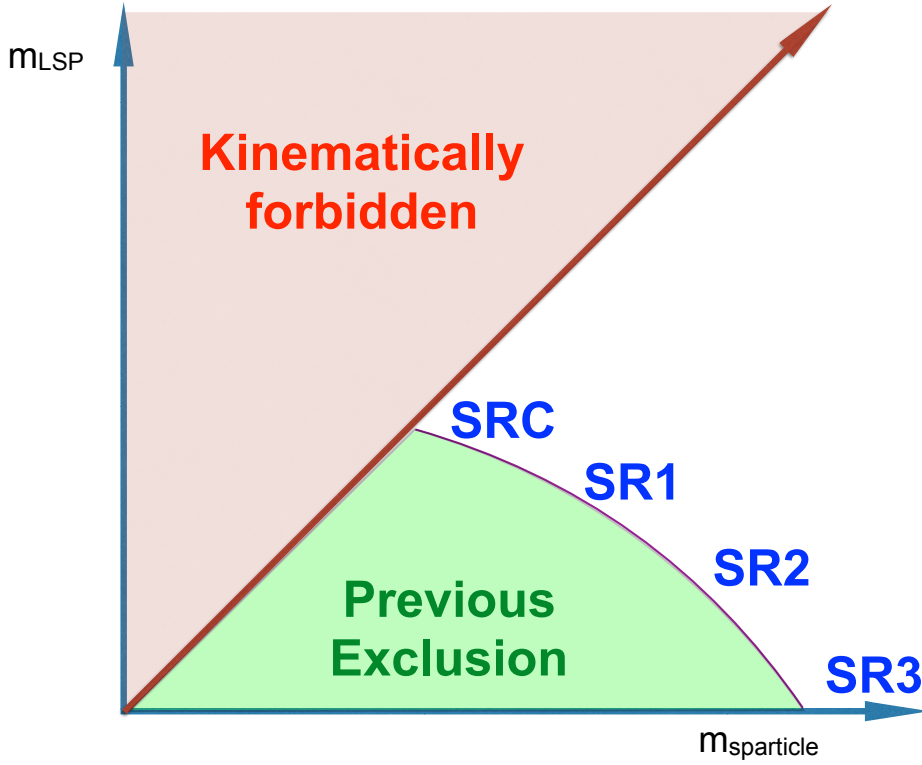


Figure 8.1: Schematic leading the development of the SUSY signal regions in this thesis. A variant of this schematic is used for most SUSY searches on ATLAS and CMS.

1850 signal events with large versus small mass splittings, leading to underfitting. Binning
 1851 as finely as possible² leads to overfitting due to the fluctuations present in the signal
 1852 and background events passing this selection. In this thesis, we use six squark signal
 1853 regions, six gluino signal regions, and five compressed regions, which we describe
 1854 below.

1855 The full table defining all signal regions is shown in 8.3. In all cases, the signal
 1856 region selections contain a combination of scaleful and scaleless cuts. Emphasis
 1857 on cuts on scaleful variables provide stronger sensitivity to larger mass splittings,
 1858 while additional sensitivity to smaller mass splittings is found using stronger cuts on
 1859 scaleless variables. One envisions walking from SR1 (with tight scaleless cuts and

²This can be defined as having a signal region for each simulated signal sample, which for this analysis is ~ 100 .

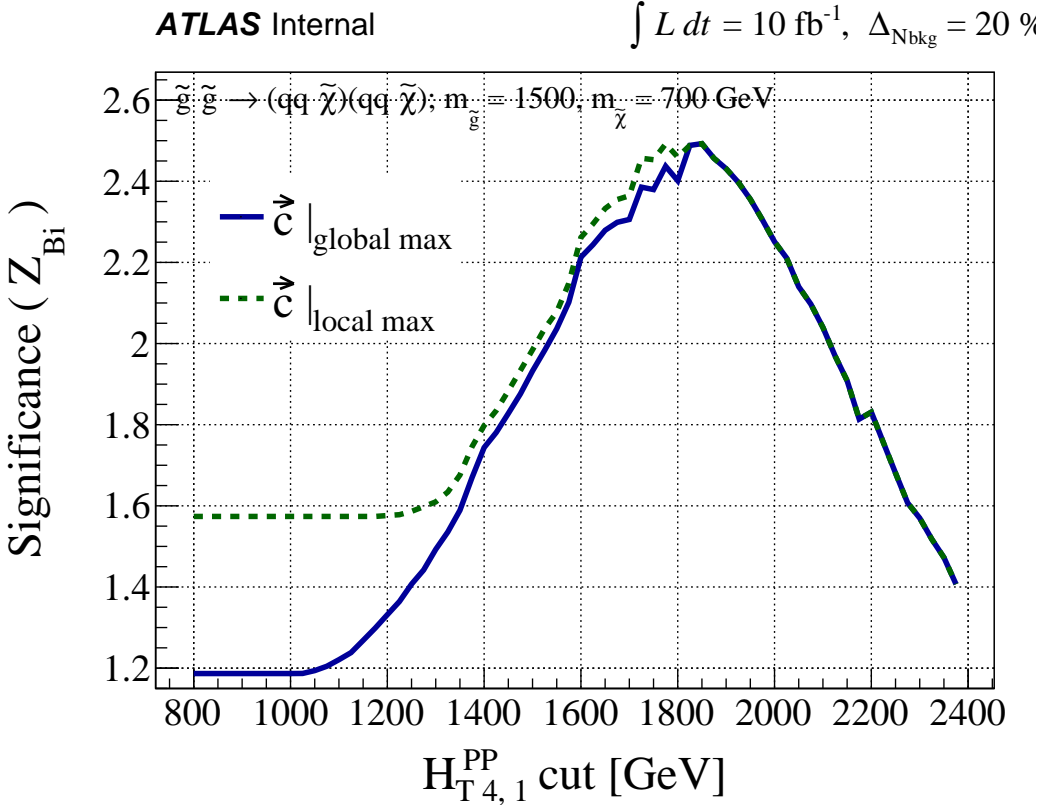


Figure 8.2: Optimization of the $H_{T,4,1}^{PP}$ cut for a gluino signal model with $(m_{\tilde{g}}, m_{\tilde{\chi}_1^0}) = (1500, 700)$ GeV assuming 10 fb^{-1} and an uncertainty of 20% on the background estimate.

1860 loose scaleful cuts) in 8.1 towards SR3 by loosening the scaleless cuts and tightening
 1861 the scaleful cuts. We will see this strategy at work in each set of signal regions.

1862 We have already described the useful variables in the previous chapter. The
 1863 question is how to choose the optimal cuts for a given set of signal models, which are
 1864 grouped in the mass splitting space. This was done by a brute force scan over the
 1865 cut values, using a guess of integrated luminosity with a fixed systematic uncertainty
 1866 scenario, motivated by that from previous analyses. We choose the lowest cut value
 1867 that maximizes the Z_{Bi} , as described in [125]. This figure of merit gives conservative
 1868 estimates, as compared to i.e. S/\sqrt{B} . A figure showing an example of this selection
 1869 tuning procedure is shown in 8.2.

1870 The compressed selections are split into five regions (SRC1-5), and due to the

1871 simplified nature of the compressed decay tree, has sensitivity in both the gluino
1872 and squark planes. The compressed regions target mass splittings with $m_{\text{sparticle}} -$
1873 $m_{\text{LSP}} \tilde{<} 200 \text{ GeV}$. For the compressed region, $M_{T,S}$ is the primary scaleful variable.
1874 We can see the general strategy of lowering increasing scale cuts while decreasing the
1875 scaleless cuts here. SRC1 targets the most compressed scenarios, with mass splittings
1876 of less than 25 GeV, and has the loosest $M_{T,S}$ cut coupled with the tightest R_{ISR} and
1877 $\Delta\phi_{\text{ISR},I}$ cuts. SRC4 and SRC5 target mass splittings of ~ 200 GeV, and are coupled
1878 with the loosest scaleless cuts on R_{ISR} and $\Delta\phi_{\text{ISR},I}$. We also note that SRC4 and
1879 SRC5 have differing cuts on N_{jet}^V , since these SRs are closest to the regions we will
1880 describe below, and can be seen as the “cross-over” where the differences between
1881 squark and gluino production begins to become manifest.

1882 The squark regions (for noncompressed spectra) are organized into six signal
1883 regions. These are labeled by a numeral 1-3 and letter a/b. SRs sharing a common
1884 numeral i.e. SRS1a and SRS1b share a common set of scaleless cuts, while differing in
1885 the main scale variable $H_{T,2,1}^{PP}$. The two SRs for each set of scaleless cuts, only differing
1886 in the main scale variable, can be seen in a naïve way as providing sensitivity to a
1887 range of luminosity scenarios³. As before, we see that the scaleless cuts are loosened
1888 as we tighten the scaleful cuts, as we move across the table from SRS1a to SRS3b.
1889 This provides strong sensitivity to signal models with intermediate mass splittings with
1890 SRS1a to large mass splittings with SR3b.

1891 The gluino signal regions are organized entirely analogously to the squark signal
1892 regions. There are six gluino signal regions, again labeled via a numeral 1-3 and letter
1893 a/b. Those SRs sharing a common numeral have a common set of scaleless cuts, but
1894 differ in their main scale variable $H_{T,4,1}^{PP}$. The SRs follow the strategy, with SRG1
1895 having the loosest scaleful cut cuts coupled with the strongest scaleless cuts, and the

³These SRs were defined before the entire collision dataset was produced, and thus need to be robust in cases where the LHC provides significantly different than expected performance.

1896 converse being true in SRG3. As in the squark case, this strategy provides strong
1897 expected sensitivity throughout the gluino-LSP plane.

Targeted signal	$\tilde{s}\tilde{s}, \tilde{s} \rightarrow q\tilde{\chi}_1^0$									
Requirement	Signal Region									
	RJR-S1		RJR-S2		RJR-S3					
$H_{1,1}^{PP}/H_{2,1}^{PP} \geq$	0.6		0.55		0.5					
$H_{1,1}^{PP}/H_{2,1}^{PP} \leq$	0.95		0.96		0.98					
$p_{PP, z}^{lab}/(p_{PP, z}^{lab} + H_{T, 2,1}^{PP}) \leq$	0.5		0.55		0.6					
$p_{j2, T}^{PP}/H_{T, 2,1}^{PP} \geq$	0.16		0.15		0.13					
$\Delta_{QCD} >$	0.001									
	RJR-S1a	RJR-S1b	RJR-S2a	RJR-S2b	RJR-S3a	RJR-S3b				
$H_{T, 2,1}^{PP} [\text{GeV}] >$	1000	1200	1400	1600	1800	2000				
$H_{1,1}^{PP} [\text{GeV}] >$	1000		1400		1600					
Targeted signal	$\tilde{g}\tilde{g}, \tilde{g} \rightarrow q\bar{q}\tilde{\chi}_1^0$									
Requirement	Signal Region									
	RJR-G1		RJR-G2		RJR-G3					
$H_{1,1}^{PP}/H_{4,1}^{PP} \geq$	0.35		0.25		0.2					
$H_{T, 4,1}^{PP}/H_{4,1}^{PP} \geq$	0.8		0.75		0.65					
$p_{PP, z}^{lab}/(p_{PP, z}^{lab} + H_{T, 4,1}^{PP}) \leq$	0.5		0.55		0.6					
$\min(p_{j2, T}^{PP}/H_{T, 2,1}^{PP}) \geq$	0.12		0.1		0.08					
$\max(H_{1,0}^{Pi}/H_{2,0}^{Pi}) \leq$	0.95		0.97		0.98					
$ \frac{2}{3}\Delta\phi_{V,P}^{PP} - \frac{1}{3}\cos\theta_p \leq$	0.5		-							
$\Delta_{QCD} >$	0									
	RJR-G1a	RJR-G1b	RJR-G2a	RJR-G2b	RJR-G3a	RJR-G3b				
$H_{T, 4,1}^{PP} [\text{GeV}] >$	1000	1200	1500	1900	2300	2800				
$H_{1,1}^{PP} [\text{GeV}] >$	600		800		900					
Targeted signal	compressed spectra in $\tilde{s}\tilde{s}$ ($\tilde{s} \rightarrow q\tilde{\chi}_1^0$); $\tilde{g}\tilde{g}$ ($\tilde{g} \rightarrow q\bar{q}\tilde{\chi}_1^0$)									
Requirement	Signal Region									
	RJR-C1	RJR-C2	RJR-C3	RJR-C4	RJR-C5					
$R_{ISR} \geq$	0.9	0.85	0.8	0.75	0.70					
$\Delta\phi_{ISR, I} \geq$	3.1	3.07	2.95	2.95	2.95					
$\Delta\phi(\text{jet}_{1,2}, \mathbf{E}_T^{\text{miss}})_{\text{min}}$	-	-	-	0.4	0.4					
$M_{TS} [\text{GeV}] \geq$	100	100	200	500	500					
$p_{TS}^{CM} [\text{GeV}] \geq$	800	800	600	600	600					
$N_{jet}^V \geq$	1	1	2	2	3					

Table 8.3: Selection criteria and targeted signal model used to define signal regions in the RJR-based search, indicated by the prefix ‘RJR’. Each SR is labelled with the targeted SUSY particle or the targeted region of parameter space, such that ‘S’, ‘G’ and ‘C’ denote regions searching for squark-, gluino-pair production, or compressed spectra, respectively.

1898 8.3 Background estimation

1899 We describe here the method of background estimation. In this thesis, we detail what
 1900 is colloquially called a “cut-and-count” analysis. This is in contrast to a “shape fit”
 1901 analysis, where one needs to consider the details of the variable distribution shapes.
 1902 Instead, we must ensure the overall normalization of the Standard Model backgrounds
 1903 are correct in the regions of phase space considered in the analysis. In order to
 1904 do this, we define a set of *control regions* which are free of SUSY contamination
 1905 based on the previously excluded analysis. We compare the number of events present
 1906 in the control regions in simulation with that in data to define a *transfer factor*
 1907 (TF). We extrapolate the number of expected events from each background using
 1908 this transfer factor to translate from the , which provides our final estimate of the
 1909 SM background in the corresponding signal region. To be explicit, each signal region
 1910 SR has a corresponding set of control regions.

More precisely, for a given signal region, we are attempting to estimate the value $N_{\text{SR}}^{\text{data}}$ for a given background. This value is estimated using the following equation:

$$N_{\text{SR}}^{\text{data,est}} = N_{\text{CR}}^{\text{data,obs}} \times \text{TF}_{\text{CR}} \equiv N_{\text{CR}}^{\text{data,obs}} \times \left(\frac{N_{\text{SR}}^{\text{MC}}}{N_{\text{CR}}^{\text{MC}}} \right) \quad (8.1)$$

1911 where the transfer factor TF is taken directly from MC. The two ingredients to our
 1912 estimation of $N_{\text{SR}}^{\text{data,obs}}$ is thus $N_{\text{CR}}^{\text{data,obs}}$ and the transfer factor taken from MC.

The transfer factor method is potentially more straightforward written in the following way:

$$N_{\text{SR}}^{\text{data,est}} = N_{\text{SR}}^{\text{MC}} \times \left(\frac{N_{\text{CR}}^{\text{data,obs}}}{N_{\text{CR}}^{\text{MC}}} \right) \equiv n \text{text} SR \text{MC} \times \mu_{\text{CR}}. \quad (8.2)$$

1913 In this form, the correction to the overall normalization is explicit. The ratio $\frac{N_{\text{CR}}^{\text{data,obs}}}{N_{\text{CR}}^{\text{MC}}}$
 1914 which we call μ informs us how to scale $N_{\text{SR}}^{\text{MC}}$ in order to get the right overall
 1915 normalization. The assumption made with this method is that the overall shape of
 1916 the distribution should not change “that much” as one extrapolates to the signal
 1917 region.

1918 The CR definitions are motivated and designed according to two (generally
1919 competing) requirements:

- 1920 1. Statistical uncertainties due to low CR statistics
1921 2. Systematic uncertainties related to the extrapolation from the CR to the SR.

1922 This motivates the desire to make the control regions as similar as possible
1923 to the signal regions without risking signal contamination while ensuring high
1924 purity in the targeted SM background.

1925 In principle, one can also apply data-driven corrections to the TF obtained for each
1926 CR.

1927 In order to validate the transfer factors obtained from MC, we also develop a series
1928 of *validation regions* (VRs). These regions are generally designed to be “in between”
1929 the control region and signal region selections in phase space, and thus provide a
1930 check on the extrapolation from the control regions into the signal regions. Despite
1931 their closeness in phase space to the signal regions, they are also designed to have
1932 low signal contamination.

1933 In practice, we perform this estimation procedure simultaneously across all control
1934 regions; we describe this later. We only note this here since in principle, we can apply
1935 Eq.8.1 to measure the contamination of backgrounds within control regions as well.
1936 This procedure also accounts for the correlations between regions due to correlated
1937 systematic uncertainties. We next describe the control region selection for the major
1938 SM backgrounds for the analysis.

1939 **Control Regions**

1940 As was hinted at in the discussion of Monte Carlo generators, the primary back-
1941 grounds of note in this analysis are $Z + \text{jets}$, $W + \text{jets}$, $t\bar{t}$, and QCD events. There is also
1942 a minor background from diboson events which is taken directly from MC with an

1943 uncertainty of 50%. We describe the strategy to estimate these various backgrounds
 1944 here. A summary table is shown in 8.4. All distributions shown in this section use
 1945 the scaling factors μ from the background fits, which we describe later.

CR	SM background	CR process	CR event selection
Meff/RJR-CR γ	$Z(\rightarrow \nu\bar{\nu}) + \text{jets}$	$\gamma + \text{jets}$	Isolated photon
Meff/RJR-CRQ	Multi-jet	Multi-jet	$\Delta_{\text{QCD}} < 0$ reversed requirement on $H_{1,1}^{PP}$ (RJR-S/G) or $R_{\text{ISR}} < 0.5$ (RJR-C)
Meff/RJR-CRW	$W(\rightarrow \ell\nu) + \text{jets}$	$W(\rightarrow \ell\nu) + \text{jets}$	$30 \text{ GeV} < m_T(\ell, E_T^{\text{miss}}) < 100 \text{ GeV}$, b -veto
Meff/RJR-CRT	$t\bar{t}(\text{+EW})$ and single top	$t\bar{t} \rightarrow b\bar{b}q\bar{q}'\ell\nu$	$30 \text{ GeV} < m_T(\ell, E_T^{\text{miss}}) < 100 \text{ GeV}$, b -tag

Table 8.4: Control regions used in this thesis.

1946 Events with a Z boson decaying to neutrinos in association with jets are the
 1947 primary irreducible background in the analysis. These events have true E_T^{miss} from
 1948 the decaying neutrinos, and can have significant values of the scaleful variables of
 1949 interest. Naively, one might expect us to use $Z \rightarrow \ell\ell$ as the control process of interest,
 1950 as $Z \rightarrow \ell\ell$ events are quite well-measured. Unfortunately, the $Z \rightarrow \ell\ell$ branching ratio is
 1951 about half of from $Z \rightarrow \nu\nu$, which necessitates loosening the control region selection
 1952 significantly. This leads to large systematic uncertainties in the transfer factor to
 1953 account for the separation in phase space.

1954 Instead, photon events are used as the control for the $Z \rightarrow \nu\nu$ events. We label
 1955 this photon control region as CRY. The photon is required to have $p_T > 150 \text{ GeV}$ to
 1956 ensure the trigger is fully efficient. The kinematic properties of photon events strongly
 1957 resemble those of Z events when the boson p_T is significantly above the mass of the Z
 1958 boson. In this regime, the neutral boson properties are scaleless, and can be treated
 1959 interchangeably, up to the differences in coupling strengths. Additionally, the cross-

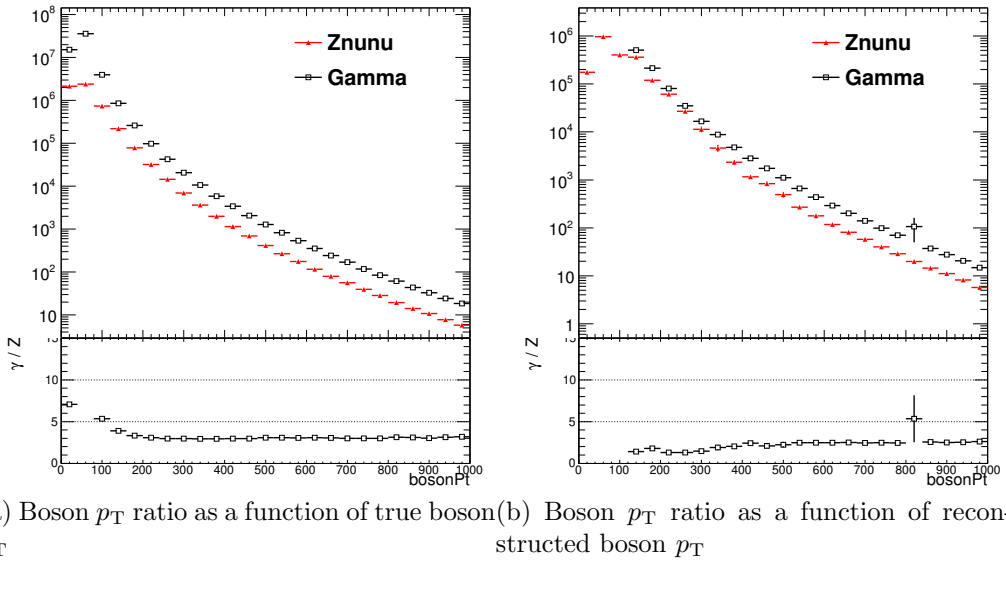


Figure 8.3

1960 section for $\gamma + \text{jetsevents}$ is significantly larger than $Z + \text{jetsevents}$ above the Z mass.
 1961 These features are shown in 8.3 in simulated $Z \rightarrow \nu\nu$ truth and reconstructed events.
 1962 The reconstructed $Z \rightarrow \nu\nu$ events define the boson p_T as simply the E_T^{miss} . In truth
 1963 events, one clearly sees the effect of the Z mass below ~ 100 GeV, with a flattening
 1964 of the ratio above ~ 300 GeV. In reconstructed events, the effects are less clear at low
 1965 boson p_T , primarily due to cut sculpting from i.e. the trigger requirement on photon
 1966 events, which necessitates a higher p_T cut on photon events for the trigger to remain
 1967 fully efficient. Still, it is clear that the ratio flattens out at high boson p_T , and we
 1968 are justified in the use of CRY to model the $Z + \text{jets}$ background.

1969 The CRY kinematic selection is slightly looser in the scaleful variables for the
 1970 noncompressed regions to provide sufficient control region statistics. This is chosen
 1971 to be $H_{1,1}^{PP} > 900$ GeV ($H_{1,1}^{PP} > 550$ GeV) for the squark (gluino) regions to properly
 1972 minimize the corresponding statistical and systematic uncertainties.

1973 One additional correction scale factor is applied to $\gamma + \text{jetsevents}$ before calculating
 1974 the transfer factors. This is known as the κ method, which is used to determine
 1975 the disagreement arising from the use of a LO generator for photon events vs. a

1976 NLO generator for Z +jetsevents, which can reduce the theoretical uncertainties from
1977 this disagreement. One can see this as a measurement of the k-factor for the LO
1978 γ +jetssample. This is effectively done with an auxiliary CRZ region, defined using
1979 two leptons associated to the Z mass. The correction factor derived for this purpose
1980 is $\kappa = 1.39 \pm 0.05$.

1981 Distributions of CRY in squark, gluino, and compressed regions are shown in ??.
1982 One can see the quite high purity of CRY in photon events from these plots.

Event with a W boson decaying leptonically via $W \rightarrow \ell\nu$ can also enter the signal region. In case, we use leptonically to include all leptons (e, μ, τ). The W +jetsevents passing the event selection either have a hadronically-decaying τ , where the neutrino is used as E_T^{miss} , or the case where a muon or electron is misidentified as a jet or missed completely due to the limited detector acceptance. To model this background, we use a sample of one-lepton events with a veto on b-jets, which we label CRW. The lepton is required to have $p_T > 27$ GeV to guarantee a fully efficient trigger. We then treat this single lepton as a jet for purposes of the RJR variable calculations. We apply a kinematic selection on the transverse mass:

$$m_T = \sqrt{2p_{T,\ell}E_T^{\text{miss}}(1 - \cos\phi_e - E_\phi^{\text{miss}})}, \quad (8.3)$$

1983 around the W mass: $30 \text{ GeV} < m_T < 100 \text{ GeV}$. Checks in simulation and experience
1984 from other analyses shows that these requirements give a sample of high purity $W \rightarrow$
1985 $\ell\nu$ background. Due to low statistics using the kinematic cuts imposed in the signal
1986 regions, the control region kinematic cuts are slightly loosened with respect to the
1987 signal region cuts. We use the loosest cut in any signal region as the control region
1988 selection for all signal regions. More clearly, the control region selection corresponding
1989 to each signal region is the *same*. As discussed above, this leads to a tolerable increase
1990 in the systematic uncertainty from the extrapolation from the CR to the SR when
1991 compared to the resulting statistical uncertainty.

1992 Distributions of CRW in squark, gluino, and compressed regions are shown in ??.

1993 There is high purity in W +jetsevents in the control region corresponding to all signal

1994 regions.

1995 Top events are also an important background, for the same reasons as the

1996 W +jetsbackground, due to the dominant top decay channel of $t \rightarrow Wb$. For a

1997 top event to be selected by the analysis criteria, as in the case of W +jets, we expect

1998 a W to decay via a τ lepton which decays hadronically or one a muon or electron to

1999 be misidentified as a jet or be outside the detector acceptance. We are not so worried

2000 about hadronic or all dileptonic tops: hadronic $t\bar{t}$ events generally have low E_T^{miss}

2001 (and $H_{1,1}^{PP}$) so they will not pass the kinematic cuts, while dileptonic $t\bar{t}$ events have a

2002 lower cross-section and good reconstruction efficiency from the two leptons. We are

2003 thus primarily concerned with semileptonic $t\bar{t}$ events with E_T^{miss} from the neutrino.

2004 To model this background, we use the same selection as the W selection, but require

2005 that one of the jets chosen by the analysis has at least one b -tag. This selection has

2006 quite high purity, as we expect the $t\bar{t}$ background to have two b -jets. Thus with

2007 the 70% b -tagging efficiency working point used in this analysis, ignoring (small)

2008 correlations between the two b -tags, we expect to tag one of the b -jets greater than

2009 90% of the time. As with CRW, we need to loosen the cuts applied to CRT with

2010 respect to the signal region in order to gain sufficient expected data statistics. We

2011 use exactly the same scheme; the CRT corresponding to each SR is identical, due to

2012 using the loosest set of cuts among the SRs. This comes at the cost of an increased

2013 systematic uncertainty for this extrapolation, but it was determined that this tradeoff

2014 resulted in the lowest overall uncertainty.

2015 Distributions of CRT in squark, gluino, and compressed regions are shown in ??.

2016 There is high purity in top events in the control region corresponding to all signal

2017 regions.

2018 The final important background is the QCD background. As briefly discussed in

2019 the previous chapter, QCD backgrounds are difficult, for a few reasons we describe
2020 here. The large cross-section for QCD events means that even very rare extreme
2021 mismeasurements can be seen in our signal regions. However, as these events are
2022 very rare, one requires extreme confidence in the tails of the distributions to use
2023 simulation as an input for background estimation. To avoid this, the strategy in
2024 these cases is to apply a strong enough cut to expect *zero* QCD events in the signal
2025 regions to avoid this issue. To produce a sample enriched in QCD, which we call CRQ,
2026 we reverse the Δ_{QCD} and $H_{1,1}^{PP}$ cuts. This analysis uses the jet smearing method, as
2027 described in [126]. This is a data-driven method which applies a resolution function
2028 to well-measured QCD events, which also an estimate of the impact of the jet energy
2029 mismeasurement on $E_{\text{T}}^{\text{miss}}$ and subsequently the RJR variables.

2030 Distributions of CRQ in squark, gluino, and compressed regions are shown in ??.
2031 There is high purity in top events in the control region corresponding to all signal
2032 regions.

2033 The final background of note in this background is the diboson background. This
2034 background is estimated directly from simulation. Due to the low cross-section of
2035 electroweak processes, this background is not significant in the signal regions. We
2036 assign a large ad-hoc 50% systematic on the cross-section, and do not attempt to
2037 define a control region for this background.

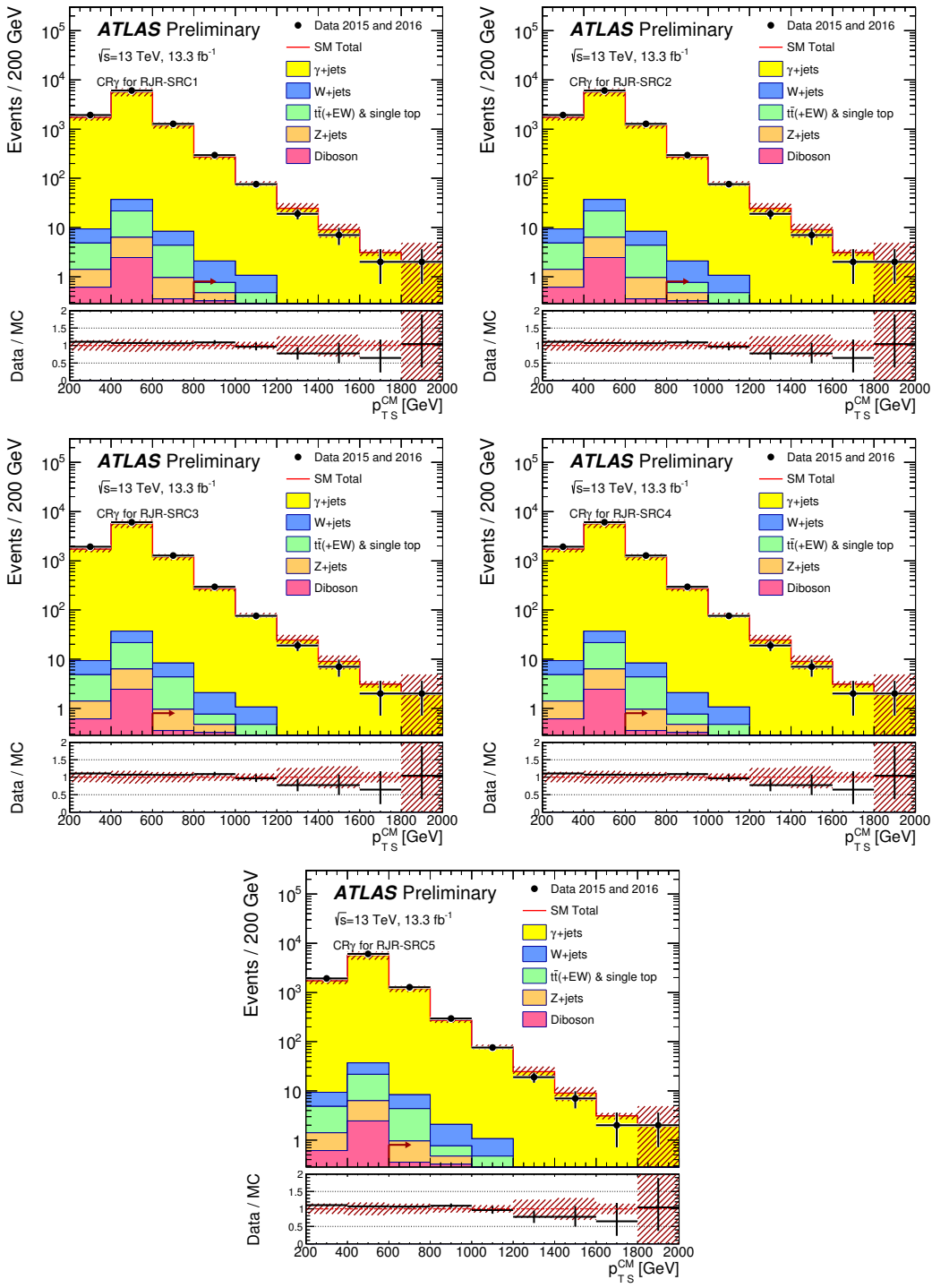


Figure 8.4: Scale variable distributions for the compressed CRY regions.

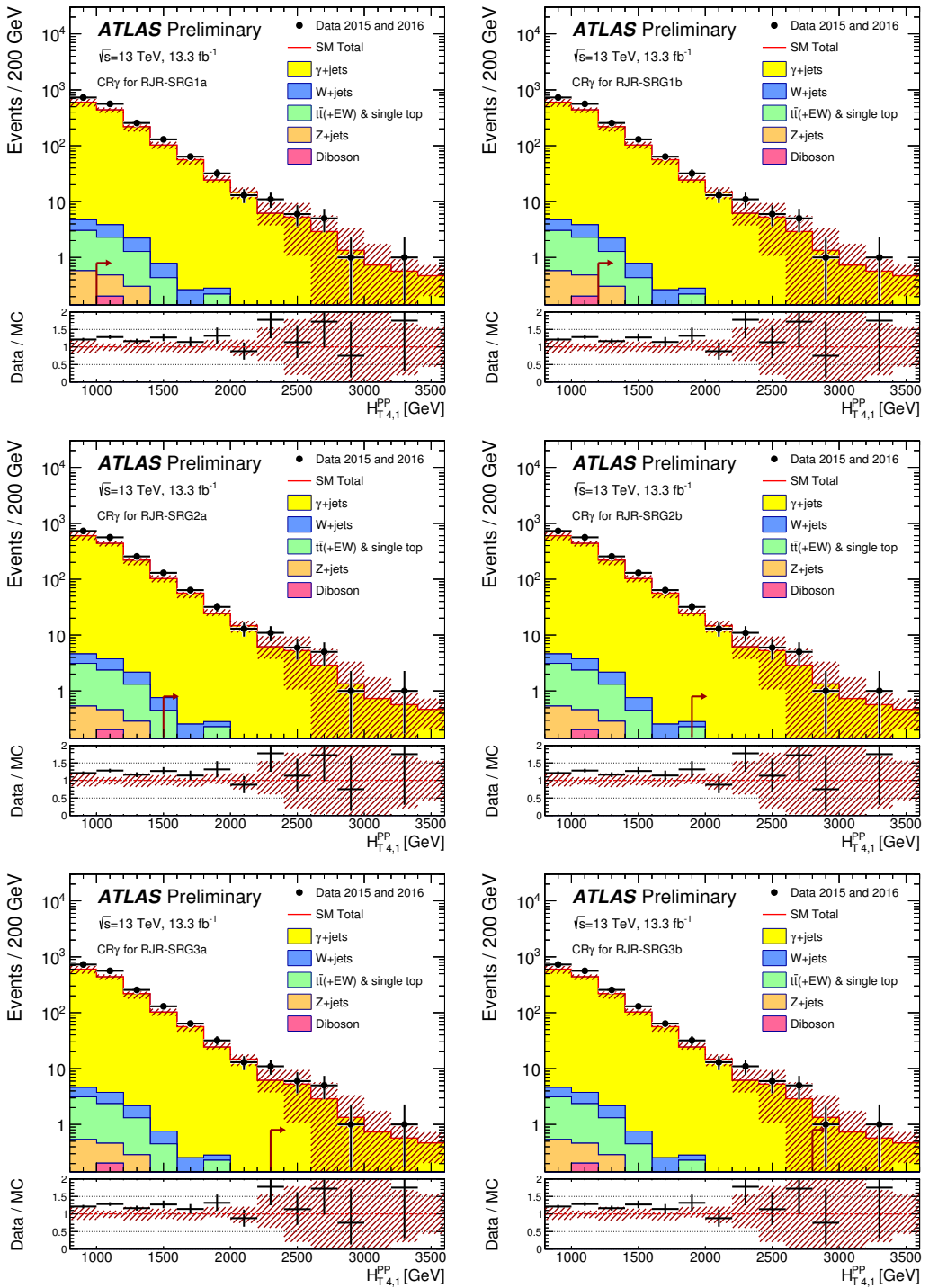


Figure 8.5: Scale variable distributions for the gluino CRY regions.

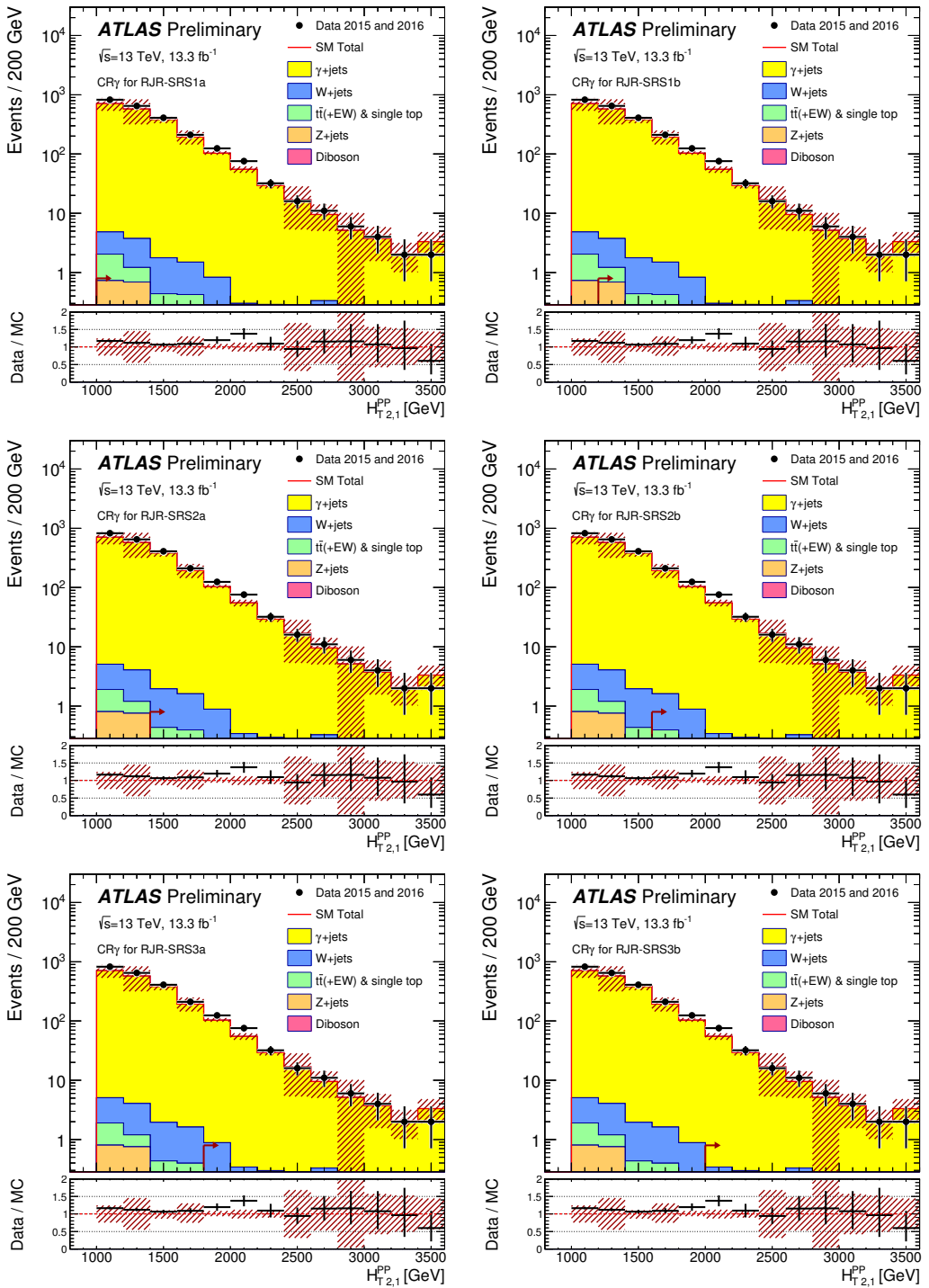


Figure 8.6: Scale variable distributions for the squark CRY regions.

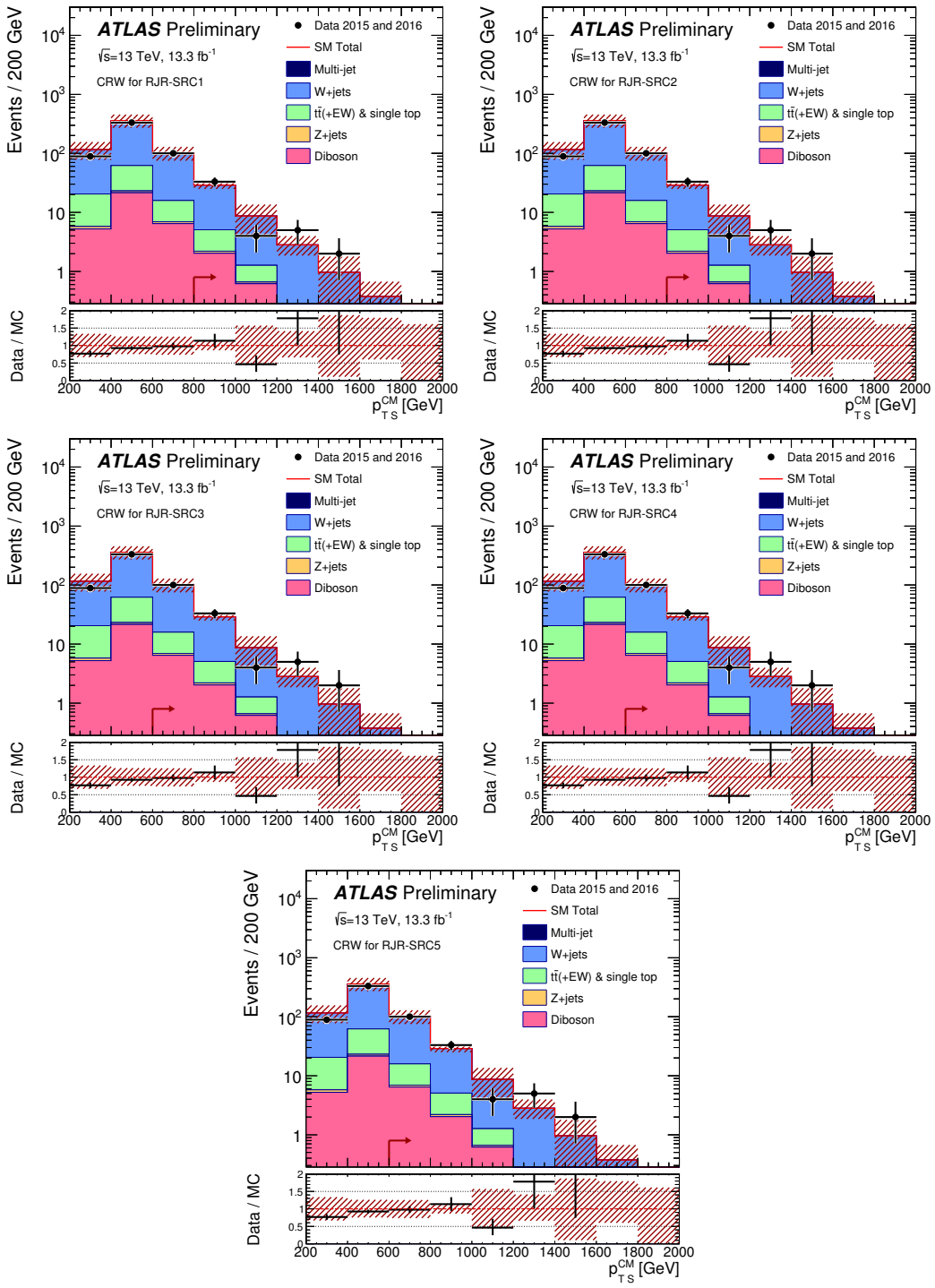


Figure 8.7: Scale variable distributions for the compressed CRW regions.

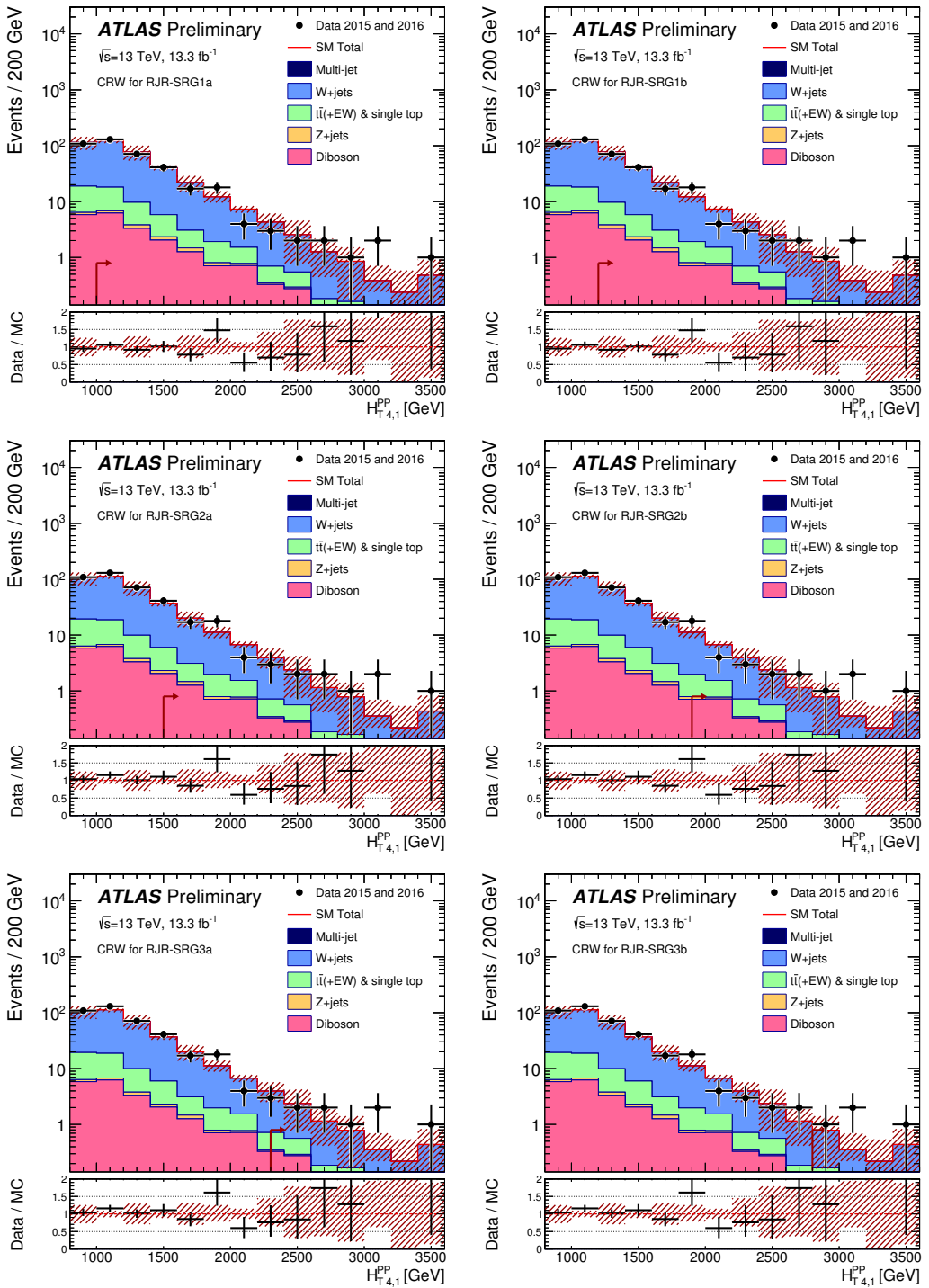


Figure 8.8: Scale variable distributions for the gluino CRW regions.

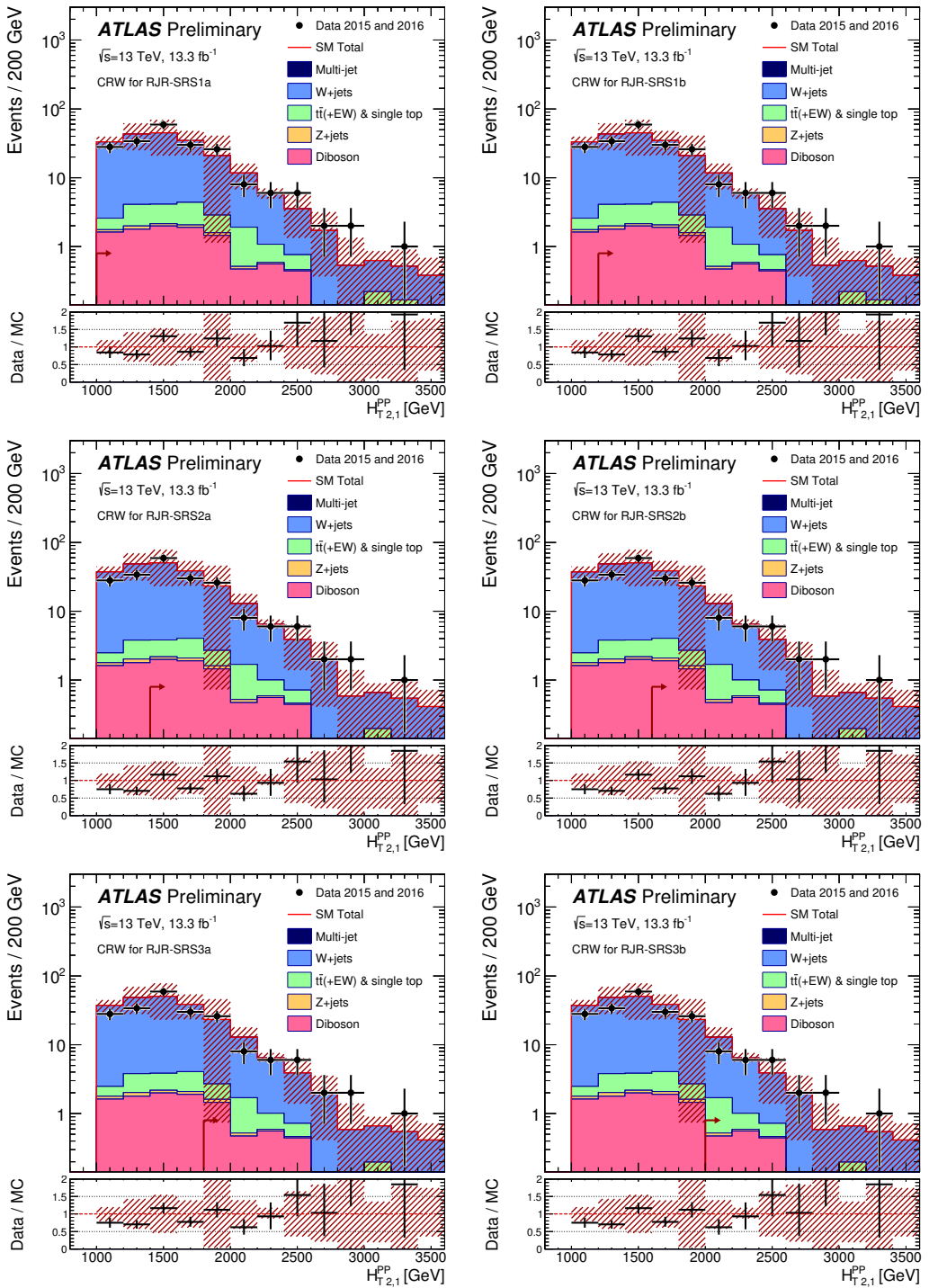


Figure 8.9: Scale variable distributions for the squark CRW regions.

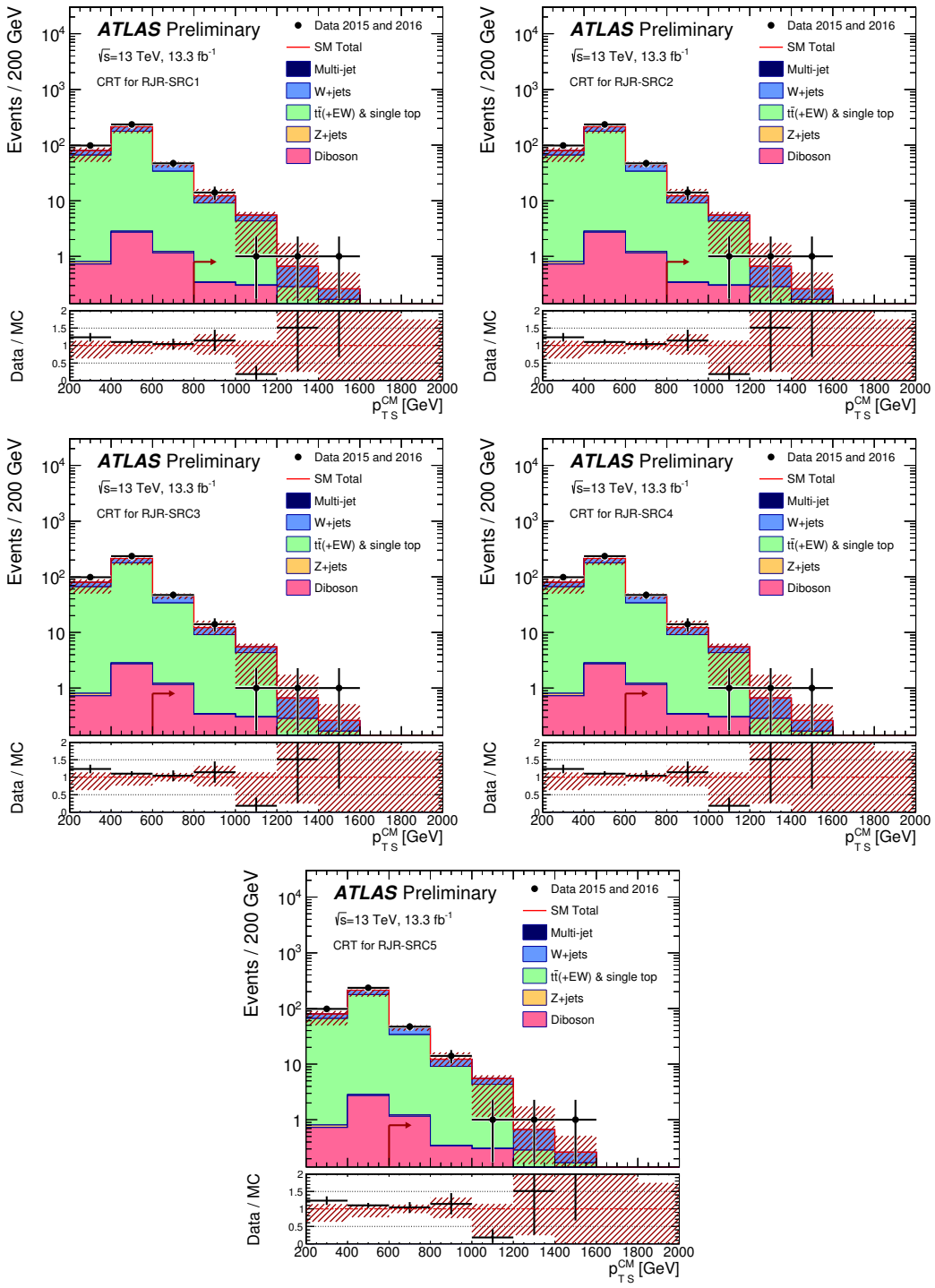


Figure 8.10: Scale variable distributions for the compressed CRT regions.

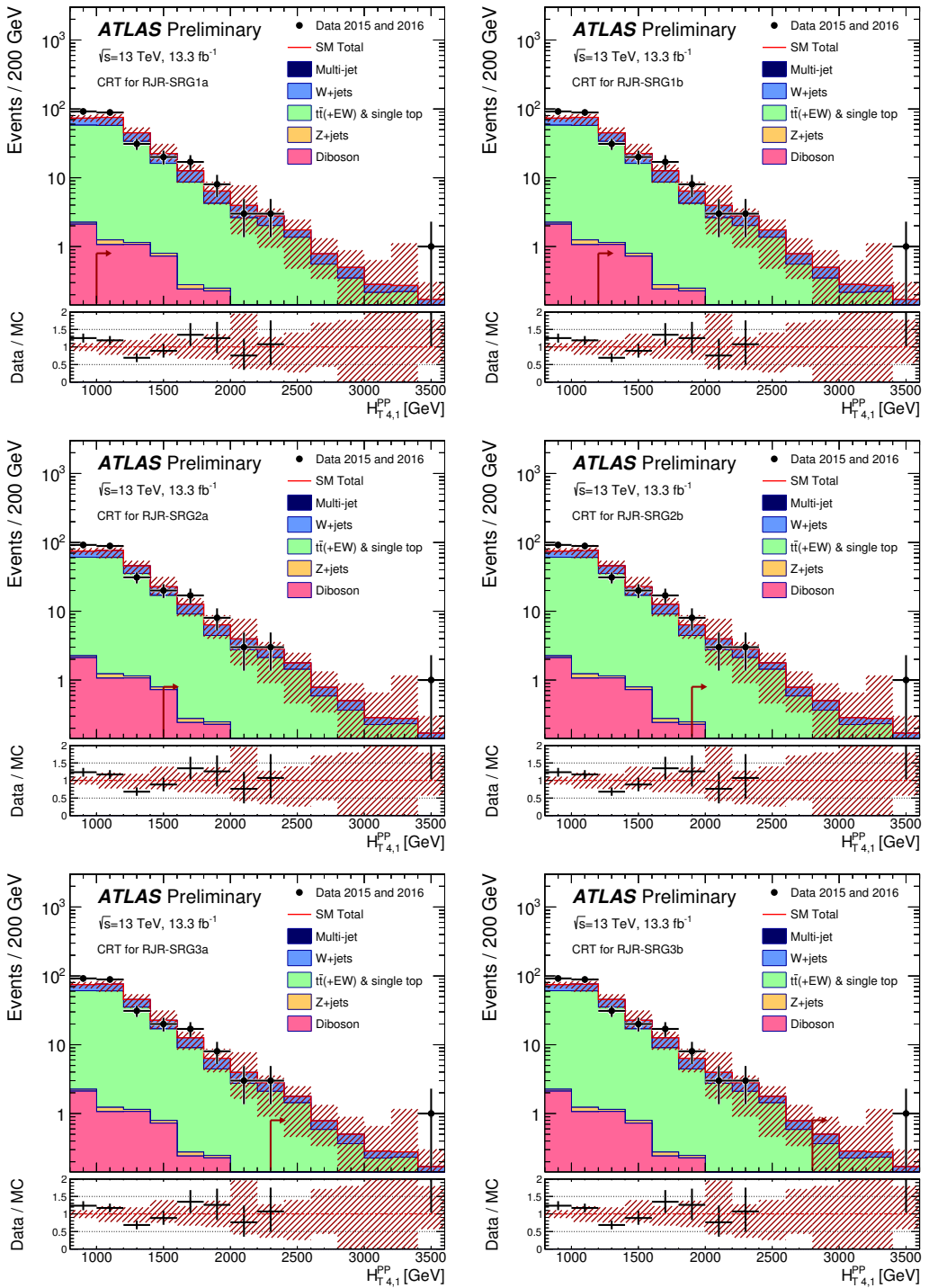


Figure 8.11: Scale variable distributions for the gluino CRT regions.

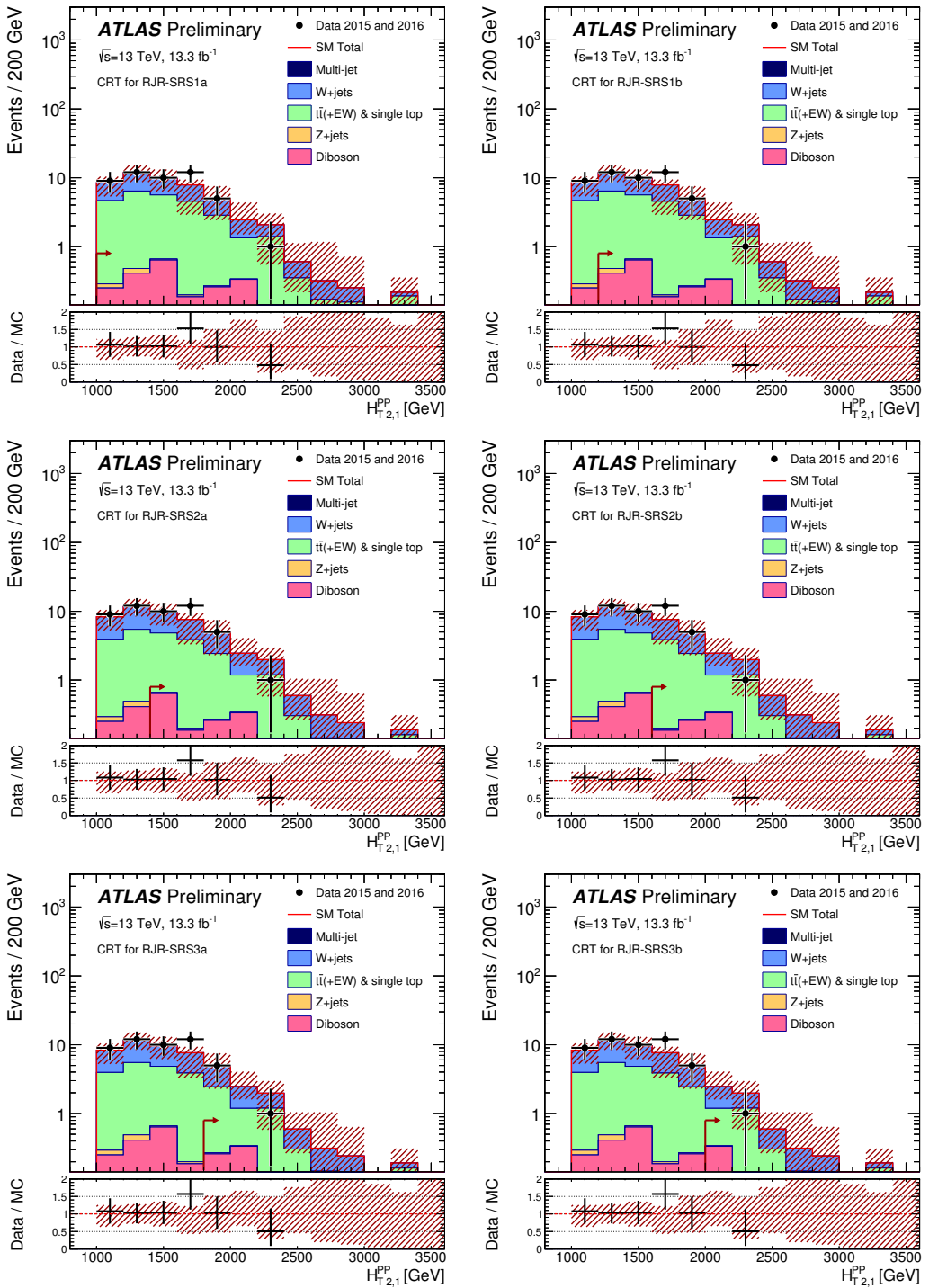


Figure 8.12: Scale variable distributions for the squark CRT regions.

2038 **Validation Regions**

2039 As discussed in general terms above, we define a set of validation regions to ensure
2040 we can properly model the particular backgrounds as we move closer to the SRs in
2041 phase space. We define at least one validation region for each major background.

2042 For the most important background $Z \rightarrow \nu\nu$, we use a series of validation regions.
2043 The primary validation region, which we label as VRZ, is defined by selection lepton
2044 pairs of opposite sign and identical flavor which lie with 25 GeV of the Z boson mass.
2045 This selection has high purity for $Z \rightarrow \ell\ell$ events as seen in simulation. We treat the
2046 two leptons as contributions to the E_T^{miss} (as we did with the photon in CRY). This
2047 selection uses the same kinematic cuts as the signal region. We also define two VRs
2048 using the same event selection but looser kinematic cuts, which we label VRZa and
2049 VRZb. VRZa has a loosened selection on $H_{1,1}^{PP}$, again to the loosest value among the
2050 signal regions, as was done for CRW and CRt. VRZa has a loosened selection on
2051 the primary scaleful variable ($H_{T,2,1}^{PP}$ or $H_{T,4,1}^{PP}$), again to the loosest value among the
2052 signal regions, as was done for CRW and CRT. These two validation regions allow use
2053 to test the modeling of each of these variables individually, as well as allowing more
2054 validation region statistics in the signal regions with tighter cuts on these variables.

2055 For the compressed regions, these Z validation region were found lacking. The
2056 leptons are highly boosted in the compressed case, and the lepton acceptance was
2057 quite low due to lepton isolation requirements in ΔR . Instead, two fully hadronic
2058 validation region were developed for the compressed regions. The first, VRZc has
2059 identical requirements to the signal regions with an inverted requirement on $\Delta\phi_{ISR,I}$.
2060 From simulation, this region was found to be at least 50% pure in Z events, which
2061 was considered enough to validate this background in this extreme portion of phase
2062 space. For additional validation region statistics, we also developed VRZca, which
2063 takes again uses the loosest set of cuts from each signal region. Note this means that
2064 each compressed signal region has an identical VRZca.

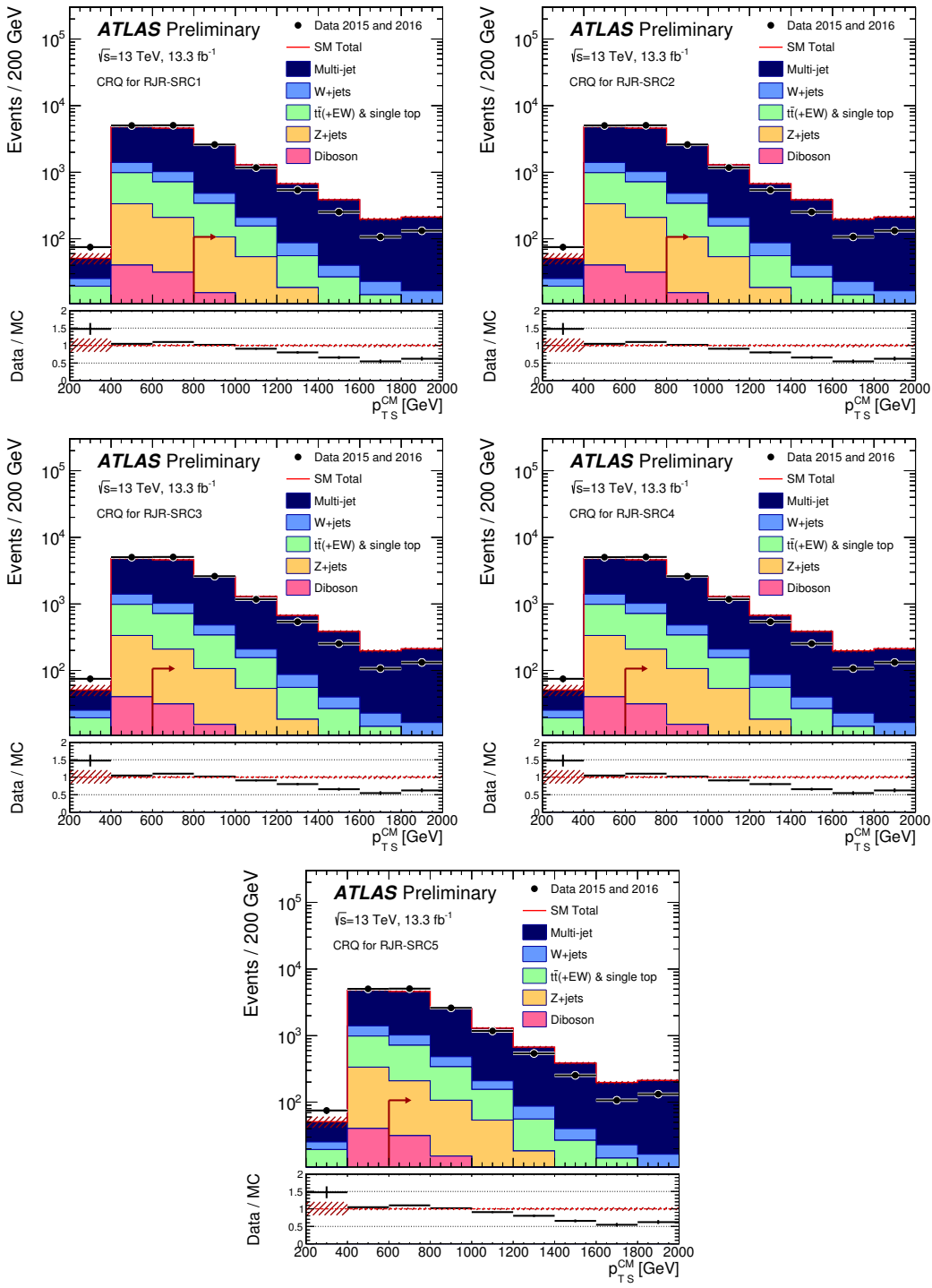


Figure 8.13: Scale variable distributions for the compressed CRQ regions.

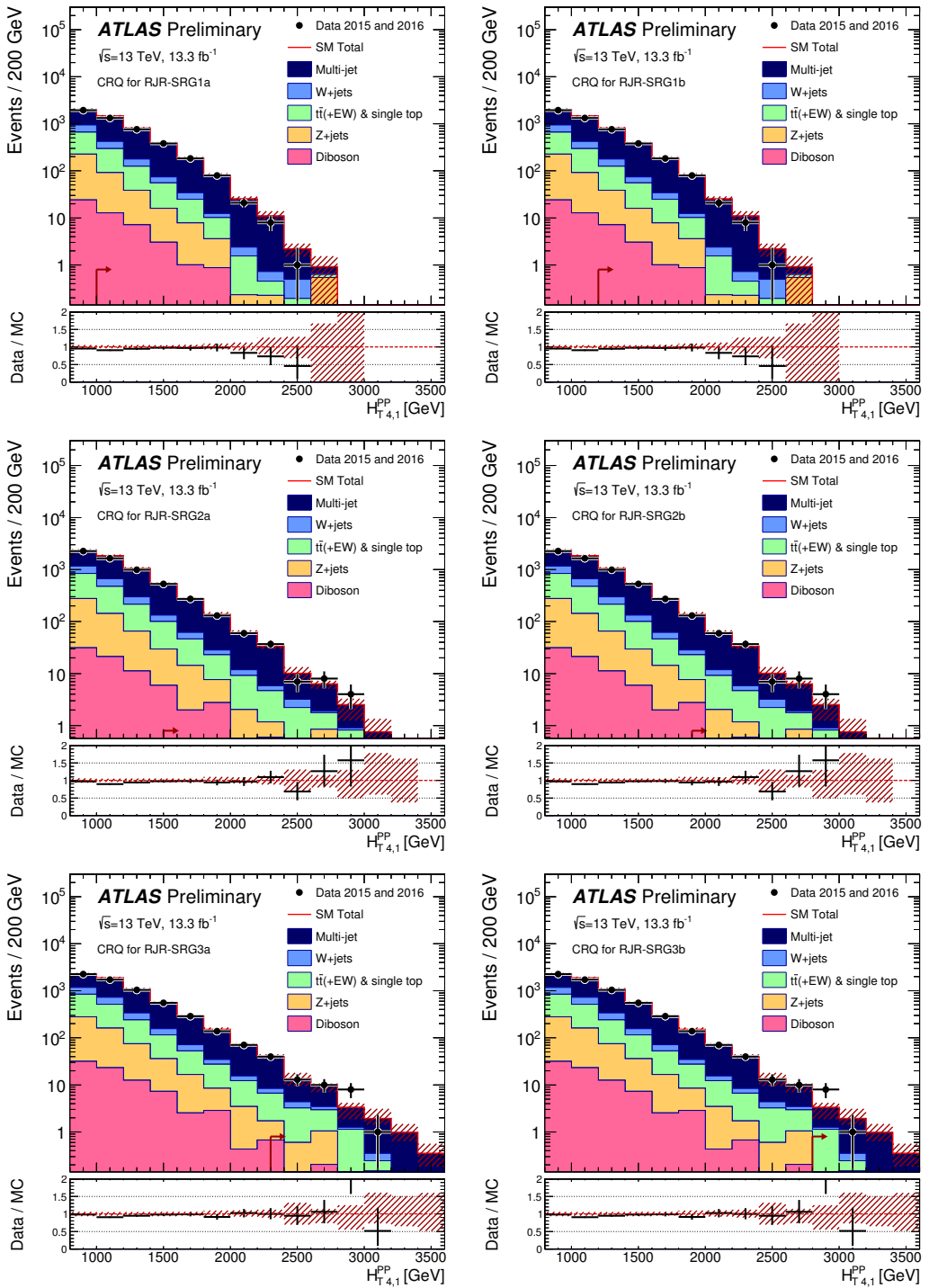


Figure 8.14: Scale variable distributions for the gluino CRQ regions.

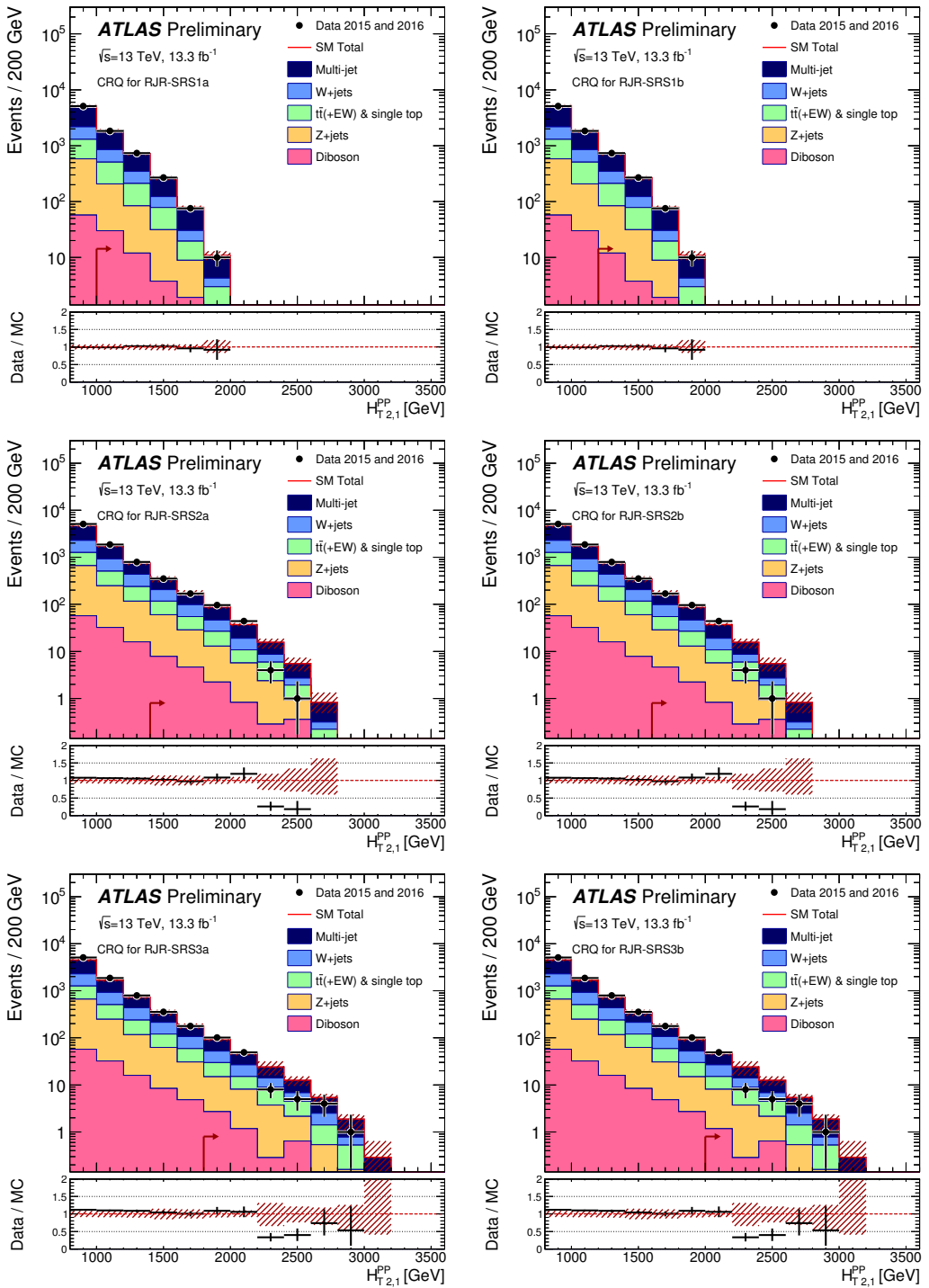


Figure 8.15: Scale variable distributions for the squark CRQ regions.

2065 The top and W validation regions use the same event selection as the correspond-
 2066 ing control regions, as described above. However, unlike the control regions, these
 2067 validation regions reimpose the SR scaleful variable selections, to be closer in phase
 2068 space to the hadronic signal regions. In the same way as we did for VRZa and
 2069 VRZb, we also define auxiliary VRs which loosen the cuts on the scale variables. We
 2070 define VRTa (VRWa) as VRT (VRW) with the same loosened cut on $H_{1,1}^{PP}$ and VRTb
 2071 (VRWb) as VRT (VRW) with the same loosened cut on the primary scale variable.

2072 The final set of validation regions are those defined to check the estimation of
 2073 the QCD background. VRQ is defined to be identical to the corresponding CRQ,
 2074 but again we use the full SR region cuts for the scaleful variables. This selection is
 2075 then closer to the corresponding signal region to validate the CRQ estimate. We also
 2076 define the auxiliary validation regions VRQa and VRQb for the noncompressed signal
 2077 regions. In this case, we reimpose one of the two inverted cuts in CRQ with respect
 2078 to the signal regions, to make each one even closer to the SRs. In CRQa (CRQb), we
 2079 reimpose the $H_{1,1}^{PP}$ (Δ_{QCD}).

2080 For the compressed case, we again define a separate validation region, due to
 2081 the special kinematics probed. We construct a validation region which is the same as
 2082 CRQ, with $.5 < R_{\text{ISR}} < R_{\text{ISR, SR}}$, where $R_{\text{ISR, SR}}$ is the cut on R_{ISR} in the corresponding
 2083 SR. Again, this can be seen as probing “in between” the CR and SR in phase space.

The results of this validation can be seen in ???. Each bin is the validation region
 corresponding to a particular signal region. This value is known as the pull, defined
 as

$$\text{Pull} = \frac{N_{\text{obs}} - N_{\text{pred}}}{\sigma_{\text{tot}}}. \quad (8.4)$$

2084 where σ_{tot} is the total uncertainty folding in all systematic uncertainties, which we
 2085 will describe later. Assuming we have well-measured our backgrounds, we expect a
 2086 Gaussian distribution of the pulls around 0, with a standard deviation of 1, as this is
 2087 measuring the number of standard deviations around the mean.

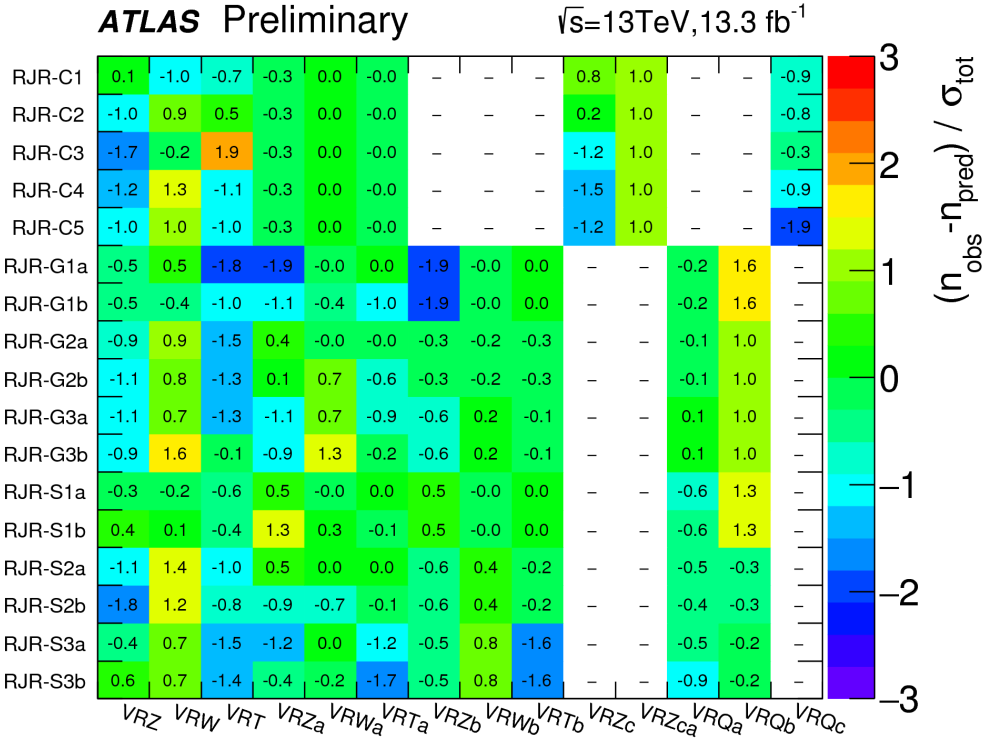


Figure 8.16: Summary of the validation region pulls

2088 Systematic Uncertainties

2089 In this section, we discuss the uncertainties considered. These generally fall into
 2090 four categories: theoretical generator uncertainties, uncertainties on the CR to SR
 2091 extrapolations, uncertainties on the data-driven transfer factor corrections, and object
 2092 reconstruction uncertainties. We discuss each of these categories here. A table
 2093 summarizing this section is in 8.5

Systematic	Uncertainty Description
alpha_GeneratorZ	Theoretical on Z cross-section
alpha_generatorW	Theoretical on W cross-section
alpha_generatorTop	Theoretical on t cross-section
alpha_radiationTop	Theoretical on t radiation tune
alpha_Pythia8Top	Theoretical on t fragmentation tune
alpha_FlatDiboson	Flat on diboson cross-section
mu_Zjets	CRY extrapolation to SR
mu_Wjets	CRW extrapolation to SR
mu_Top	CRT extrapolation to SR
mu_Multijets	CRQ extrapolation to SR
alpha_Kappa	κ factor
alpha_QCDError	Jet smearing
alpha_JET_GroupedNP_1	JES NP group 1
alpha_JET_GroupedNP_2	JES NP group 2
alpha_JET_GroupedNP_3	JES NP group 3
alpha_JER	JER
alpha_MET_SoftTrk_ResoPerp	Soft E_T^{miss} resolution perpendicular to hard object system
alpha_MET_SoftTrk_ResoPara	Soft E_T^{miss} resolution parallel to hard object system
alpha_MET_SoftTrk_Scale	Soft E_T^{miss} scale

Table 8.5: Description of the systematic uncertainties in the analysis.

2094 The theoretical generator uncertainties are evaluated by using alternative sim-
 2095 ulation samples or varying scale uncertainties. In the case of the $Z+jets$ and
 2096 $W+jets$ backgrounds, the related theoretical uncertainties are estimated by varying
 2097 the renormalization, factorization, and resummation scales by two, and decreasing
 2098 the nominal CKKW matching scale by 5 GeV and 10 GeV respectively. In the
 2099 case of $t\bar{t}$ production, we compare the nominal Powheg-Box generator with
 2100 MG5_aMC@NLO, as well as comparing different radiation and generator tunes. As
 2101 stated above, we account for the uncertainty on the small diboson background by
 2102 imposition of a flat 50% uncertainty.

2103 The CR to SR extrapolation uncertainties, or what could be called the transfer

2104 factor uncertainties, are listed in 8.5 as μ_{-} . There is one normalization factor μ
2105 for each major background, and its uncertainty is often a dominant one for many
2106 backgrounds. This uncertainty is generally dominated by the statistical uncertainty
2107 in the CR.

2108 There are two uncertainties from the data-driven corrections to the transfer
2109 factors. The first is the uncertainty on κ , which is measured using an auxiliary $Z \rightarrow \ell\ell$
2110 control region. This is labeled alpha_Kappa. The other is the uncertainty is that
2111 assigned to the jet smearing method, which is seen in the table as alpha_QCDError.

2112 The final set of uncertainties are those related to object reconstruction. In the
2113 case of the hadronic search presented, the important uncertainties are those assigned
2114 to the jet energy and E_T^{miss} . The uncertainties on the lepton reconstruction and
2115 b -tagging uncertainties were found to be negligible in all SRs. The measurement
2116 of the jet energy scale (JES) uncertainty is quite complicated, and described in
2117 [Aad:2011he, Aad:2012vm, 127]. After a complicated procedure to decorrelate
2118 the various components of the JES uncertainty, there are three components which
2119 remain, which are labeled as alpha_JET_GroupedNP_1,2,3. The jet energy resolution
2120 uncertainty is estimated using the methods discussed in Refs. [Aad:2012ag, 127],
2121 and is labeled alpha_JER.

2122 The E_T^{miss} soft term uncertainties are described in [112, 113, 128]. The
2123 uncertainty on the E_T^{miss} soft term resolution is parameterized into a component
2124 parallel to direction of the rest of the event (the sum of the hard objects p_T)
2125 and a component perpendicular to this direction. There is also an uncertainty
2126 on the E_T^{miss} soft term scale. These are labeled as alpha_MET_SoftTrk_ResoPara,
2127 alpha_MET_SoftTrk_ResoPerp, and alpha_MET_SoftTrk_Scale.

2128 **Fitting procedure**

2129 In this section, we describe the fitting procedure employed, which properly accounts
2130 for the correlations between the uncertainties through the use of a likelihood fit as
2131 described in ???. We use three classes of likelihood fits: *background-only*, *model-*
2132 *independent*, and *model-dependent* fits. The background-only fits estimate the
2133 background yields in each signal region. These fits use only the control region event
2134 yields as inputs; they do not include the information from the signal regions besides
2135 the simulation event yield. The cross-contamination between CRs is also fit by this
2136 procedure. The systematic uncertainties described in the previous section are used as
2137 nuisance parameters. This background only fit also estimates the background event
2138 yields in the validation regions. When designing the analysis (before unblinding
2139 the signal regions), checking the validation region agreement is the primary way to
2140 validate the consistency and accuracy of the background estimation procedure.

2141 In the case no excess is observed, we use a model-independent fit to set upper
2142 limits on the possible number of possible beyond the Standard Model events in each
2143 SR. The fitting procedure has one difference from the background-only fit: we add the
2144 number of observed events as an input to the fit, and we fit the signal strength as a new
2145 non-negative free parameter. Using the CL_S [129] and neglecting the possible (small)
2146 signal contamination in control regions, we derive the the observed and expected
2147 limits on the number of events from BSM phenomena in each signal region.

2148 Model-dependent fits are used to set exclusion limits on the specific SUSY
2149 models considered in this thesis, particular the gluino or squark pair production
2150 with various mass splittings. This can be seen as identical to the background-only
2151 fit with an additional simulation input from the particular model of interest, with
2152 its corresponding systematic uncertainties from detector effects account for as in the
2153 background-only fit.

Title of Chapter 1

2156 Here you can write some introductory remarks about your chapter. I like to give each
2157 sentence its own line.

2158 When you need a new paragraph, just skip an extra line.

2159 **9.1 Statistical Analysis**

2160 maybe to be moved to an appendix

2161 **9.2 Signal Region distributions**

2162 **Scale variable distributions in the signal regions**

2163 In ??, we can see the distributions of the last scale cut used for each signal region.
2164 These distributions include scale factors derived via the fitting procedure which are
2165 applied to the Standard Model background, which we will describe later in this
2166 chapter. These scale factors are all ~ 1 . The systematic uncertainties, shown in
2167 the banded stripe, are also described later in this section. Each plot shows the
2168 distribution from a signal model which is targetted by the given signal region.

2169 These distributions have all cuts applied except for the cut on this scale variable,
2170 which allows us to see the additional discrimination provided by the given variable.
2171 Since signal regions with the same numeral have identical cuts on all cuts other than
2172 the main scale variable, we show (a) and (b) on the same figure. The left-most (right-

2173 most) arrow shown is the location of the a (b) cut applied in the analysis. We call
2174 these plot $N - 1$ plots, where N refers to the number of cuts applied in the analysis.
2175 The full set of $N - 1$ plots in the signal regions for the other variables used in the
2176 analysis are shown in 9.5. We can see that for the signal models targeted by each
2177 signal region, each cut provides unique discrimination against the Standard Model
2178 backgrounds.

2179 **9.3 Pull Plots**

2180 **9.4 Exclusion plots**

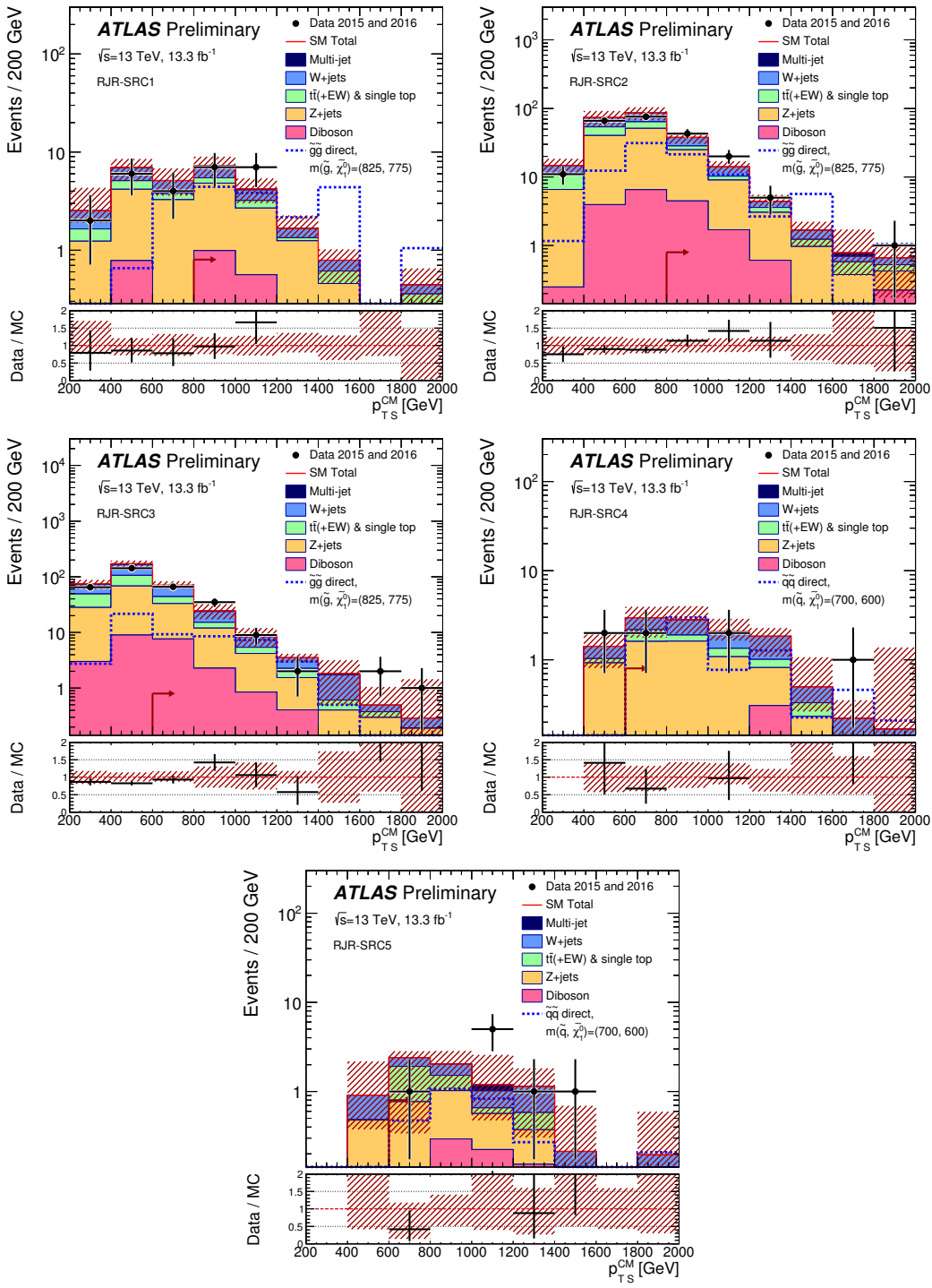


Figure 9.1: Scale variable distributions for the compressed signal regions.

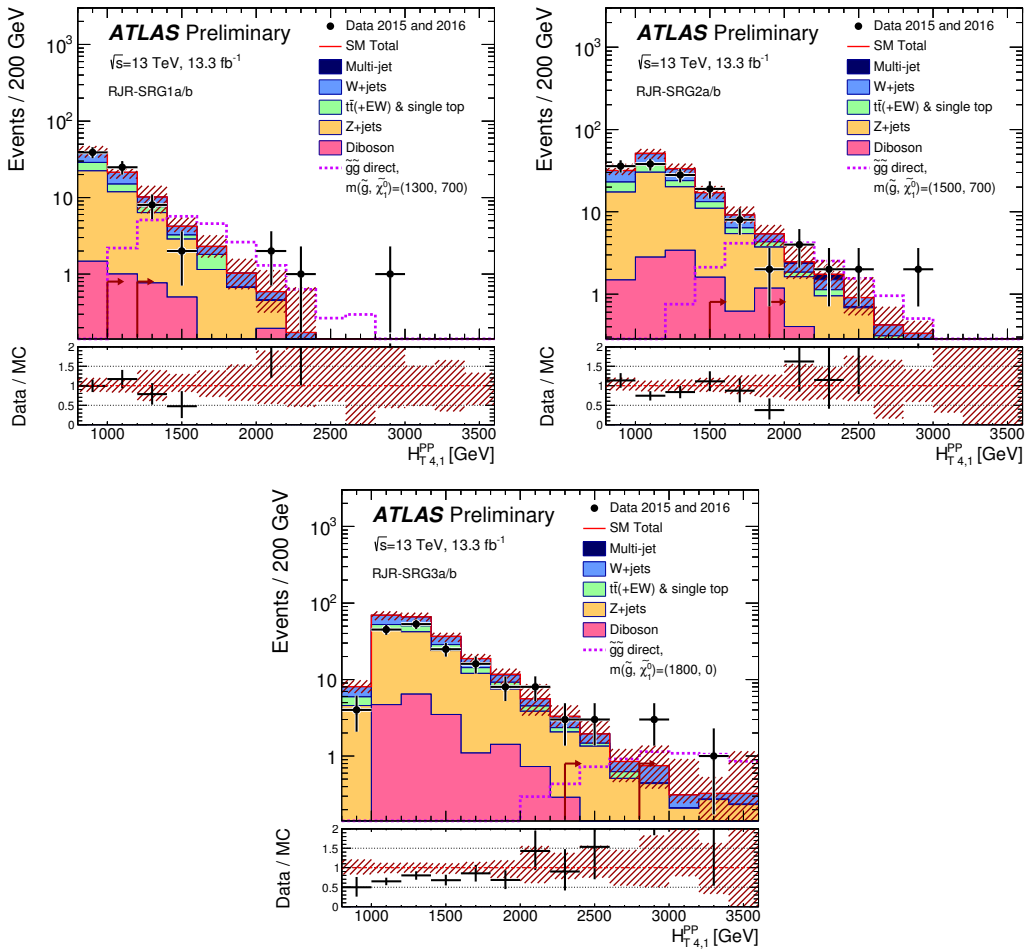


Figure 9.2: Scale variable distributions for the gluino signal regions.

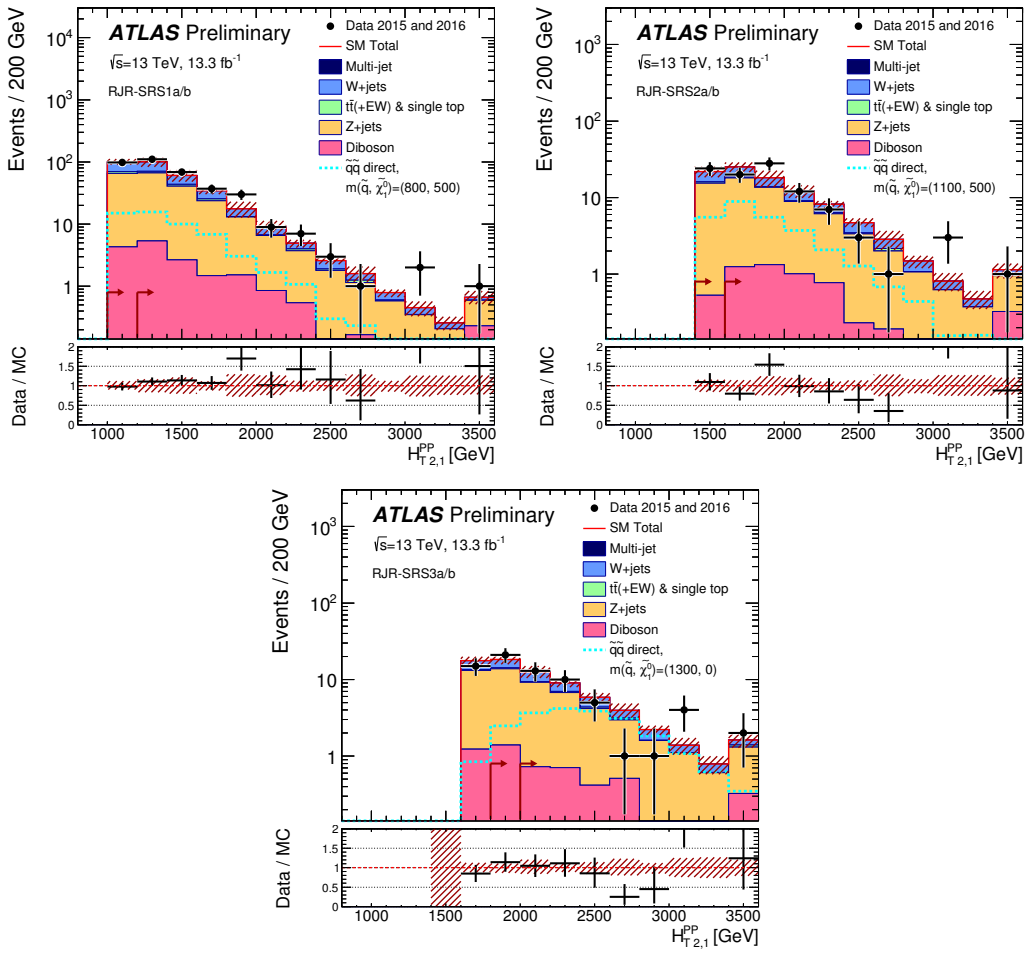


Figure 9.3: Scale variable distributions for the squark signal regions.

2181

Conclusion

2182 Here you can write some introductory remarks about your chapter. I like to give each
2183 sentence its own line.

2184 When you need a new paragraph, just skip an extra line.

2185 **9.5 New Section**

2186 By using the asterisk to start a new section, I keep the section from appearing in the
2187 table of contents. If you want your sections to be numbered and to appear in the
2188 table of contents, remove the asterisk.

2189

Bibliography

- 2190 [1] O. Perdereau, *Planck 2015 cosmological results*,
2191 AIP Conf. Proc. **1743** (2016) p. 050014.
- 2192 [2] N. Aghanim et al.,
2193 *Planck 2016 intermediate results. LI. Features in the cosmic microwave*
2194 *background temperature power spectrum and shifts in cosmological parameters*
2195 (2016), arXiv: [1608.02487 \[astro-ph.CO\]](https://arxiv.org/abs/1608.02487).
- 2196 [3] J. S. Schwinger,
2197 *On Quantum electrodynamics and the magnetic moment of the electron*,
2198 Phys. Rev. **73** (1948) p. 416.
- 2199 [4] S. Laporta and E. Remiddi,
2200 *The Analytical value of the electron (g-2) at order alpha**3 in QED*,
2201 Phys. Lett. **B379** (1996) p. 283, arXiv: [hep-ph/9602417 \[hep-ph\]](https://arxiv.org/abs/hep-ph/9602417).
- 2202 [5] S. Schael et al., *Precision electroweak measurements on the Z resonance*,
2203 Phys. Rept. **427** (2006) p. 257, arXiv: [hep-ex/0509008 \[hep-ex\]](https://arxiv.org/abs/hep-ex/0509008).
- 2204 [6] S. L. Glashow, *Partial Symmetries of Weak Interactions*,
2205 Nucl. Phys. **22** (1961) p. 579.
- 2206 [7] S. Weinberg, *A Model of Leptons*, Phys. Rev. Lett. **19** (1967) p. 1264.
- 2207 [8] A. Salam, *Weak and Electromagnetic Interactions*,
2208 Conf. Proc. **C680519** (1968) p. 367.
- 2209 [9] M. Gell-Mann, *A Schematic Model of Baryons and Mesons*,
2210 Phys. Lett. **8** (1964) p. 214.
- 2211 [10] G. Zweig, “An SU(3) model for strong interaction symmetry and its
2212 breaking. Version 2,” *DEVELOPMENTS IN THE QUARK THEORY OF*
2213 *HADRONS. VOL. 1. 1964 - 1978*, ed. by D. Lichtenberg and S. P. Rosen,
2214 1964 p. 22,
2215 URL: <http://inspirehep.net/record/4674/files/cern-th-412.pdf>.

- 2216 [11] S. Weinberg, *Implications of Dynamical Symmetry Breaking*,
2217 Phys. Rev. **D13** (1976) p. 974.
- 2218 [12] S. Weinberg, *Implications of Dynamical Symmetry Breaking: An Addendum*,
2219 Phys. Rev. **D19** (1979) p. 1277.
- 2220 [13] E. Gildener, *Gauge Symmetry Hierarchies*, Phys. Rev. **D14** (1976) p. 1667.
- 2221 [14] L. Susskind, *Dynamics of Spontaneous Symmetry Breaking in the*
2222 *Weinberg-Salam Theory*, Phys. Rev. **D20** (1979) p. 2619.
- 2223 [15] S. P. Martin, “A Supersymmetry Primer,” 1997,
2224 eprint: [arXiv:hep-ph/9709356](https://arxiv.org/abs/hep-ph/9709356).
- 2225 [16] V. C. Rubin and W. K. Ford Jr., *Rotation of the Andromeda Nebula from a*
2226 *Spectroscopic Survey of Emission Regions*, Astrophys. J. **159** (1970) p. 379.
- 2227 [17] M. S. Roberts and R. N. Whitehurst,
2228 “*The rotation curve and geometry of M31 at large galactocentric distances*,
2229 Astrophys. J. **201** (1970) p. 327.
- 2230 [18] V. C. Rubin, N. Thonnard, and W. K. Ford Jr.,
2231 *Rotational properties of 21 SC galaxies with a large range of luminosities and*
2232 *radii, from NGC 4605 /R = 4kpc/ to UGC 2885 /R = 122 kpc/*,
2233 Astrophys. J. **238** (1980) p. 471.
- 2234 [19] V. C. Rubin et al., *Rotation velocities of 16 SA galaxies and a comparison of*
2235 *Sa, Sb, and SC rotation properties*, Astrophys. J. **289** (1985) p. 81.
- 2236 [20] A. Bosma,
2237 *21-cm line studies of spiral galaxies. 2. The distribution and kinematics of*
2238 *neutral hydrogen in spiral galaxies of various morphological types.*,
2239 Astron. J. **86** (1981) p. 1825.
- 2240 [21] M. Persic, P. Salucci, and F. Stel, *The Universal rotation curve of spiral*
2241 *galaxies: 1. The Dark matter connection*,
2242 Mon. Not. Roy. Astron. Soc. **281** (1996) p. 27,
2243 arXiv: [astro-ph/9506004](https://arxiv.org/abs/astro-ph/9506004) [astro-ph].
- 2244 [22] M. Lisanti, “Lectures on Dark Matter Physics,” 2016,
2245 eprint: [arXiv:1603.03797](https://arxiv.org/abs/1603.03797).
- 2246 [23] H. Miyazawa, *Baryon Number Changing Currents*,
2247 Prog. Theor. Phys. **36** (1966) p. 1266.

- 2248 [24] J.-L. Gervais and B. Sakita, *Generalizations of dual models*,
 2249 *Nucl. Phys.* **B34** (1971) p. 477.
- 2250 [25] J.-L. Gervais and B. Sakita,
 2251 *Field Theory Interpretation of Supergauges in Dual Models*,
 2252 *Nucl. Phys.* **B34** (1971) p. 632.
- 2253 [26] Yu. A. Golfand and E. P. Likhtman, *Extension of the Algebra of Poincare
 2254 Group Generators and Violation of p Invariance*,
 2255 *JETP Lett.* **13** (1971) p. 323, [*Pisma Zh. Eksp. Teor. Fiz.* **13**, 452 (1971)].
- 2256 [27] A. Neveu and J. H. Schwarz, *Factorizable dual model of pions*,
 2257 *Nucl. Phys.* **B31** (1971) p. 86.
- 2258 [28] A. Neveu and J. H. Schwarz, *Quark Model of Dual Pions*,
 2259 *Phys. Rev.* **D4** (1971) p. 1109.
- 2260 [29] D. V. Volkov and V. P. Akulov, *Is the Neutrino a Goldstone Particle?*
 2261 *Phys. Lett.* **B46** (1973) p. 109.
- 2262 [30] J. Wess and B. Zumino,
 2263 *A Lagrangian Model Invariant Under Supergauge Transformations*,
 2264 *Phys. Lett.* **B49** (1974) p. 52.
- 2265 [31] A. Salam and J. A. Strathdee, *Supersymmetry and Nonabelian Gauges*,
 2266 *Phys. Lett.* **B51** (1974) p. 353.
- 2267 [32] S. Ferrara, J. Wess, and B. Zumino, *Supergauge Multiplets and Superfields*,
 2268 *Phys. Lett.* **B51** (1974) p. 239.
- 2269 [33] J. Wess and B. Zumino, *Supergauge Transformations in Four-Dimensions*,
 2270 *Nucl. Phys.* **B70** (1974) p. 39.
- 2271 [34] J. D. Lykken, “Introduction to supersymmetry,” *Fields, strings and duality. Proceedings, Summer School, Theoretical Advanced Study Institute in Elementary Particle Physics, TASI’96, Boulder, USA, June 2-28, 1996*, 1996
 2272 p. 85, arXiv: [hep-th/9612114](https://arxiv.org/abs/hep-th/9612114) [hep-th],
 2273 URL: http://lss.fnal.gov/cgi-bin/find_paper.pl?pub=96-445-T.
- 2276 [35] A. Kobakhidze, “Intro to SUSY,” 2016, URL: <https://indico.cern.ch/event/443176/page/5225-pre-susy-programme>.
- 2278 [36] G. R. Farrar and P. Fayet, *Phenomenology of the Production, Decay, and
 2279 Detection of New Hadronic States Associated with Supersymmetry*,
 2280 *Phys. Lett.* **B76** (1978) p. 575.

- 2281 [37] ATLAS Collaboration,
 2282 *Search for the electroweak production of supersymmetric particles in*
 2283 $\sqrt{s} = 8 \text{ TeV}$ *pp collisions with the ATLAS detector,*
 2284 *Phys. Rev. D* **93** (2016) p. 052002, arXiv: [1509.07152 \[hep-ex\]](#).
- 2285 [38] ATLAS Collaboration, *Summary of the searches for squarks and gluinos*
 2286 *using $\sqrt{s} = 8 \text{ TeV}$ pp collisions with the ATLAS experiment at the LHC,*
 2287 *JHEP* **10** (2015) p. 054, arXiv: [1507.05525 \[hep-ex\]](#).
- 2288 [39] ATLAS Collaboration, *ATLAS Run 1 searches for direct pair production of*
 2289 *third-generation squarks at the Large Hadron Collider,*
 2290 *Eur. Phys. J. C* **75** (2015) p. 510, arXiv: [1506.08616 \[hep-ex\]](#).
- 2291 [40] CMS Collaboration, *Search for supersymmetry with razor variables in pp*
 2292 *collisions at $\sqrt{s} = 7 \text{ TeV}$, Phys. Rev. D* **90** (2014) p. 112001,
 2293 arXiv: [1405.3961 \[hep-ex\]](#).
- 2294 [41] CMS Collaboration, *Inclusive search for supersymmetry using razor variables*
 2295 *in pp collisions at $\sqrt{s} = 7 \text{ TeV}$, Phys. Rev. Lett.* **111** (2013) p. 081802,
 2296 arXiv: [1212.6961 \[hep-ex\]](#).
- 2297 [42] CMS Collaboration, *Search for Supersymmetry in pp Collisions at 7 TeV in*
 2298 *Events with Jets and Missing Transverse Energy,*
 2299 *Phys. Lett. B* **698** (2011) p. 196, arXiv: [1101.1628 \[hep-ex\]](#).
- 2300 [43] CMS Collaboration, *Search for Supersymmetry at the LHC in Events with*
 2301 *Jets and Missing Transverse Energy, Phys. Rev. Lett.* **107** (2011) p. 221804,
 2302 arXiv: [1109.2352 \[hep-ex\]](#).
- 2303 [44] CMS Collaboration, *Search for supersymmetry in hadronic final states using*
 2304 *M_{T2} in pp collisions at $\sqrt{s} = 7 \text{ TeV}$, JHEP* **10** (2012) p. 018,
 2305 arXiv: [1207.1798 \[hep-ex\]](#).
- 2306 [45] CMS Collaboration, *Searches for supersymmetry using the M_{T2} variable in*
 2307 *hadronic events produced in pp collisions at 8 TeV, JHEP* **05** (2015) p. 078,
 2308 arXiv: [1502.04358 \[hep-ex\]](#).
- 2309 [46] CMS Collaboration, *Search for new physics with the M_{T2} variable in all-jets*
 2310 *final states produced in pp collisions at $\sqrt{s} = 13 \text{ TeV}$, JHEP* (2016),
 2311 arXiv: [1603.04053 \[hep-ex\]](#).
- 2312 [47] ATLAS Collaboration, *Multi-channel search for squarks and gluinos in*
 2313 $\sqrt{s} = 7 \text{ TeV}$ *pp collisions with the ATLAS detector at the LHC,*
 2314 *Eur. Phys. J. C* **73** (2013) p. 2362, arXiv: [1212.6149 \[hep-ex\]](#).

- 2315 [48] Y. Grossman, “Introduction to the SM,” 2016, URL: <https://indico.fnal.gov/sessionDisplay.py?sessionId=3&confId=11505#20160811>.
- 2316
- 2317 [49] W Buchmuller and C Ludeling, *Field Theory and Standard Model* (Sept. 2006) p. 70, URL: <https://cds.cern.ch/record/984122>.
- 2318
- 2319 [50] P. W. Higgs, *Broken Symmetries and the Masses of Gauge Bosons*, Phys. Rev. Lett. **13** (1964) p. 508.
- 2320
- 2321 [51] ATLAS Collaboration, *Observation of a new particle in the search for the Standard Model Higgs boson with the ATLAS detector at the LHC*, Phys. Lett. B **716** (2012) p. 1, arXiv: [1207.7214 \[hep-ex\]](https://arxiv.org/abs/1207.7214).
- 2322
- 2323
- 2324 [52] CMS Collaboration, *Observation of a new boson at a mass of 125 GeV with the CMS experiment at the LHC*, Phys. Lett. B **716** (2012) p. 30, arXiv: [1207.7235 \[hep-ex\]](https://arxiv.org/abs/1207.7235).
- 2325
- 2326
- 2327 [53] A. Chodos et al., *A New Extended Model of Hadrons*, Phys. Rev. **D9** (1974) p. 3471.
- 2328
- 2329 [54] A. Chodos et al., *Baryon Structure in the Bag Theory*, Phys. Rev. **D10** (1974) p. 2599.
- 2330
- 2331 [55] J. C. Collins, D. E. Soper, and G. F. Sterman, *Factorization of Hard Processes in QCD*, Adv. Ser. Direct. High Energy Phys. **5** (1989) p. 1, arXiv: [hep-ph/0409313 \[hep-ph\]](https://arxiv.org/abs/hep-ph/0409313).
- 2332
- 2333
- 2334
- 2335 [56] K. A. Olive et al., *Review of Particle Physics*, Chin. Phys. **C38** (2014) p. 090001.
- 2336
- 2337 [57] N. Cabibbo, *Unitary Symmetry and Leptonic Decays*, Phys. Rev. Lett. **10** (1963) p. 531, [[648\(1963\)](#)].
- 2338
- 2339 [58] M. Kobayashi and T. Maskawa, *CP Violation in the Renormalizable Theory of Weak Interaction*, Prog. Theor. Phys. **49** (1973) p. 652.
- 2340
- 2341
- 2342 [59] W. F. L. Hollik, *Radiative Corrections in the Standard Model and their Role for Precision Tests of the Electroweak Theory*, Fortsch. Phys. **38** (1990) p. 165.
- 2343
- 2344
- 2345 [60] D. Yu. Bardin et al., *ELECTROWEAK RADIATIVE CORRECTIONS TO DEEP INELASTIC*
- 2346

- 2347 *SCATTERING AT HERA! CHARGED CURRENT SCATTERING,*
 2348 *Z. Phys. C***44** (1989) p. 149.
- 2349 [61] D. C. Kennedy et al.,
 2350 *Electroweak Cross-Sections and Asymmetries at the Z0,*
 2351 *Nucl. Phys. B***321** (1989) p. 83.
- 2352 [62] A. Sirlin, *Radiative Corrections in the SU(2)-L x U(1) Theory: A Simple*
 2353 *Renormalization Framework*, *Phys. Rev. D***22** (1980) p. 971.
- 2354 [63] S. Fanchiotti, B. A. Kniehl, and A. Sirlin,
 2355 *Incorporation of QCD effects in basic corrections of the electroweak theory*,
 2356 *Phys. Rev. D***48** (1993) p. 307, arXiv: [hep-ph/9212285 \[hep-ph\]](#).
- 2357 [64] C. Quigg, “Cosmic Neutrinos,” *Proceedings, 35th SLAC Summer Institute on*
 2358 *Particle Physics: Dark matter: From the cosmos to the Laboratory (SSI*
 2359 *2007): Menlo Park, California, July 30- August 10, 2007*, 2008,
 2360 arXiv: [0802.0013 \[hep-ph\]](#),
 2361 URL: http://lss.fnal.gov/cgi-bin/find_paper.pl?conf-07-417.
- 2362 [65] S. R. Coleman and J. Mandula, *All Possible Symmetries of the S Matrix*,
 2363 *Phys. Rev. 159* (1967) p. 1251.
- 2364 [66] R. Haag, J. T. Lopuszanski, and M. Sohnius,
 2365 *All Possible Generators of Supersymmetries of the s Matrix*,
 2366 *Nucl. Phys. B***88** (1975) p. 257.
- 2367 [67] A. Salam and J. A. Strathdee, *On Superfields and Fermi-Bose Symmetry*,
 2368 *Phys. Rev. D***11** (1975) p. 1521.
- 2369 [68] S. Dimopoulos and H. Georgi, *Softly Broken Supersymmetry and SU(5)*,
 2370 *Nucl. Phys. B***193** (1981) p. 150.
- 2371 [69] S. Dimopoulos, S. Raby, and F. Wilczek,
 2372 *Supersymmetry and the Scale of Unification*, *Phys. Rev. D***24** (1981) p. 1681.
- 2373 [70] L. E. Ibanez and G. G. Ross,
 2374 *Low-Energy Predictions in Supersymmetric Grand Unified Theories*,
 2375 *Phys. Lett. B***105** (1981) p. 439.
- 2376 [71] W. J. Marciano and G. Senjanovic,
 2377 *Predictions of Supersymmetric Grand Unified Theories*,
 2378 *Phys. Rev. D***25** (1982) p. 3092.

- 2379 [72] L. Girardello and M. T. Grisaru, *Soft Breaking of Supersymmetry*,
 2380 *Nucl. Phys.* **B194** (1982) p. 65.
- 2381 [73] D. J. H. Chung et al.,
 2382 *The Soft supersymmetry breaking Lagrangian: Theory and applications*,
 2383 *Phys. Rept.* **407** (2005) p. 1, arXiv: [hep-ph/0312378 \[hep-ph\]](#).
- 2384 [74] J. Hisano et al., *Lepton flavor violation in the supersymmetric standard*
 2385 *model with seesaw induced neutrino masses*, *Phys. Lett.* **B357** (1995) p. 579,
 2386 arXiv: [hep-ph/9501407 \[hep-ph\]](#).
- 2387 [75] F. Gabbiani et al., *A Complete analysis of FCNC and CP constraints in*
 2388 *general SUSY extensions of the standard model*,
 2389 *Nucl. Phys.* **B477** (1996) p. 321, arXiv: [hep-ph/9604387 \[hep-ph\]](#).
- 2390 [76] F. Gabbiani and A. Masiero,
 2391 *FCNC in Generalized Supersymmetric Theories*,
 2392 *Nucl. Phys.* **B322** (1989) p. 235.
- 2393 [77] J. S. Hagelin, S. Kelley, and T. Tanaka, *Supersymmetric flavor changing*
 2394 *neutral currents: Exact amplitudes and phenomenological analysis*,
 2395 *Nucl. Phys.* **B415** (1994) p. 293.
- 2396 [78] J. S. Hagelin, S. Kelley, and V. Ziegler, *Using gauge coupling unification and*
 2397 *proton decay to test minimal supersymmetric SU(5)*,
 2398 *Phys. Lett.* **B342** (1995) p. 145, arXiv: [hep-ph/9406366 \[hep-ph\]](#).
- 2399 [79] D. Choudhury et al.,
 2400 *Constraints on nonuniversal soft terms from flavor changing neutral currents*,
 2401 *Phys. Lett.* **B342** (1995) p. 180, arXiv: [hep-ph/9408275 \[hep-ph\]](#).
- 2402 [80] R. Barbieri and L. J. Hall, *Signals for supersymmetric unification*,
 2403 *Phys. Lett.* **B338** (1994) p. 212, arXiv: [hep-ph/9408406 \[hep-ph\]](#).
- 2404 [81] B. de Carlos, J. A. Casas, and J. M. Moreno,
 2405 *Constraints on supersymmetric theories from mu —> e gamma*,
 2406 *Phys. Rev.* **D53** (1996) p. 6398, arXiv: [hep-ph/9507377 \[hep-ph\]](#).
- 2407 [82] J. A. Casas and S. Dimopoulos,
 2408 *Stability bounds on flavor violating trilinear soft terms in the MSSM*,
 2409 *Phys. Lett.* **B387** (1996) p. 107, arXiv: [hep-ph/9606237 \[hep-ph\]](#).
- 2410 [83] C. Borschensky et al., *Squark and gluino production cross sections in pp*
 2411 *collisions at $\sqrt{s} = 13, 14, 33$ and 100 TeV*,
 2412 *Eur. Phys. J.* **C74** (2014) p. 3174, arXiv: [1407.5066 \[hep-ph\]](#).

- 2413 [84] M. Klasen, M. Pohl, and G. Sigl, *Indirect and direct search for dark matter*,
 2414 Prog. Part. Nucl. Phys. **85** (2015) p. 1, arXiv: [1507.03800](https://arxiv.org/abs/1507.03800) [hep-ph].
- 2415 [85] L. Evans and P. Bryant, *LHC Machine*, JINST **3** (2008) S08001.
- 2416 [86] Vladimir Shiltsev, “Accelerator Physics and Technology,” Aug. 2016,
 2417 URL: [https://indico.fnal.gov/sessionDisplay.py?sessionId=3&](https://indico.fnal.gov/sessionDisplay.py?sessionId=3&confId=11505#20160811)
 2418 [confId=11505#20160811](https://indico.fnal.gov/sessionDisplay.py?sessionId=3&confId=11505#20160811).
- 2419 [87] *LEP design report*, Copies shelved as reports in LEP, PS and SPS libraries,
 2420 Geneva: CERN, 1984, URL: <https://cds.cern.ch/record/102083>.
- 2421 [88] ATLAS Collaboration,
 2422 *The ATLAS Experiment at the CERN Large Hadron Collider*,
 2423 JINST **3** (2008) S08003.
- 2424 [89] ATLAS Collaboration, *2015 start-up trigger menu and initial performance*
 2425 *assessment of the ATLAS trigger using Run-2 data*,
 2426 ATL-DAQ-PUB-2016-001, 2016,
 2427 URL: <https://cds.cern.ch/record/2136007/>.
- 2428 [90] ATLAS Collaboration, *Performance of the ATLAS Inner Detector Track and*
 2429 *Vertex Reconstruction in High Pile-Up LHC Environment*,
 2430 ATLAS-CONF-2012-042, 2012,
 2431 URL: <https://cds.cern.ch/record/1435196>.
- 2432 [91] ATLAS Collaboration, *Early Inner Detector Tracking Performance in the*
 2433 *2015 Data at $\sqrt{s} = 13 \text{ TeV}$* , ATL-PHYS-PUB-2015-051, 2015,
 2434 URL: <https://cds.cern.ch/record/2110140>.
- 2435 [92] K Hamano, A Morley, and A Salzburger,
 2436 “Track Reconstruction Performance and Efficiency Estimation using different
 2437 ID geometry samples,” tech. rep. ATL-COM-PHYS-2012-1541,
 2438 plots for a poster at HCP: CERN, Oct. 2012,
 2439 URL: <https://cds.cern.ch/record/1489674>.
- 2440 [93] ATLAS Collaboration,
 2441 *Electron reconstruction and identification efficiency measurements with the*
 2442 *ATLAS detector using the 2011 LHC proton–proton collision data*,
 2443 Eur. Phys. J. C **74** (2014) p. 2941, arXiv: [1404.2240](https://arxiv.org/abs/1404.2240) [hep-ex].
- 2444 [94] ATLAS Collaboration, *Topological cell clustering in the ATLAS calorimeters*
 2445 *and its performance in LHC Run 1* (2016), arXiv: [1603.02934](https://arxiv.org/abs/1603.02934) [hep-ex].

- 2446 [95] ATLAS Collaboration, *Jet energy resolution in proton–proton collisions at*
 2447 $\sqrt{s} = 7 \text{ TeV}$ *recorded in 2010 with the ATLAS detector,*
 2448 *Eur. Phys. J. C* **73** (2013) p. 2306, arXiv: [1210.6210](https://arxiv.org/abs/1210.6210) [hep-ex].
- 2449 [96] M. Aaboud et al., *Measurement of the photon identification efficiencies with*
 2450 *the ATLAS detector using LHC Run-1 data* (2016),
 2451 arXiv: [1606.01813](https://arxiv.org/abs/1606.01813) [hep-ex].
- 2452 [97] ATLAS Collaboration, *Electron and photon energy calibration with the*
 2453 *ATLAS detector using LHC Run 1 data*, *Eur. Phys. J. C* **74** (2014) p. 3071,
 2454 arXiv: [1407.5063](https://arxiv.org/abs/1407.5063) [hep-ex].
- 2455 [98] “Electron and photon energy calibration with the ATLAS detector using
 2456 data collected in 2015 at $\sqrt{s} = 13 \text{ TeV}$,”
 2457 tech. rep. ATL-PHYS-PUB-2016-015, CERN, Aug. 2016,
 2458 URL: <https://cds.cern.ch/record/2203514>.
- 2459 [99] ATLAS Collaboration, *Muon reconstruction performance of the ATLAS*
 2460 *detector in proton–proton collision data at $\sqrt{s} = 13 \text{ TeV}$,*
 2461 *Eur. Phys. J. C* **76** (2016) p. 292, arXiv: [1603.05598](https://arxiv.org/abs/1603.05598) [hep-ex].
- 2462 [100] ATLAS Collaboration, *Jet energy measurement with the ATLAS detector in*
 2463 *proton–proton collisions at $\sqrt{s} = 7 \text{ TeV}$* , *Eur. Phys. J. C* **73** (2013) p. 2304,
 2464 arXiv: [1112.6426](https://arxiv.org/abs/1112.6426) [hep-ex].
- 2465 [101] ATLAS Collaboration,
 2466 *Jet energy measurement and its systematic uncertainty in proton–proton*
 2467 *collisions at $\sqrt{s} = 7 \text{ TeV}$ with the ATLAS detector,*
 2468 *Eur. Phys. J. C* **75** (2015) p. 17, arXiv: [1406.0076](https://arxiv.org/abs/1406.0076) [hep-ex].
- 2469 [102] S. D. Ellis and D. E. Soper,
 2470 *Successive combination jet algorithm for hadron collisions,*
 2471 *Phys. Rev. D* **48** (1993) p. 3160, arXiv: [hep-ph/9305266](https://arxiv.org/abs/hep-ph/9305266) [hep-ph].
- 2472 [103] M. Cacciari and G. P. Salam, *Dispelling the N^3 myth for the k_t jet-finder*,
 2473 *Phys. Lett. B* **641** (2006) p. 57, arXiv: [hep-ph/0512210](https://arxiv.org/abs/hep-ph/0512210) [hep-ph].
- 2474 [104] M. Cacciari, G. P. Salam, and G. Soyez,
 2475 *The Anti- $k(t)$ jet clustering algorithm*, *JHEP* **04** (2008) p. 063,
 2476 arXiv: [0802.1189](https://arxiv.org/abs/0802.1189) [hep-ph].
- 2477 [105] *Particle-Flow Event Reconstruction in CMS and Performance for Jets, Taus,*
 2478 *and MET* (2009).

- 2479 [106] ATLAS Collaboration,
 2480 *Tagging and suppression of pileup jets with the ATLAS detector*,
 2481 ATLAS-CONF-2014-018, 2014,
 2482 URL: <https://cds.cern.ch/record/1700870>.
- 2483 [107] M. Cacciari, G. P. Salam, and G. Soyez, *The Catchment Area of Jets*,
 2484 JHEP **04** (2008) p. 005, arXiv: [0802.1188 \[hep-ph\]](https://arxiv.org/abs/0802.1188).
- 2485 [108] “Optimisation of the ATLAS b -tagging performance for the 2016 LHC Run,”
 2486 tech. rep. ATL-PHYS-PUB-2016-012, CERN, June 2016,
 2487 URL: <https://cds.cern.ch/record/2160731>.
- 2488 [109] G. Aad et al., *Performance of algorithms that reconstruct missing transverse*
 2489 *momentum in $\sqrt{s} = 8$ TeV proton-proton collisions in the ATLAS detector*
 2490 (2016), arXiv: [1609.09324 \[hep-ex\]](https://arxiv.org/abs/1609.09324).
- 2491 [110] ATLAS Collaboration,
 2492 *Prospects for Supersymmetry discovery based on inclusive searches at a*
 2493 *7 TeV centre-of-mass energy with the ATLAS detector*,
 2494 ATL-PHYS-PUB-2010-010, 2010,
 2495 URL: <https://cds.cern.ch/record/1278474>.
- 2496 [111] ATLAS Collaboration,
 2497 *Expected sensitivity studies for gluino and squark searches using the early*
 2498 *LHC 13 TeV Run-2 dataset with the ATLAS experiment*,
 2499 ATL-PHYS-PUB-2015-005, 2015, URL:
 2500 [https://atlas.web.cern.ch/Atlas/GROUPS/PHYSICS/PUBNOTES/ATL-](https://atlas.web.cern.ch/Atlas/GROUPS/PHYSICS/PUBNOTES/ATL-PHYS-PUB-2015-005)
 2501 [PHYS-PUB-2015-005](https://atlas.web.cern.ch/Atlas/GROUPS/PHYSICS/PUBNOTES/ATL-PHYS-PUB-2015-005).
- 2502 [112] ATLAS Collaboration, *Expected performance of missing transverse*
 2503 *momentum reconstruction for the ATLAS detector at $\sqrt{s} = 13$ TeV*,
 2504 ATL-PHYS-PUB-2015-023, 2015,
 2505 URL: <https://cds.cern.ch/record/2037700>.
- 2506 [113] ATLAS Collaboration,
 2507 *Performance of missing transverse momentum reconstruction with the*
 2508 *ATLAS detector in the first proton–proton collisions at $\sqrt{s} = 13$ TeV*,
 2509 ATL-PHYS-PUB-2015-027, 2015,
 2510 URL: <https://cds.cern.ch/record/2037904>.
- 2511 [114] P. Jackson, C. Rogan, and M. Santoni, *Sparticles in Motion - getting to the*
 2512 *line in compressed scenarios with the Recursive Jigsaw Reconstruction*
 2513 (2016), arXiv: [1607.08307 \[hep-ph\]](https://arxiv.org/abs/1607.08307).

- 2514 [115] ATLAS Collaboration,
2515 *Further searches for squarks and gluinos in final states with jets and missing*
2516 *transverse momentum at $\sqrt{s} = 13$ TeV with the ATLAS detector,*
2517 ATLAS-CONF-2016-078, 2016,
2518 URL: <https://cds.cern.ch/record/2206252>.
- 2519 [116] C. Rogan, *Kinematical variables towards new dynamics at the LHC* (2010),
2520 arXiv: [1006.2727 \[hep-ph\]](https://arxiv.org/abs/1006.2727).
- 2521 [117] M. R. Buckley et al.,
2522 *Super-Razor and Searches for Sleptons and Charginos at the LHC*,
2523 Phys. Rev. D **89** (2014) p. 055020, arXiv: [1310.4827 \[hep-ph\]](https://arxiv.org/abs/1310.4827).
- 2524 [118] CMS Collaboration, *Search for supersymmetry using razor variables in*
2525 *events with b-tagged jets in pp collisions at $\sqrt{s} = 8$ TeV,*
2526 Phys. Rev. D **91** (2015) p. 052018, arXiv: [1502.00300 \[hep-ex\]](https://arxiv.org/abs/1502.00300).
- 2527 [119] Chris Rogan, “RestFrames,” URL: [{http://restframes.com}](http://restframes.com).
- 2528 [120] M. Baak et al., *HistFitter software framework for statistical data analysis*,
2529 Eur. Phys. J. C **75** (2015) p. 153, arXiv: [1410.1280 \[hep-ex\]](https://arxiv.org/abs/1410.1280).
- 2530 [121] ATLAS Collaboration, *Monte Carlo Generators for the Production of a W*
2531 *or Z/ γ^* Boson in Association with Jets at ATLAS in Run 2*,
2532 ATL-PHYS-PUB-2016-003, 2016,
2533 URL: <https://cds.cern.ch/record/2120133>.
- 2534 [122] ATLAS Collaboration, *Simulation of top-quark production for the ATLAS*
2535 *experiment at $\sqrt{s} = 13$ TeV*, ATL-PHYS-PUB-2016-004, 2016,
2536 URL: <https://cds.cern.ch/record/2120417>.
- 2537 [123] ATLAS Collaboration, *Multi-boson simulation for 13 TeV ATLAS analyses*,
2538 ATL-PHYS-PUB-2016-002, 2016,
2539 URL: <https://cds.cern.ch/record/2119986>.
- 2540 [124] ATLAS Collaboration,
2541 *Search for squarks and gluinos in final states with jets and missing transverse*
2542 *momentum at $\sqrt{s} = 13$ TeV with the ATLAS detector*,
2543 Eur. Phys. J. C **76** (2016) p. 392, arXiv: [1605.03814 \[hep-ex\]](https://arxiv.org/abs/1605.03814).
- 2544 [125] R. D. Cousins, J. T. Linnemann, and J. Tucker,
2545 *Evaluation of three methods for calculating statistical significance when*
2546 *incorporating a systematic uncertainty into a test of the background-only*
2547 *hypothesis for a Poisson process*, Nucl. Instrum. Meth. A **595** (2008) p. 480.

- 2548 [126] ATLAS Collaboration, *Search for squarks and gluinos with the ATLAS*
2549 *detector in final states with jets and missing transverse momentum using*
2550 *4.7 fb⁻¹ of $\sqrt{s} = 7$ TeV proton–proton collision data,*
2551 *Phys. Rev. D* **87** (2013) p. 012008, arXiv: [1208.0949 \[hep-ex\]](https://arxiv.org/abs/1208.0949).
- 2552 [127] ATLAS Collaboration, *Jet Calibration and Systematic Uncertainties for Jets*
2553 *Reconstructed in the ATLAS Detector at $\sqrt{s} = 13$ TeV,*
2554 ATL-PHYS-PUB-2015-015, 2015,
2555 URL: <https://cds.cern.ch/record/2037613>.
- 2556 [128] ATLAS Collaboration,
2557 *Performance of algorithms that reconstruct missing transverse momentum in*
2558 *$\sqrt{s} = 8$ TeV proton–proton collisions in the ATLAS detector* (2016),
2559 arXiv: [1609.09324 \[hep-ex\]](https://arxiv.org/abs/1609.09324).
- 2560 [129] G. J. Feldman and R. D. Cousins,
2561 *A Unified approach to the classical statistical analysis of small signals,*
2562 *Phys. Rev. D* **57** (1998) p. 3873,
2563 arXiv: [physics/9711021 \[physics.data-an\]](https://arxiv.org/abs/physics/9711021).

2564

The Standard Model

2565 In this appendix, we provide a brief overview of the basic ingredients involved in
2566 construction of the Standard Model Lagrangian : quantum field theory, symmetries,
2567 and symmetry breaking.

2568 Quantum Field Theory

2569

2570 In this section, we provide a brief overview of the necessary concepts from
2571 Quantum Field Theory (QFT).

2572 In modern physics, the laws of nature are described by the “action” S , with the
2573 imposition of the principle of minimum action. The action is the integral over the cite
2574 spacetime coordinates of the “Lagrangian density” \mathcal{L} , or Lagrangian for short. The
2575 Lagrangian is a function of “fields”; general fields will be called $\phi(x^\mu)$, where the
2576 indices μ run over the space-time coordinates. We can then write the action S as

$$S = \int d^4x \mathcal{L}[\phi_i(x^\mu), \partial_\mu \phi_i(x^\mu)] \quad (9.1)$$

2577 where we have an additional summation over i (of the different fields). Generally,
2578 we impose the following constraints on the Lagrangian :

- 2579 1. Translational invariance - The Lagrangian is only a function of the fields ϕ and
2580 their derivatives $\partial_\mu \phi$
- 2581 2. Locality - The Lagrangian is only a function of one point x_μ in spacetime.

cite Yuval's
lectures
and notes
somehow

cite

- 2582 3. Reality condition - The Lagrangian is real to conserve probability.
- 2583 4. Lorentz invariance - The Lagrangian is invariant under the Poincarégroup of
2584 spacetime.
- 2585 5. Analyticity - The Lagrangian is an analytical function of the fields; this is to
2586 allow the use of perturbation theory.
- 2587 6. Invariance and Naturalness - The Lagrangian is invariant under some internal
2588 symmetry groups; in fact, the Lagrangian will have *all* terms allowed by the
2589 imposed symmetry groups.
maybe add 2589
in ref here
- 2590 7. Renormalizability - The Lagrangian will be renormalizable - in practice, this
2591 means there will not be terms with more than power 4 in the fields.
- 2592 The key item from the point of view of this thesis is that of “Invariance and
2593 Natural”. We impose a set of “symmetries” and then our Lagrangian is the most
2594 general which is allowed by those symmetries.

2595 Symmetries

2596 Symmetries can be seen as the fundamental guiding concept of modern physics.

cite? 2597 Symmetries are described by “groups”. To illustrate the importance of symmetries
2598 and their mathematical description, groups, we start here with two of the simplest
2599 and most useful examples : \mathbb{Z}_2 and $U(1)$.

2600 \mathbb{Z}_2 symmetry

2601 \mathbb{Z}_2 symmetry is the simplest example of a “discrete” symmetry. Consider the most
2602 general Lagrangian of a single real scalar field $\phi(x_\mu)$

$$\mathcal{L}_\phi = \frac{1}{2}\partial_\mu\phi\partial^\mu\phi - \frac{m^2}{2}\phi^2 - \frac{\mu}{2\sqrt{2}}\phi^3 - \lambda\phi^4 \quad (9.2)$$

Now we *impose* the symmetry

$$\mathcal{L}(\phi) = \mathcal{L}(-\phi) \quad (9.3)$$

2603 This has the effect of restricting the allowed terms of the Lagrangian. In particular,
 2604 we can see the term $\phi^3 \rightarrow -\phi^3$ under the symmetry transformation, and thus must
 2605 be disallowed by this symmetry. This means under the imposition of this particular
 2606 symmetry, our Lagrangian should be rewritten as

$$\mathcal{L}_\phi = \frac{1}{2}\partial_\mu\phi\partial^\mu\phi - \frac{m^2}{2}\phi^2 - \lambda\phi^4 \quad (9.4)$$

2607 The effect of this symmetry is that the total number of ϕ particles can only change
 2608 by even numbers, since the only interaction term $\lambda\phi^4$ is an even power of the field.
 2609 This symmetry is often imposed in supersymmetric theories, as we will see in Chapter
 2610 3.

2611 **$U(1)$ symmetry**

2612 $U(1)$ is the simplest example of a continuous (or *Lie*) group. Now consider a theory
 2613 with a single complex scalar field $\phi = \text{Re } \phi + i \text{Im } \phi$

$$\mathcal{L}_\phi = \delta_{i,j} \frac{1}{2}\partial_\mu\phi_i\partial^\mu\phi_j - \frac{m^2}{2}\phi_i\phi_j - \frac{\mu}{2\sqrt{2}}\phi_i\phi_j\phi_k\phi_l - \lambda\phi_i\phi_j\phi_k\phi_l \quad (9.5)$$

2614 where $i, j, k, l = \text{Re}, \text{Im}$. In this case, we impose the following $U(1)$ symmetry
 2615 : $\phi \rightarrow e^{i\theta}, \phi^* \rightarrow e^{-i\theta}$. We see immediately that this again disallows the third-order
 2616 terms, and we can write a theory of a complex scalar field with $U(1)$ symmetry as

$$\mathcal{L}_\phi = \partial_\mu\phi\partial^\mu\phi^* - \frac{m^2}{2}\phi\phi^* - \lambda(\phi\phi^*)^2 \quad (9.6)$$

2617 **Local symmetries**

2618 The two examples considered above are “global” symmetries in the sense that the
2619 symmetry transformation does not depend on the spacetime coordinate x_μ . We know
2620 look at local symmetries; in this case, for example with a local $U(1)$ symmetry, the
2621 transformation has the form $\phi(x_\mu) \rightarrow e^{i\theta(x_\mu)}\phi(x_\mu)$. These symmetries are also known
2622 as “gauge” symmetries; all symmetries of the Standard Model are gauge symmetries.

There are wide-ranging consequences to the imposition of local symmetries. To begin, we note that the derivative terms of the Lagrangian 9.2 are *not* invariant under a local symmetry transformation

$$\partial_\mu \phi(x_\mu) \rightarrow \partial_\mu(e^{i\theta(x_\mu)}\phi(x_\mu)) = (1 + i\theta(x_\mu))e^{i\theta(x_\mu)}\phi(x_\mu) \quad (9.7)$$

GET THIS
RIGHT

2623 This leads us to note that the kinetic terms of the Lagrangian are also not invariant
2624 under a gauge symmetry. This would lead to a model with no dynamics, which is
2625 clearly unsatisfactory.

2627 Let us take inspiration from the case of global symmetries. We need to define a
2628 so-called “covariant” derivative D^μ such that

$$D^\mu \phi \rightarrow e^{iq\theta(x^\mu)D^\mu}\phi \quad (9.8)$$

$$D^\mu \phi^* \rightarrow e^{-iq\theta(x^\mu)D^\mu}\phi^* \quad (9.9)$$

$$(9.10)$$

2629 Since ϕ and ϕ^* transforms with the opposite phase, this will lead the invariance
2630 of the Lagrangian under our local gauge transformation. This D^μ is of the following
2631 form

$$D^\mu = \partial_\mu - igqA^\mu \quad (9.11)$$

2632 where A^μ is a vector field we introduce with the transformation law

$$A^\mu \rightarrow A^\mu - \frac{1}{g} \partial_\mu \theta \quad (9.12)$$

2633 and g is the coupling constant associated to vector field. This vector field A^μ is
2634 also known as a “gauge” field.

2635 Since we need to add all allowed terms to the Lagrangian, we define

$$F^{\mu\nu} = A^\mu A^\nu - A^\nu A^\mu \quad (9.13)$$

2636 and then we must also add the kinetic term :

$$\mathcal{L}_{\text{gauge}} = -\frac{1}{4} F^{\mu\nu} F_{\mu\nu} \quad (9.14)$$

2637 The most general renormalizable Lagrangian with fermion and scalar fields can
2638 be written in the following form

$$\mathcal{L} = \mathcal{L}_{\text{kin}} + \mathcal{L}_\phi + \mathcal{L}_\psi + \mathcal{L}_{\text{Yukawa}} \quad (9.15)$$

2639 Symmetry breaking and the Higgs mechanism

2640 Here we view some examples of symmetry breaking. We investigate breaking of a
2641 global $U(1)$ symmetry and a local $U(1)$ symmetry. The SM will break the electroweak
2642 symmetry $SU(2)xU(1)$, and in Chapter 3 we will see how supersymmetry must also
2643 be broken.

2644 There are two ideas of symmetry breaking

- 2645 • Explicit symmetry breaking by a small parameter - in this case, we have a small
2646 parameter which breaks an “approximate” symmetry of our Lagrangian. An
2647 example would be the theory of the single scalar field 9.2, when $\mu \ll m^2$ and

$\mu \ll \lambda$. In this case, we can often ignore the small term when considering low-energy processes.

- Spontaneous symmetry breaking (SSB) - spontaneous symmetry breaking occurs when the Lagrangian is symmetric with respect to a given symmetry transformation, but the ground state of the theory is *not* symmetric with respect to that transformation. This can have some fascinating consequences, as we will see in the following examples

Symmetry breaking a

U(1) global symmetry breaking

Consider the theory of a complex scalar field under the $U(1)$ symmetry, or the transformation

$$\phi \rightarrow e^{i\theta} \phi \quad (9.16)$$

The Lagrangian for this theory is

$$\mathcal{L} = \partial^\mu \phi^\dagger \partial_\mu \phi + \frac{\mu^2}{2} \phi^\dagger \phi + \frac{\lambda}{4} (\phi^\dagger \phi)^2 \quad (9.17)$$

Let us write this theory in terms of two scalar fields, h and ξ : $\phi = (h + i\xi)/\sqrt{2}$.

The Lagrangian can then be written as

$$\mathcal{L} = \partial^\mu h \partial_\mu h + \partial^\mu \xi d\mu \xi - \frac{\mu^2}{2} (h^2 + \xi^2) - \frac{\lambda}{4} (h^2 + \xi^2)^2 \quad (9.18)$$

First, note that the theory is only stable when $\lambda > 0$. To understand the effect of SSB, we now enforce that $\mu^2 < 0$, and define $v^2 = -\mu^2/\lambda$. We can then write the scalar potential of this theory as :

$$V(\phi) = \lambda(\phi^\dagger \phi - v^2/2)^2 \quad (9.19)$$

Minimizing this equation with respect to ϕ , we can see that the “vacuum expectation value” of the theory is

$$2 < \phi^\dagger \phi > = < h^2 + \xi^2 > = v^2 \quad (9.20)$$

2657 We now reach the “breaking” point of this procedure. In the (h, ξ) plane, the
 2658 minima form a circle of radius v . We are free to choose any of these minima to expand
 2659 our Lagrangian around; the physics is not affected by this choice. For convenience,
 2660 choose $\langle h \rangle = v, \langle \xi^2 \rangle = 0$.

Now, let us define $h' = h - v, \xi' = \xi$ with VEVs $\langle h' \rangle = 0, \langle \xi' \rangle = 0$. We can
 then write our spontaneously broken Lagrangian in the form

$$\mathcal{L} = \frac{1}{2}\partial_\mu h'\partial^\mu h' + \frac{1}{2}\partial_\mu \xi'\partial^\mu \xi' - \lambda v^2 h'^2 - \lambda v h'(h'^2 + \xi'^2) - \lambda(h'^2 + \xi'^2)^2 \quad (9.21)$$

2661

The Standard Model

2662

2663 **Compressed region N-1 plots**

add some
text or cut
this

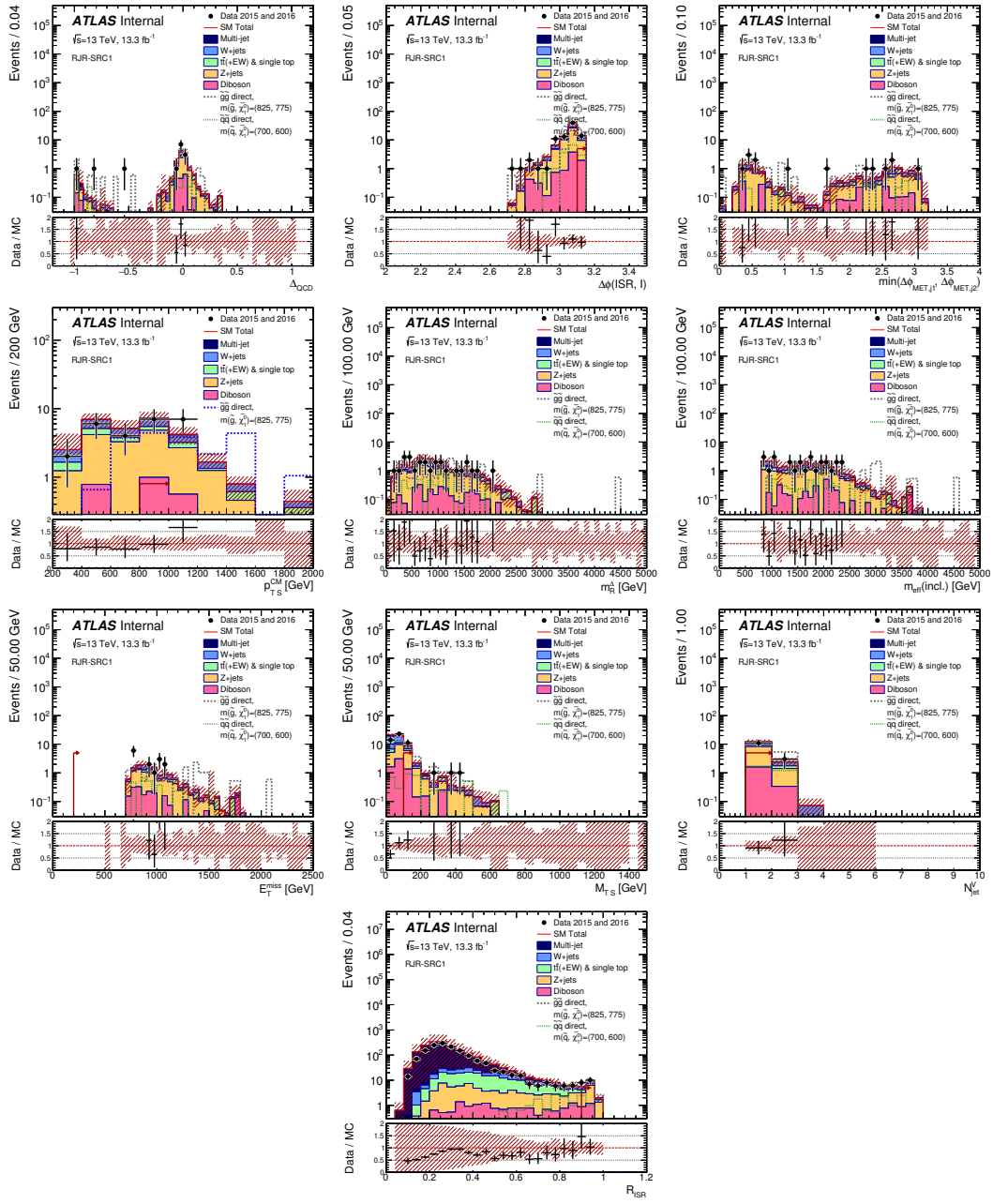


Figure 1

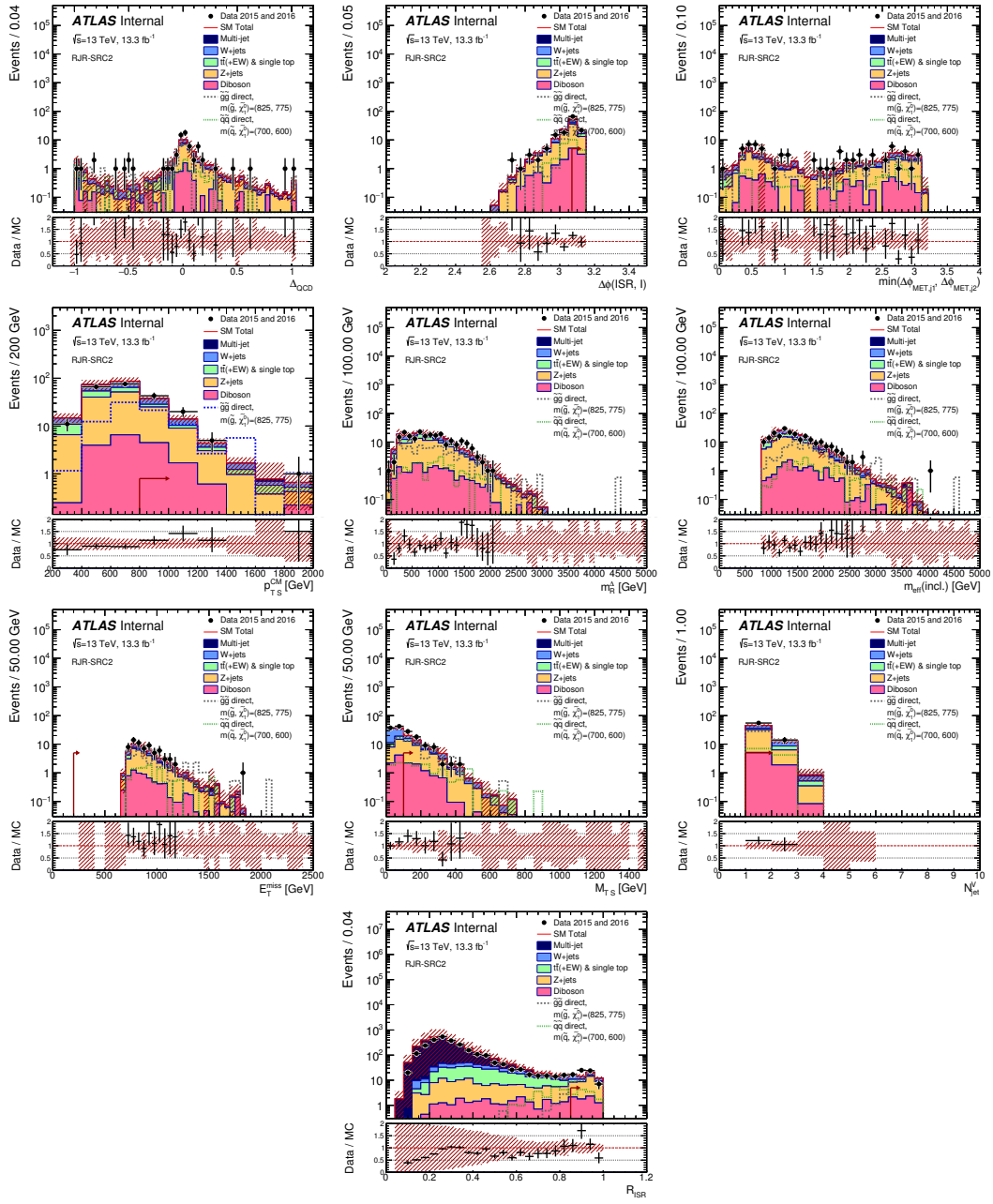


Figure 2

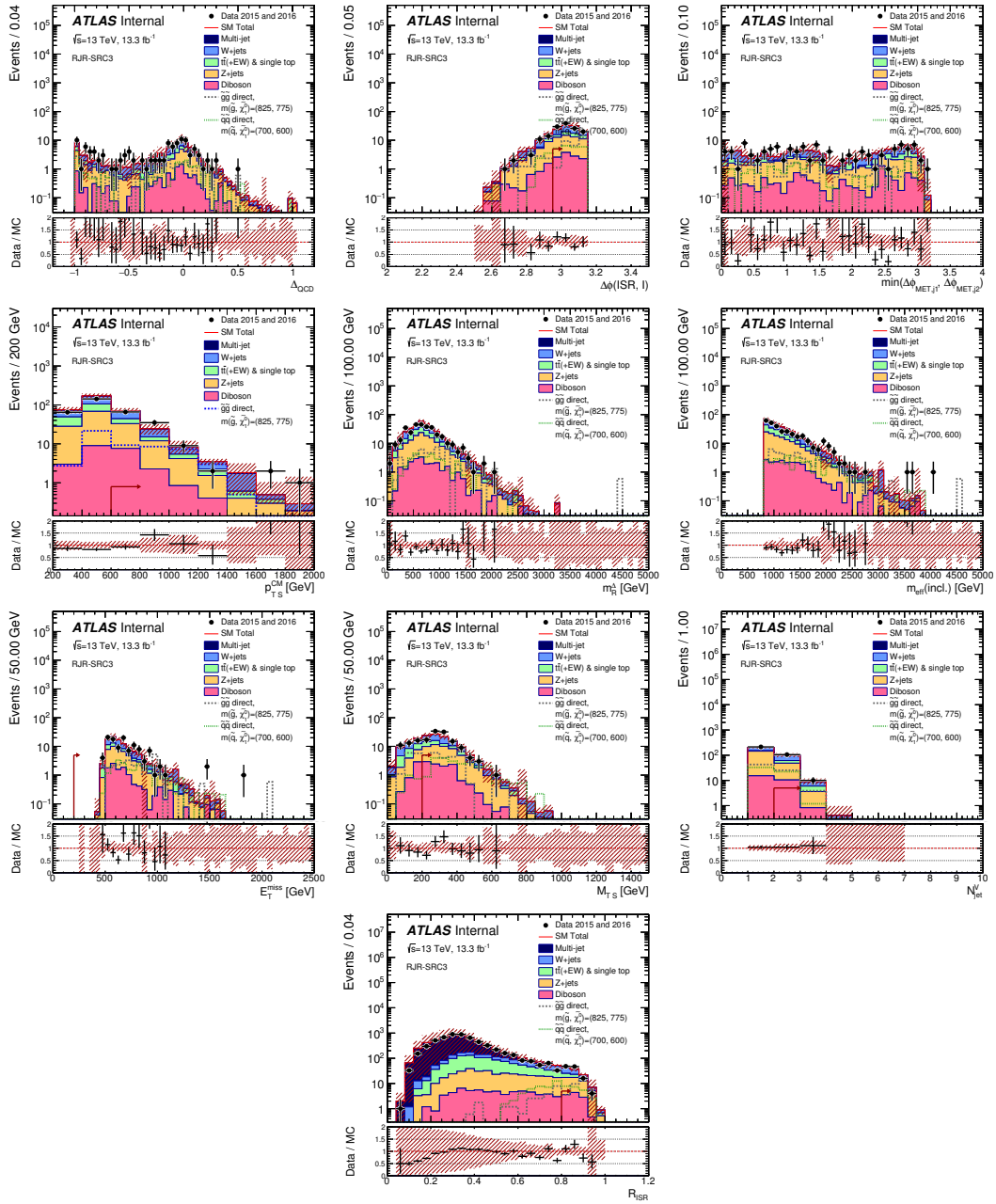


Figure 3

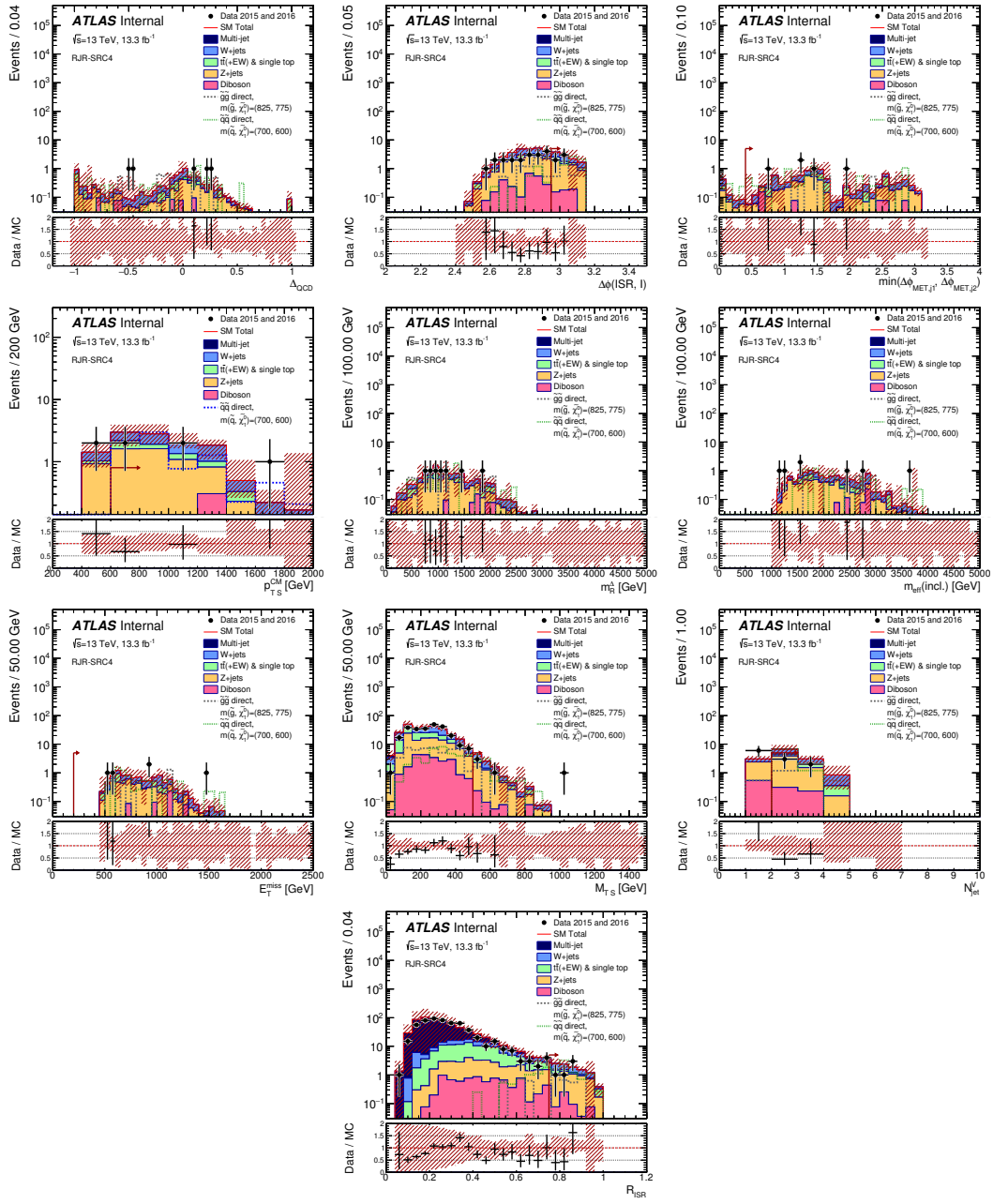


Figure 4

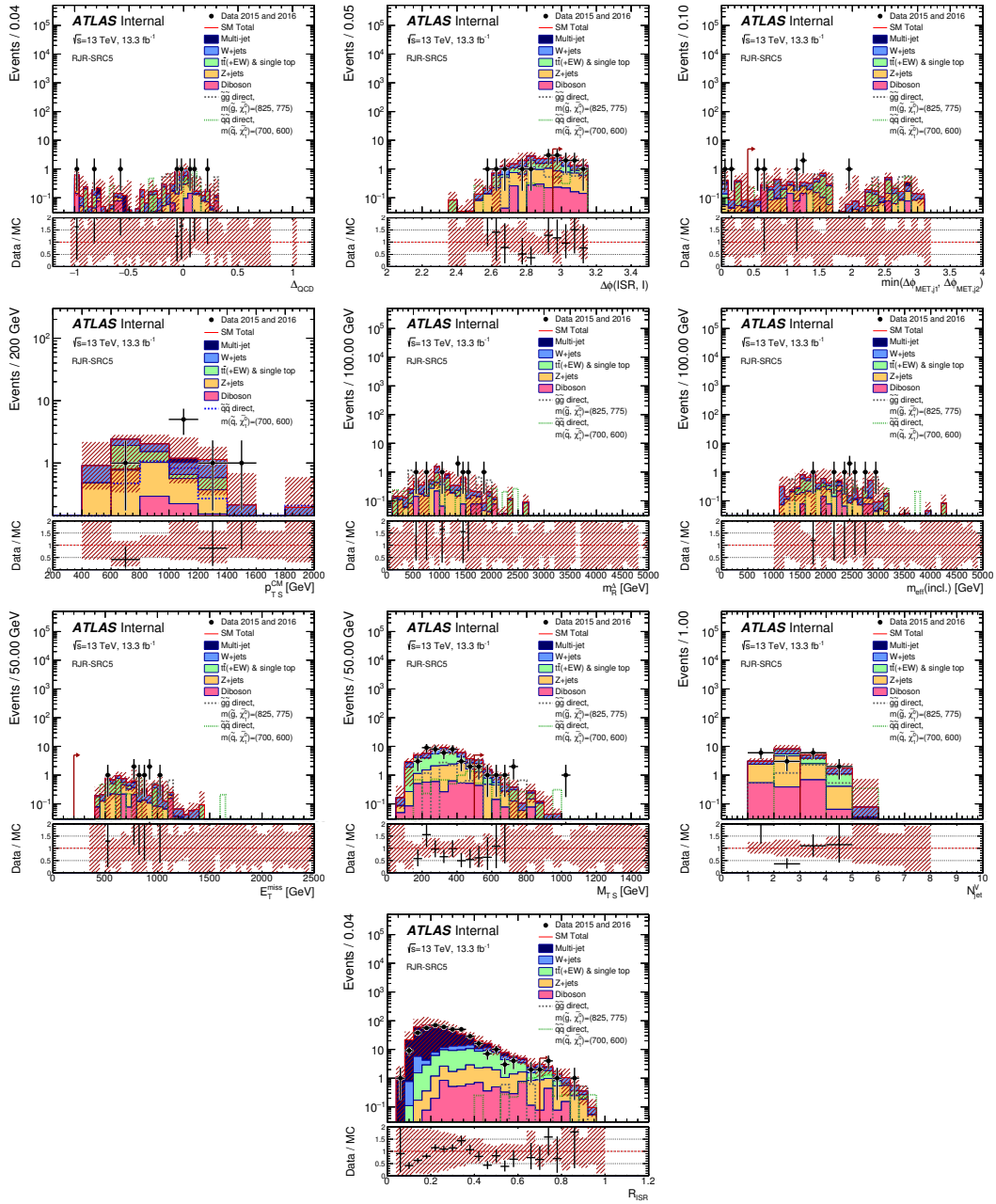


Figure 5

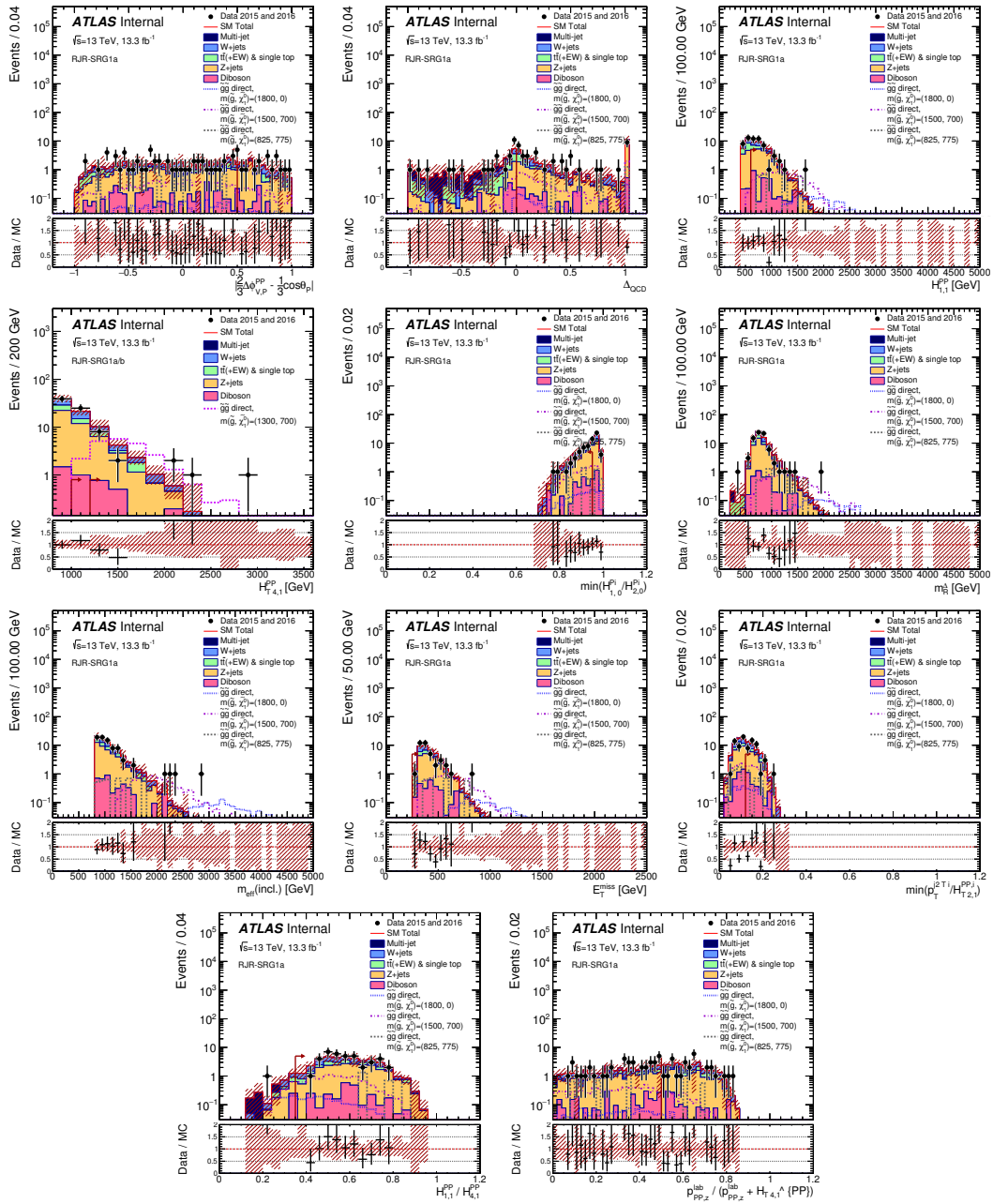


Figure 6

Figure 7

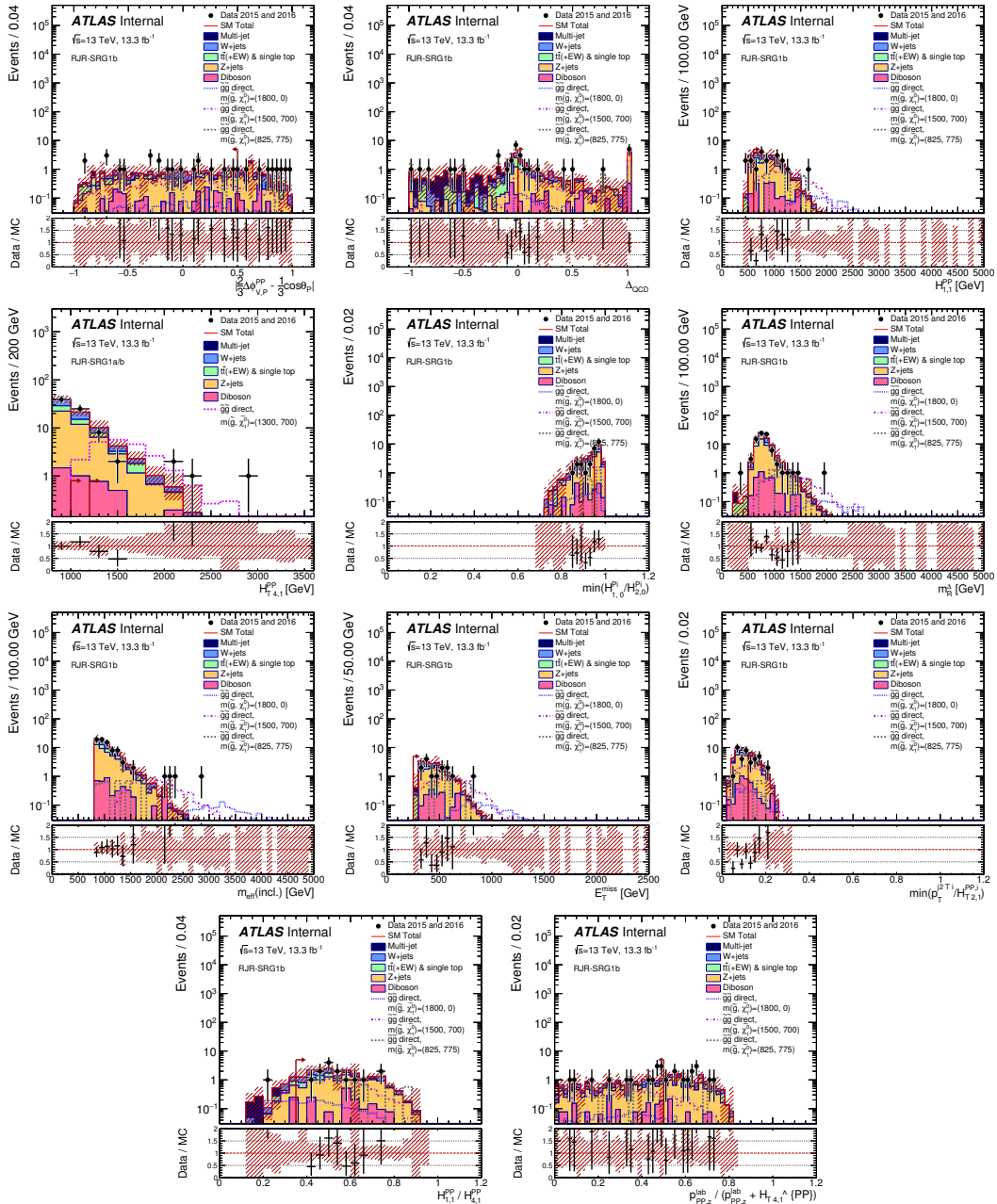


Figure 8

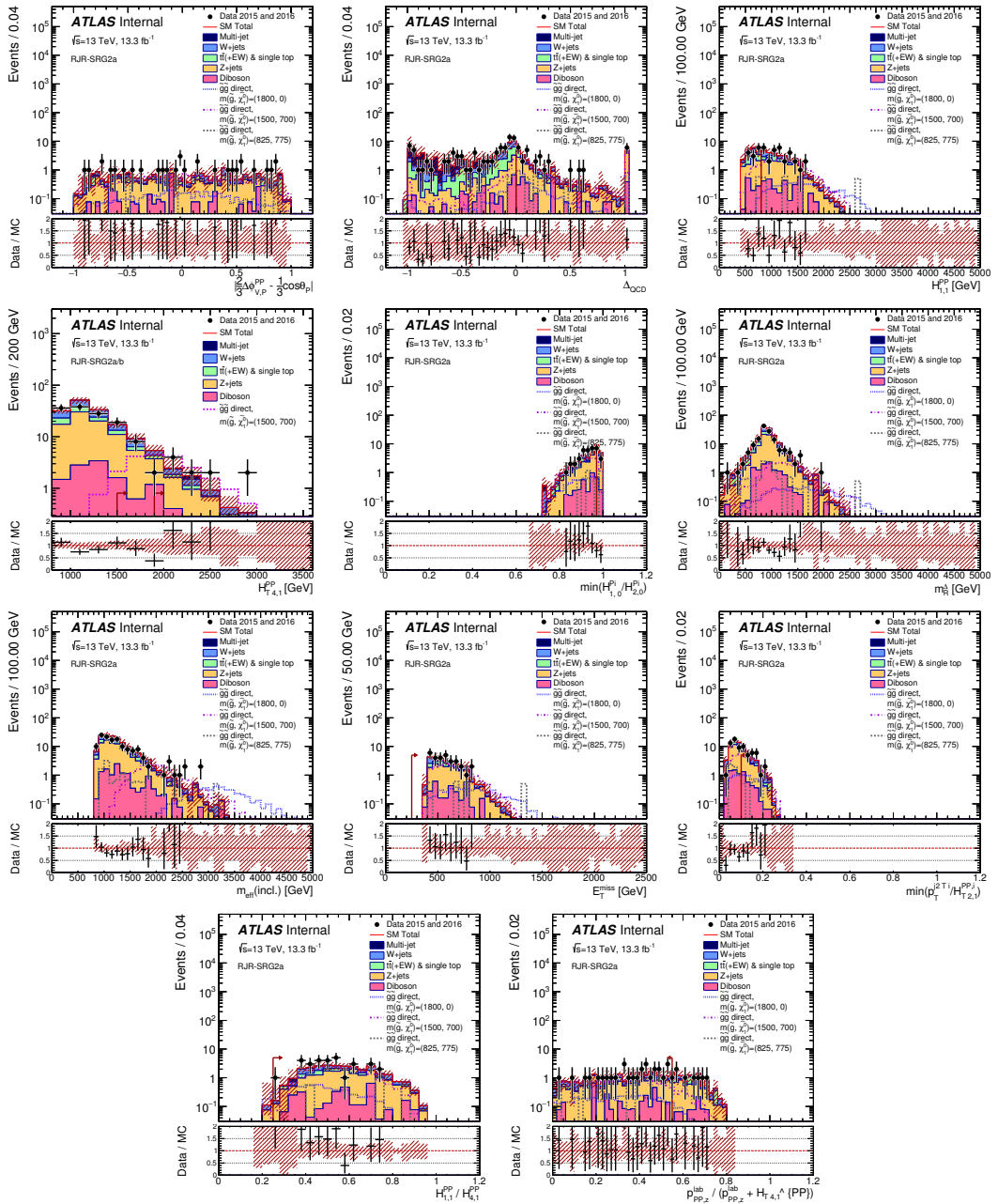


Figure 9

Figure 10

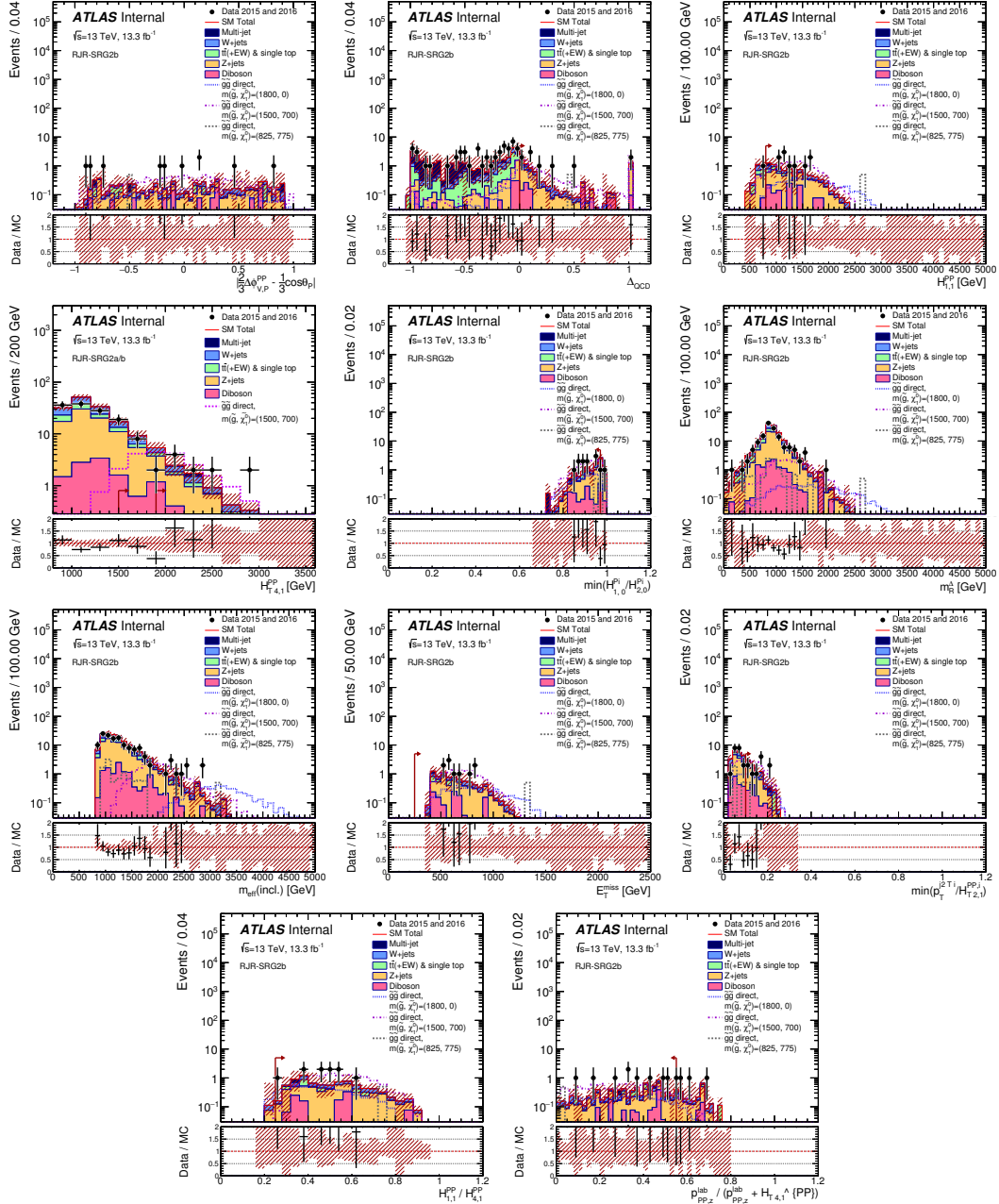


Figure 11

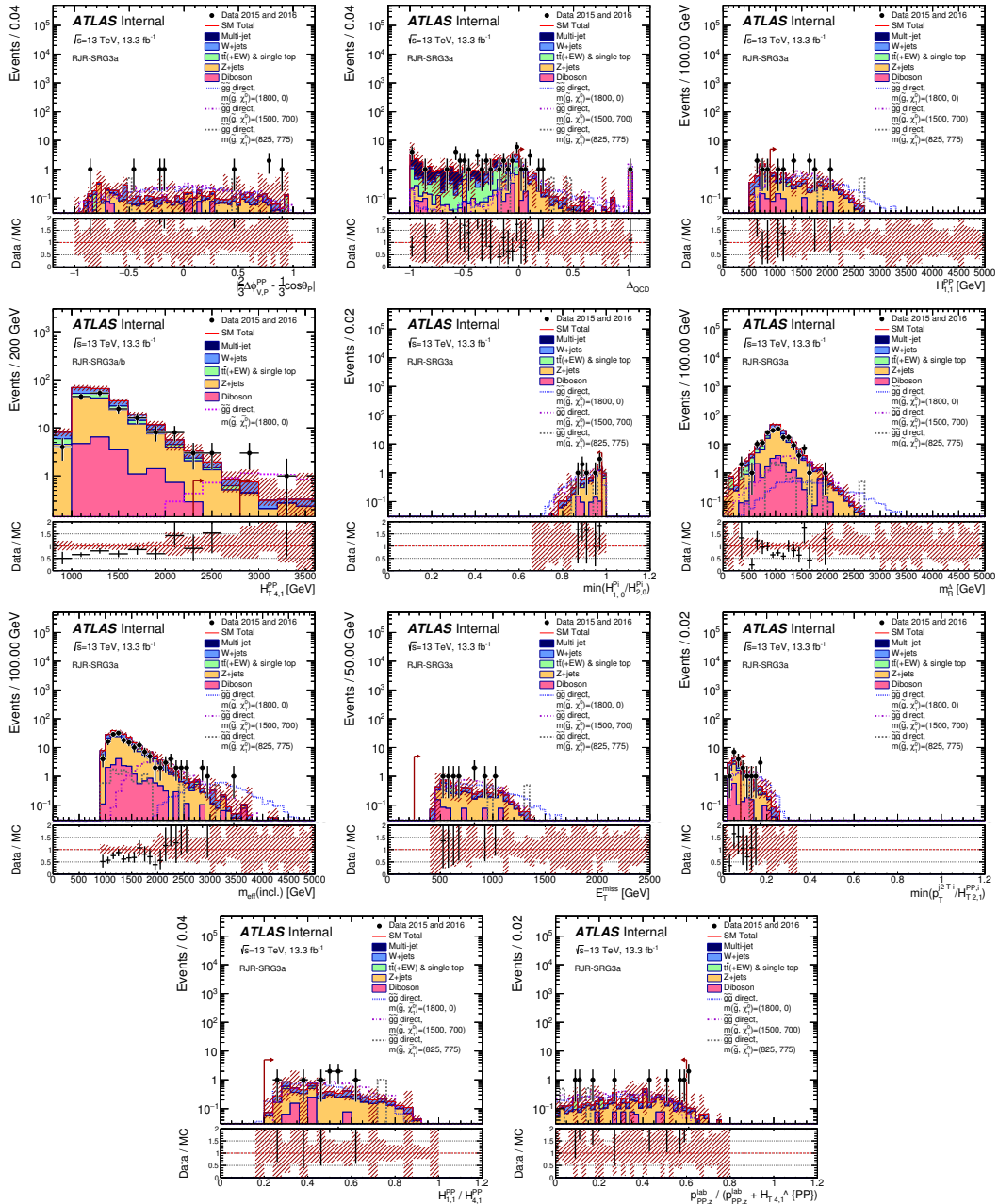


Figure 12

Figure 13

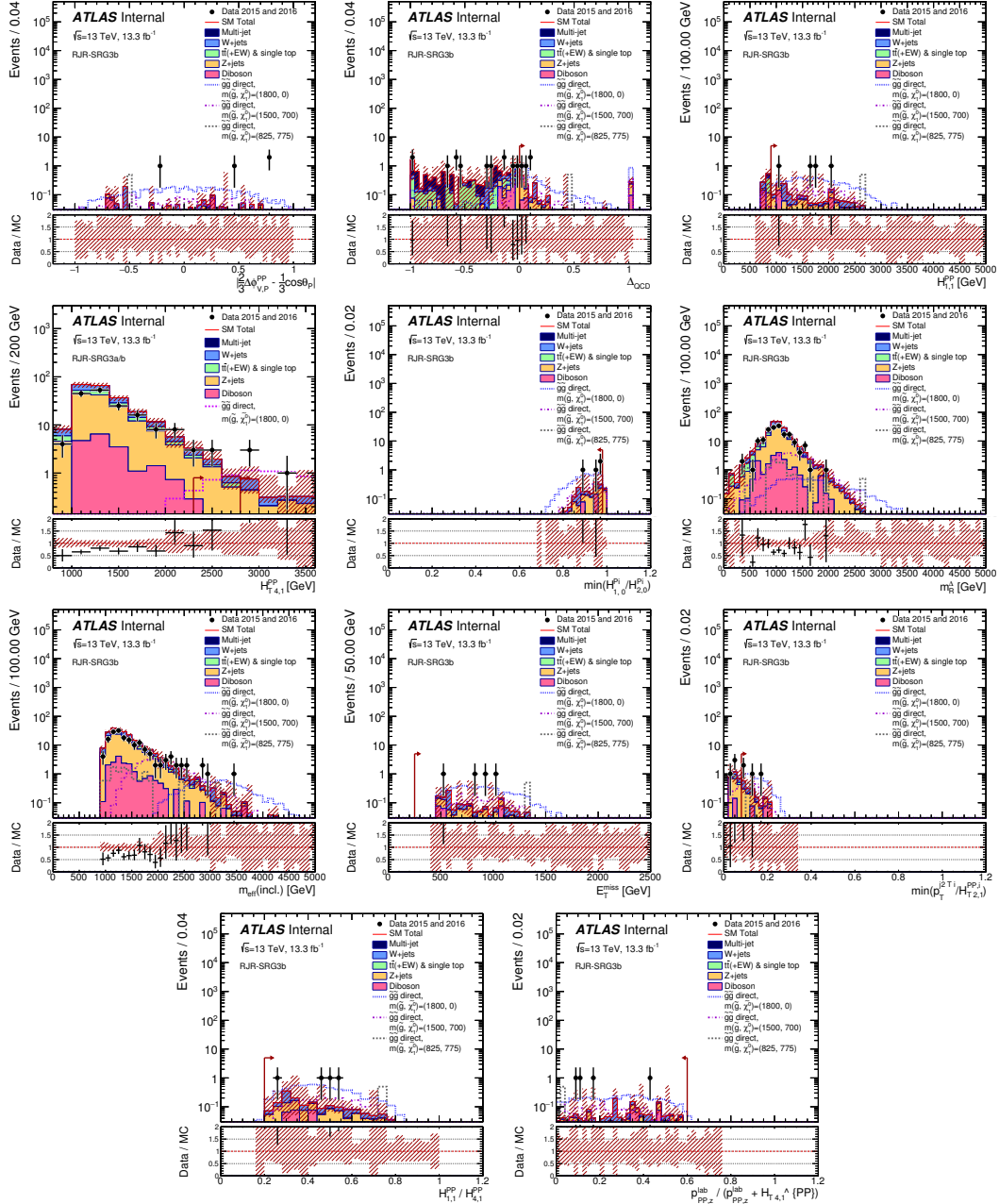


Figure 14

Figure 15

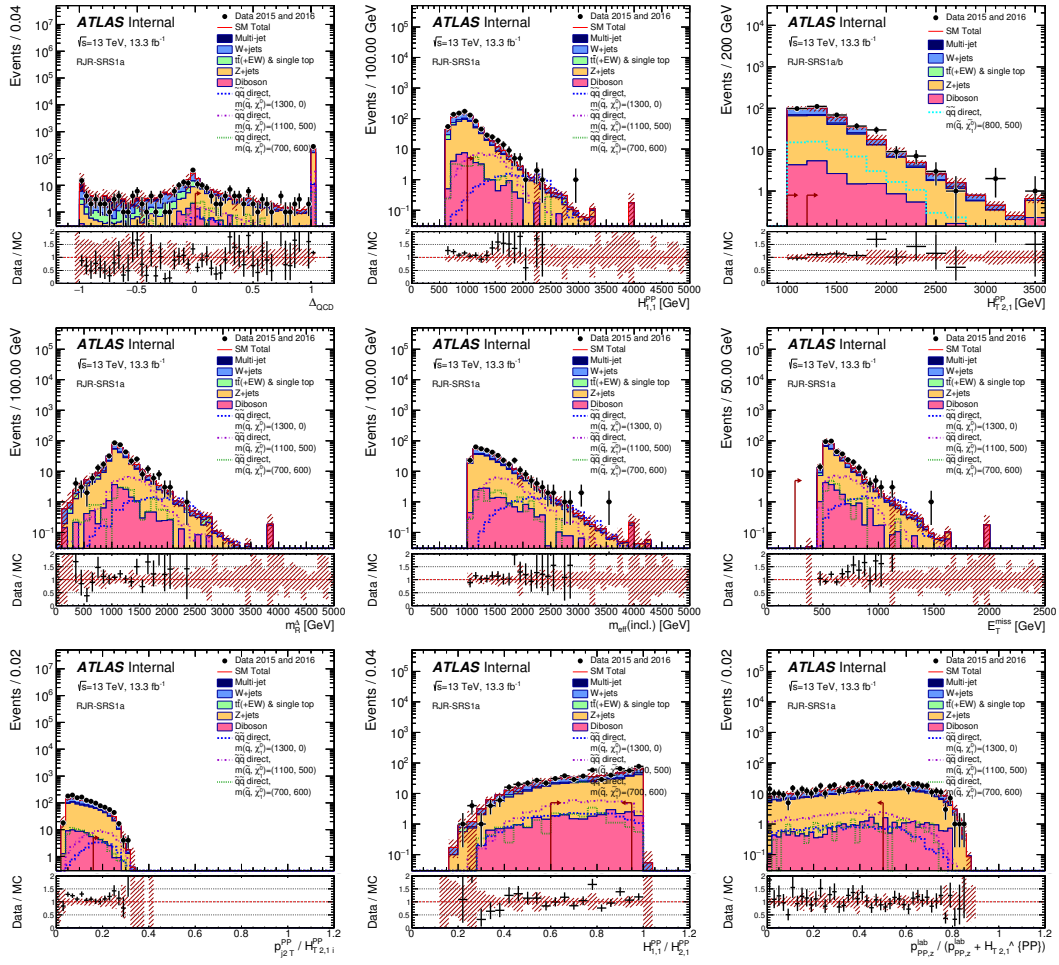


Figure 16

Figure 17

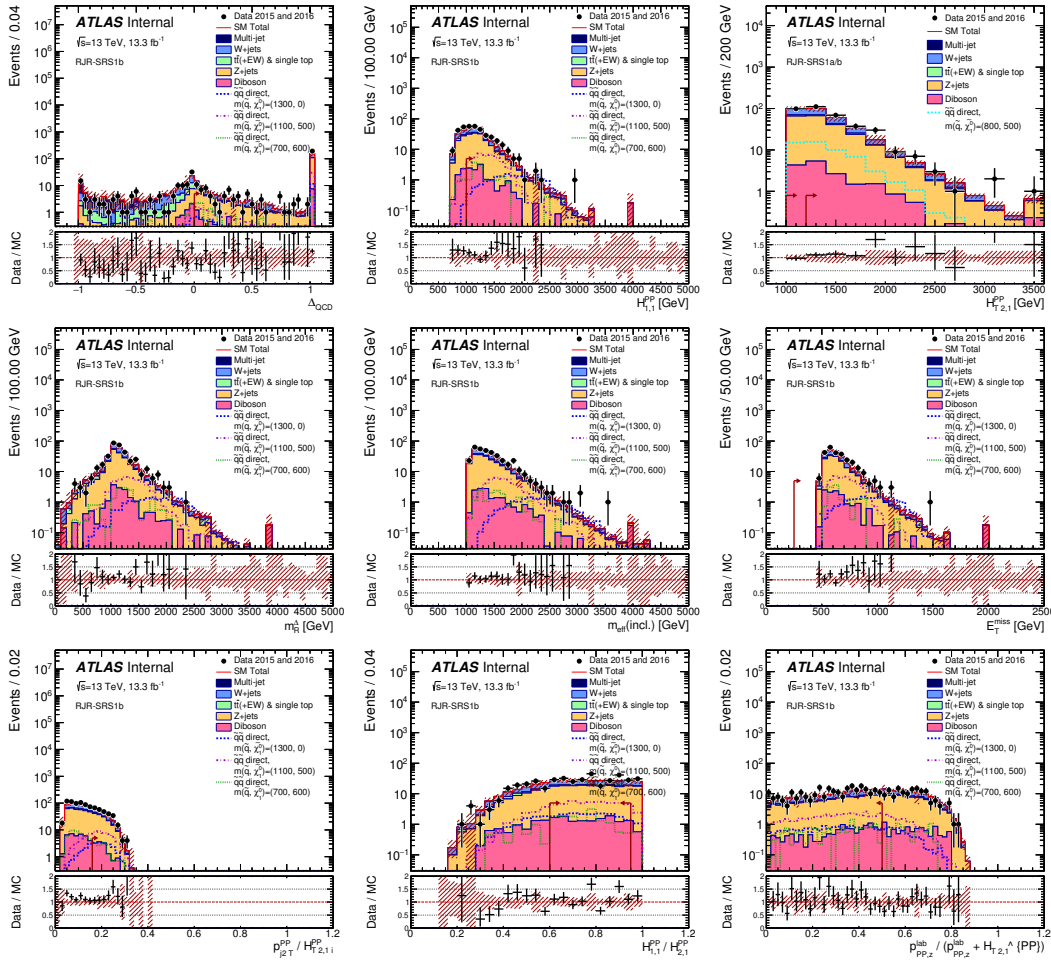


Figure 18

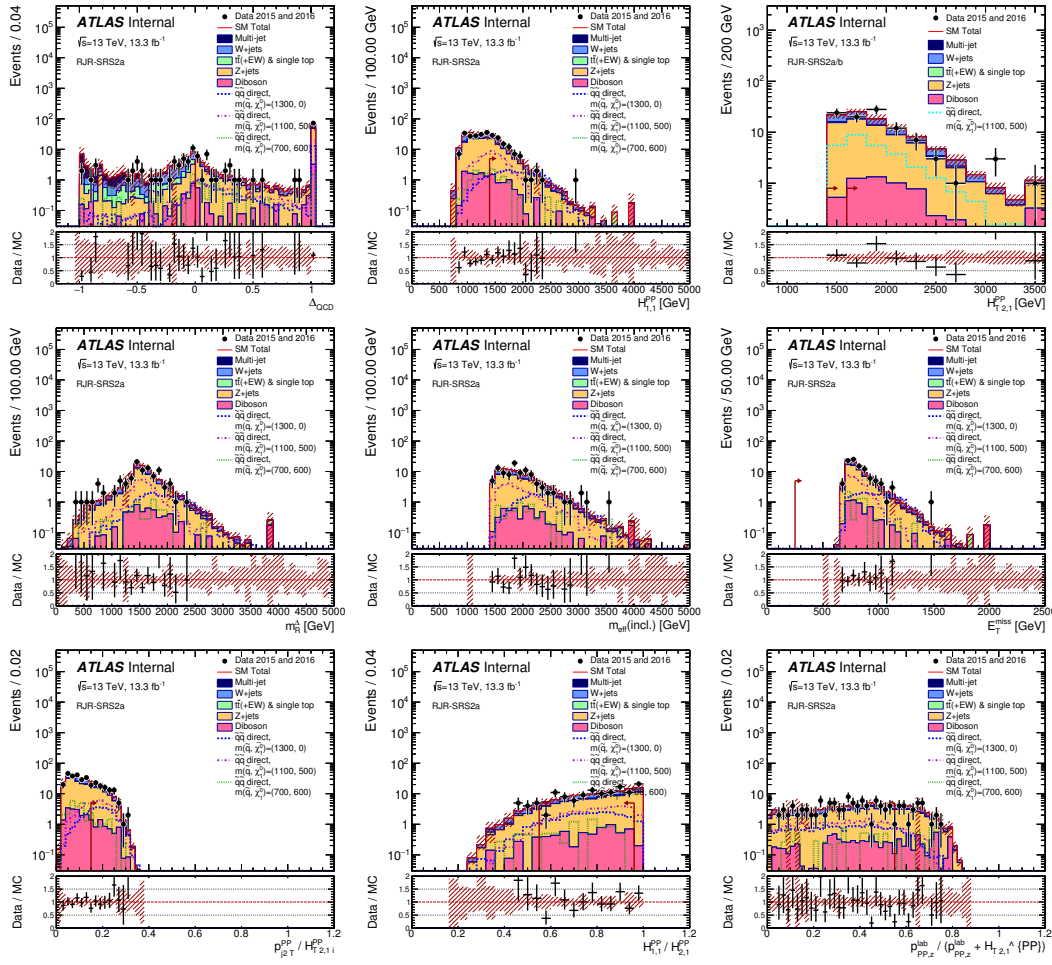


Figure 19

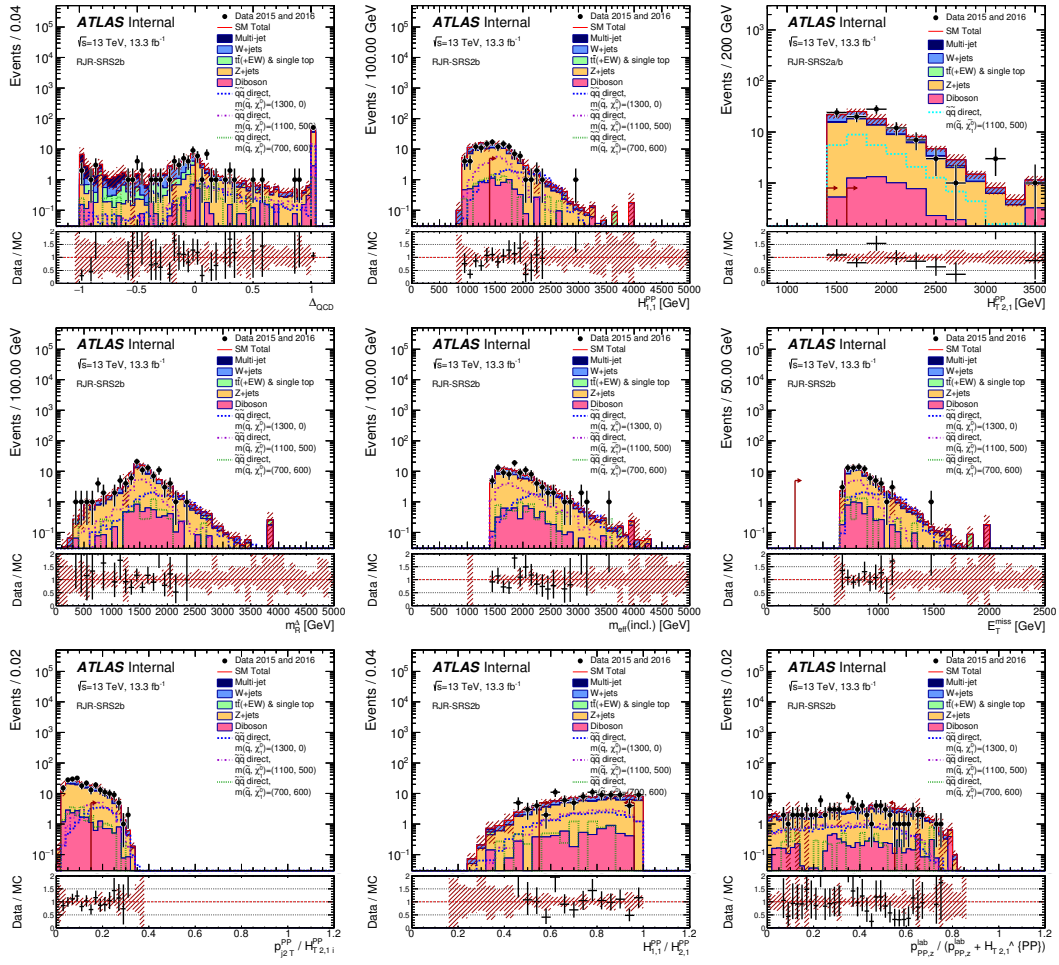


Figure 20

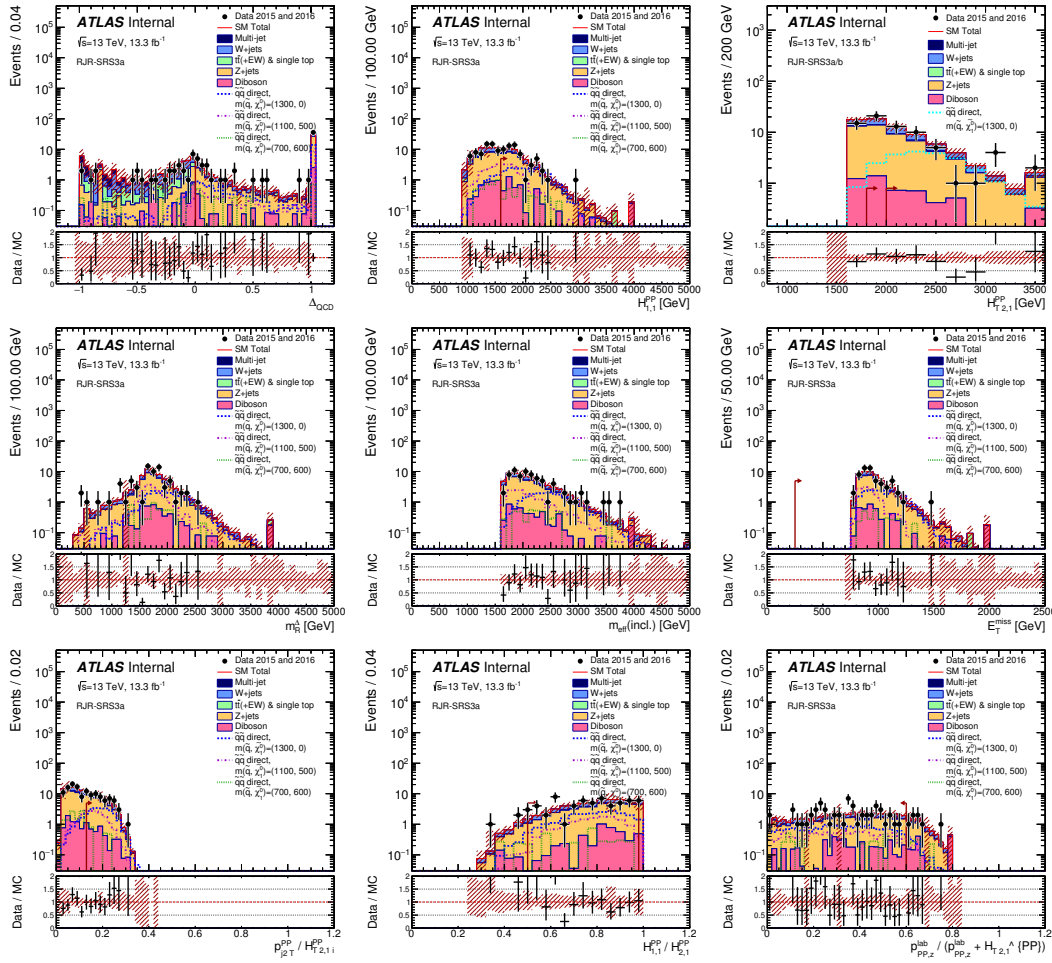


Figure 21

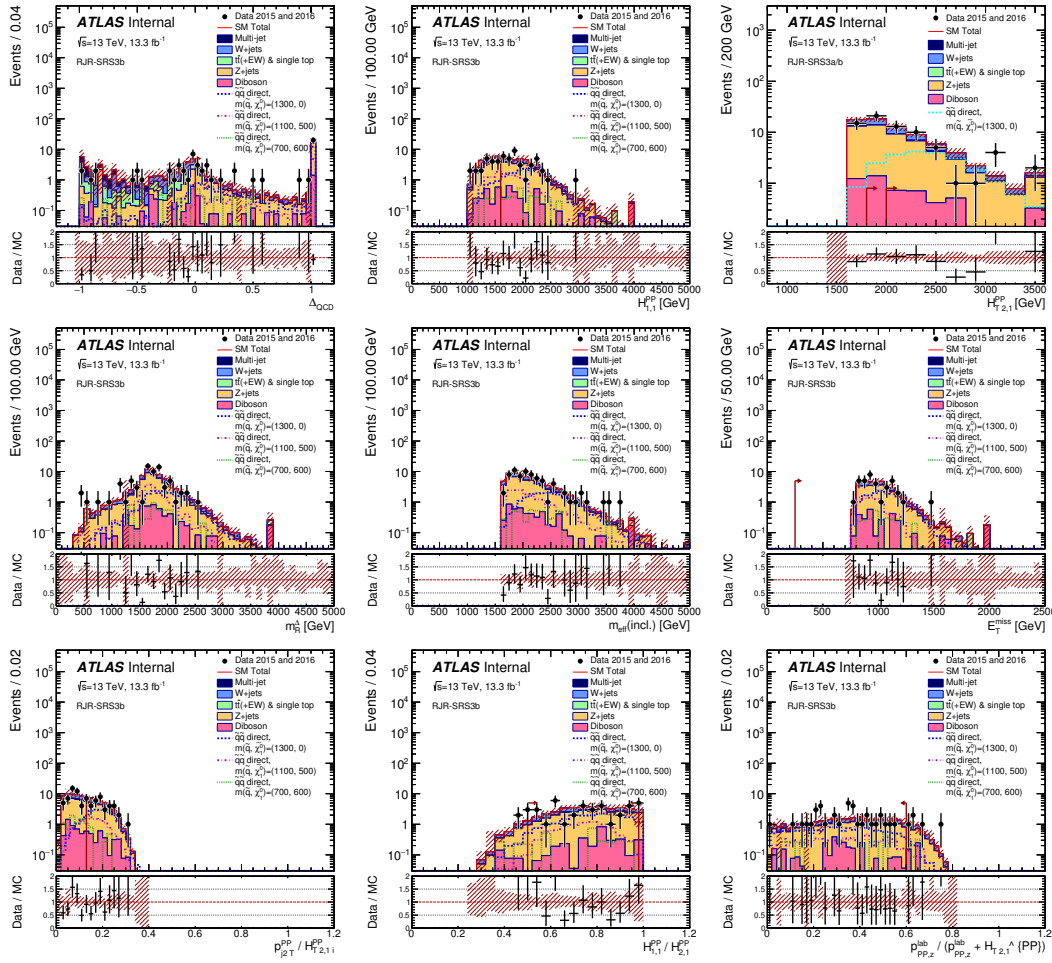


Figure 22